

Investigation of Pulverized, Pre-Dried Lignite Combustion under Oxy-Fired Conditions in a Large-Scale Laboratory Furnace

Von der Fakultät für Maschinenbau, Elektrotechnik und
Wirtschaftsingenieurwesen der Brandenburgischen Technischen
Universität Cottbus zur Erlangung des akademischen Grades eines
Doktor-Ingenieurs genehmigte Dissertation

vorgelegt von

Rodrigo Corrêa da Silva, M.Sc.

geboren am 08.02.1984 in Videira,
Bundesstaat Santa Catarina, Brasilien

Vorsitzender: Prof. Dr. rer. pol. habil. Daniel Baier (BTU Cottbus)

Gutachter: Prof. Dr.-Ing. Hans Joachim Krautz (BTU Cottbus)

Gutachter: Prof. Dr.-Ing. Fabian Mauß (BTU Cottbus)

Gutachter: Prof. Dr. Paulo Smith Schneider (UFRGS, Brasilien)

Tag der mündlichen Prüfung: 25. Februar 2013

Preface and Acknowledgments

Worldwide demand for energy is rapidly increasing and this trend is expected to continue over the coming years mainly in industrialized nations which account for the greatest use of power. Renewable resources are forecast to be a significant player in power generation but most of the future energy demand will be met by conventional fossil fuels. Coal will continue to be one of the major energy resources in the long term because of its abundant reserves, competitive low prices, and the flexibility to adjust to various operational demands. Therefore, the use of base-load power generation delivered by coal power stations is crucial for a safe energy supply, especially in coal-dependent countries. However, evidence suggests that the increase of average global temperature over the last decades is well correlated with the increase of atmospheric CO₂. Reduction of CO₂ emissions from coal-fired power stations can be achieved by improving the overall thermal efficiency, but substantial reduction can be obtained only by Carbon Capture and Sequestration (CCS).

Within this context, a strategic research program has been developed at the Chair of Power Plant Technology at the Brandenburg University of Technology Cottbus aimed at technologies for capturing CO₂ from the flue gas generated by coal-fired power plants. This research project is funded by the Federal Ministry of Education and Research (BMBF) within the framework of the InnoProfile program. The research activities are focused on the development of power plants with near-zero greenhouse gas emissions by applying oxy-fuel technology. The goal of the project is to develop a competitive oxy-fuel firing process based on the integration of power plant components, focusing on such critical technology gaps as combustion fundamentals. Additionally, strategies for the implementation of new technologies such as coal drying are to be studied in parallel to issues related to reliability, availability, and maintainability.

The work presented in this dissertation was carried out as part of this research program with the purpose of gaining an in-depth understanding of the behavior of pre-dried lignite combustion under oxy-fired conditions. The investigation includes theoretical studies and experimental activities based on a recently constructed test facility with a firing capacity of 0.40 MW_{th} conceived specifically for conducting investigations of pulverized coal combustion in oxy-fired environments. It is hoped that the present work will be of value to other researchers and engineers. The researcher will find experimental data useful for further analysis and the validation of mathematical models, while the engineer will appreciate the discussion of some important intricacies of oxy-coal combustion and key insights regarding burner settings and design concepts.

My respect and thanks goes out to everyone who supported this work and who are here gladly acknowledged. In the first place, my grateful thanks to the

Prof. Dr.-Ing. Hans Joachim Krautz for taking me on as a research assistant and for his subsequent interest and advice during this project. My sincere thanks to Dipl.-Ing. Alexander Lisk for his continual support during the entire project. I also express my gratitude to Dr.-Ing. Matthias Klatt for the fruitful discussions and valuable suggestions in the context of this work. Special thanks to my colleagues Raimo Kaufmann, Torsten Sanger, Martin Baldzer, Heinz Schallmea, and Jorg Waske, for their assistance during the commissioning of the test facility and for their efforts during the experimental activities. My gratitude also to Doris Seifert, who helped by analyzing the samples.

I am very thankful to Prof. Dr. rer. pol. habil. Daniel Baier, Prof. Dr.-Ing. Fabian Mau, and Prof. Dr. Paulo Smith Schneider (Federal University of Rio Grande do Sul, Porto Alegre, Brazil) for kindly reviewing the manuscript. Useful discussions during the project with Dr.-Ing. Bernd Schumann from Julich Research Institute and the colleagues from Korting Hannover AG, in special Dipl.-Ing. Marco Meyer, were greatly appreciated. My grateful thanks also to Prof. Dr. Edson Bazzo (Federal University of Santa Catarina, Florianpolis, Brazil) for encouraging me to take up the challenge of doing research in Germany.

My thanks to Matthias Schreiber who assisted me in my early days in Cottbus; to Stephanie Tappe for the first insights in oxy-combustion; to Kristin Schierack for the kindly help every time necessary, and to Tanin Kangwanpongpan, colleague and co-author of so many papers. Special thanks to the undergraduate students and interns: Sunil Ramachandra, Roland Cunha Montenegro, Arne Wagner, Enes Tamdogan, Felipe Meirelles, and Tran Quan Ahn, who assisted in the execution of the work presented in this thesis. To all my colleagues at the Chair of Power Plant Technology: my sincerely thanks for the great work atmosphere.

Finally, I express my gratitude to all my family and friends who supported my endeavors all throughout my life: to my mother, Ednise, who encouraged me in all aspects of my life and gave me the deepest parts of humanity; to my father, Osni, who passed away too young and too soon to see the full impact of his guidance and example; to my grandmother, Ieda, for her endearment; and to my cherished sister, Renata, for her fondness even miles away. My most sincere thanks to my lovely wife, Cristiane, the inspiration of my life, without whom I would not have had the will to journey to new lands.

Table of Contents

Preface and Acknowledgments	iv
Table of Contents	vi
Nomenclature	x
Abbreviation	xvi
Abstract.....	xviii
Kurzfassung.....	xx
1 Introduction	2
1.1 The Future of Coal Energy	2
1.2 Development Pathway of Oxy-Fuel Technology	5
1.3 Objectives and Present Contribution	6
1.4 Outline	7
2 Literature Review.....	10
2.1 Introduction.....	10
2.2 General Impacts of Oxy-Fired Conditions.....	10
2.3 The Physical Chemistry of Oxy-Coal Combustion.....	12
2.4 Considerations for Temperature and Flame Characteristics	15
2.5 Considerations for Heat Transfer	19
2.6 Considerations for Oxygen, Carbon Monoxide, and Carbon Dioxide ...	20
2.7 Considerations for Emissions of Nitrogen Oxides	22
2.8 Considerations for Emissions of Sulfur Oxides	28
2.9 Major Findings from Previous Studies and Remaining Research Issues	30
3 Experimental Method	34
3.1 Description of the Laboratory Facility	34
3.1.1 <i>Coal Feed System</i>	35
3.1.2 <i>Furnace</i>	36
3.1.3 <i>Staged Feed-Gas Burner</i>	37
3.1.4 <i>Flue Gas Scrubber</i>	39
3.1.5 <i>Other Components</i>	40
3.2 Instrumentation and Measurements.....	41
3.2.1 <i>Combustion Inputs and Outputs</i>	41

3.2.2	<i>Local Gas-Phase Temperature</i>	42
3.2.3	<i>Local Gas Species</i>	44
3.2.4	<i>Solid Sampling</i>	45
3.2.5	<i>Total Radiative Heat Flux</i>	45
3.2.6	<i>Surface Temperature and Heat Flux at the Water-Cooled Walls</i> 47	
3.2.7	<i>Flame Pattern and Peak Flame Temperatures</i>	48
3.2.8	<i>Sampling Points and Data Presentation</i>	49
4	Theoretical Study of Combustion-Related Parameters and Burner Aerodynamics	52
4.1	Introduction.....	52
4.2	Basic Combustion Parameters	52
4.2.1	<i>Mathematical Formulation</i>	52
4.2.2	<i>Oxygen-Fuel Ratio</i>	53
4.2.3	<i>Adiabatic Flame Temperature and Feed Gas Flow Rate</i>	54
4.2.4	<i>Flue Gas Composition</i>	56
4.3	Flow Pattern.....	57
4.3.1	<i>Mathematical Models</i>	58
4.3.2	<i>Computational Domain and Mesh Refinement</i>	61
4.3.3	<i>Test Cases and Boundary Conditions</i>	62
4.3.4	<i>Results</i>	63
4.3.4.1	<i>Mesh Analysis</i>	63
4.3.4.2	<i>Effect of Vane Angles</i>	65
4.3.4.3	<i>Effect of Feed Gas Distribution</i>	66
4.3.4.4	<i>Effect of Feed Gas Composition</i>	68
4.3.4.5	<i>Swirl Number</i>	73
5	Experimental Results and Discussion	76
5.1	Introduction.....	76
5.2	Operating Conditions	76
5.3	Flame Pattern	79
5.4	Peak Flame Temperatures.....	83
5.5	Flame Stability	85
5.6	Heat Transfer Performance	88
5.7	Carbon Monoxide Emission and Burnout Efficiency	93
5.8	Nitric Oxide Emissions	94

5.9	Sulfur Dioxide Emissions.....	98
5.10	Detailed In-Flame Measurements.....	99
5.10.1	<i>Local Gas-Phase Temperature</i>	101
5.10.2	<i>Local Oxygen and Carbon Dioxide Concentration</i>	106
5.10.3	<i>Local Carbon Monoxide and Methane Concentration</i>	112
5.10.4	<i>Local Nitric Oxide Concentration</i>	118
5.10.5	<i>Total Radiative Heat Flux</i>	122
6	Conclusions and Recommendations	126
6.1	Summary and Major Findings from the Theoretical Study.....	127
6.2	Summary and Major Findings from the Experimental Study	128
6.3	Suggestions for Further Study	132
7	References	134
Appendix A - Experimental Uncertainty Assessment		146
A.2	General Procedure for Determining Uncertainty	146
A.2.1	<i>Modeling the Measurement</i>	146
A.2.2	<i>Evaluating Standard Uncertainty</i>	146
A.2.3	<i>Determining Combined Standard Uncertainty</i>	148
A.2.4	<i>Determining Expanded Uncertainty</i>	148
A.3	Assessing Measurement Uncertainty of Input and Output Combustion Parameters	150
A.4	Assessing Measurement Uncertainty of Local Gas Temperature	167
A.5	Assessing Measurement Uncertainty of Peak Flame Temperatures	169
A.6	Assessing Uncertainty in Local Gas Species Measurement.....	170
A.7	Assessing Measurement Uncertainty of Total Radiative Heat Flux	176
A.8	Assessing Measurement Uncertainty of Local Heat Flux at the Water- Cooled Walls	178
Appendix B - Experimental Data Sets.....		180
B.1	Air-Flame	180
B.2	Oxy-Flame 1	194
B.3	Oxy-Flame 2	208
B.4	Oxy-Flame 3	222
B.5	Oxy-Flame 4	236

Nomenclature

Latin Letters

A	Cross sectional area	m^2
A_i	Internal area of the blackbody	m^2
A_o	Area of the opening of the blackbody	m^2
c_p	Specific heat at constant pressure	J/kg.K
c_0	Speed of light in vacuum (2.998×10^8 m/s)	m/s
C	Discharge coefficient of orifice plate	-
$C_{\epsilon 1}$ $C_{\epsilon 2}$ $C_{\epsilon 3}$	Model constants	-
C_A	Species concentration	-
C_μ	Empirical constant of turbulence model	-
d	Diameter of the orifice plate	m
D	Exit diameter of swirler	m
D	Diffusion coefficient	m^2/s
D_H	Hydraulic diameter	m
D_{mean}	Mean diameter of a particle size distribution	μm
D_{10}	10 th percentile of a particle size distribution	μm
D_{90}	90 th percentile of a particle size distribution	μm
f	Conversion factor of mg/m ³ to ppm	-
f	Functional relationship between measurand and input quantities	-
G_{ii}	Generation of turbulence kinetic energy	-
h	Planck's constant (6.626×10^{-34} J/s)	J/s
i_λ	Energy per unit wavelength	W/m ³ .sr

k	Boltzmann's constant (1.380×10^{-23} J/K)	J/K
k	Turbulent kinetic energy	kg/m.s^3
k	Coverage factor	-
\dot{m}	Mass flow rate	kg/h, kg/s
\bar{m}_i	Mass of element i per mass of coal	$\text{kg}_i/\text{kg}_{\text{coal}}$
M	Molecular mass of the feed or flue gas	kg/kmol
M_i	Molecular mass of specie i	kg/kmol
M_j	Molecular mass of specie j contained in the coal	kg/kmol
n	Number of repeated observations	-
N	Number of input quantities X_i on which measurand Y depends.	-
p	Probability; level of confidence	-
P	Pressure	Pa
P	Heat flux emitted by a surface	W/m^2
P_{ii}	Production of Reynolds stresses	-
\dot{Q}	Heat transfer rate; firing rate	kW
\bar{q}	Arithmetic mean or average of n independent observations q_k of randomly-varying quantity q	-
q_k	k_{th} independent repeated observation of randomly-varying quantity q	-
q''	Heat flux	kW/m^2
r	Radial distance	m
$r(x_i, x_j)$	Estimated correlation coefficient associated with input estimates x_i and x_j	-
R	Gas constant	J/mol.K

R	Exit radius of swirler	m
R	Recycle ratio	-
Re	Reynolds number	-
$s(\bar{q})$	Experimental standard deviation of the mean \bar{q} and standard uncertainty obtained from a Type A evaluation	-
$s^2(\bar{q})$	Experimental variance of the mean \bar{q}	-
$s^2(q_k)$	Estimate of the variance of the probability distribution of q	-
$s(q_k)$	Experimental standard deviation	-
S	Swirl number	-
S^c S^e	Source term	-
t	Time	S
T	Temperature	K, °C
$t_p(v_{\text{eff}})$	Factor from t-distribution for v_{eff} degrees of freedom corresponding to a given probability p	-
u	Axial component of the velocity vector	m/s
$u_c^2(y)$	Combined variance associated with output estimate y	-
$u_c(y)$	Combined standard uncertainty of output estimate y	-
u_i u_j u_k	Mean velocity components	m/s
u_i' u_j' u_k'	Fluctuating velocity components	m/s
$\overline{u_i' u_j'}$	Reynolds stress component	m^2/s^2
$u(x_i)$	Standard uncertainty of input estimate x_i	-
$u^2(x_i)$	Estimated variance associated with input estimate x_i	-
$u(x_i, x_j)$	Estimated covariance associated with two input	-

	estimates x_i and x_j	
U	Expanded uncertainty of output estimate y	-
U	Axial velocity of the primary stream	m/s
\dot{V}	Volume flow rate	m ³ /s, m ³ /h
$W_{\text{ash,coal}}$	Ash mass fraction in the input coal (dry basis)	-
$W_{\text{H}_2\text{O, waf}}$	Water mass fraction in the coal (wet and ash free)	-
$W_{j,\text{daf}}$	Mass fraction of specie j in the coal (dry and ash free)	-
$W_{j,\text{ar}}$	Mass fraction of specie j in the coal (as received)	-
$W_{\text{ash,sample}}$	Ash mass fraction in the sample (dry basis)	-
w	Tangential component of the velocity vector	m/s
x	Volume fraction	vol%
x_i	Estimate of an input quantity	-
$x_i \ x_j \ x_k$	Space directions	m
X_i	Input quantity	-
y_i	Concentration of specie i on dry basis	mg/m ³
y	Estimate of measurand	-
\bar{y}	Average of observations	-
Y	Measurand	-

Greek letters

β	Ratio between the orifice diameter and pipe inner diameter	-
ΔP	Differential pressure	Pa
ε	Turbulence dissipation rate	kg/m.s

ε	Emissivity	-
ε	Expansion coefficient of an orifice plate	-
ε_0	Emissivity of blackbody	-
$\eta_{j \rightarrow i}$	Conversion ratio of fuel-N to NO and fuel-S to SO ₂	%
θ	Angle at which the opening is viewed from the back of the furnace	Degrees
κ	Isentropic exponent	-
λ	Excess oxygen ratio; stoichiometric ratio	-
λ	Wavelength in free space	m
σ	Stefan-Boltzmann constant ($5.7 \times 10^8 \text{ W/m}^2\text{K}^4$)	$\text{W/m}^2\cdot\text{K}^4$
σ_ε	Turbulent Pradtl number for dissipation rate	-
σ_k	Turbulent Pradtl number for kinetic energy	-
μ	Dynamic viscosity	Pa.s
μ_T	Turbulent viscosity	Pa.s
ν	Degrees of freedom	-
ν_{eff}	Effective degrees of freedom	-
ρ	Density	kg/m^3
φ_i	Emission rate of specie i	mg/MJ
ψ	Particle burnout	%

Abbreviation

ANSI	American National Standards Institute
ar	As received
ASU	Air separation unit
BMBF	Federal Ministry of Education and Research
BTU	Brandenburg University of Technology Cottbus
CCD	Charged coupled device
CCS	Carbon capture and storage
CFB	Circulating fluidized bed
CFD	Computational fluid dynamics
CPU	Central processing unit
daf	Dry and ash-free
DF	Degrees of freedom
DIN	German Institute for Standardization
EN	European Norm
ESP	Electrostatic precipitator
FGC	Flue gas condenser
FGD	Flue gas desulfurization
FVM	Finite volume method
GPU	Gas processing unit
GUM	Guide to the expression of uncertainty in measurement
IFRF	International Flame Research Foundation
IGCC	Integrated gasification combined cycle

IRZ	Internal recirculation zone
ISO	International Organization for Standardization
JCGM	Joint Committee for Guides in Metrology
LHV	Lower heating value of the fuel
OFR	Oxygen-fuel ratio
QUICK	Quadratic upwind interpolation for convective kinematics
PC	Pulverized coal
PRESTO	Pressure staggering option
PFG	Product flue gas
RANS	Reynolds-averaged Navier Stokes
RFG	Recycled flue gas
RNG	Re-Normalization Group
RSM	Reynolds stress model
RTD	Resistance temperature detector
SIMPLE	Semi-implicit method for pressure linked equations
SST	Shear stress transport
STP	Standard temperature and pressure (273.15 K and 100 kPa)
TD	Turn down value of a differential pressure transmitter
TGA	Thermogravimetric analysis
URL	Upper range limit
URV	Upper range value
UV	Ultraviolet
VDI	Association of the German Engineers
waf	Wet and ash-free

Abstract

The oxy-fuel combustion process with subsequent CO₂ storage has received attention as a promising technology for capturing CO₂ from fossil fuel power plants. Recent progress in understanding pulverized coal combustion under oxy-fired conditions is attributable in part to studies performed at laboratory bench-scale. Previous investigations have underlined some significant differences between conventional air-fired and oxy-fired combustion with regard to temperature, heat flux distribution, and pollutant emissions. While most studies provide information on the impacts of O₂ concentration in the feed gas, the impact of burner configuration and operating settings on oxy-coal combustion have been investigated by only a handful of studies. The present study addresses the impact of oxy-fired conditions on the chemistry and dynamics of pulverized coal flames generated by a staged feed-gas burner operating with pre-dried lignite. Investigations were carried out in a newly constructed test facility where the combustion takes place in a horizontal up-fired furnace with a rated capacity of 0.40 MW_{th}. Since the focus of this work is on adapting oxy-fuel combustion techniques to existing furnaces, great emphasis is placed on maintaining flame temperatures and heat transfer similar to that of conventional air combustion.

The strategy adopted to investigate the impacts of burner settings is divided into theoretical and experimental investigations. In the theoretical study, the combustion-related parameters are calculated based on thermodynamic balances and act as a background for the definition of some important operating settings. Non-reacting flow simulations which include the burner and part of the furnace are performed using a CFD commercial code aimed at a qualitative evaluation of feed gas distribution and swirl strength on the flow pattern formed in the near burner region. These predictions assist in the interpretation of the experimental data and in the calculation of the swirl number at the exit of the burner. During the experimental investigations, the characteristics of diffusion flames were first investigated in a parametric study to evaluate the impact of secondary swirl numbers at three levels and secondary/tertiary flow ratios on the overall combustion performance. The second part of the test program involved detailed in-flame measurements for selected flames. Measurements of local gas temperature, gas species concentrations, and radiative heat flux were performed with standard water-cooled probes with special focus on the near burner region. Theoretical and experimental studies are also carried out under air-fired conditions and used as a benchmark throughout this study.

The overall O₂ fraction upstream of the burner was kept at 31 vol% and was defined with basis on a similar adiabatic flame temperature as air-firing. Flame stabilization was shown to be strongly dependent on the O₂ fraction of the primary stream, feed gas distribution between the secondary and tertiary registers, and strength of the secondary swirl. Type-1 flames operating at a stoichiometric ratio

of 1.17 were generated under air-fired and oxy-fired conditions and investigated in detail. Detailed flow pattern and flame structure studies show evidence of radial flame stratification consistent with gradual O₂ admixing to the central fuel jet. Increasing the swirl number and the secondary/tertiary flow ratio enhances the mixing of coal particles and increases the temperatures close to burner. Much lower temperatures on the flame axis are observed under oxy-fired conditions. In the same region, higher CO concentrations were also observed, possibly as a result of CO₂ dissociation and/or gasification reactions by water vapor and CO₂ which contribute to lower temperatures. Very low CO concentration at the furnace exit and high particle burnout indicate that oxy-fired conditions are not an obstacle to achieving a high combustion efficiency for type-1 flames. Although SO₂ concentrations were higher under oxy-fired conditions, the emission rates were very similar, indicating that SO₂ emissions are exclusively dependent on the sulfur content of the coal. Experimental data obtained from the parametric study and in-flame measurements suggest great potential for NO abatement through flame aerodynamics for oxy-coal combustion. The experiments demonstrate that feed gas staging in a burner is an effective technique for improving the flame stratification in fuel-rich and fuel-lean zones. In particular, a combination of high swirl and high secondary/tertiary flow ratio results in significant NO reduction.

Kurzfassung

Oxyfuel-Verbrennung mit anschließender Speicherung von CO₂ erhält viel Aufmerksamkeit, da sie als eine vielversprechende Technologie zur CO₂-Abscheidung bei fossilen Kraftwerken gilt. Jüngste Fortschritte im Verständnis der Kohlenstaubverbrennung unter Oxyfuel-Bedingungen sind zum Teil auf Untersuchungen im Labormaßstab und Testanlagen zurückzuführen. Frühere, grundlegende Untersuchungen haben einige bedeutende Unterschiede zwischen luftgefeuerter und sauerstoffgefeuerter Verbrennung hinsichtlich Temperaturen, Wärmestromverteilung und Schadstoffemissionen aufgezeigt. Während in den meisten Studien Informationen über die Auswirkungen der O₂-Konzentration im Speisegas und die Auswirkungen der Brenneinstellungen nur in wenigen Arbeiten untersucht wurden, befasst sich die vorliegende Promotion mit dem Einfluss der Oxyfuel-Verbrennung in einem gestuften Kohlestaubbrenner. Die Untersuchungen wurden in einer kürzlich erbauten Testanlage durchgeführt. Die Verbrennung erfolgt in einem zunächst horizontal und dann vertikal verlaufenden Verbrennungsraum mit einer Nennleistung von 0,40 MW_{th}. Da der Schwerpunkt dieser Arbeit auf der Anpassung bestehender Feuerungen auf die Oxyfuel-Verbrennung liegt, wird großer Wert auf die Beibehaltung der Flammentemperatur sowie der Wärmeübertragung, wie sie bei konventioneller Luftfeuerung vorherrschen, gelegt.

Die Vorgehensweise zur Untersuchung der Auswirkungen von Brenneinstellungen ist grundsätzlich in theoretische und experimentelle Betrachtungen unterteilt. In dem theoretischen Teil werden die relevanten Verbrennungskenngrößen auf Basis thermodynamischer Gleichgewichte berechnet und dienen als Grundlage zur Festlegung einiger wichtiger Betriebsbedingungen. Mithilfe eines kommerziellen CFD-Codes werden Simulationen einer nicht-reagierenden Strömung im Bereich des Brenners und Teilen des Feuerraums durchgeführt, um die Verteilung des Speisegases und Drallstärke im Brennernahbereich qualitativ bewerten zu können. Diese Vorhersagen werden zur Unterstützung der physikalischen Interpretationen der Daten und zur Berechnung der Drallzahl am Brenneraustritt angewendet. Während der experimentellen Untersuchungen wurden die Charakteristika der Diffusionsflammen zunächst in einer parametrischen Studie untersucht, um den Einfluss der Drallzahlen für drei verschiedene Werte sowie der Massenstromverhältnisse von sekundären zu tertiären Strömen auf die gesamte Verbrennung auszuwerten. Der zweite Teil des Testprogramms enthielt detaillierte Messungen innerhalb der Flamme für ausgewählte Betriebspunkte. Als Referenz diente die Luftverbrennung; insgesamt wurden vier Oxyfuel-Flammen untersucht. Messungen der lokalen Gastemperatur, der Gaszusammensetzung und des Strahlungswärmeaustauschs wurden mit standardisierten, wassergekühlten Messsonden insbesondere im Nahbrennerbereich durchgeführt.

Der O₂-Anteil vor dem Brenner wurde bei 31 Vol.-% gehalten und auf Grundlage der gleichen adiabatischen Flammentemperatur wie bei luftgefeuerter Verbrennung definiert. Messungen innerhalb der Flamme zeigten, dass die Verteilung der einfallenden Wärmestrahlung entlang der Flammenlänge nur geringfügig verändert ist, was darauf schließen lässt, dass die Festlegung des O₂-Anteils für die Oxyfuel-Verbrennung passend gewählt wurde. Die Flammenstabilisierung erwies sich als stark abhängig vom O₂-Anteil im Primärstrom, der Speisegas-Verteilung zwischen den sekundären und tertiären Zuführungen und der Drallstärke. Typ 1 Flammen mit einem stöchiometrischen Verhältnis von 1,17 wurden unter Luft- und Oxyfuel-Bedingungen erzeugt und detailliert untersucht.

Aus detaillierten Untersuchungen der Strömungsmuster und Flammenstrukturen ergaben sich Hinweise auf eine radiale Flammenschichtung mit schrittweiser O₂-Entmischung in dem zentralen Kohlejet. Die Erhöhung der Drallzahl und des Verhältnisses von Sekundär- zu Tertiär-Strömung verbessert die Vermischung der Kohlepartikel untereinander und erhöht die Temperaturen in der Nähe des Brenners. Eine bemerkenswerte Reduzierung der Temperaturen auf der Flammenachse wurde unter Oxyfuel-Bedingungen beobachtet. In der gleichen Region wurden höhere CO-Konzentrationen als mögliche Folge der CO₂-Dissoziation und/oder der Vergasungsreaktion mit Wasserdampf und CO₂ beobachtet. Sehr niedrige CO-Konzentrationen am Feuerraumaustritt, die einem hohen Partikelaustritt zugeordnet werden, zeigen an, dass Oxyfuel-Bedingungen hohe Wirkungsgrade für Typ 1 Flammen nicht verhindern. Obwohl die SO₂-Konzentrationen bei Oxyfuel-Bedingungen höher waren, waren die Emissionsraten sehr ähnlich, was darauf hinweist, dass die SO₂-Emissionen ausschließlich vom Schwefelgehalt der Kohle abhängig sind. Die aus der Parameteruntersuchung sowie Messungen in der Flamme erhaltenen experimentellen Daten deuten darauf hin, dass ein großes Potenzial zur NO-Reduktion durch die Flammenaerodynamik für die Oxyfuel-Verbrennung besteht. Die Experimente zeigten, dass die gestufte Zufuhr der Gasströme in einen Brenner eine effektive Technik zur Verbesserung der Flammenschichtung in brennstoffreiche und brennstoffmagere Zonen ist. Insbesondere die Kombination von hohem Drall und hohem Verhältnis von Sekundär- zu Tertiär-Strömung resultierte letztendlich in eine signifikante NO-Reduktion.

1 Introduction

1.1 The Future of Coal Energy

Fossil fuels will continue to dominate energy supplies for the conceivable future [1-6]. Within this context, coal use will continue to grow solidly, remaining the leading fuel for power generation and an essential input for other industrial applications. Fossil fuels will account for around 85% of world energy supply in 2030, with coal providing over 21% [1]. However, while coal makes an important contribution to economical and social development worldwide, its environmental impact is a challenge, with the release of pollutants being the main problem. The pollutants include sulfur and nitrogen oxides (SO_x and NO_x), and particulate and trace elements such as mercury. More recently, greenhouse gas emissions, including (CO_2) and methane (CH_4), have become a concern because of their link to climate change [4,7].

Coal is one of the biggest contributors to anthropogenic CO_2 emissions into the atmosphere [4,5]. Research and development efforts aim at finding technologies to meet this new environmental challenge. An important step in reducing CO_2 emissions from coal combustion is improving the thermal efficiencies of coal-fired power plants, by such strategies as the application of supercritical and ultra-supercritical systems and fuel drying technologies. Although much has been done to improve thermal efficiency, it is still not enough to achieve the levels established in international agreements [8,9]. One of the most promising options for reducing CO_2 emissions from coal use is Carbon Capture and Storage (CCS), which offers the potential for moving towards near-zero emissions to the atmosphere in the future [4-6,8,9]. This technology strips CO_2 from the flue gases and disposes of it in such way that it do not emit to the atmosphere. After flue gas treatment, almost-pure CO_2 is compressed to a supercritical stage for transport and geological storage [4,10]. The liquid CO_2 is pumped deep underground and flows into the pores between the grains of rock. Geological features being considered for CO_2 storage include gas or oil fields, deep saline aquifers and unmineable coal seams [10,11]. Alternatively, the CO_2 could be applied as a medium for enhancing oil recovery or used in various industrial applications [12].

Among the available CO_2 capture technologies, three options are generally pointed to as having the best potential for commercial applications [4,6,8,9,13]:

- i Post-combustion capture systems,
- ii Pre-combustion capture systems, and
- iii Oxy-fuel combustion.

The post-combustion capture process involves a conventional combustion system combined with flue gas scrubbing through a chemical absorbent or dry CO₂ adsorption at higher temperatures [13,14]. Pre-combustion capture involves supplying a combined gas and steam turbine process (IGCC - Integrated Gasification Combined Cycle) with a synthetic gas from coal gasification. The gas, found behind the gasifier and the shift converter, consists of CO₂ and H₂. CO₂ capture can be performed relatively simply with the aid of a physical absorption process, so that almost pure hydrogen is then available as fuel for a gas turbine and steam cycle or in fuel cells, or a combination of both [13]. The oxy-fuel process involves combustion of coal in a mixture of recycled flue gas and pure O₂ instead of air. By avoiding the introduction of N₂ into the combustion cycle, the amount of CO₂ in the power plant exhaust stream is greatly concentrated, making it easier to capture and compress. In addition, oxy-fuel combustion can be applied to conventional coal combustion plants with only minor modifications. All three of these capture technologies are illustrated in the Figure 1.1.

Each of these options has its own particular advantages and disadvantages. For instance, pre-combustion and oxy-fuel technologies require an O₂ production unit, while a CO₂ removal system becomes necessary in the case of both post-combustion and pre-combustion [9]. Post-combustion and oxy-fuel technologies offer the possibility of being retrofitted to an existing plant. However, the implementation of the oxy-fuel combustion technology will induce a larger change of the plant configuration compared to the post-combustion process [15]. Higher capital costs are associated with construction of pre-combustion plants and IGCC plants are generally more complicated systems than oxy-fuel and post-combustion technologies that apply commercially proven equipments and operate in the same manner as a conventional pulverized coal-fired plant [14-16]. However, all three technologies increase higher production costs due to the addition of CO₂ compression, transport, and storage.

Although several studies indicate that oxy-fuel combustion might be the most energy and cost efficient technology [16,17], it is generally thought that it cannot yet be predicted which of three main concepts will prove most successful from a technological and economic perspective [6,8,9,15,18-21]. All three main options should be developed and demonstrated in fully-integrated large scale test platforms in order to prove their practicality and to reduce costs. Additionally, public acceptance is an important pre-condition for the large-scale deployment of such technologies [16].

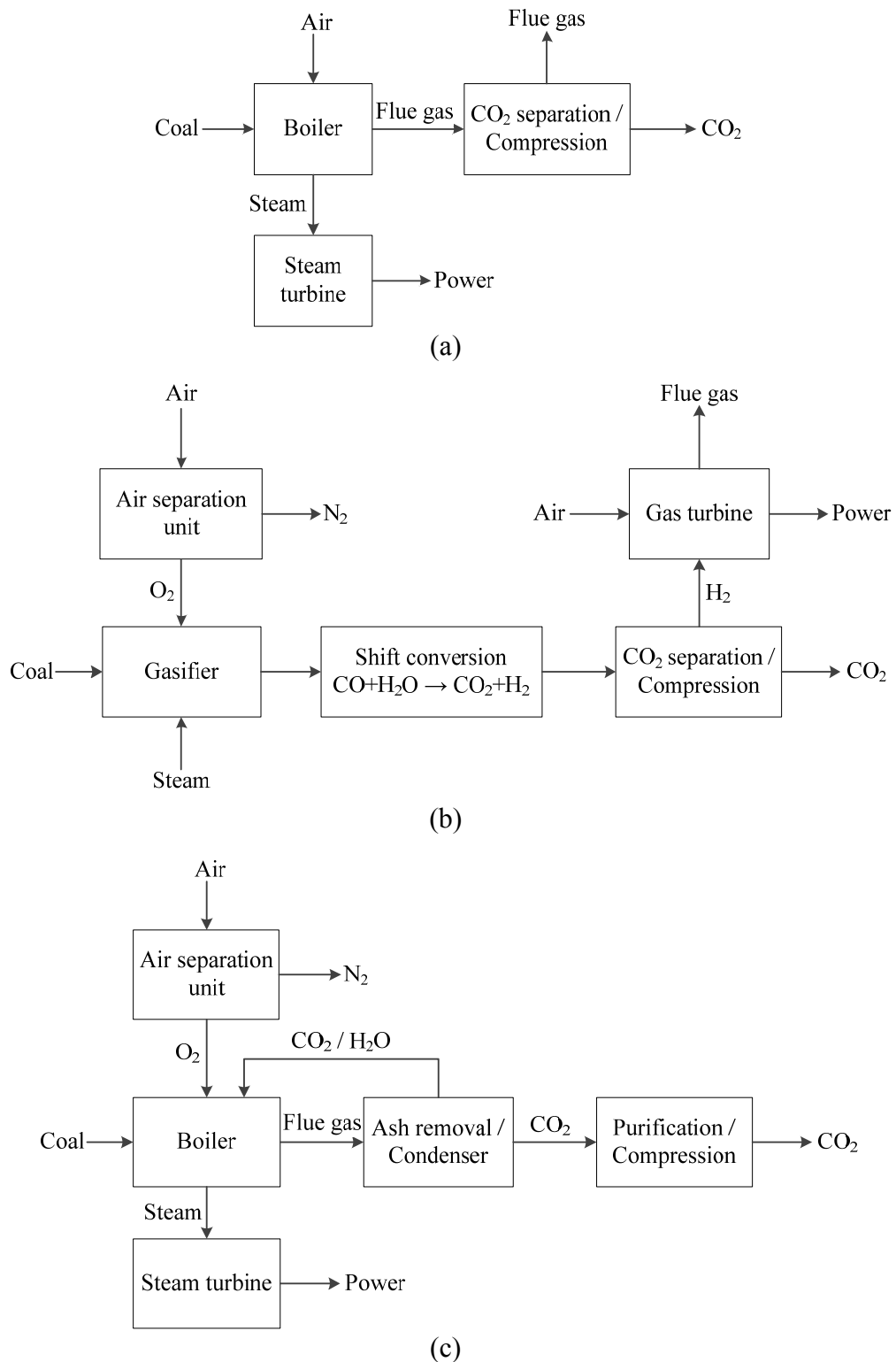


Figure 1.1: Process alternatives for CCS technologies: (a) post-combustion, (b) pre-combustion, and (c) oxy-fuel combustion. Adapted from [9].

1.2 Development Pathway of Oxy-Fuel Technology

The oxy-fuel concept was proposed almost simultaneously in 1982 by Abraham et al [22] and by Horn and Steinberg [23]. Abraham and his co-workers focused on development of a technology able to produce a CO₂-rich flue gas to enhance the oil recovery, whereas Horn and Steinberg proposed this technology mainly for mitigating the emissions of CO₂ from fossil fuel power plants. More interest for reducing CO₂ emissions from power plants started in the 1990s, when research began on oxy-fuel combustion [24-27]. Since then, several research projects have been carried out worldwide and a detailed overview can be found elsewhere [9,13,15,21]. In Germany, research first began in 2005 with a joint project of the BTU Cottbus and several companies. The goal of the project was to further understanding of the impacts of recycled flue gas on the various operational processes. A 0.50 MW_{th} test facility with a cycloidal furnace was constructed next to the 3.00 GW Jämschwalde power plant and used to carry out several trials over the course of a four-year research program [28-30].

The outcome of this research provided the necessary information for the construction of the world's first oxy-fuel pilot plant. This 30 MW_{th} pilot was built south of Cottbus at the Schwarze Pumpe power plant and is one of the key milestones on the way towards a commercial scale power plant [31-33]. During the last few years, global research on oxy-coal power generation has also increased to the point where several other demonstration projects are underway. Demonstration plants are already in operation or in development in South Korea [34], Australia [35], the United States [36], and Spain [37]. Together, these demonstration projects will be the last development step prior to the technology being commercially introduced [38,39]. A list of the ongoing and proposed large-scale oxy-coal combustion demonstration projects are presented in Table 1.

The oxy-fuel technology requires more research to bring it closer to the commercial stage. Problems identified during this process will drive future research and development [38]. Items which currently still require research include the development of new and less expensive O₂ generation technologies, reduction of air leakage into the flue gas system, increase in plant efficiency, assessment of retrofits for electricity cost and cost of CO₂ avoided, and necessity of flue gas treatment [9,13,15,21]. In terms of the combustion process, further investigations into the physical and chemical characteristics of pulverized coal flames, pollutant formation and destruction, and heat transfer performance are still necessary.

Table 1: Overview of ongoing and proposed demonstrations projects. Adapted from [40].

Project	Location	Power	Scale	Firing Technology	CO ₂ Capture	Start
Jupiter	USA	22 MW _{th}	Pilot	PC	No	2007
B&W pilot plant	USA	30 MW _{th}	Pilot	PC	No	2008
Oxy-coal UK	UK	40 MW _{th}	Pilot	PC	No	2009
Alstom Windsor	USA	15 MW _{th}	Pilot	PC	No	2009
Schwarze Pumpe	Germany	30 MW _{th}	Pilot	PC	Yes	2008
Callide-A	Australia	30 MW	Pilot	PC	Yes	2011
Compostilla	Spain	17 MW	Pilot	CFB	Yes	2012
Jamestown	USA	43 MW	Demo	CFB	Yes	2013
FutureGen	USA	200 MW	Demo	PC	Yes	2015
Compostilla	Spain	300 MW	Demo	CFB	Yes	2015
Youngdong	South Korea	100 MW	Demo	PC	Yes	2016
Black Hills	USA	100 MW	Demo	PC	Yes	2016

1.3 Objectives and Present Contribution

This work furthers the development of oxy-fuel technology with a methodical investigation of the combustion process of pulverized coal. The research is based mainly on experimental activities carried out in a large-scale laboratory furnace constructed recently by the Chair of Power Plant Technology at the Brandenburg University of Technology Cottbus. In this test facility, the combustion process takes place in a horizontal up-fired furnace with a rated capacity of 0.40 MW_{th} fired by an industrial-type burner. Because of the extremely high costs and scarcity of experimental furnaces, the body of data on pulverized coal firing in large-scale burners under oxy-fired conditions is very small given the complexity of the phenomenon. This work attempts to fill the gap between small laboratory scale experiments and full scale furnaces.

The coal applied in this research is Lusatian pre-dried lignite which is abundantly available and affordable in the region surrounding Cottbus and supplies some of the main coal power plants in Germany. The oxy-fuel literature has expanded drastically over the last few years but has focused mainly on the impacts of oxy-fired conditions on bituminous, sub-bituminous or anthracite coals, leaving lignite relatively unexplored. The resulting knowledge gap regarding the effects of oxy-firing of lignite is another focus of this work.

The fundamental issues and technological challenges of oxy-coal combustion are addressed in this study. While previous research analyzed the impact of the O₂ content in the feed gas on relatively small-scale and down-fired combustors, this work focuses on the influence of swirling effects and feed gas distribution on pulverized coal flames. The fluid flow dynamics in the near burner field are investigated by detailed non-combustion numerical simulations. Prior to any combustion experiments, the flow patterns generated by the burner are studied and

important parameters such as swirl numbers are also determined and applied in assessing the experimental data.

Parametric studies of swirl intensity and feed gas distribution are carried out experimentally to investigate the feasibility of oxy-firing using a staged feed-gas burner. The overall impacts of oxy-fired conditions on key parameters such as flame pattern, peak flame temperature, stability limits, and emission and heat flux performance are evaluated. Selected flames are also thoroughly tested using in-flame measurements of gas temperature, gas species concentration, and incident radiation heat flux. This work presents new swirl burner data, which emphasize the near burner region and supplement the limited quantity of data amassed in other experimental furnaces scattered worldwide. Theoretical and experimental studies are also carried out under air-fired conditions and used as a benchmark throughout this study. Apart from the investigation of the oxy-coal combustion, parallel efforts are also made to determine the accuracy of experimental data.

1.4 Outline

A comprehensive review of the literature on the oxy-fuel technology is presented in Chapter 2. The concept of the flue gas recirculation ratio and its impacts on burner and furnace design are discussed. Experimental studies carried out in small-scale reactors are reviewed in order to compare the combustion chemistry in O_2/CO_2 and in O_2/N_2 environments. Then, the experimental data from studies conducted in laboratory and pilot-scale facilities are discussed. Flame characteristics, temperatures, heat transfer, species concentration, and pollutant formation and destruction are discussed in turn. The most relevant findings based on scientific publications are summarized and critical gaps identified.

Chapter 3 presents the materials and methods applied in this research, including a detailed description of the 0.40 MW_{th} laboratory facility. The physical characteristics of the applied instrumentation are discussed along with the method and theory behind each measurement technique. A theoretical study aimed at predicting the flow pattern in the near burner region and to evaluate the burner parameters is outlined in Chapter 4. The mathematical formulation applied to the calculation of basic combustion-related parameters, including the oxygen-fuel ratio, adiabatic flame temperature, and flue gas composition is presented and followed by a discussion of results. The numerical strategy for investigating the flow dynamics in the near burner field is also fully described. The procedure for the solution of the conservation equations is discussed, including a description of the turbulence model adopted for the solution of Reynolds stresses. Velocity profiles and flow patterns are compared by varying the feed gas composition, i.e. air or oxy-fuel, and its distribution among the burner registers. The impacts of the

degree of secondary swirl are also addressed. The swirl number for the secondary stream is also calculated and used in interpreting the experimental results.

The experimental results are presented and discussed in Chapter 5. The results obtained during the parametric study to determine the impacts of burner operating conditions on combustion-related parameters and heat transfer performance are discussed. Based on the evaluation of flow dynamics and burner characteristic parameters by non-reacting simulations, the flame pattern and stability limits are investigated. It is also shown to what extent the feed gas distribution and swirling flows reduce pollutant emissions under oxy-fired conditions. The second part of the experimental test program involved detailed mapping of selected flames from the parametric study. Detailed in-flame profiles of local gas temperature, gas species, and radiative heat flux are reported and carefully examined.

Chapter 6 summarizes the main conclusions and findings obtained in this work. The limitations of the present study and recommendations for further work are then presented. The uncertainty of the experimental data obtained in the study is assessed in the Appendix A. The approach used in the evaluation of the experimental data accuracy is summarized and then followed by the individual evaluation of uncertainty of each type of measurement. Appendix B contains the complete data sets collected during detailed in-flame measurements.

2 Literature Review

2.1 Introduction

The literature on the coal reaction process is very extensive and it is beyond the scope of this work to provide a comprehensive treatment of theories of coal combustion. For detailed information on this topic, the reader is referred to the many publications quoted in the text and to extensive fundamental literature such as [41-44], which contains a wealth of useful data and information. In this chapter, emphasis is placed on the impact of oxy-fired environments on the combustion mechanism, and pollutant formation and destruction. Selected experimental data are presented to illustrate the behavior of oxy-coal flames in various laboratory-scale furnaces and the main differences and relationships between air and oxy-firing combustion are discussed.

2.2 General Impacts of Oxy-Fired Conditions

Burning coal in a pure O₂ atmosphere produces higher temperatures within the furnace and a reduced volume of flue gas compared to conventional combustion process. To control flame temperature and dilute corrosive substances in oxy-coal combustion, a portion of flue gas is cleaned and recycled back to the furnace [3,9,15,21,40]. The high temperatures associated with corrosive constituents such as SO₂, SO₃, and water vapor would exponentially increase corrosion rates and much higher metal temperatures will require higher grade and therefore more expensive materials. In addition, to keep the same conditions of heat transfer in the furnace, it becomes necessary to make up for the missing N₂. The effects of the oxy-fuel atmosphere on combustion and heat transfer will be detailed in the following sections. Higher temperatures allow for smaller heat transfer surfaces due to higher gradients. However, the expected cost savings due to decreased heat transfer surface in the boiler is quickly overcome by the increased material costs [16].

Concepts for the second or third generation of oxy-fuel power plants with low or no recycle rates of flue gas have been proposed [17,45]. The problem with these designs is that the increased boiler cost outweighs the costs savings in the equipment downstream of the furnace, and the reduced electric power requirement for the flue gas recirculation fans [16]. Retrofitting the first generation of coal power plants would leave the boiler geometry unchanged. To maintain the same heat transfer conditions as air-firing, a rather significant recirculation rate of flue gas (typically around two thirds the volume flow of flue gas) becomes necessary [9,13,19,21,46,47]. One of the most important parameters in a practical oxy-fuel system therefore is the recycle ratio which is defined as:

$$R = \frac{\dot{m}_{\text{RFG}}}{\dot{m}_{\text{RFG}} + \dot{m}_{\text{PFG}}} \quad (2.1)$$

The position of the flue gas extraction is mainly determined by the fuel quality and, in particular, by the coal's sulfur content, which determines the acid dew point and corrosion potential [48]. Two recycle streams are necessary: a primary stream for coal transport and a secondary stream, which provides the additional gas ballast to the burners and furnace. The primary stream should be cooled, scrubbed, and dried before being reheated and entering the coal mills [15,46]. In the case of secondary stream, several configurations were evaluated by Nakayama et al [49] and Dillon et al [50]; the general consensus is that wet flue gas recirculation is the best strategy. Even though for the recirculation fan, a dry recycle would be most favorable, this option requires higher capacities of the preheater, cooling, and drying units compared to the wet recycle case.

A wet recirculation of the flue gas without desulfurization would lead to several problems in the burners, furnace, heat exchanger, and pipes. It results in sulfur and chloride levels in the furnace that are three to four times higher than air-firing [13]. When burning low-sulfur coals, the flue gas should be tapped for recirculation downstream of the dust removal; with higher-sulfur coal, desulfurization of the flue gas should be upstream of the recirculation bleed/tap [48]. Figure 2.1 shows an overview of the oxy-fuel technology for a high-sulfur coal.

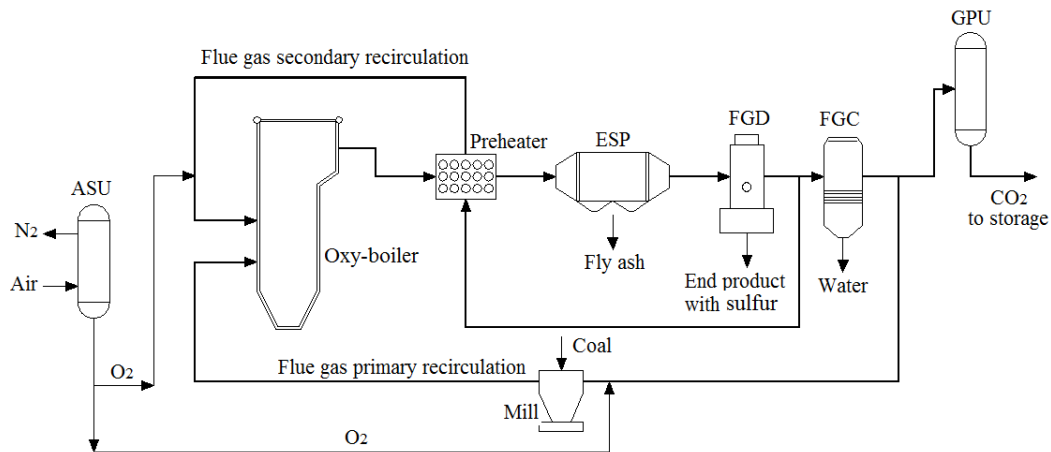


Figure 2.1: Configuration of an oxy-fuel power plant for high-sulfur coals. ASU: air separation unit; ESP: electrostatic precipitator; FGD: flue gas desulfurization; FGC: flue gas condenser; GPU: gas processing unit. Adapted from [48].

The injection of O_2 into the recycled flue gas is another important aspect to be considered during oxy-coal combustion. For safety reasons, O_2 should not be added to the primary stream before entering the mills [15]. Since CO_2 has an inhibitory effect on explosions, it might be possible to increase the O_2 fraction

above 21 vol% upstream of the mill [50]. The O₂ concentration considerably affects pollutant emissions and flame stability. Reducing the O₂ concentration in the primary stream has the benefit of causing a fuel-rich flame core, but the downside of difficult flame stabilization [27,51].

2.3 The Physical Chemistry of Oxy-Coal Combustion

The difference in the physical and chemical properties of CO₂ and N₂ has motivated several studies in order to understand in deep the impacts of oxy-fired environments on pyrolysis and char combustion. The first studies were carried out in a microgravity environment using a drop shaft facility [25]. One high-volatile bituminous coal had a lower flame propagation speed in an O₂/CO₂ atmosphere than in an O₂/N₂ atmosphere. The authors pointed out the higher specific heat of CO₂ compared to N₂ as main reason for such behavior. Single-particle studies using an entrained-flow reactor showed that higher concentrations of CO₂ increase ignition delay and decrease the temperature of the volatile cloud flame surrounding the particle and consequently the rate of volatiles combustion [52]. Similar trends were also observed in experiments for a group of particles [53]. These results prove that the presence of CO₂ have an important influence on particle devolatilization and ignition.

The effects of enhanced O₂ concentrations on the devolatilization and ignition of bituminous coals have been also investigated [25,53-55]. Results show that as the O₂ fraction increases, both devolatilization and ignition occur more rapidly. The variation of ignition delay and devolatilization times were of the order of 1.00 ms. Coal devolatilization is an endothermic process and this difference of 1.00 ms is result of a closer proximity of the volatile flame to the coal particle, and a higher temperature of the volatile flame [54]. Molina and Shaddix [55] explained these results with the increased thermal capacity of CO₂ compared to N₂. The ignition time decreases as the mixture reactivity and heat release increase. Conversely, it increases with higher heat capacities. The authors also suggest that the diffusivity of the volatile components in a CO₂ environment is lower than in N₂, so that the volatile consumption rate in CO₂ is expected to be slightly lower.

The amount of volatile yield under oxy-firing has been also extensively investigated. Rathnam et al [56] investigated the reactivity of three Australian coals under O₂/N₂ and O₂/CO₂ environments using a drop tube furnace maintained at 1400 °C and a thermogravimetric analysis. The particle size ranged between 69-90 μm. The results showed 4-24% higher volatile yields in CO₂ environments. Al-Makhadmeh [57] investigated a South African bituminous coal and Lusatian pre-dried lignite applying an entrained-flow reactor at temperatures of 700 to 1000 °C in 100% N₂ and 100% CO₂ environments. Volatile yields increased by

approximately 10% for the South African coal and 11-14% for the pre-dried lignite when N_2 was replaced with CO_2 . Both authors suggest the gasification reactions of the char as the main reason for the higher volatile yields, particularly at temperatures above 850 °C.

Opposite trends have been also obtained by other authors. Brix et al [58] examined the reactivity of a South American bituminous coal (90-106 μm) in an entrained flow reactor at temperatures of 900-1400 °C under CO_2 and N_2 atmospheres. Results from this study showed that under identical conditions, CO_2 has no pronounced effect on volatile yield. Borrego and Alvarez [59] performed devolatilization analysis using low and high volatile bituminous coal particles in the size range 36-75 μm in a drop tube furnace at 1300 °C. A decrease in volatile yield of 62% and 32% was observed under oxy-fired condition for low volatile and high volatile coals, respectively.

As well as having an effect on devolatilization and ignition of coal particles, oxy-fired atmospheres may also affect the burnout of both char and volatiles. With help of the well-known Arrhenius diagram (Figure 2.2), it is possible to analyze and compare the effect of temperature on the rates of chemical reaction in various conditions. It is known that at very high temperatures, the char combustion is controlled by diffusion of O_2 through the external gas boundary layer (regime III). At moderate temperatures, the reaction is controlled by a combination of reaction kinetics and by diffusion of O_2 through the porous char (regime II) and at very low temperatures only by reaction kinetics (regime I). Nevertheless, the combustion conditions in pulverized coal combustors generally lead to char combustion being controlled only by regimes II and III [15,21,56,60].

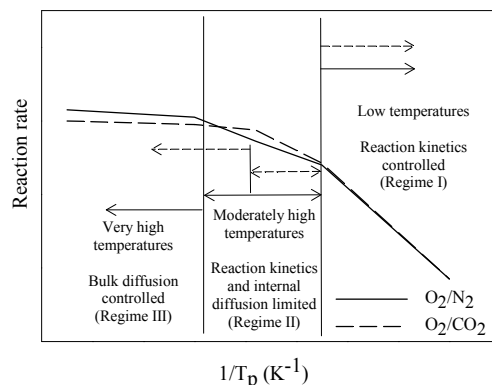


Figure 2.2: Arrhenius diagram of coal combustion in air and oxy-fired atmospheres [21].

In the Arrhenius diagram proposed by Wall et al [21], it can be observed that in regime I, the combustion rate is similar for both air and oxy-fuel. However, as the temperature rises, the conditions for regime II are reached. As described above, some authors believe that these temperatures can lead to increased char reactivity

due to char gasification [56,57]. At very high temperatures (regime III), lower combustion rates are observed since the diffusivity of O₂ is lower in CO₂ than in N₂ [21].

Besides the oxidation of the carbon described by Equations 2.2 and 2.3, the higher amount of CO₂ could affect the char burnout through the gasification reaction described by Equation 2.4. Additionally, in the case of wet recirculation, the higher amount of water vapor may contribute to char gasification and the formation of H₂ and CO (Equation 2.5). Although most experiments [52-57] have been carried out without water vapor, thus leaving its impact unclear, it seems that the influence of water vapor and CO₂ on char gasification is important at later stages of the combustion when the O₂ concentration is significantly reduced [61].



An important point is that gasification reactions in both CO₂ and water vapor are strongly endothermic, 172 kJ/mole and 131 kJ/mole, respectively [62]. Shaddix et al [62] suggest that while normally the inclusion of an additional means of carbon oxidation would be presumed to increase the overall rate of char gasification, the high endothermicity of the gasification reactions tends to cool the char particle and therefore reduce its oxidation rate. Thus, it is unclear whether gasification would increase or decrease the overall rate of char consumption or whether it could strongly affect regime II by increasing the char reactivity.

Experimental studies to investigate the effects of coal rank were carried out by Tappe [63] in an atmospheric cyclone reactor. The combustion process in this small-scale facility is characterized by high heating rates of fuel particles as well as turbulent and swirling flow within the combustion reactor. With the help of a solid zirconium oxide probe, the O₂ partial pressure inside the combustion chamber is registered and used as main parameter for analyzing burnout times. Results show that as the O₂ concentration is increased in oxy-fired atmospheres, the combustion time is reduced with the oxidation of volatiles and char occurring simultaneously. Under lower O₂ concentrations, higher ignition and volatile combustion times were observed because of the higher heat capacity of CO₂. The overall burnout time in a mixture of 21 vol% O₂ and 79 vol% CO₂ was shown to be lower when compared to conventional air-fired combustion, especially for more reactive coals; in case of hard coals, this difference is less noticeable.

The effect of oxy-fired environments on coal rank was also investigated in an entrained flow reactor using 100 μm diameter pulverized coal particles [64]. Char particle temperatures were compared and showed no significant differences when a moderate temperature (860 $^{\circ}\text{C}$) was applied in O_2/CO_2 and in O_2/N_2 environments. At a higher temperature (1380 $^{\circ}\text{C}$), low and mid-rank coals burned at lower temperatures in the presence of CO_2 compared to N_2 . Anthracite showed no significant differences in the mean particle temperature measured in both environments. The authors concluded that the predominant effect of CO_2 on char burning rates is the lower diffusivity of O_2 in CO_2 relative to its diffusivity in N_2 .

2.4 Considerations for Temperature and Flame Characteristics

Changes in the oxidant medium also have a significant influence on temperature and flame characteristics. Studies conducted by Tan et al [65] demonstrated that the oxy-fuel flames are much more compact and that a concentration of 21 vol% O_2 in the feed gas significantly lowers flame temperatures compared to air-firing. Additionally, these flames are visually much less bright due to the absorption of radiation by CO_2 . To increase flame temperature and stability, it was necessary to increase the O_2 fraction in the feed gas. Results obtained from a concentration of 35 vol% O_2 show slightly higher temperatures at furnace centerline compared to air-firing at the same fuel feed rate. The test facility operating conditions are given in Table 2.

Table 2: Test conditions of the work performed by Tan et al [65].

Parameter	Conditions
Thermal power	0.30 MW_{th}
Furnace type	Down-fired and refractory-lined
Furnace dimensions	8.30 m long with inner diameter of 1.00 m
Coals tested	Bituminous, sub-bituminous, and lignite
Recirculation type	Dry
Feed gas composition	Air (baseline) Oxy-fuel (35 vol% O_2)

Khare et al [66] investigated oxy-fuel flames in a vertical pilot-scale furnace with a maximum thermal capacity of 1.20 MW_{th} . Further information on operating conditions is given in Table 3. Under full load furnace operation, the air and oxy-fuel flames were stable but fluctuating; under partial load operation, the oxy-fuel case displayed an ignition delay. Nevertheless, similar flame temperatures were shown to be possible for both cases. In addition to the different physical and chemical properties of oxy-fired conditions, fluid mechanics in the near burner region also influence the flame pattern and the location of the ignition point. The authors mentioned that for retrofit situations, the possibility of high-swirling type-2 flames (with internal recirculation), becoming type-0 (without internal recirculation) is possible, necessitating burner modifications to re-establish

operation with the type-2 flame for which many industrial operations are designed. This is caused by the lower volume flow rates when a higher O₂ fraction upstream of the furnace is necessary to reach a similar flame temperature.

Table 3: Test conditions of the work performed by Khare et al [66].

Parameter	Conditions
Thermal power	0.80 and 0.48 MW _{th}
Furnace type	Down-fired, water-cooled, and refractory-lined
Furnace dimensions	7.20 m long with inner diameter of 1.30 m
Coal tested	Low-volatile bituminous coal
Recirculation type	Wet
Burner configuration	Swirl burner with two feed gas streams Secondary stream swirled (30 degree vane angle and S=0.20)
Feed gas composition	Air (baseline) Oxy-fuel (approximately 30 vol% O ₂)

Studies applying Lusatian lignite were carried out by Hjærtstam et al [67] in a 0.10 MW_{th} test furnace (Table 4). The recycle rates were chosen to achieve flame temperatures comparable to the air-fired baseline. The ratios of the flows in the primary and secondary registers of the burner were kept constant, and therefore the inlet gas velocities are reduced in proportion to the volumetric flows. Trials were also carried out under a reduced stoichiometric ratio in order to evaluate the sensitivity of the oxy-fuel flames. The most stable flames were obtained at O₂ feed gas fractions of 27-29 vol%. A stable flame at 25 vol% O₂ was only possible using an optimized burner configuration. Although the baseline air flame and the oxy-fuel with 25 vol% O₂ had similar temperature distributions, the air-fired flame was more stable. The temperatures of oxy-fuel flames with 27 and 29 vol% O₂ were on average 50 and 100 °C (respectively) higher than the temperatures of the air flame. The highest gas temperature throughout the tests was 1350 °C, which lies between the lower and upper ash melting temperatures of the fuel. All test flames were luminous, and the point of ignition was detectable from photometric differences in the images. The standoff distance in the 27 vol% oxy-fuel flame was shorter than that of air-firing. This result is attributed to the higher O₂ concentration in the feed gas. In addition, the lower velocities of the feed gas stream in the oxy-fuel cases increased the particle residence time, which improved the ignition condition.

Further flame observation studies were performed by Woycenko et al [27] in a 2.50 MW_{th} furnace (Table 5). Experimental data demonstrated that a flue gas recycle ratio of 0.58 yielded flame characteristics similar to that of conventional combustion. At this ratio, the oxy-fuel flame was classified as a type-2 flame, slightly longer than the baseline case and with a clearly defined internal recirculation zone. Difficulties in sustaining a stable flame at a flue gas recycle ratio of 0.76 were noted. The flame at this condition was observed to be detached

from the quarl with low intensity and low temperature. Poor conversion efficiency with combustion occurring throughout entire length of furnace was observed. By reducing the flue gas recycle ratio to 0.73, the flame re-attached itself the burner quarl and was marginally stable but with a significantly longer flame length compared to the baseline case. In this case, a flame shape closer to type-2 was obtained, although it was difficult to define because of a weak internal recirculation zone. Further observations with lower recycle ratio (0.52) revealed that combustion intensity was even greater than the baseline, with more compact and luminous flames inside the quarl even for a low swirl number (about 0.60). Interesting is that in the optimal flame (0.58 recycle ratio), all the O₂ required for complete combustion was placed in the secondary stream, while in the other cases O₂ was also injected in the primary stream.

Table 4: Test conditions of the work performed by Hjærtstam et al [67].

Parameter	Conditions
Thermal power	0.10 MW _{th}
Furnace type	Down-fired, water-cooled, and refractory-lined
Furnace dimensions	2.40 m long with inner diameter of 0.80 m
Coal tested	Lignite
Recirculation type	Dry
Burner configuration	Swirl burner with two feed gas streams Primary stream swirled (45 degree vane angle) Secondary stream swirled (15 degree vane angle)
Feed gas composition	Air (baseline) Oxy-fuel (25, 27, and 29 vol% O ₂)
Stoichiometric ratio	1.18

Table 5: Test conditions of the work performed by Woycenko et al [27].

Parameter	Conditions
Thermal power	2.50 MW _{th}
Furnace type	Horizontal, water-cooled, and refractory-lined
Furnace dimensions	6.25 m long with square cross-section of 2.00 x 2.00 m
Coal tested	High-volatile bituminous coal
Recirculation type	Wet
Burner configuration	Swirl burner with two feed gas streams Primary stream velocity at 20 m/s Secondary stream swirled (Air-firing S=1.03; Oxy-firing S= 0.84)
Feed gas composition	Air (baseline) Oxy-fuel (R= 0.58, 0.73, and 0.76)

Smart et al [68-70] investigated the impact of oxy-coal combustion on flame characteristics using imaging techniques. The test conditions for a semi-anthracite and a bituminous coal carried out in a 0.50 MW_{th} once-through combustion facility are summarized in Table 6. It was observed that air-firing produced a non-luminous flame similar to oxy-firing at a 0.75 recycle ratio. By reducing this ratio to 0.68, a luminous and intense flame anchored to the burner quarl was achieved.

Oscillation frequencies computed by the imaging system were used as an indicator of flame stability. Results showed that flame oscillation frequency generally decreases with the recycle ratio, indicating that a high recycle ratio has an adverse effect on the flame stability. In most cases, the flame oscillation frequency in the root region was lower than that in the middle region, indicating ignition problems under oxy-fired conditions.

Table 6: Test conditions of the work performed by Smart et al [68-70].

Parameter	Conditions
Thermal power	0.50 MW _{th}
Furnace type	Horizontal and refractory-lined
Furnace dimensions	4.00 m long with square cross-section of 0.80 x 0.80 m
Coals tested	Semi-anthracite and bituminous coal
Recirculation type	Dry (once-through)
Burner configuration	Swirl burner with two feed gas streams Secondary stream swirled
Feed gas composition	Air (baseline) Oxy-fuel (R= 0.62, 0.65, 0.68, 0.72, and 0.75)

More recently, Fry et al [71] investigated the impacts of various strategies for oxy-fired operation of the burner primary register, where the primary mass flow rate, momentum, and velocity were matched to the air-fired conditions (Table 7). Additionally, experiments were performed where the primary feed gas was not enriched with O₂. For oxy-firing, matching the primary gas/fuel mass ratio and the primary momentum to the air-fired case resulted in a flame stabilized within the quarl. Setting the primary velocity equal to that of the air-fired conditions resulted in a lifted flame. These data indicated a fundamental difference in flame behavior with a delay in flame ignition under oxy-fired conditions. A decrease of 13% in the primary velocity was necessary in order to stabilize a flame within the quarl. Experiments also showed that an oxy-fuel flame could be stabilized with no O₂ enrichment of the primary stream. However, the luminosity of the flame was decreased, suggesting delayed ignition.

Table 7: Test conditions of the work performed by Fry et al [71].

Parameter	Conditions
Thermal power	1.50 MW _{th}
Furnace type	Horizontal and refractory-lined
Furnace dimensions	14.00 m long with square cross-section of 1.0 x 1.0 m
Coal tested	Bituminous coal
Recirculation type	Wet
Burner configuration	Swirl burner with three feed gas streams Secondary stream swirled
Feed gas composition	Air (baseline) Oxy-fuel with primary stream at 2.70-21 vol% O ₂ and other registers at 30-35 vol% O ₂

2.5 Considerations for Heat Transfer

One of the key factors that defines the performance of a boiler and which must remain relatively unchanged after a retrofit is the heat transfer rate. The higher concentration of CO₂ and water vapor in the flue gas yields increased non-luminous radiation within the furnace. Because of the higher concentration of these gases and their emissivities, the radiative heat transfer may exceed that of conventional air-fired operation at the same adiabatic flame temperature. In order to obtain the required heat transfer profile in both the radiative and convective passes, the O₂ concentration should be slightly lower (by 2-3 %) than that required to reach a similar adiabatic flame temperature [9,13,15].

Luminous radiation is affected by the amount of particulate in the flame [15]. The absolute amount of ash remains the same for air and oxy-fuel given the same fuel input. Although a recent investigation showed that oxy-coal combustion may reduce soot formation [72], the lower flow rates at lower recycle ratios increase the concentrations of soot and char within the flame envelope, leading to an increase in the flame emissivity [70]. Changes in the burnout rate of char affect likewise the location of heat transfer by radiation in the flame zone [15].

As described previously, to obtain an adequate temperature and heat uptake in the radiative section, the recycle ratio is reduced due to the necessary increase in O₂ concentration upstream of the furnace. The resulting heat transfer rate in the convective section is not necessarily reduced in comparison with air-fired conditions as consequence of the reduced flue gas flow rate [15]. The heat transfer coefficient is an appropriate parameter for the analysis of the convective heat transfer [51]. In the case of a flow across a tube bundle, such as in superheaters and reheaters, results suggest that a convective heat transfer similar to a baseline air-fired case is obtained at a 0.58 recycle ratio. Depending on the type of recirculation and other operating parameters, it seems that this value might be insufficient to bring about the baseline adiabatic flame temperature.

Measurements of total heat flux were performed by Tan et al [65]. Results obtained at 35 vol% O₂ showed slightly higher heat fluxes compared to air-firing, while tests performed with 28 vol% O₂ in the feed gas resulted in slightly lower values. Woycenko et al [27] identified an optimal recycle ratio of 0.58 which yields heat transfer performance similar to normal air-fired operation. As described in the previous section, at this condition, combustion performance, flame length, and stability were comparable to the air-fired baseline. At a recycle ratio of 0.76, an overall heat transfer efficiency significantly lower than the baseline case was observed. Detailed measurements showed clearly that a recycle ratio of 0.58 provided significantly higher values of hemispherical radiative heat flux than a recycle ratio of 0.73 (i.e. nearly double in most locations). This clearly shows that as the recycle ratio decreases, the radiative heat transfer to the combustion chamber walls increases. It should be noted that the maximum

radiative heat flux was observed at a larger distance from the burner quarl compared to the baseline. This suggests that, although the flame was attached, a significant amount of the volatile combustion occurred farther away from the burner resulting in a longer flame.

Radiative and convective heat transfer in a semi-industrial scale furnace was studied by Smart et al [70]. Measurements were performed with recycle ratios of 0.65-0.75. It was observed that the radiative heat flux profiles can be significantly manipulated by varying the recycle ratio. For anthracite, a radiative heat flux profile similar to air-firing can be obtained for recycle ratios of 0.68-0.72 at 3 vol% O₂ at the furnace exit or 0.68-0.75 at 6 vol% O₂ at the furnace exit. Bituminous coal displayed heat fluxes similar to air-fired conditions using a recycle ratio of 0.72-0.75 and an O₂ excess of 3 vol%. Another important observation is that the axial position of the peak in radiative fluxes moves downstream as the recycle ratio is increased due to the combustion process being delayed because of lower levels of O₂ enrichment. The authors suggested that radiative and convective heat transfer components cannot be matched precisely in terms of an optimum recycle ratio compared to the performance of air-firing. However, there was a good indication that an acceptable operational range exists in terms of matching the radiative and convective heat transfer components using oxy-fuel. A matching radiative heat flux was attained at a recycle ratio of approximately 0.74 with an adiabatic flame temperature slightly lower than that of the air-fired condition.

2.6 Considerations for Oxygen, Carbon Monoxide, and Carbon Dioxide

In-flame measurements of O₂, CO, and CO₂ for the optimum oxy-fired flame (0.58 recycle ratio) and the air-fired baseline flame were compared by Woycenko et al [27]. At 1.25 m from the burner quarl, the O₂, CO, and CO₂ profiles were flattened and representative of the flue gas composition. This indicates that macro-mixing and volatile combustion were approaching completion at this point and that most of the char was consumed in the volatile flame zone. Based on these measurements, the flame length was estimated to vary between 0.97-1.25 m. Because all the O₂ required for the combustion was injected in the secondary stream, a higher O₂ concentration in the near burner field was observed, which suggests ignition occurring very close to the burner. The CO₂ concentration for the optimum oxy-fuel case at 1.25 m from the burner was nearly six times greater than the air-fired baseline. CO levels significantly increased within the flame zone. However, the combustion of CO was complete before exiting the furnace with no significant CO emissions.

Hjærtstam et al [67] found that an oxy-fuel flame with 25 vol% O₂ produced O₂ profiles similar to the air-fired case. Both cases displayed similar O₂ concentrations at 0.65 m distant from the burner, whereas the profiles of oxy-fired flame with 29 vol% O₂ attained stabilized values closer (at approximately 0.35 m). At 0.22 m from the burner, no O₂ was detected on the flame axis for oxy-firing with 29 vol% O₂; with 25 vol% O₂ and air-firing cases, the O₂ concentrations were approximately 7 and 5 vol%, respectively. In the oxy-fired case with 27 vol% O₂, less than 1 vol% O₂ was observed at this position. This indicates earlier ignition and more intense combustion in the oxy-fuel cases with 27 and 29 vol% O₂, consuming the available O₂ faster. The authors pointed to the reduced volumetric flow and the correspondingly higher residence time as the main factors in bringing combustion closer to the burner.

Detailed measurements of CO were also performed in the flame region by Hjærtstam et al [67]. Oxy-firing with 27 and 29 vol% O₂ led to peaks of centerline CO concentration of approximately 7 and 9 vol%, whereas the concentrations obtained by air-firing and oxy-firing with 25 vol% O₂ were similar, with a maximum concentration of 1.24 and 1.13 vol% at 0.10 m from the centerline. Even though higher concentrations of CO were observed in the oxy-coal flame at 27 and 29 vol% O₂, the CO concentration in the gas exiting the furnace was similar to that of the air-fired case, indicating that controlling CO emissions during oxy-fuel combustion should not be more difficult than during air-firing.

Higher amounts of CO observed in the experiments are explained by the higher partial pressures of CO₂ and H₂O in the furnace. In addition to the gasification reactions detailed previously (Equations 2.4 and 2.5), thermal dissociation of CO₂ can likewise contribute to increased CO concentrations in the flame zone under oxy-fired conditions (Equation 2.6).



Toftegaard et al [15] suggested that an even more important pathway to increasing the CO concentrations in the flame zone may be the reaction between CO₂ and H radicals. The increased level of CO₂ induces a possible alteration of the composition of the O/H radical pool during oxy-fuel combustion due to the competition between O₂ and CO₂ for H radicals (Equations 2.7 and 2.8) [15,73,74]. Furthermore, the reaction of CO₂ with CH₂ radicals may contribute to increased CO concentrations in the flame zone.



2.7 Considerations for Emissions of Nitrogen Oxides

In conventional pulverized coal combustion, NO is generally formed by prompt, thermal, or fuel mechanisms. Prompt-NO is formed by fast reactions between nitrogen, oxygen, and hydrocarbon radicals in regions near the flame [75,76]. The general scheme of the prompt NO mechanism is that hydrocarbon radicals react with molecular nitrogen to form amines and cyano compounds. The amines and cyano compounds are then converted to intermediate compounds that ultimately form NO. However, the prompt mechanism does not contribute to more than 5% of the total NO formed in a coal-fired furnace and is often neglected in the evaluation of NO_x emissions.

Thermal NO is primarily formed from N₂ present in the combustion air, following the extended Zeldovich mechanisms described by Equations 2.9-2.11 [75,76]. The thermal NO formation rate is highly dependent upon temperature and O₂ availability associated with long residence times. The reaction presented in Equation 2.9 is the rate-controlling step because of its high activation energy and the high temperatures (above 1500 °C) required to initiate it. In general, it is assumed that up to 20% of the total NO_x from pulverized coal combustion in air is due to thermal mechanism [77,78].



Formation of NO from the oxidation of fuel-N is the main source of NO emissions in coal combustion, constituting 70-90% of the total NO [77,79]. Between 15 and 100% of fuel-bound nitrogen is converted to NO [76]. In pulverized coal combustion, the nitrogen present in the fuel is split between the volatile and char. This distribution depends on the fuel structure, temperature, and residence time. During devolatilization of coal, nitrogen evolves comparatively late in the primary pyrolysis process [80-84]. The light nitrogen species finally released in the gas phase consist mostly of hydrogen cyanide (HCN) and ammonia (NH₃). Although some details of the kinetic mechanism for fuel-N conversion in the flame are unresolved at the present time, there is a consensus that the reactions proceed as illustrated in Figure 2.3.

A significant quantity of nitrogen still remains in the coal after the pyrolysis, and this can be heterogeneously oxidized to form NO. Detailed understanding of the reaction pathways for the conversion of char-N has still not been established and is still an area of active research [15]. It is clear though, that NO forms via the reaction with O₂ on the surface of the char as given by Equation 2.12. C(N) and

$C(O)$ denote the concentration of the surface of the char for the nitrogen and O_2 , respectively [85].

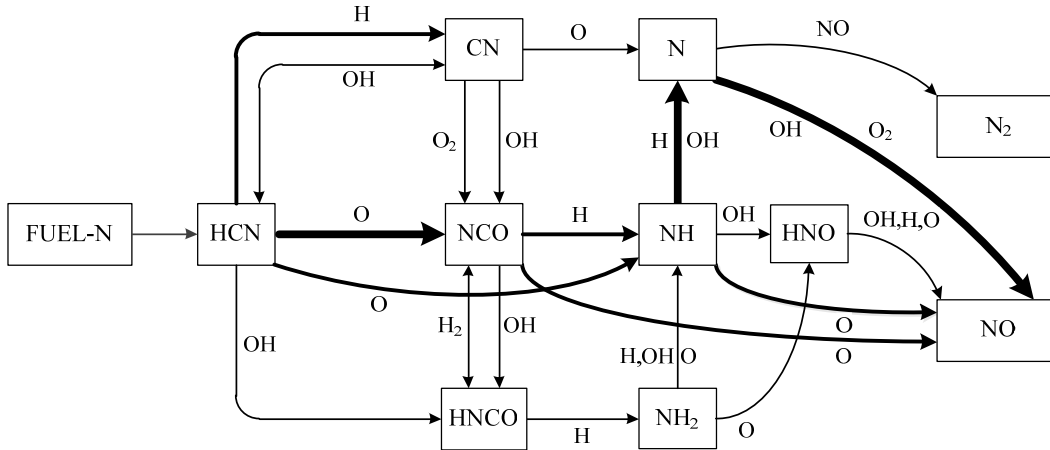


Figure 2.3: Schematic diagram of the principal reaction paths in the fuel-N conversion [99].

Experiments performed by Woycenko et al [27] showed that the product flue gas NO_x concentration was significantly higher under oxy-firing with a recycle ratio of 0.58 (NO_x concentration of 1932 mg/m^3) than under conventional air-firing (574 mg/m^3). Increasing the recycle ratio to 0.76 brought the NO_x concentration down to 917 mg/m^3 . This change in concentration is a result of the temperature change because the adiabatic flame temperature at 0.76 recycle ratio is considerably lower than the baseline. A general trend observed was that as the recycle ratio was reduced, more NO_x was formed; plus, the O_2 fraction and flame temperature increased, which consequently encouraged the formation of NO. Nevertheless, the quantity of NO_x formed in all evaluated oxy-fired cases was considerably below the baseline air-firing; the baseline flame yielded a value of 321 mg/mJ , with the oxy-fuel cases with recycle ratios of 0.58, 0.73, and 0.76 resulting in 110, 39, and 52 mg/MJ , respectively.

Experimental data for Lusatian lignite was obtained by Wilhelm [86] in a 50 kW_{th} down-fired test facility and also assessed the impact of the recycle ratio on NO emissions (Table 8). The NO emission rate of approximately 260 mg/MJ under air-firing was reduced to 60-140 mg/MJ by varying the O_2 fraction in the feed gas. Hjærtstam et al [67] reported likewise that NO_x emissions under oxy-firing are dependent on the recycle ratio. However, the NO emission rates calculated downstream of the flue gas recirculation were much lower. Under baseline conditions the emission rate was approximately 160 mg/MJ , whereas the values found for oxy-firing at 25, 27, and 29 vol% O_2 were 41, 47, and 48 mg/MJ , respectively. An interesting focus of this work was the impact of air in-leakage on the NO_x emissions. Experimental data indicated that the NO emission rate is

drastically increased from 30% to 80% (depending on the recycle ratio) when air in-leakage is maintained at 4%. The results also showed that NO_2 can be important under oxy-firing. In experiments using an O_2 fraction of 33%, the NO_2 contribution to the total NO_x emission was approximately 28%. This value was reduced to 19% when trials were carried out simulating a fraction of air in-leakage of 4%.

Table 8: Test conditions of the work performed by Wilhelm [86].

Parameter	Conditions
Thermal power	50 kW _{th}
Furnace type	Horizontal, water-cooled, and refractory-lined
Furnace dimensions	2.50 m long with inner diameter of 0.29 m
Coals tested	Lignite
Recirculation type	Dry
Burner configuration	Swirl burner with two feed gas streams Secondary stream swirled
Feed gas composition	Air (baseline) Oxy-fuel (17-33 vol% O_2)

NO profiles measured by Tan et al [65] showed that in the case of a sub-bituminous coal, the NO concentration along the furnace centerline increased from 736 mg/m³ under air-firing to 1472 mg/m³ under oxy-firing with 35 vol% O_2 upstream of the burner. The NO_x emission rates were 148 mg/MJ (oxy-fired) and 236 mg/MJ (air-fired). This is the result of reduced volume flow rate under oxy-firing. In the case of lignite, use of an improved burner optimized for oxy-firing resulted in a significant reduction of NO emissions. Under air- and oxy-firing, the volumetric concentrations of NO were 980 and 490 mg/m³ and the emissions rates 269 and 68 mg/MJ, respectively.

Detailed investigations were carried out in an entrained flow reactor by Hu et al [87]. It was observed that the NO_x concentration generally increases with an increasing O_2 concentration, displaying peaks at near stoichiometric conditions. The NO_x conversion rate increases linearly to a stoichiometric ratio close to unity, when changing from fuel-rich to fuel-lean conditions, and approaches asymptotic values at high O_2 excess. The authors also observed increasing NO emission with decreasing coal rank. Reactive coals usually produce slightly higher temperatures which promote NO_x formation at the fuel-lean conditions; with less reactive coals, more unburned char exists in the flame zone which may promote reduction of the previously formed NO_x . Nevertheless, experimental results obtained by Liu et al [88] did not show a clear correlation between the conversion rate and the coal rank, volatile matter, and nitrogen content.

Impacts of burner configurations were investigated experimentally and numerically by Chui et al [89] using the same test facility evaluated in the work of Tan et al [65]. The operating parameters are summarized in Table 9. It was found that NO emissions are dependent on the swirl number and it may be even higher

than the air-fired baseline in some burner operating conditions. Increasing the swirl number in the burner configuration A from 1.00 to 2.00 decreases the NO emission rate by 34% according to experimental values. In the case of a swirl number close to 1.00 in the secondary stream, numerical predictions indicated that the secondary stream cannot quite spin the coal particles outwards before they devolatilize and hence volatile matter and fuel-bound nitrogen evolve near the middle of the furnace, where O₂ is abundant and NO formation is encouraged. When a stronger swirl is applied in the secondary stream, some of the particles are spun out and some stay with the central jet prior to pyrolysis. Thus, a considerable amount of volatile matter and fuel-N are released outside of the central jet in the fuel-rich region that suppresses NO production. The differences in burner configurations between type A and B did not significantly change total NO production and stable flames were obtained for both cases. However, NO emissions under oxy-firing were higher than for air-firing: 140-150 versus 110 mg/MJ. These values were reduced to 40 mg/MJ only with improved oxy-coal burner and furnace design [90].

Table 9: Test conditions of the work performed by Chui et al [89].

Parameter	Conditions
Thermal power	0.30 MW _{th}
Furnace dimensions	8.30 m long with inner diameter of 0.61 m
Coal tested	Sub-bituminous coal
Recirculation type	Dry
Burner configuration	Burner A: Swirl burner with three feed gas streams Oxygen jet inside of the primary stream Secondary stream swirled Burner B: Swirl burner with three feed gas streams Oxygen jet outside of the primary stream
Feed gas composition	Air (baseline) Oxy-fuel with primary stream at 100 vol% CO ₂ , secondary stream at 28 vol% O ₂ , and tertiary stream at 100 vol% O ₂

An interesting point of the study performed by Woycenko et al [27] was the investigation of the impact of a low-NO_x flame by moving the coal injection forward until the flame changed from a type-2 (i.e. with stronger internal recirculation) to a type-1 (i.e. with weaker recirculation zone penetrated by primary jet). The baseline type-2 flame was generated with the coal injector positioned at the burner throat. In the new flame pattern, the coal particle trajectory was outside of the internal recirculation zone (IRZ) with ignition occurring in the shear layer between the IRZ and coal jet. Devolatilization and combustion of the volatiles occur in an oxygen-rich region, which produces a high-NO flame. In the new flame pattern, the ignition occurs outside the coal jet, while devolatilization and combustion of the volatile occur in the fuel-rich recirculation region. NO_x emission rates from the baseline (air) flames were reduced from approximately 375 to 250 mg/MJ; oxy-firing emissions were reduced from 160 to 75 mg/MJ.

Dhungel [91] investigated the effects of furnace combustion staging in oxy-fired environments. Experiments were carried out in a once-through vertical furnace with a jet burner (without swirl) mounted at the top (Table 10). Two pre-dried lignites, a medium volatile bituminous coal, a high volatile bituminous coal, and a lignite char were investigated. The total volume flow rate of feed gas was kept the same for air-firing and oxy-firing in order to ensure a similar flame shape and similar residence times within the reactor. Thus, the coal feed rate needed to increase when 27 and 35 vol% O₂ were applied in the feed gas to keep the same stoichiometric ratio.

Table 10: Test conditions of the work performed by Dhungel [91].

Parameter	Conditions
Thermal power	20 kW _{th}
Furnace type	Down-fired ceramic tube (Once through reactor)
Furnace dimensions	2.50 m long with inner diameter of 0.20 m
Coals tested	Lignite, bituminous coals, and char
Recirculation type	Without flue gas recirculation
Burner configuration	Jet burner with three feed gas streams
Feed gas composition	Air (baseline) Oxy-fuel (21, 27, and 35 vol% O ₂)
Stoichiometric ratio	1.15 Staged combustion (0.75, 0.85, and 0.95)

The NO formation rate in the near burner region was highest under air-firing and reached a peak of approximately 1060 mg/m³ at 0.50 m from the burner. Although the NO formation rate was lower under oxy-firing with 27 vol% O₂, the NO concentration reached a peak at the same location. With 21 vol% O₂, the NO peak was found at larger distances (approximately 0.70 m) from burner. This was probably a result of delayed combustion in a CO₂ medium when the O₂ volumetric fraction is similar to air [25,52-55]. NO concentration profiles were observed to be a function of the nitrogen and volatile content of the coal, i.e. the higher the fuel-N content (for coals with comparable volatile content), the more NO was formed. On the other hand, the higher the volatile content (for coals with comparable fuel-N content), the faster was the conversion of fuel-N to NO. Coals with higher volatile content release more fuel-N via the gas phase, which is then oxidized to NO during fuel-lean combustion.

Conversion of fuel-N in the gas phase to NO_x is the primary path for fuel-NO_x formation. NO_x formed from char-N offers almost no opportunity for reduction by the application of feed gas or fuel staging [91]. For a similar burner stoichiometric ratio and a residence time in the reduction zone, the NO_x emission rate was generally lower during oxy-fuel combustion with feed gas staging. The NO_x emission rate decreased with lower burner stoichiometric ratios and higher residence times in the reduction zone under oxy-firing. When compared to unstaged combustion, a NO_x reduction of approximately 90% was obtained for Lusatian pre-dried lignite. The percentage conversion of fuel-N to NO during

unstaged combustion under air- and oxy-firing with 27 vol% O₂ was approximately the same in both cases (34 and 33%). These values decayed to 3.00 and 4% with staged combustion, a burner stoichiometric ratio of 0.75, and a residence time of 3 seconds in the reduction zone.

As reviewed above, most studies point out the ability to lower NO_x emissions under oxy-fired conditions. Several mechanisms can contribute to this reduction. At a very low concentration of N₂ in the feed gas, the thermal NO formation mechanism can be neglected, since the oxy-fuel combustion atmosphere will be oversaturated with NO at all times [15,92,93]. Gas phase reaction modeling of lignite combustion shows that the absence of N₂ at higher temperatures (>1400 °C) enables the reverse Zeldovich mechanism to destroy NO and convert it to N₂. However, to obtain an effective reduction through the reverse Zeldovich mechanism, air ingress into the furnace must be avoided [93].

The high concentrations of CO in the combustion zone reduce the previously formed NO on char surfaces by Equation 2.13 [85]. Although the promoting effect of CO on NO was observed in some works, this mechanism is mostly important at low temperatures, similar to those found in fluidized bed combustion [15].



The reduction of the recycle-NO in a fuel-rich environment and reburning are the most dominant mechanisms during oxy-coal combustion [15]. The reduction of HCN to N₂ in fuel-rich conditions can be summarized by the reactions presented in Equations 2.14-2.16 [91,94]. A similar set can be also written for NH₃ with fuel-rich conditions favoring the reduction of NO.



The heterogeneous reduction of NO on the char surface can be summarized as [91,95-97]:



Reburn reactions are chemically complex processes in which NO is abated using fuels as reducing agents. The process involves partial oxidation of the reburning agent under fuel-rich conditions, reduction of NO by reaction with fuel fragments, and subsequent conversion of the intermediate nitrogenous species [15]. The reactions presented in Equations 2.20-2.22 summarize the reburning process [91, 94]. It is important to note that the HCN formed in these reactions may then react to form N₂ under fuel-rich conditions or it may reform NO if the O₂ concentration is too high.



2.8 Considerations for Emissions of Sulfur Oxides

Sulfur in coal occurs in three forms: as pyrite, organically bound, or as sulfates. The sulfates represent a very small fraction of the total sulfur while pyritic and organically-bound sulfur comprise the majority [98]. The basic reactions for the formation of sulfur dioxide (SO₂) and sulfur trioxide (SO₃) are:



Sulfur dioxide (SO₂) tends to occur at higher temperatures while sulfur trioxide (SO₃) occurs mainly at lower temperatures [99]. Under typical combustion conditions, virtually all sulfur in the fuel is converted into SO₂. Sulfur speciation in pulverized coal combustion under air-fired conditions has been extensively studied and many of the reaction mechanisms are expected to be similar for oxy-fuel combustion [100].

Tan et al [65] reported values of SO₂ concentrations in oxy-firing with dry flue gas recirculation without SO₂ removal. Due to the lack of SO₂ removal, there were significant increases in SO₂ concentration in the furnace due to the accumulative effect of flue gas recycling and reduced volume flow rates. In case of sub-bituminous coal, measured furnace centerline SO₂ showed peaks of 262 mg/m³ for air-firing and 1047 mg/m³ for oxy-firing at 1.00 m from the burner. Concentrations of SO₂ were significantly higher for lignite with peaks of 1570 (air-fired) and 3141 mg/mm³ (oxy-fired). However, the mass of emitted SO₂ per

unit of energy input were mostly slightly lower than combustion in air even though the concentrations were 3-4 times higher in the oxy-fuel case. Another conclusion obtained from this study is that the specific SO₂ emissions were almost exclusively dependent on the sulfur content in the coal.

Croiset and Thambimuthu [101] reported on SO₂ emissions when burning a bituminous coal in the same test facility used by Tan et al [65]. The experiments were run at 0.21 MW_{th} under various conditions: air, O₂/CO₂ mixture (once-through test), O₂ mixed with dry flue gas recycle, and O₂ mixed with wet flue gas recycle. Comparisons between 28 and 35 O₂ vol% showed that the emission rate was slightly lower in recycle experiments (280 mg/MJ) than for the once-through runs (320 mg/MJ). Similar to the once-through experiments, the SO₂ emission rate in the baseline air case was 310 mg/MJ. Although the SO₂ emission rate did not vary heavily, SO₂ concentrations differed greatly inside the reactor. The concentration of SO₂ is indeed much higher (about double) when part of the flue gas was recycled than in the case of once-through O₂/CO₂ mixtures. Measured SO₂ concentrations under oxy-firing with 35 vol% O₂ were 2.75 times higher than air-firing. Experimental runs with wet flue gas recycle did not differ much from the dry case and the conversion of fuel-S into SO₂ was independent of O₂ concentration. However, the type of environment (air, O₂/CO₂, or O₂ with flue gas recycle) did have an effect on the conversion. For air, the conversion was 91%, which means that almost all fuel-S was converted into SO₂. For combustion in O₂/CO₂ mixture, the conversion dropped on average to 75%, and for recycle combustion the average conversion in only 64%.

Similar trends were observed in the experiments conducted by Woycenko et al [27] in a 2.50 MW_{th} test facility employing wet recirculation without desulfurization. Although the SO₂ concentration was significantly higher than in the case of air-firing, the emission rates decreased from 645 to 375-418 mg/MJ in oxy-fuel cases. The conversion ratio of fuel-S into SO₂ was also found to be lower for oxy-fuel (60-67%) than for air (100%). The amount of SO₂ in the flue gas was relatively independent of the recycle ratio.

Possible explanations for the lower emission rates of SO₂ under oxy-fired conditions found in these studies and others [21,25,102] are that part of the sulfur is retained in the ash; a fraction of SO₂ is further oxidized to SO₃; or a possible removal with the condensates during dry recycling. SO₃ concentrations have been reported to be about 2.5-3 times higher during oxy-coal combustion [21]. Tan et al [65] reported that the conversion of SO₂ to SO₃ was about 5%, whereas it is typically 1-5% under conventional air-firing [15]. From an analysis of ash deposits, it is known that less than 2% of the input sulfur from the bituminous coal was retained; this retention was 14% in the case of sub-bituminous coal. These results were expected given the low alkali metal (Na, K) and alkaline earth metal (Ca, Mg) contents of the bituminous coal and the low sulfur content and high alkaline content of the sub-bituminous coal. Dhungel [91] investigated the

mechanisms of sulfur retention in the ash. Although the alkaline earth metals and alkali metals may be responsible for retention of sulfur due to formation of sulfates (SO_4), it is widely accepted that calcium in the ash plays a dominant role in sulfur retention, while the contribution from other elements is limited [103]. It was seen that the sulfates are stable at temperatures below $1000\text{ }^\circ\text{C}$ and thereby some of SO_2 is retained in the ash in regions downstream of the furnace.

2.9 Major Findings from Previous Studies and Remaining Research Issues

The differences in heat and mass transfer as well as reaction kinetics of combustion observed under oxy-fired conditions result from the different physical and chemical properties of the feed gas [25,52-57,62-64]. Therefore, the implementation of oxy-coal combustion considerably changes the flame characteristics, heat transfer, and emission performance. In general, these changes depend on the burner geometry and the composition of the feed gas. In the case of a feed gas composed of 21 vol% O_2 , the flame temperature was found to be significantly lower than that found under air-firing [27,65]. The effect of the O_2 fraction in the feed gas has been extensively investigated by many authors [27,65-70,91,104]. Flame temperatures similar to the air-firing case were found at O_2 fractions of 25-38 vol% (depending mainly on coal characteristics and type of recirculation: dry or wet). The matching radiative heat flux has been reported with an adiabatic flame temperature slightly lower than air-firing probably because differences in flame emissivities [9,13,15,21,70].

Oxy-coal technology not only offers the possibility of a method for CO_2 capture, but also reduces NO_x emissions through the partial elimination of N_2 and through reduction mechanisms [15,40,88,91]. In general terms, the amount of NO_x emitted from an oxy-fuel plant can be one-third to a half of that emitted by conventional combustion in air [15]. It is also clear from previous studies that a decrease in the recycle ratio (and thereby an increase of the O_2 concentration in the feed gas and flame temperatures) yields an increase in both flue gas NO_x concentration and emission rate [27,65,67,86,87,91]. Most measurements during oxy-coal combustion also showed a lower conversion of sulfur to SO_2 . Because most experiments were carried without desulfurization of the flue gas prior to being recirculated back into the furnace, the retention of SO_2 by sulfate forming elements in the ash is the dominant factor [21,25,27,65,101,102]. Emissions of CO have been addressed only by a small number of authors [27,67]. Higher in-flame CO concentrations were also reported, which can be explained by dissociation mechanisms and gasification reactions by higher partial pressure of CO_2 and water vapor. However, the CO emission leaving the furnace was to be similar to air-firing.

From the works reviewed in this thesis, it is observed that experimental data for pulverized combustion in oxy-fired conditions has emerged mainly from studies conducted in once-through [70,91] and vertically orientated down-fired furnaces [65-67,89]. Although some authors claim that once-through reactors provide more operational flexibility, the influence of wet recirculation cannot be simulated in most cases. Additionally, depending on the size of the test facility, a large number of trials cannot be performed because of the high costs of the oxy-fuel feed gas. Vertical cylindrical combustion chambers offer many advantages, e.g. to minimize the asymmetry effects caused by particle deposition and natural convection, and to facilitate removal of particulates. However, it may bring favorable conditions to the combustion process in the case of low confinement ratios (the ratio of the furnace diameter to the burner diameter). Entrained flow reactors and small-scale combustors with high wall temperatures may increase the radiative heat transfer to the particles and thereby accelerating the devolatilization and ignition process, which in turn lead to the flame stabilization. Obviously, these conditions may be desirable to some specific investigations, such as determination of coal reactivity, but they may be inappropriate for evaluating burner stability limits, flame pattern, heat transfer, and emission performance. In order to ensure the essential physics of industrial scale furnaces are reproduced (i.e. particle heating rates and gas-temperature and -composition), the furnace should be large enough to combine a fully turbulent flow and an appropriately high thermal radiation heat transfer. In short, there is still a lack of information on oxy-coal combustion using staged burners under practical conditions, i.e. those found in full-scale furnaces.

Studies evaluating the impacts of burner configurations and operating settings on flame pattern, temperature, and gas emissions were performed by a handful of authors [27,66,71,90,104] and therefore, it is one of the main focuses of this work. Most of these authors define burner operating conditions by fixing an overall stoichiometric ratio and flue gas recycle ratio and then mixing the O₂ feed into the various streams at arbitrary concentrations or injecting it independently through O₂ nozzles. The challenges in maintaining a stable oxy-coal flame have been thoroughly commented upon [27,65,68-71]. Few works were successful in obtaining a stable oxy-fired pulverized coal flame with O₂ concentrations at 21 vol% [104,105]. O₂ fractions in the feed gas which provide a lower adiabatic flame temperature are necessary when membrane-based air separation units are employed [106]; they also reduce the radiative heat transfer in the furnace and thereby require new boiler designs. Nevertheless, the flexibility in supplying O₂ to combustion zone to match the baseline flame temperature and heat transfer within the furnace was proven to be possible and is one of the advantages of the oxy-fuel technology. Injection of pure O₂ has been introduced to stabilize the combustion at a favorable location in the furnace and to produce compact flames. Chen et al [40] reviewed many strategies for the stabilization of oxy-coal combustion. It is suggested that the injection of pure O₂ must be used with caution because overheating of the burner front may occur if excessive O₂ is delivered. On the other hand, a mild mixing strategy may enhance flame stability, reduce NO_x, and

improve carbon burnout. Another important aspect is the carrier gas composition. Cases where pure CO₂ is used as carrier gas in the primary stream may lead to destabilization and detached flames. Increasing the O₂ concentration in the secondary stream above stoichiometric ratio may decrease the standoff distance and enhance flame stability.

Flame pattern and stability changed when the firing environments were changed from air to oxy-fuel [27,66-71,107]; as a consequence, emissions and heat transfer performance were also affected. It seems that these differences depend not only on feed gas composition, but also on the reduced volume flow rate under oxy-fired conditions and its distribution among the burner registers. Although different burner configuration and operating parameters are used in the test facilities throughout the world, many authors neglect reference parameters or dimensionless numbers in assessing the interpretation of results and it therefore becomes difficult to transfer results to other configurations and industrial-scale burners. The very interesting work performed by Fry et al [71] focused on the effects of the primary stream flow characteristics on flame stability. By matching the primary gas-fuel mass flow ratio and primary stream momentum to that of air-firing, a stable and attached flame was obtained that closely resembled the air-fired flame. It is well-known that the primary stream plays an important role in flame stabilization; however, most of the feed gas is injected by secondary or tertiary registers, which may also be swirled to promote reverse flows in the vicinity of the burner and facilitate the flame stabilization. Chui et al [89] observed that NO_x emissions from oxy-coal combustion can be higher than from air-firing within a certain range of swirl number. These findings suggest that further investigations are necessary for a better explanation since the measurements were limited to the furnace centerline.

The combustion of Lusatian pre-dried lignite combustion under oxy-fired conditions have been investigated by few authors [67,86,91]. In the work performed by Hjærtstam et al [67], it was reported that upward adjustments of the O₂ fraction in the feed gas (from 25 to 29 vol%) led to significant local differences in gas composition in the furnace, change in combustion intensity, and consequently changing the flame stability. However, CO and NO concentrations at the furnace exit were not affected. Gas concentrations and temperature distributions similar to the air-fired case were achieved when the oxy-fuel flame operated with 25 vol% O₂. These experiments were carried out using dry flue gas recirculation; a higher O₂ fraction in the feed gas would probably be necessary in order to reach similar flame temperatures in the case of a recycle wet flue gas. In the experiments conducted by Dhungel [91], the impacts of feed gas staging on emission performance were investigated. To keep a similar flame shape and a similar residence time inside the reactor, the total volumetric flow of feed gas through the burner was kept the same for all experiments while the coal feed rate and stoichiometric ratio were varied. Further investigations are necessary before

being able to make predictions regarding large-scale furnaces. Experimental data reported in the work of Wilhelm [86] for wide range of O₂ fraction upstream of the burner (17-33 vol% O₂) showed clearly that air in-leakage enhances NO formation. Uniquely, significant levels of NO₂ were observed under oxy-fired conditions.

Overall, much of the experimental data regarding gas phase temperature and concentration profiles is limited, i.e. usually confined to the centerlines of the furnaces and with poor information regarding the near burner region [65,66,89-91]. Because of difficulties associated to the measurement of velocity profiles in particle-laden flows and solid fuel combustion, only one study was successful in obtaining experimental data for a pulverized oxy-coal flame [104]. Similarly, heat flux profiles in oxy-coal flames were reported in only a small number of works [27,65,70]. Another important point is that only mean values have been reported, which is usually insufficient due to stochastic aspects of the combustion process. Additionally, the absence of statistical reproducibility and experimental errors leads to difficulties in interpreting the experimental data and in its use for further validation purposes.

3 Experimental Method

3.1 Description of the Laboratory Facility

The test facility used for carrying out the experimental investigations was conceived specifically for conducting research on oxy-fuel combustion processes, applying firing conditions approximating those found in full-scale plants. The test facility can be broken down into four main systems: fuel feeding system, furnace, flue gas treatment, and water cooling system. Other important sub-systems include: storage tanks for O₂ and CO₂, fans, heat exchangers, and supervisory system. Figure 3.1 provides a schematic of the plant configuration.

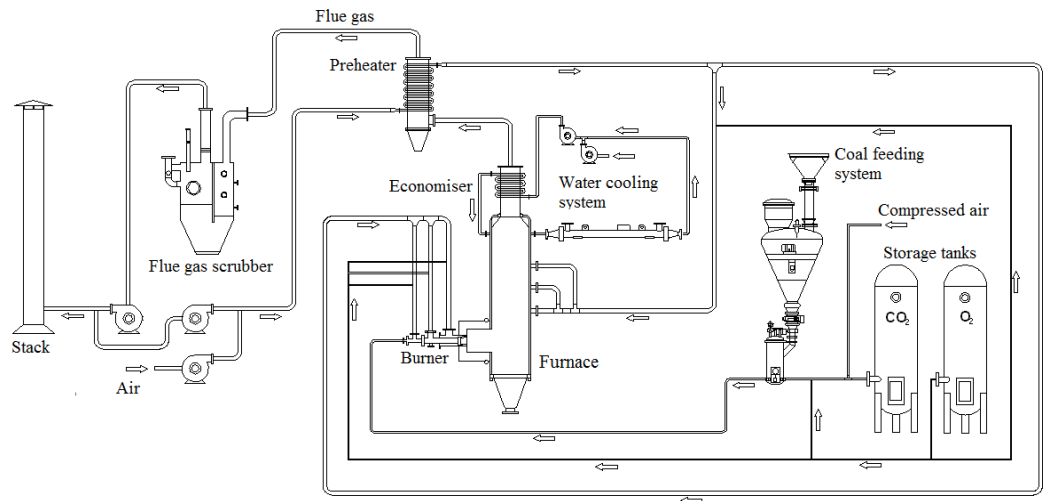


Figure 3.1: Schematics of the test facility.

Crushed coal is transported to a storage silo which feeds a pulsation-free metering and pneumatic conveyance system capable of maintaining a steady flow of fuel up to the burner. Air or recycled flue gas combined with O₂ and CO₂ from the bulk storage vessels is supplied as feed gas, while a preheater is used to increase its temperature before it enters into the furnace. The feed gas can be split into a maximum of four streams with their composition and volume flow rate continuously monitored to ensure the desired amount of feed gas at each burner register. The combustion takes place in a horizontal up-fired furnace with a rated capacity of 0.40 MW_{th} designed to reproduce the time-temperature history of a fuel particle entering in a full-scale furnace. The burner geometry is typical of that used in power stations for wall-fired boilers and provides stable flames over a wide range of operating conditions capable of firing coal or combustible gases. After the furnace and economizer, the flue gas is passed through a preheater to reduce its temperature before being directed to the sulfur and fly ash wet scrubber.

3.1.1 Coal Feed System

The feed system is depicted schematically in Figure 3.2 and consists of a homogenous fluidized bed of coal within a container, where a metering disk with several coaxial holes determines the amount of material fed into the furnace. As the disk rotates about the horizontal axis of its drive unit, the coal passes between two floating ring seals into the pneumatic conveying line. Due to the same number of holes in the feed line during the rotation of the disk, coal is fed free of pulsations. When the minimum fill level is reached, the vessel is filled back up to the upper filling level via a feed pipe.

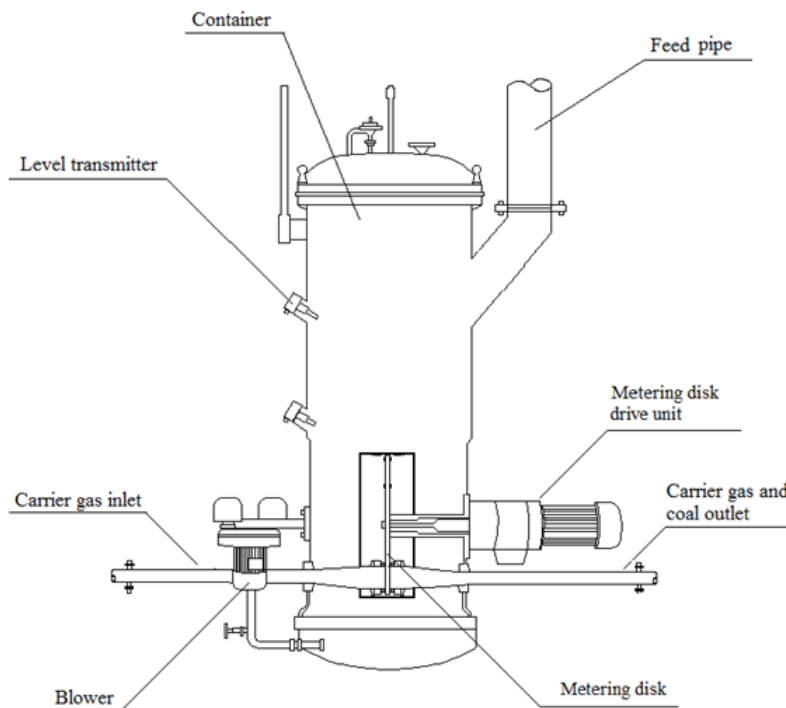


Figure 3.2: Overview of the metering system.

The maximum coal throughput of the feeding system is 72 kg/h and pressurized air or a mixture of CO_2 and O_2 is used as a fluidizing medium and carrier gas. The maximum O_2 fraction in the carrier gas is limited to 21vol% due to safety constraints. Homogeneity, particle density, and a complete filling of the holes in the metering disk are important for achieving a constant and pulsation-free coal feed. The fluidization gas passes through a filter and is discharged outside, while the carrier gas and coal particles flow along the conveying line to the burner. Additionally, the floating ring seal prevents the entry of unwanted gas and fluidized material into the feed line.

3.1.2 Furnace

In the initial design studies of the test facility, the sizing of the furnace was a crucial consideration. It consists of a vertical water-cooled boiler and a cylindrical refractory section where the burner is attached. The arrangement of the combustion system is depicted in Figure 3.3. The cylindrical section of the furnace has an internal diameter 0.95 m and is 1.068 m long. The boiler consists of membrane walls where parallel tubes are connected by fins welded in between. The boiler has an internal square cross-section of 1.012 x 1.012 m and a height of 4.40 m. The floor section and the lower 2.20 m of the boiler are lined with a 0.05 m layer of refractory. Chemically treated water flowing through the membrane walls at temperatures of 180-190 °C decreases the time required to reach steady state and prevents slagging. The boiler was designed for a thermal power of the 0.33 MW and an operating pressure of 21 bar. The cooling water flow rate and the temperature at the inlet and outlet are continuously monitored in order to determine the total heat extraction from the furnace and economizer.

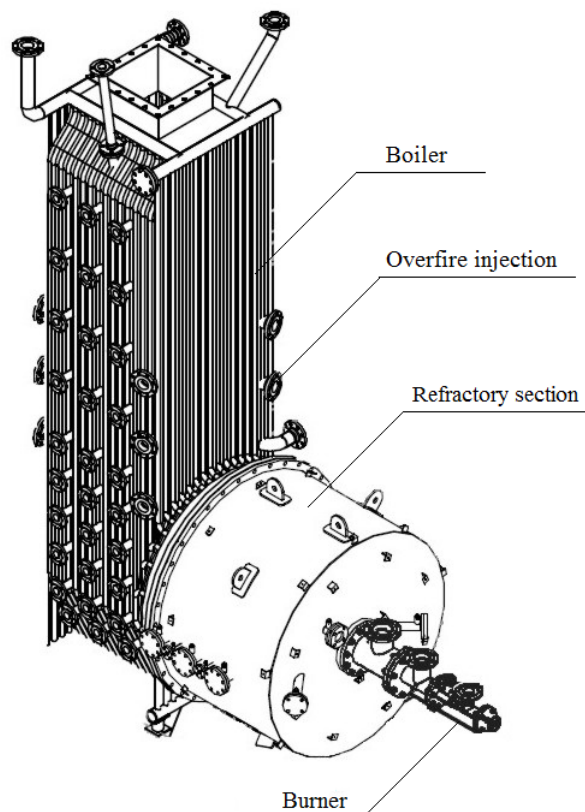


Figure 3.3: Large-scale laboratory furnace.

Although not used in this study, three over-fired levels of feed gas injections above the flame zone are available at the boiler and can be used to reduce the

stoichiometry, temperature, and velocity levels at the burner region and consequently achieve complete burnout and to encourage the formation of N_2 rather than NO_x . A major advantage of this laboratory furnace is that it is large enough to ensure that the physical phenomena of full-scale furnaces are reproduced (i.e. fully turbulent flow combined with significant heat transfer by radiation). The influence of a back wall and recirculation zones allow for the simulation of full scale combustors, mainly those with one side wall and opposite side wall burners. Detailed and reliable data are obtained at the 33 access ports provided along the combustion chamber for probing and visual observations.

3.1.3 Staged Feed-Gas Burner

The industry-type burner designed for the laboratory facility has a thermal output of 0.40 MW and can operate either with natural gas or pulverized coal (Figure 3.4). The burner uses natural gas to preheat the furnace before each test; only at temperatures above 850 °C does the furnace provide the necessary conditions for the sustained combustion of coal. If the coal is fired before the walls are hot enough, a steady-state, coal-fired operation cannot be maintained.

The goal of the burner design was to develop a stratified flame structure with specific sections of the flame operating fuel-rich and other sections operating fuel-lean. The primary stream, used for the introduction of pulverized coal, is positioned in the center of the burner and enclosed by inner and outer secondary feed gas registers. To simplify the analysis, the inner secondary stream was not used in this study. In order to provide easier flame stabilization and increase the residence time, both secondary streams can be swirled by swirler assemblies installed close to the outlet. In case of the outer secondary register, each swirler includes 6-16 vanes, which are attached radially about the central shaft and set with various angles varying from 0 to 60 degrees with respect to axial directions as illustrated in Figure 3.4 (b). The outer diameter and the axial length of the swirler are 112.7 and 25 mm, respectively; the radial length of each vane is 11.35 mm.

To increase the flexibility of combustion staging and flame shaping, part of the feed gas stream is also injected through an annulus orifice enclosing the burner quarl (i.e. tertiary stream). Due to the divergent format of the quarl (4.55 degree half-angle), the jet is forced to follow the slope of the wall, thus increasing the radial distance of separation between peaks of axial and tangential velocities and increasing the reverse flow rate. The confinement ratio, defined as the ratio of diameter of the cylindrical muffle to the quarl exit diameter, is 6.21. The maximum volume concentration of O_2 at the primary inlet is 21% and 39% at the other inlets. The main dimensions of the burner based on the outlet diameter of the outer secondary annulus are presented in Figure 3.5.

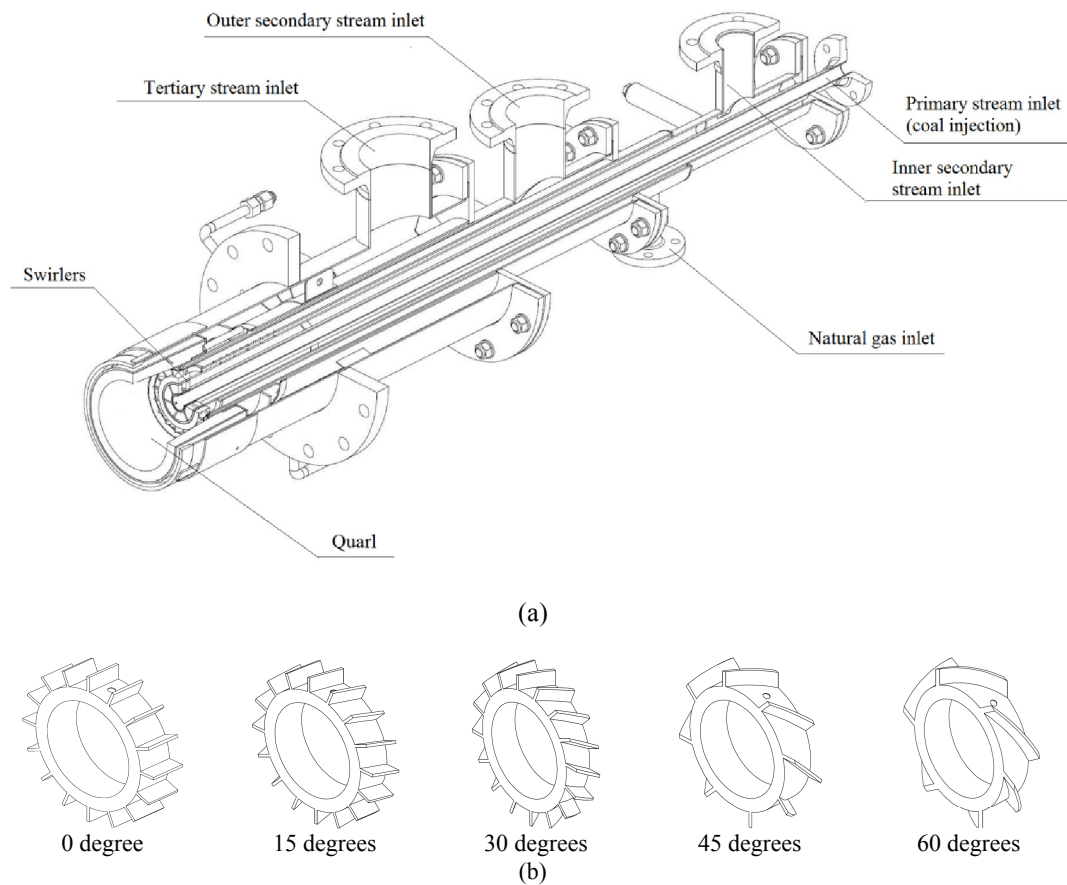


Figure 3.4: Overview of the (a) staged feed-gas burner and (b) swirlers of outer secondary stream.

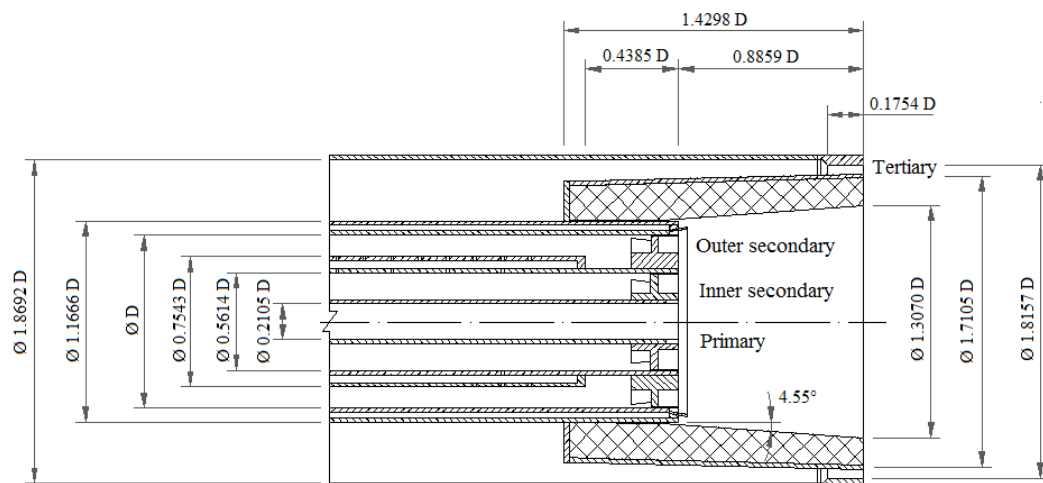


Figure 3.5: Main dimensions of staged feed-gas burner as used in the investigation ($D = 0.114 \text{ m}$).

3.1.4 Flue Gas Scrubber

The technology employed for removing SO_2 and particulate consists of a wet flue gas scrubber (Figure 3.6). The flue gas stream first passes through a jet scrubber where the flue gas is cooled and a large amount of SO_2 and some particulate are removed. This is accomplished by passing the flue gas through a spray of 10% sodium hydroxide solution (NaOH). Most of the particulate is then removed using a venturi scrubber, a traditional and well-known method for removing fine dust particles in industrial applications. At the precipitator, the fluid and gas phases are separated and the absorbing solution is collected. For a complete scrubbing, a packed column is installed where the flue gas enters the bottom of a cylindrical tower and flows upward through a shower of NaOH solution. A droplet separator is also installed within the packed column to eliminate the droplets from the flue gas before leaving the scrubber.

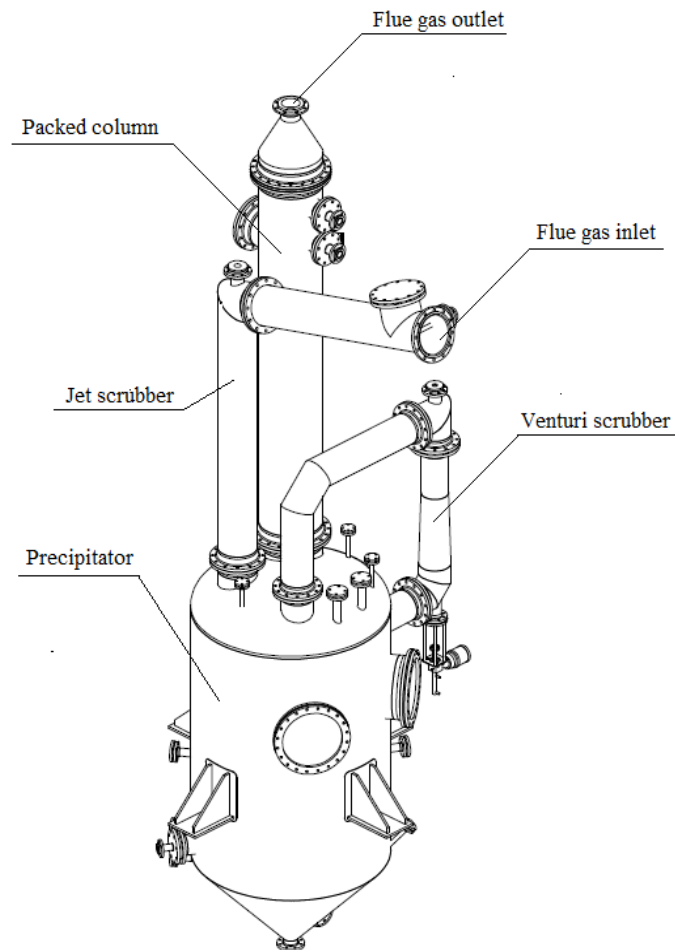


Figure 3.6: Overview of the flue gas scrubber.

3.1.5 Other Components

Two stainless steel fans control what amount of flue gas goes to the stack and what gets recycled back to the furnace. For conventional operation and start-up, a separate fan provides the air for the combustion; for oxy-fuel operation, two storage tanks installed outside supply the necessary O₂ and CO₂. Both gases are supplied as a liquid since this requires much less storage capacity; the liquid is then vaporized in two evaporators and delivered as a gas via the supply pipe to the furnace.

To improve plant efficiency by recovering waste heat from the flue gas stream, heat exchangers (the economizer and preheater) are installed in the flue gas path. The economizer, positioned at the top and downstream of the furnace, consists of multiple horizontal tube bundles. The heat is transferred mainly by convection and non-luminous radiation which provide a heat transfer rate of up to 70 kW_{th}. Similar to the economizer, the preheater has a maximal heat transfer rate of 36 kW_{th} and increases the feed gas temperature prior to the furnace. A cooling system removes the heat absorbed by the water walls of the furnace. It is composed of two pumps which continuously circulate the water through a heat exchanger, where the temperature is lowered before being returned to the economizer. This shell and tube heat exchanger with a capacity of 0.40 MW_{th} uses water as its cooling medium.

A premix pilot burner operated with natural gas ignites and stabilizes the fuel/feed gas mixture delivered by the main burner. In addition, this pilot burner is kept in operation during the switching from air-firing to oxy-firing. A pilot flame is projected in front of the main burner into the combustion space including the quarl. With help of a flame supervision system, the fuel supplied to this premix pilot burner must be turned off once the flame from main burner is stabilized. Two UV scanners are installed at well-sighted observation ports to detect the flame and confirm ignition and the establishment of combustion.

Plant supervision and data acquisition is run with a commercial control-system software. This system provides communication and control between the field devices and other nodes on the network by specifying loops and other functions with high flexibility. An intuitive user interface displays all the process devices and allows for easy monitoring and control. During system start-up and shut-down, and in various situations during normal operation, the control system verifies or changes the status of the main components of the test facility. Additionally, the control system continuously monitors all safety parameters and shuts down the combustion system if any of the safety parameters are not met.

3.2 Instrumentation and Measurements

To assess the impact of operating conditions on the furnace performance, certain information is typically monitored during the combustion process. A detailed description of the experimental techniques used in obtaining values for the scalar characteristics are presented here. The requirements for the measuring systems are briefly summarized and probe methods are outlined. The need to minimize errors arising from in-flame measurements is also discussed.

3.2.1 Combustion Inputs and Outputs

To conduct a successful test, many variables have to be measured throughout testing. A comprehensive fuel analysis is carried out prior to and after the combustion tests. Coal samples are characterized using standard techniques such as proximate and ultimate analysis, particle size distribution, calorific value, and ash melting point. The methods and equipment used in coal characterization are summarized in the Table 11.

Table 11: Methods for coal characterization.

Parameter	Specie	Method	Standard
Proximate analysis	Water	Drying chamber	DIN 51718
	Ash	Ashing furnace	DIN 51719
	Volatile matter	TGA	DIN 51005
	Fixed carbon	By difference	
Ultimate analysis	C, S, H, N	Combustion in O ₂ and thermal conductivity sensors	DIN 51721 DIN 51727
	O ₂	By difference	
Heating value	-	Calorimetry	DIN 51900
Particle size distribution	-	Static laser light scattering	ISO 13320
Ash melting point	-	Heating chamber	DIN 51730

One of the most important aspects of burner testing is fuel metering. The amount of coal conveyed by the feed system is determined continuously by measuring the loss of weight per time period. The flow rate in the primary stream is measured using thermal mass flow meters upstream of the fuel feed system; the rest amount of feed gas is measured with orifice plates installed upstream of the burner. Exhaust and recycled gas flow rates are also determined by measuring the differential pressure across a known orifice plate. In-situ measurements of temperature are performed at several points in the feed gas and flue gas streams using standard thermocouples and resistance thermometers. Pressure transmitters are used to provide an analog pressure signal through a diaphragm coupled to a

variable resistance, which modifies a loop current in proportion to the range in which it is calibrated. Thermocouples are also installed in the cooling-water circuit to record inlet and outlet temperatures at the economizer, boiler, and cooling heat exchanger. Additionally, the flow rate is controlled and monitored by an orifice plate so that heat balance calculations can be performed.

Gas samples are collected after the furnace and at the stack, and conducted to the gas analyzers through electrically heated tubes. The sampling gas is cooled and its moisture removed before entering the analyzer. The analytical instrumentation includes a magnetic pressure analyzer for O₂ measurement and non-dispersive infrared absorption gas analyzers for CO and CO₂. A process photometer which measures a gas filter correlation and a wavelength comparison in an ultraviolet spectrum is used for NO and SO₂ measurements, respectively. These instruments are calibrated, zeroed, and spanned before each measurement run. Water vapor and O₂ volumetric fractions downstream and upstream of the furnace are also measured by gas humidity and gas potentiometric analysis, respectively.

For comparison purposes, NO and SO₂ emission are calculated in terms of the mass of the emission per unit of energy input by using the Equation 3.1. To assess emission performance, the conversion ratio of fuel-bound nitrogen or sulfur to NO or SO₂ can be estimated by the Equation 3.2.

$$\phi_i = \frac{1000 y_i \dot{V}_{\text{flue gas (STP)}}(1-x_{\text{H}_2\text{O}})}{\dot{m}_{\text{coal}} \text{LHV}} \quad (3.1)$$

$$\eta_{j \rightarrow i} = \frac{y_i f M_j \rho_{i,\text{stp}} \dot{V}_{\text{flue gas (STP)}}(1-x_{\text{H}_2\text{O}})}{10000 M_i w_{j,\text{ar}} \dot{m}_{\text{coal}}} \quad (3.2)$$

3.2.2 Local Gas-Phase Temperature

The most common device used in measuring temperature is the thermocouple, but several factors lead to inaccuracies when used in aggressive environments such as furnaces [108-110]. The equilibrium temperature of the measurement junction is a resultant temperature of the heat transfer by convection and radiation with the environment, and by conduction along the thermocouple wires when they are exposed to temperatures gradients. In practice, one way of increasing the accuracy of measurements within the furnace is to use an intrusive suction pyrometer in which the temperature of the gas is measured under known conditions. At the desired measurement location, gas is extracted from the flame through a sampling tube. A thermocouple is mounted on the axis of a system of shields through which

the sucked gas flows at higher velocity. An overview of the complete measuring system is illustrated in Figure 3.7.

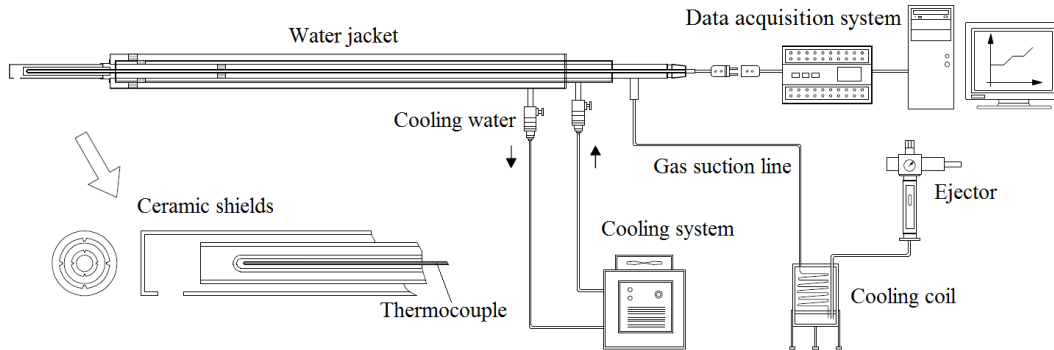


Figure 3.7: Experimental setup for measurement of temperature.

The water-cooled suction pyrometer used in the experiments was constructed according to the IFRF standard, wherein the thermocouple is protected by three concentric radiation shields of sillimanite. The outer ceramic shield has external and internal diameters of 27 and 21 mm, respectively; the inner ceramic has diameters of 17 and 11 mm. The ceramic shield, where the measuring point of the thermocouple is positioned, has an external diameter of 7 mm. A lateral hole with a diameter of 14 mm at 12 mm distant from the end of the outer ceramic shield allows the suction of combustion gases. A compressed air injector draws the combustion gases in at a velocity of 80 m/s, which is maintained by a flow meter. Because the gases pass over the thermocouple sheath with a sufficiently high velocity, the equilibrium thermocouple temperature is nearly that of the gases and hence there is no need to correct for radiation [111,112].

Two thermocouple types were used during the experimental runs. A mineral insulated metal sheath ANSI type B thermocouple (Pt/30%/Rh-Pt/6%Rh) with a 1.50 mm outer diameter is used in the near burner field where temperatures reach 1700 °C. In regions farther from the burner, where temperatures are lower than 1200 °C, a mineral insulated metal sheath ANSI type K thermocouple (NiCr-Ni) with a 3.00 mm external diameter is used. All thermocouples were calibrated prior to each experimental run. The details of the sources of uncertainty and experimental errors are fully discussed in Appendix A.

3.2.3 Local Gas Species

The information regarding the gas composition is useful not only in determining the combustion efficiency at various points within the combustion chamber, but also useful for studying the mixture among the different jets and the recirculated gas species in the near burner field. However, one of the major difficulties in measuring gas composition is in maintaining the initial characteristics of the sample [111]. There are several potential uncertainties with most extractive gas sampling techniques, the most important of which is due to the subsequent chemical reactions in the gas sampling system. The sampling probe must be cooled in combustion environments, leading to a larger probe size which is more intrusive on the flame [108]. This also adversely affects the spatial resolution of the measurement. Extractive gas sampling systems are unable to measure large gradients, since such gradients occur near the reaction zone and the residence time of the gases on the sampling system is much larger than the time scales of turbulent flames. Thus, in common with other experimental methods presented here, only time-averaged measurements are possible with such techniques.

An overview of the measuring system used to quantify the gas species within the furnace is illustrated in Figure 3.8. Sampling for the measurement of local mean values of gas species are achieved using a titan water-cooled probe, constructed according to VDI 2066 and EN 13284-1, where the reaction quenching is accomplished by drawing the sample through the cooled probe tube. The probe outlet is connected to a fiber filter to remove the particulates. The analytical instrumentation includes a magnetic pressure analyzer for O₂ measurement and a non-dispersive infrared absorption analyzer for CO, CO₂, and CH₄ measurements. A process photometer with a gas filter correlation in an ultraviolet spectrum is used for NO measurements. Because the sampling probe is cooled, in-flame SO₂ is not measured. Similar to other measuring systems used in this research, analog outputs of the analyzers and transmitters are sent to a data acquisition system and a computer where the signals are processed and the mean values computed. Zero and span calibrations with standard mixtures are performed before and after each measurement session. The measurement ranges and the experimental uncertainty of measurements are discussed in Appendix A.

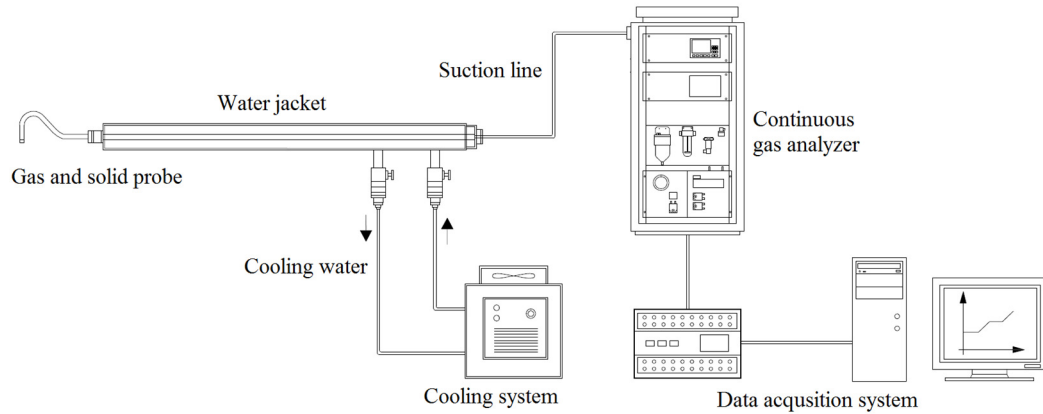


Figure 3.8: Experimental setup for measurement of gas species.

3.2.4 Solid Sampling

Solid sampling from the flue gas is performed with the same titan water-cooled probe used for measuring gas composition. The main difference is that the phase separation takes place in a high dust tubular filter device installed at outlet of the water-cooled probe. Coal samples are taken only at the access port closest to the furnace exit. Once the solid sample has been collected, it is dehydrated in an oven at approximately 110 °C before analysis is performed. The analysis consists of determining the amount of unburned carbon remaining in the ash, which is subsequently used to calculate the combustion efficiency. Several different bases can be used to describe burnout (percent carbon loss is common) and the results are given on a dry and ash-free basis (daf) [113]. The same procedure used to perform the ultimate analysis can be employed for the analysis of solid char and ash samples retrieved from a reacting flow. The particle burnout data can be obtained by the following equation [114]:

$$\psi = \frac{\left[1 - \left(\frac{W_{\text{ash,coal}}}{W_{\text{ash,sample}}} \right) \right]}{(1 - W_{\text{ash,coal}})} \quad (3.3)$$

3.2.5 Total Radiative Heat Flux

Thermal radiation is the dominant heat transfer mechanism in pulverized coal combustion flames. Coal, ash, and soot particles are all effective emitters and play an important role in transferring thermal energy at the furnace walls. Thus,

magnitudes and distributions of radiant incident heat flux at the furnace walls are important parameters to be quantified when flame pattern and temperatures are changed. In this study, total radiative flux is measured using an ellipsoidal radiometer, which consists of a water-cooled cavity having an aperture at one end and a thermopile at the other [115]. A schematic of the measuring system using a total radiation flow meter is presented in Figure 3.9.

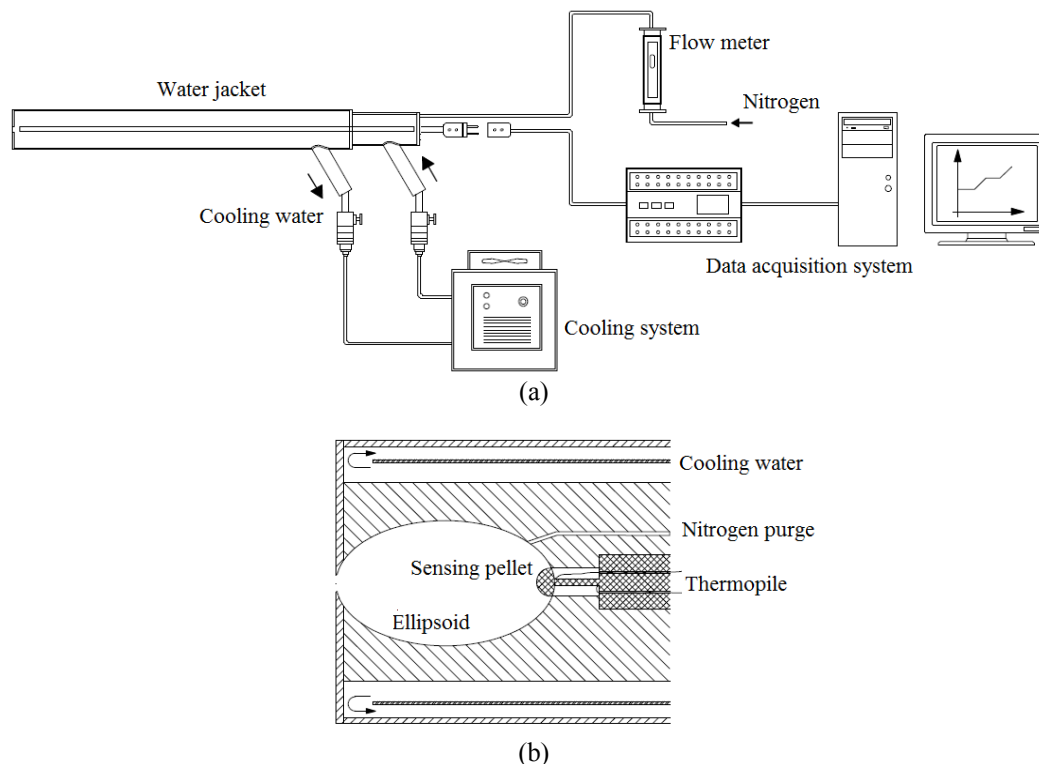


Figure 3.9: (a) Experimental setup for measurement of radiant incident heat flux and (b) overview of ellipsoidal cavity.

The ellipsoidal radiometer uses a cavity plated with a 0.50 mm gold layer in order to minimize the radiation loss by absorption at the surface of the ellipsoid. To prevent the entry of combustion gases and particles into the cavity, a purge flow of dry N_2 is injected through small holes. The thermopile consists of a heat flow plug of stainless steel with two thermocouple junctions at each end (constantan wire) which produce an electromotive force as a linear function of the energy absorbed at the pellet due to the temperature gradient. This heat sensitive pellet absorbs practically all the radiation, i.e. from 95% to 98%, independent of wavelength [111].

The radiometer is calibrated against a blackbody furnace having a known internal temperature prior to each experiment. Mechanical shock may change the position of the thermopile and damage its receiving surface. In addition, the size of the cavity's orifice may change over time. Additionally, the N_2 injected into the

ellipsoid may carry a few particles or droplets of oil that can settle on the mirror. The volume flow rate of N_2 injected into the ellipsoid is carefully controlled and kept at 50 l/h (STP) during the whole of the measurements and calibration. Any more would cool the receiving pellet and modify the sensitivity of the thermopile [111]. Further details on the calibration procedure and the uncertainty of measurements are detailed in Appendix A.

3.2.6 Surface Temperature and Heat Flux at the Water-Cooled Walls

Temperature measurements at the boiler are performed using resistance temperature detectors (RTD) installed on the fin at the outer side of the water-cooled walls. As illustrated in Figure 3.10, a welded-on contact screw nut is applied to keep the measurement junction in contact with the outer surface. The resistance thermometer consists of a platinum resistive with a threaded measurement end. The main advantage of using resistance thermometers is their high accuracy combined with long-term stability [116,117]. Inner surface temperature in the cylindrical refractory section of the furnace is monitored with standard ANSI type B thermocouples embedded in the ceramic lining 20 mm from the fireside wall.

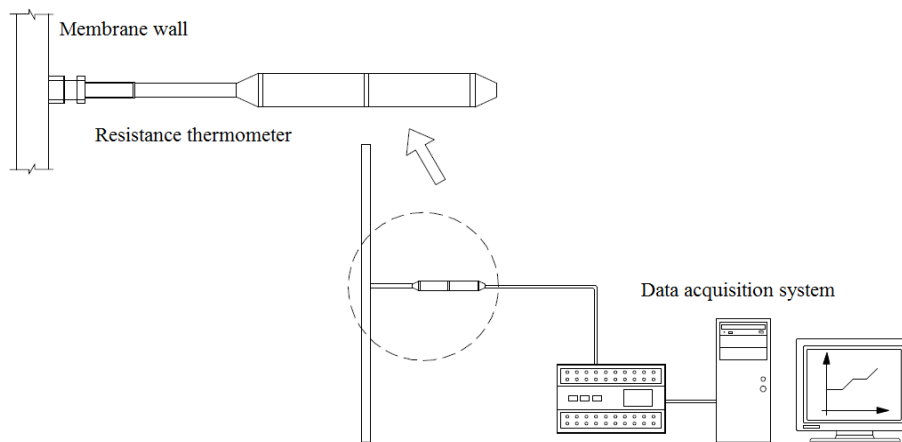


Figure 3.10: Experimental setup for measurement of surface temperatures at the membrane walls.

Knowing the distribution and magnitude of the heat flux absorbed by the membrane water-cooled walls is helpful for a proper understanding of the heat transfer within the furnace, mainly when the firing conditions are changed. However, the measurement of the heat flux absorbed by the water walls with satisfactory accuracy is a challenging task and considerable work has been done in recent years [118]. The method used in this study is based on the measurement of the temperature difference of the water wall temperature at two characteristic

positions (at the middle of the fin and tube) by means of standard ANSI type T thermocouples (Figure 3.11). Using mathematical models it is possible to evaluate the temperature profile and the distribution of the heat flux at the water walls for different values of heat flux. Thus, a relation between the signal generated by the thermocouples and the heat flux can be established [119]. Further information on the correlation curves and measurement errors are detailed in Appendix A.

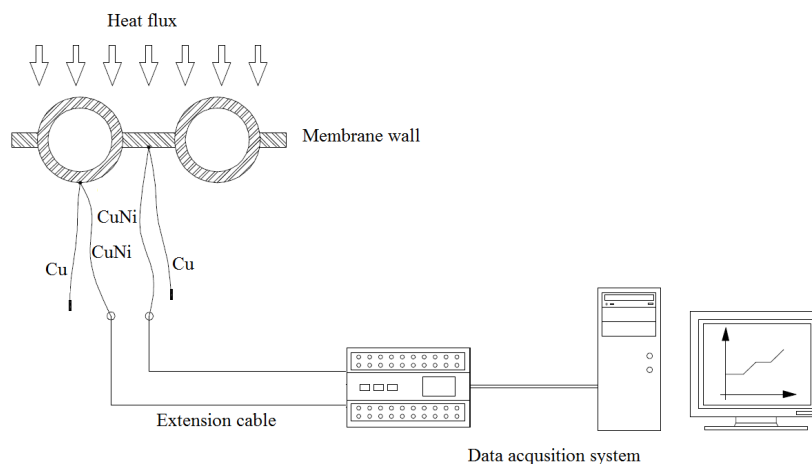


Figure 3.11: Experimental setup for measurement of heat flux at the membrane walls.

3.2.7 Flame Pattern and Peak Flame Temperatures

The flame's shape, size, and intensity are important parameters to be investigated. Implementation of oxy-fuel combustion may bring about changes in the flame structure and fuel/feed gas mixing pattern. Therefore, the control of the flame shape and size is important in ensuring that there is proper heat distribution in the combustion and that the flame does not impinge on the furnace walls and damage the tubes. In this study, the flames are observed and recorded by a digital camera through the sight quartz glass installed at 0.050 from burner quarl. Additionally, in order to obtain high-resolution views of the burner flames and to monitor the combustion process, a digital imaging system is installed at one of the view ports at the back wall. Such visualization techniques have been applied to study coal-fired flames in both laboratory and industrial environments for a variety of applications [120-123]. Figure 3.12 shows schematically the constituent elements and structure of the vision-based flame monitoring system used in this work.

In this system, an optical probe shielded by a water-cooled jacket transmits light from the flame into the camera. The objective lens of the probe has a 90 degree viewing angle and its surface is kept dust-free by a purged air or CO₂ flow. A CCD (charged coupled device) camera visualizes the flame zone. CCD sensors

can reveal spectroscopic radiation information of combustion flames and are suitable for the temperature distribution measurement [124]. The video signals from the camera are transmitted into the computer and digitized by the frame grabber into two-dimensional digital images. Temperature contours are continuously derived from flame images using various digital image and signal processing algorithms.

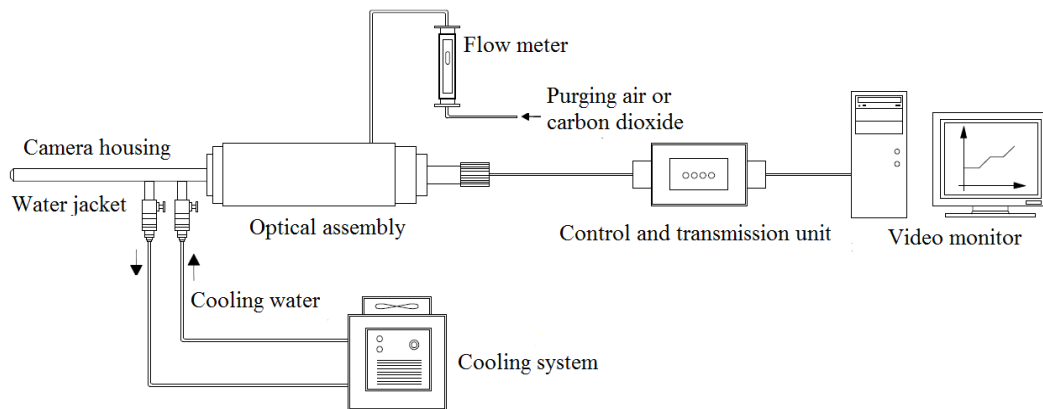


Figure 3.12: Flame digital imaging system.

For a particle-laden flame, primary color signals in a color radiation image are received by the CCD camera in the image processing system. These obey the Planck's radiation expressed as

$$i_{\lambda} = \varepsilon \frac{2h c_0^2}{\lambda^5 \left[\exp\left(\frac{hc_0}{k\lambda T}\right) - 1 \right]} \quad (3.4)$$

With the assumption of gray radiation for coal-fired flames [124], the emissivity of the flame is independent of the wavelength. A common approximation allows the emissivity to vary between the emissivity of unburned carbon (1.00) and fly ash (0.60) [125]. Calibration was accomplished using a two-color pyrometer and the maximum deviations used in the evaluation of the uncertainty of measurements are detailed in Appendix A.

3.2.8 Sampling Points and Data Presentation

Figure 3.13 illustrates the measuring points where the probes for local gas-phase temperature and species concentrations are inserted for the acquisition of transversal profiles. In the case of measurements with the ellipsoidal radiometer, the tip of the probe was aligned with the inside firewall of the furnace. In total, 8

access ports are used to insert probes into the furnace as listed in Table 12. Local surface temperature and heat flux at water-cooled walls are continuously monitored at 7 and 20 measuring points, respectively, as detailed in Figure 3.14. Average sampling time at each position was varied between 2 to 3 minutes after reaching a steady-state condition (usually within 3 minutes). The number of observations at each point was varied between 120-180; sufficient enough to ensure that the arithmetic mean provides a reliable estimate of the expectation of the random variable and a reliable estimate of the standard deviation.

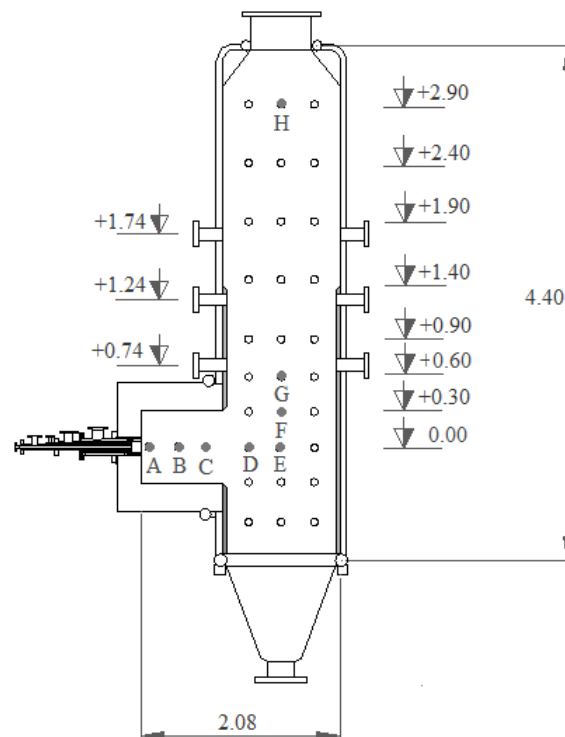


Figure 3.13: Overview of probe access openings (dimensions in meters).

Along with the extensive experimental measurements, great emphasis was also given to analyzing the experimental uncertainty of each measurement. The result of a measurement is only an approximation or estimate of the real value of the measurand and thus an experimental value of a variable is complete only when accompanied by the uncertainty of that estimate. The approach upon which the uncertainty is evaluated, is that outlined in Guide to the Expression of Uncertainty in Measurement (GUM) [126]. For further information, the reader is referred to the Appendix A. Graphical methods assisted in analyzing the data from the experiments. In addition to line and scatter plots of the arithmetic mean, box plots are also used to graphically describe the variability of results. In these plots, the lower and upper quartiles, (the 25th percentile and 75th percentiles, respectively), and the median (the 50th percentile) on a rectangular box aligned vertically are displayed. Two lines extend from the ends of the box to the 90th and 10th

percentile values, whereas two small circles represent the 5th and 95th percentile. Contour plots using mean values are also included to assess the interpretation of the experimental data.

Table 12: Overview of the measuring points.

Position	Axial distance from burner quartz (m)	Transversal distance from burner axis (m)		
		Local gas temperature and species concentration	Radiative heat flux	Solid sampling
A	0.050	-0.45, -0.25, -0.15, -0.10,	-0.48	
B	0.355	-0.05, 0.00, +0.05, +0.01,		-
C	0.660	+0.15, +0.25, +0.45		
D	1.274	-0.45, -0.25, -0.15, -0.05,	-0.46	-
E	1.554	0.00, +0.05, +0.15, +0.25, +0.45		
F	1.554	-0.45, -0.30, -0.15, 0.00,	-0.46	-
G	1.554	+0.15, +0.30, +0.45		
H	1.554	-	-	0.00
Total number of points		65	7	1

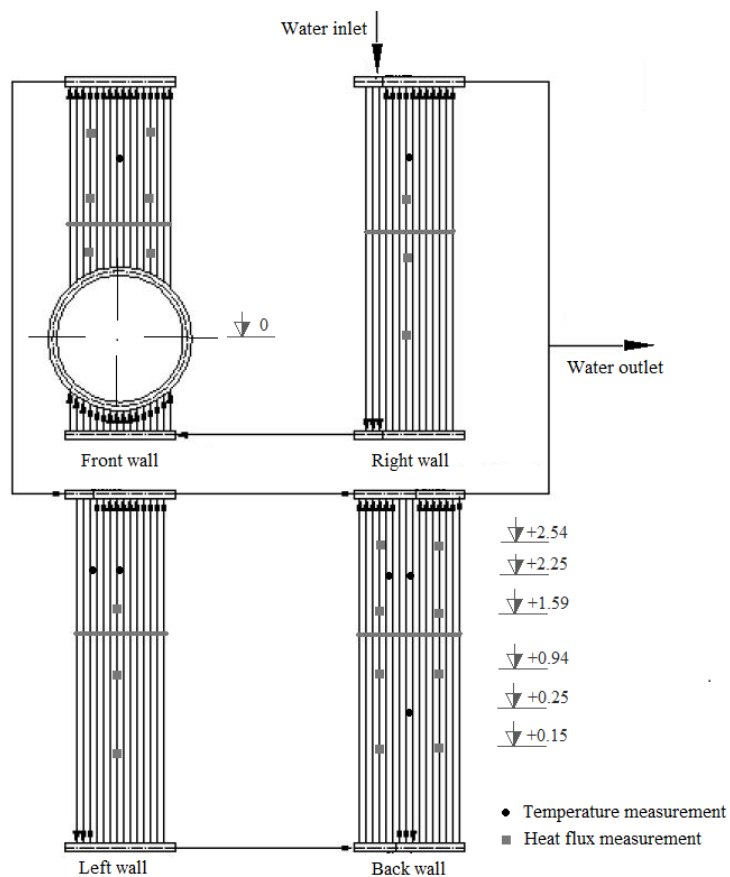


Figure 3.14: Measuring points of heat flux and temperature at the membrane walls (distances from burner axis).

4 Theoretical Study of Combustion-Related Parameters and Burner Aerodynamics

4.1 Introduction

In this chapter, a theoretical study is performed to estimate basic combustion parameters and to determine the main operating settings of the furnace during the experiments. The calculations include parameters such as excess of oxygen, adiabatic flame temperature, and flue gas composition. Even though solid fuel combustion is extremely complex, there are a number of basic engineering calculations that can be performed easily based on mass balances and energy balances. A numerical study of aerodynamics in the near burner region applying non-combustion (isothermal) conditions is performed with help of the CFD-package Fluent 12.1. Because the aggressive environment makes it difficult to measure velocities in the near burner region, the main objectives of this analysis includes an investigation of effects of various burner settings (e.g. vane angle of swirler and feed gas composition and distribution in the burner registers) on the generated flow pattern. The swirl number at the outlet of the secondary stream is also calculated. The results obtained from the theoretical study are also applied to evaluate experimental results.

4.2 Basic Combustion Parameters

4.2.1 Mathematical Formulation

The fundamental parameters such as the oxygen-fuel ratio, adiabatic flame temperature, and approximated flue gas composition exiting the furnace are computed for a wide range of operating conditions. For convenience, only the main equations are summarized here. These equations are derived from thermodynamic balances; detailed information can be found elsewhere [127-129].

The oxygen-fuel ratio (OFR) is computed by

$$\text{OFR} = \left(w_{C,daf} \frac{M_{O_2}}{M_C} + \frac{w_{H,daf}}{4} \frac{M_{O_2}}{M_H} + w_{S,daf} \frac{M_{O_2}}{M_S} - w_{O,daf} \right) (1 - w_{H_2O,waf}) \lambda \quad (4.1)$$

The equilibrium composition of flue gas is only dependent on thermodynamics, i.e. it is independent of chemical kinetics. However, in most combustion process, and especially for emissions such as CO, equilibrium does not prevail. Thus, the product flue gas composition is calculated by assuming complete combustion, neglecting CO₂ reactions and formation/reduction mechanisms. The main

combustion products, including CO₂, water vapor (H₂O), N₂, and O₂, are calculated from the knowledge of fuel ultimate analysis and the composition of feed gas introduced into the furnace by the following equations.

$$\bar{m}_{\text{CO}_2, \text{flue gas}} = w_{\text{C,daf}} \frac{M_{\text{CO}_2}}{M_{\text{C}}} (1 - w_{\text{H}_2\text{O,waf}}) + \bar{m}_{\text{CO}_2, \text{feed gas}} \quad (4.2)$$

$$\bar{m}_{\text{H}_2\text{O, flue gas}} = w_{\text{H,daf}} \frac{M_{\text{H}_2\text{O}}}{M_{\text{H}_2}} (1 - w_{\text{H}_2\text{O,waf}}) + w_{\text{H}_2\text{O, coal}} + \bar{m}_{\text{H}_2\text{O, feed gas}} \quad (4.3)$$

$$\bar{m}_{\text{N}_2, \text{flue gas}} = w_{\text{N,daf}} (1 - w_{\text{H}_2\text{O,waf}}) + \bar{m}_{\text{N}_2, \text{feed gas}} \quad (4.4)$$

$$\bar{m}_{\text{O}_2, \text{flue gas}} = \frac{\bar{m}_{\text{O}_2, \text{feed gas}}}{\lambda} (\lambda - 1) \quad (4.5)$$

The energy in the coal calculated by Equation 4.6 is the chemically stored energy released as the fuel is combusted and converted to final products in the flue gas. The sensible heat of the preheated feed gas entering into the furnace is determined by Equation 4.7 using a reference temperature of 20 °C.

$$\dot{Q}_{\text{coal}} = \dot{m}_{\text{coal}} [\text{LHV} + c_{\text{P, coal}} (T_{\text{coal}} - T_{\text{reference}})] \quad (4.6)$$

$$\dot{Q}_{\text{feed gas}} = \sum \dot{m}_{i, \text{feed gas}} c_{\text{P}, i, \text{feed gas}} (T_{i, \text{feed gas}} - T_{\text{reference}}) \quad (4.7)$$

Assuming ideal conditions, such as complete combustion under adiabatic conditions (i.e. no heat loss or gain), the adiabatic flame temperature can be determined. This reference parameter is based on the first law of thermodynamics and takes into account the fact that the heat of combustion is used entirely for heating the fuel, the feed gas, and the combustion product. In the case of coal combustion, the adiabatic flame temperature can be easily determined by the following equation:

$$T_{\text{adiabatic}} = T_{\text{reference}} + \frac{\dot{Q}_{\text{coal}} + \dot{Q}_{\text{feed gas}}}{\dot{m}_{\text{flue gas}} c_{\text{P, flue gas}} + \dot{m}_{\text{ash}} c_{\text{P, ash}}} \quad (4.8)$$

4.2.2 Oxygen-Fuel Ratio

Plots of the oxygen-fuel ratio against O₂ excess are presented in Figure 4.1. For convenience, the firing rate and total O₂ flow rate are also included. The results are plotted on daf (dry and ash-free), waf (wet and ash-free) and ar (as received)

bases. The typical stoichiometric ratio for coal varies between 1.15 and 1.30 depending on feed gas mixing and coal type. Under these conditions, approximately 1.30-1.47 m³ (STP) of oxygen is necessary for each kilogram of coal on as-received basis. If an insufficient amount of O₂ is supplied to the burner, then unburned fuel, soot, and CO exit the furnace as exhaust. This results in heat transfer surface fouling, pollution, lower combustion efficiency, and flame instability. To avoid inefficient and unsafe conditions, furnaces operate at excess O₂ levels. This excess also provides protection from insufficient O₂ conditions caused by variations in fuel composition and operating variations in the coal and feed gas control system. However, an excessively fuel-lean mixture decreases the combustion temperature mainly due to heating of inert N₂ in case of air-firing, or CO₂ and water vapor mixture in oxy-fired combustion.

The excess of O₂ for oxy-fuel combustion carries a much greater penalty than conventional combustion in air. This is because the power consumption of the air separation unit (ASU), proportional to the amount of O₂ fed to the furnace, is directly responsible for decreasing the efficiency of oxy-fuel power plants [15]. Therefore, the stoichiometric ratio needs to be carefully controlled and if possible reduced relative to air-firing.

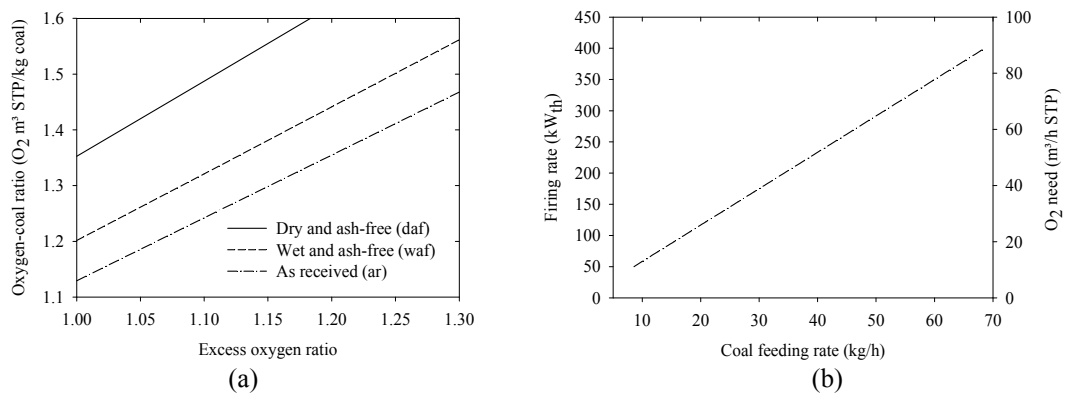


Figure 4.1: (a) Oxygen-fuel ratio and (b) firing rate of pre-dried lignite and O₂ need for a stoichiometric ratio of 1.17.

4.2.3 Adiabatic Flame Temperature and Feed Gas Flow Rate

The adiabatic flame temperature gives an indication of the radiative heat transfer in the combustion process, while the volume flow rate influences the particle residence time and the convective heat transfer within the furnace. Figure 4.2 demonstrates the effect of feed gas composition on the adiabatic flame temperature and on the mass and volume flow rates. The plots suggest that an increase in the O₂ fraction in the feed gas is a determining factor for the increase

of adiabatic flame temperature and decrease of volume and mass flow rate in comparison to conventional air combustion. From the plots it is also clear that such parameters vary considerably as a function of water vapor concentration in the feed gas at a constant excess O_2 ratio.

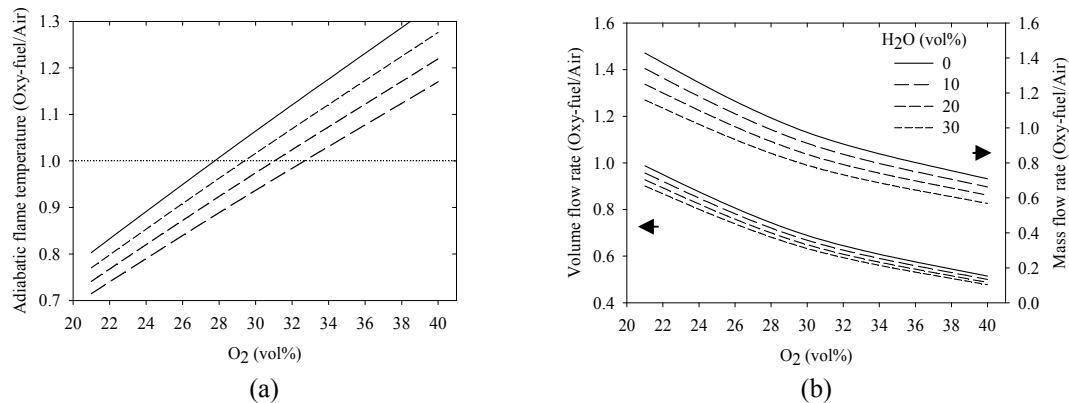


Figure 4.2: (a) Adiabatic combustion temperature and (b) mass and volume flow rate normalized to air-firing as a function of O_2 and water vapor volume fractions for a stoichiometric ratio of 1.17.

A same O_2 concentration in the feed gas as with normal air-firing yields an approximate volume flow rate under oxy-fired conditions. On the other hand, adiabatic flame temperature is considerably lower than air because of the higher specific heat capacity of CO_2 . Results obtained from the FluidEXL property library [130] show an increase of approximately 7% in specific heat of CO_2 in comparison to N_2 at 1300 °C and 1 atm. Between 30 and 40 vol% O_2 , depending on the water vapor content in the feed gas, it is possible to obtain approximate adiabatic flame temperature as with normal air operation mainly because of the reduced mass flow rate of flue gas. With an O_2 fraction of 30 vol%, the ratio of volumetric feed gas flow to that of air is about 25-35% lower. Another important aspect is that under these conditions, the feed gas stream leaves the burner registers at lower velocities, which results in increased particle residence time in the furnace. At this stage, it is very difficult to exactly determine the particle residence time, mainly because it depends on the temperature distribution of the flame and on the strength of swirl imparted by the burner.

Figure 4.3 shows the influence of the stoichiometric ratio and feed gas temperature on the adiabatic flame temperature. The plots show that the adiabatic flame temperature decreases linearly with the increase of O_2 excess, mainly due to the heating of flue gas components such as N_2 , CO_2 , and water vapor. Much more similar values of adiabatic flame temperature in air-firing are achieved for a wide range of feed gas temperature by applying an overall O_2 fraction of 31 vol% upstream of the burner.

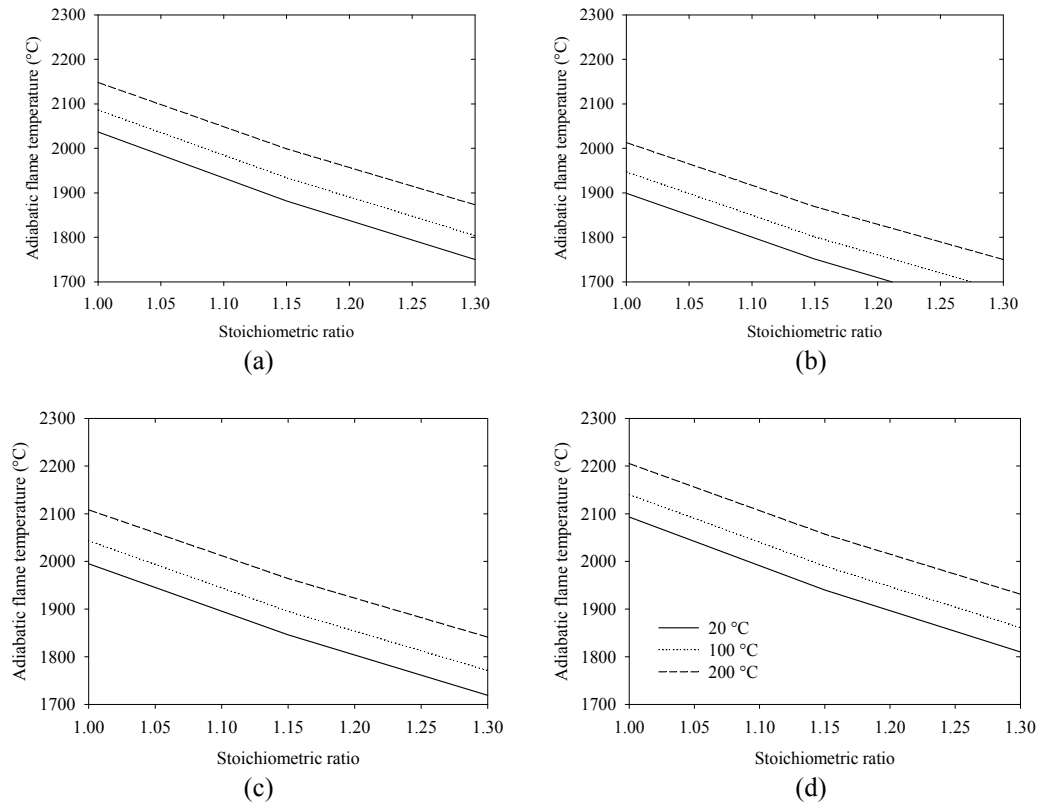


Figure 4.3: Adiabatic combustion temperature as a function of stoichiometric ratio and feed gas temperature for (a) air-firing, (b) oxy-firing with 29 vol% O₂, (c) oxy-firing with 31 vol% O₂, and (d) oxy-firing with 33 vol% O₂. Note: water vapor fraction kept at 20 vol%.

4.2.4 Flue Gas Composition

The approximated flue gas composition, including the major species CO₂, H₂O, N₂, and O₂, was calculated for air and oxy-fuel combustion using various O₂ fractions (21, 31, and 39 vol%) upstream of the burner; the results are depicted in Figure 4.4. The effect of air in-leakage was not considered in the calculations for oxy-firing and for this reason the N₂ concentration was not measured. The results clearly indicate that because of flue gas recirculation, the concentrations of CO₂ and H₂O are drastically increased under oxy-firing. It is also interesting to note that the O₂ excess in the flue gas at the furnace exit increases as the O₂ in the feed gas increases for the same stoichiometric ratio. This information is extremely important for the burner operation if a similar stoichiometric ratio needs to be maintained for various feed gas compositions. Although the oxygen-fuel ratio is left unaltered, the reduced volume flow rate of the flue gas under oxy-fired conditions contributes to an increase in the O₂ excess at the furnace exit.

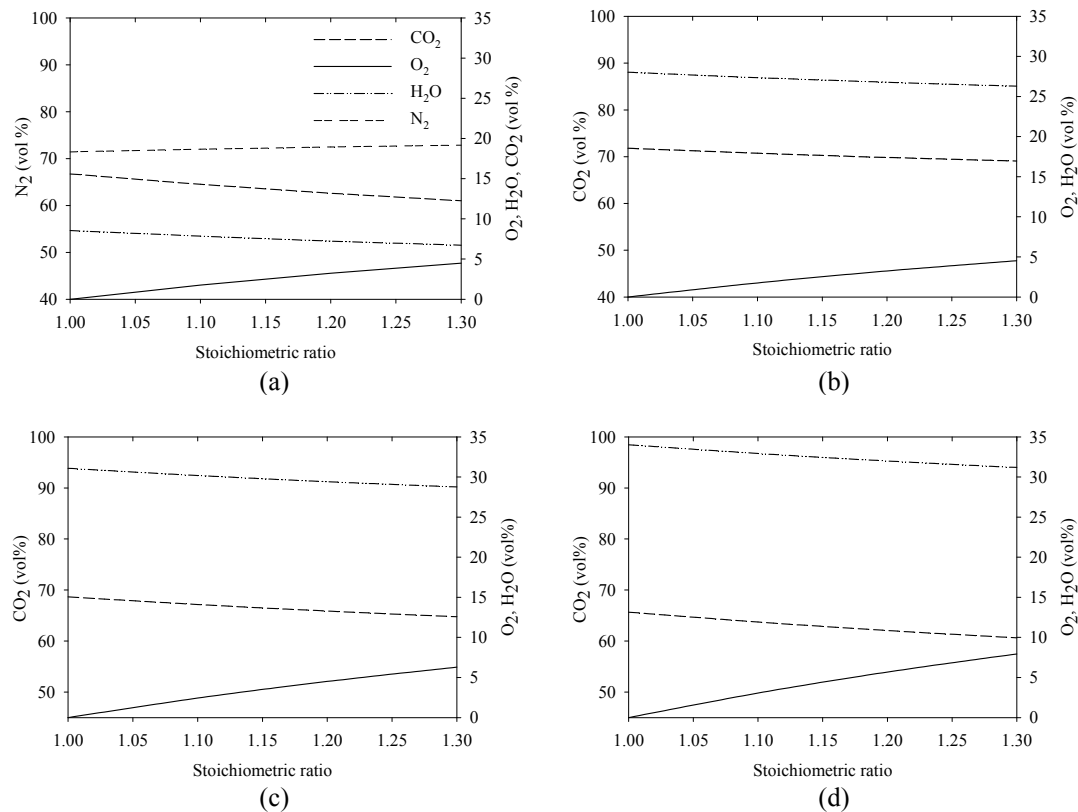


Figure 4.4: Theoretical flue gas composition for (a) air-firing, (b) oxy-firing at 21/59/20 vol%, (c) oxy-fuel at 31/49/20 vol%, and (d) oxy-fuel at 39/41/20 vol%. Note: O₂/CO₂/H₂O vol%.

4.3 Flow Pattern

Flame structure and stability, and pollutant emissions strongly depend on the aerodynamic and mixing characteristics of the fuel and feed gas jets in the near burner region [131-135]. Swirling flows are found in industrial applications when stable and high-intensity flames are desired. A swirl jet flow is created by a swirler within the burner which imparts a tangential component [132]. An excessive swirl produces a large adverse pressure gradient in the direction of flow, which promotes reverse flows. The formation of such a flow pattern provides an aerodynamic blockage and prevents velocities necessary for a stable flame [132-133].

The recirculation zone acts as a reservoir of heat and active chemical species, which cyclically transport hot combustion products from downstream regions into the flame region [134]. The high temperature products serve as an energy source for preheating the fuel and consequently for evaporation, devolatilization, and ignition [132]. Reverse flows close to the burner determine not only the flame

pattern and stability, but also the heat release rates and emission of pollutants [135]. Additionally, the effect of swirl on the performance and efficiency of a combustor are closely related to the changes in the particles' residence times. The percentage of unburned carbon determined from solid particle samples obtained along the axis of the flame was shown to decrease strongly as the degree of swirl was increased [134]. Although the usage of recirculation zones may be beneficial in extending the range of flame stability and enhancing the mixing rates between the fuel and oxidant, large recirculation zones may lead to oscillations in the combustion chamber and thus creating flame pulsations and noise pollution [132].

Computational Fluid Dynamics (CFD) has been helpful in the design and operation of aerodynamic equipment. Numerous studies indicate a great potential for the application of CFD in the investigation of combustion processes. In addition, previous works show how CFD, coupled with cold-flow physical modeling and hot-flow burner tests, provides a powerful and cost-effective tool [132,136]. Combustion considerably affects the flow field by accelerating the velocity, expanding the gas, and lowering the density. However, such interactions may be intuitively evaluated by examining the swirl number by application of isothermal analysis [132,137].

Even though pollutant emissions, and flame stabilization and pattern are important parameters in combustion applications, the recirculation zone is essentially an aerodynamics phenomenon and an examination under carefully controlled and restricted conditions is preferable [132]. Thus, simple isothermal data sets are analyzed prior to considering the complexities which accompany equilibrium/kinetic reactions in combustion processes and other hypotheses and considerations when the flow is loaded with solid particles. Most of the previous studies investigated single jets of swirling flows or maximum swirling flows with a central jet. Therefore, information on swirling flows combined with more than two jets of feed gas is still limited.

4.3.1 Mathematical Models

Mathematical modeling of swirling flows involves numerical solutions of the conservation equations. Supplementary equations are solved to determine the turbulent momentum. This study uses the finite volume method (FVM), which involves the discretization of the calculation domain into a number of control volumes (cells), over which the governing partial differential equations are integrated. The equations for continuity, transport of momentum, and species for a turbulent flow in the Cartesian-tensor form, ready to be integrated by the FVM, can be written as

$$\frac{\partial \rho}{\partial t} + \frac{\partial(\rho u_i)}{\partial x_i} = 0 \quad (4.9)$$

$$\frac{\partial(\rho u_i)}{\partial t} + \frac{\partial(\rho u_i u_j)}{\partial x_j} = -\frac{\partial P}{\partial x_i} + \frac{\partial}{\partial x_j} \left(\mu \frac{\partial u_j}{\partial x_i} \right) - \frac{\partial(\rho u_i' u_j')}{\partial x_j} \quad (4.10)$$

$$\frac{\partial(\rho C_A)}{\partial t} + \frac{\partial(\rho u_i C_A)}{\partial x_i} = \frac{\partial}{\partial x_j} \left(\rho D \frac{\partial C_A}{\partial x_i} \right) + S^{C_A} \quad (4.11)$$

Most combustion applications are turbulent because this enhances the mixing of reactants and oxidizers over that of laminar flow. Reliable predictions in the near burner region depend on the accuracy of the turbulent flow field calculation. Thus, the last term (source term) on the right side of Equation 4.10 is described in terms of time-averaged values of the fluctuating velocity tensors ($u_i' u_j'$), generally identified as Reynolds stresses. The numerical solution of Equations 4.9-4.11 for a turbulent flow can be obtained only by introducing additional equations for the Reynolds stresses in order to close the system of Reynolds-average equations.

It is outside the scope of this work to provide a review of all the work on turbulence closure models for the Reynolds-averaged Navier-Stokes (RANS) equations for the prediction of swirling flows. The impact of turbulence models and the validations of the numerical results were performed in the past by several authors; the main purpose here is to identify the main impacts of oxy-fired conditions on the flame pattern and to determine burner parameters for the evaluation of the experimental results. However, some publications relevant in the context of turbulence modeling of swirling flows are here briefly summarized.

German and Mahmud [131] discussed the limitations of the $k-\varepsilon$ model. Although this model is generally employed for flow calculations, it is limited in its ability to predict the size and strength of the swirl-induced IRZ. Sloan et al [132] investigated the accuracy of the $k-\varepsilon$ model by comparing it to available experimental cases and conclude that the $k-\varepsilon$ model fails to display the correct size or strength of the reverse flow regions. Additionally, the radial velocities predicted by this model decay to zero more rapidly than the experimental results and the tangential velocity often diffuses to a forced vortex distribution prematurely, while the experimental profiles maintain a large free vortex profile. Its performance is generally poor in the vicinity of the breakdown bubble. However, in the recovery region, the results from the $k-\varepsilon$ model are very satisfactory and even superior to the other corrective variations of this model. Later versions of the $k-\varepsilon$ model (RNG and realizable $k-\varepsilon$ models) show improvement in predicting the characteristics of swirling flows but are still less accurate compared to experimental data [138]. The shear-stress transport (SST) $k-\omega$ model, although performing better than both standard and RNG $k-\varepsilon$ models [139], still yields

excessive radial diffusive transport both upstream and downstream of a strongly swirling flow [140]. The persistent deficiency of these models is believed to be a result of their use of the isotropic eddy-viscosity concept by the Boussinesq approximation, where the Reynolds stresses are related to mean velocity gradients. The advantage of this approximation is its relatively low computational cost.

In swirling flows, the anisotropy of turbulence has a dominant effect on the mean flow [139] and more satisfactory predictions are achieved by using the standard Reynolds stress model (RSM) [131,135,138,141], where the transport equations are solved for each of the terms in the Reynolds stress terms. The RSM model closes the Reynolds-averaged Navier Stokes (RANS) equations by solving equations for the six Reynolds stresses ($\overline{u'_i u'_j}$). The Reynolds stress transport equations are expressed according to Equation 4.12 [139].

$$\begin{aligned} \frac{\partial(\rho\overline{u'_i u'_j})}{\partial t} + \frac{\partial(\rho u_k \overline{u'_i u'_j})}{\partial x_k} = & - \frac{\partial}{\partial x_k} \left(\frac{\mu}{\sigma_k} \frac{\partial \overline{u'_i u'_j}}{\partial x_k} \right) + \frac{\partial}{\partial x_k} \left(\mu \frac{\partial \overline{u'_i u'_j}}{\partial x_k} \right) \\ & - \rho \left(\overline{u'_i u'_k} \frac{\partial u_j}{\partial x_k} + \overline{u'_j u'_k} \frac{\partial u_i}{\partial x_k} \right) + P \left(\frac{\partial u'_i}{\partial x_j} + \frac{\partial u'_j}{\partial x_i} \right) - 2\mu \frac{\partial \overline{u'_i}}{\partial x_k} \frac{\partial \overline{u'_j}}{\partial x_k} \end{aligned} \quad (4.12)$$

The first term on the right side of the equation, defined as turbulent diffusive transport, is modeled with a simplified gradient-diffusion model [139]. The last two terms on the right side, defined respectively as pressure strain and dissipation tensor, also need to be modeled to close the equations. These terms contain in their respective models the turbulence dissipation rate (ϵ), which is computed with a model transport equation similar to that used in the standard k- ϵ model [139]:

$$\frac{\partial(\rho\epsilon)}{\partial t} + \frac{\partial(\rho\epsilon u_i)}{\partial x_i} = \frac{\partial}{\partial x_j} \left[\left(\mu + \frac{\mu_t}{\sigma_\epsilon} \right) \frac{\partial \epsilon}{\partial x_j} \right] \frac{C_{\epsilon 1}}{2} (P_{ii} + C_{\epsilon 3} G_{ii}) \frac{\epsilon}{k} - C_{\epsilon 2} \rho \frac{\epsilon^2}{k} + S^\epsilon \quad (4.13)$$

Further information on the RSM can be found elsewhere [139]. In this study, the QUICK scheme (quadratic upwind interpolation for convective kinematics) is used for discretization of the convective terms in Equations 4.10-4.13. This scheme is based on weighted average second-order-upwind and central interpolations of the variable [142]. The advantage of employing the QUICK scheme for swirling flows has been confirmed by previous studies, since it can minimize numerical diffusion [131,139]. In this type of flow, where body forces are large, the PRESTO (pressure staggering option) scheme is used for discretization of the pressure term. Finally, the discretized momentum equations

are solved iteratively for the velocity components and pressure using a SIMPLE algorithm proposed by Patankar and Spalding [143,144].

4.3.2 Computational Domain and Mesh Refinement

One of the key issues in developing a CFD model for an industrial burner is to select the appropriate domain for analysis. The computational domain is displayed in Figure 4.5 and extends $7.64D$ downstream of the secondary and primary stream exits and $8.33D$ in the radial direction. The domain includes $1.88D$ upstream of the burner exit, allowing the inlet condition to be well defined and computing the flow also through the swirl generator. The numerical representation of the swirler is considered in the burner and it is evaluated by five different vane angles (0 , 15 , 30 , 45 , and 60 degrees).

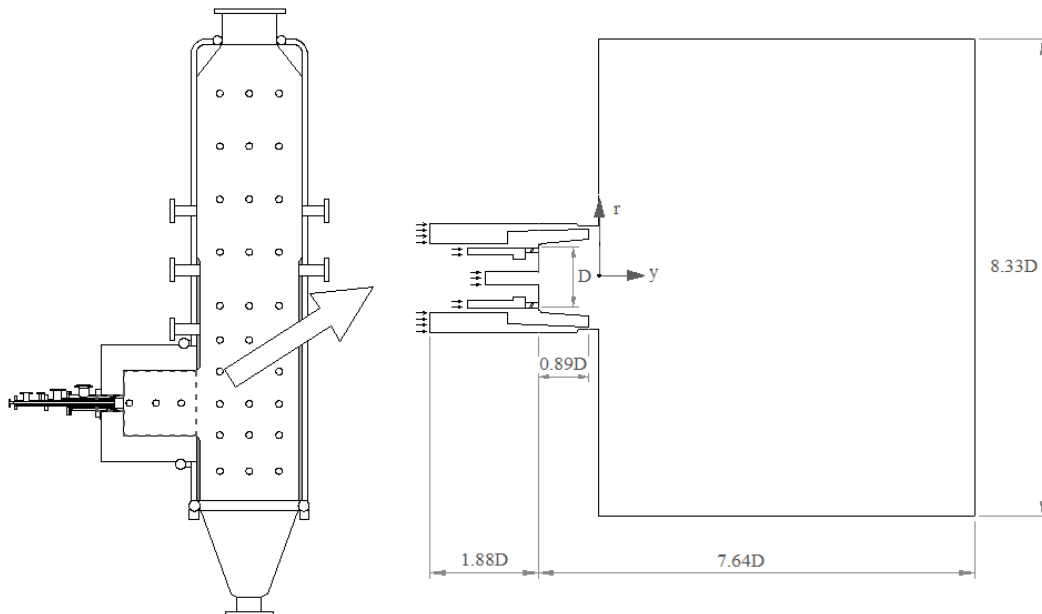


Figure 4.5: Schematic of the computational domain ($D = 0.114$ m).

To calculate the velocity fields, the transport equations summarized in Section 4.3.1 must be solved. Since a steady-state solution is desired, the discretization in time is not necessary. Thus, only the effect of spatial discretization on the predicted profiles is investigated in this study. Mesh resolutions are varied from coarser to finer grids with a total number of cells of 1.10, 1.20, and 1.40 million. The mesh refinement at different points in the domain of analysis is presented in Figure 4.6. The density of the grid cells is increased in the regions where the highest velocity gradients are expected, primarily in the near burner region. Thus, block-structured meshes consist of 11, 13, and 15 cells in the radial direction at

the outlet of outer secondary stream for the three evaluated mesh refinements. The mesh is stretched in both the axial and radial directions to keep an acceptable refinement within the quarl and in the near burner region.

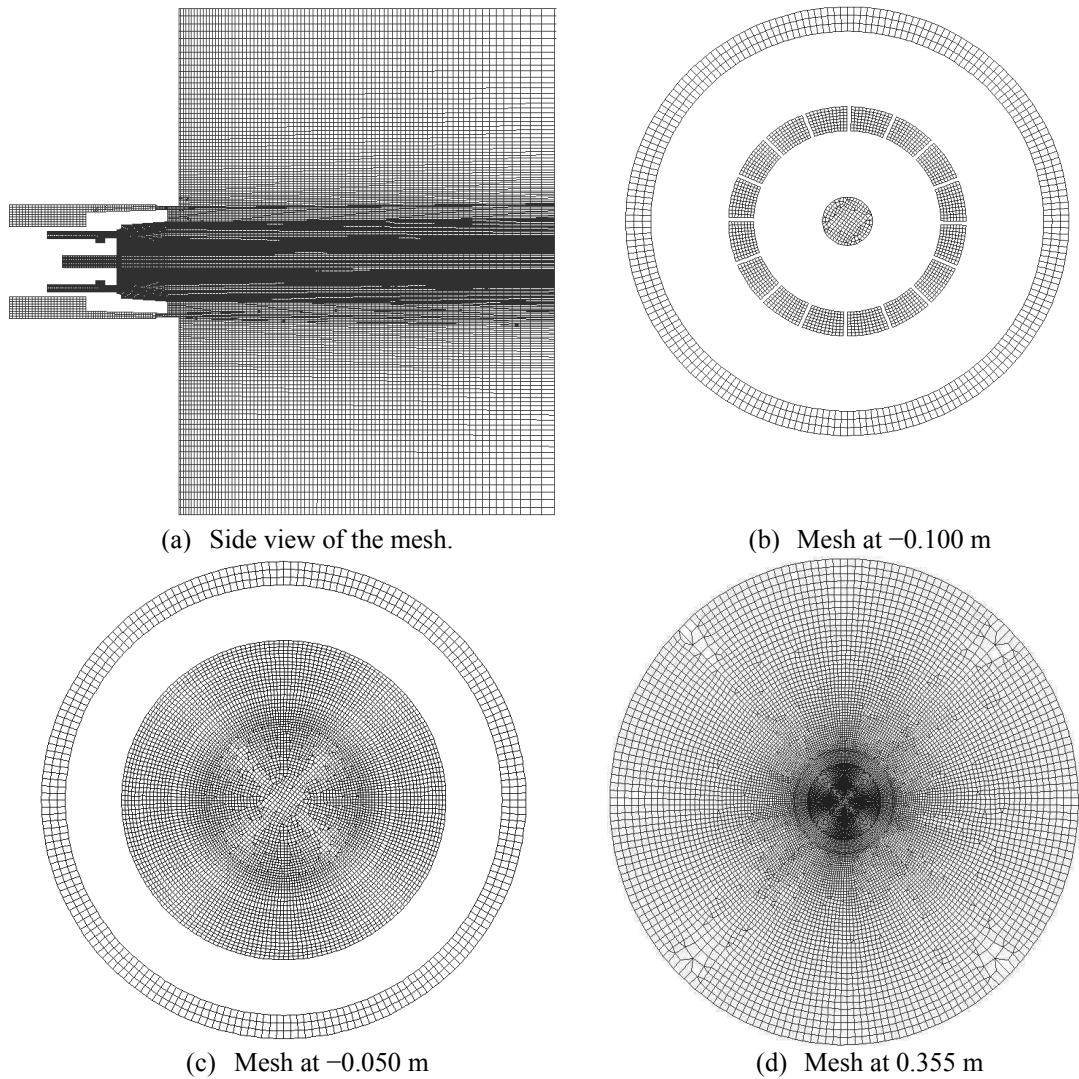


Figure 4.6: Overview of the mesh refinement (1.10 million cells).

4.3.3 Test Cases and Boundary Conditions

The boundary conditions for air-firing and oxy-firing were set according to expected operating parameters during the experimental activities. In addition to the baseline numerical simulation using air, oxy-fired conditions are evaluated using an overall O_2 fraction of 31 vol%. As described previously, the total amount

of feed gas is divided into primary, secondary, and tertiary streams. In order to keep the same axial momentum at the exit of the primary stream (0.47 N), the velocity is kept at 23 and 28 m/s for air and oxy-fuel, respectively. This strategy is discussed in detail in the next chapter. The rest amount of feed gas is divided into the secondary and tertiary registers using mass flow ratios or volume flow ratios (at STP conditions) of secondary to tertiary stream between 0.40-1.30. Higher ratios led to convergence problems and for this reasons the results are not included in this section. The feed gas composition and mass flow rates used in the simulations are presented in Table 13. The properties were calculated at a temperature of 20 °C and absolute pressure of 1.00 bar.

Table 13: Evaluated operating conditions in the numerical study.

	Air	Oxy-fuel
Total feed gas flow rate (kg/h)	458	423
Velocity of primary stream (m/s)	28	23
Composition of primary stream	Air	20 vol% O ₂ 80 vol% CO ₂
Composition of secondary and tertiary stream	Air	33 vol% O ₂ 47 vol% CO ₂ 20 vol% H ₂ O
Mass flow ratio of secondary to tertiary stream	0.40, 0.70, 1.00, 1.30	
Swirler vane angles	0, 15, 30, 45, 60 degrees	

Linear profiles for the axial velocity component are assumed at all inlets of the burner. No-slip conditions are also applied at the solid walls, while at the outlet of the domain of analysis a pressure boundary condition is adopted. Boundary conditions for the turbulent parameters (i.e. turbulent kinetic energy and dissipation rate) are approximated by the following empirical correlations [139]:

$$k = 1.5 \left(0.16 u \operatorname{Re}_{D_H}^{-1/8} \right)^2 \quad (4.14)$$

$$\varepsilon = C_\mu^{3/4} \frac{k^3}{0.07 D_H} \quad (4.15)$$

4.3.4 Results

4.3.4.1 Mesh Analysis

The results of the grid refinement study for three structured meshes are summarized in Table 14. Simulations were performed using air and a flow ratio of secondary to tertiary stream of 0.40. As expected, the computational time required per 1000 iterations slightly increases with the number of cells. The CPU time was based on simulations running on two 2.93 GHz Xeon X5570 quad-core processors with a total of 48 GB RAM (6 GB RAM/core). The solution was considered

converged when the absolute residuals reached a value of 10^{-5} . The base mesh reached the mentioned convergence criteria after approximately 35,000 iterations. For the same convergence level, the medium mesh required almost 37,000 iterations and the fine mesh approximately 42,000 iterations.

Table 14: Grid refinement study.

Mesh	Number of cells	CPU time per 1000 iterations	Number of iterations for convergence
Base	1.10 Million	50 min 10 s	~35,000
Medium	1.20 Million	53 min 5 s	~37,000
Fine	1.40 Million	62 min 5 s	~42,000

Figures 4.7 and 4.8 show the calculated velocity profiles at the outlet of swirler and at various axial distances from the origin. It is important to note that dimensionless distances and velocity profiles are based on the outlet radius of the tertiary stream (0.057 m) and the mean axial velocity of the primary jet for oxy-fired conditions (23 m/s). At the outlet of the swirler, the three meshes predict slight differences in the axial velocity profiles. However, such discrepancies are considered negligible. Farther downstream, axial velocity predictions are identical for all three mesh refinements and are not mesh dependent for refinement levels studied here. Since finer meshes increase the computational effort, it was decided to use the base mesh as a baseline in further simulations presented in this work.

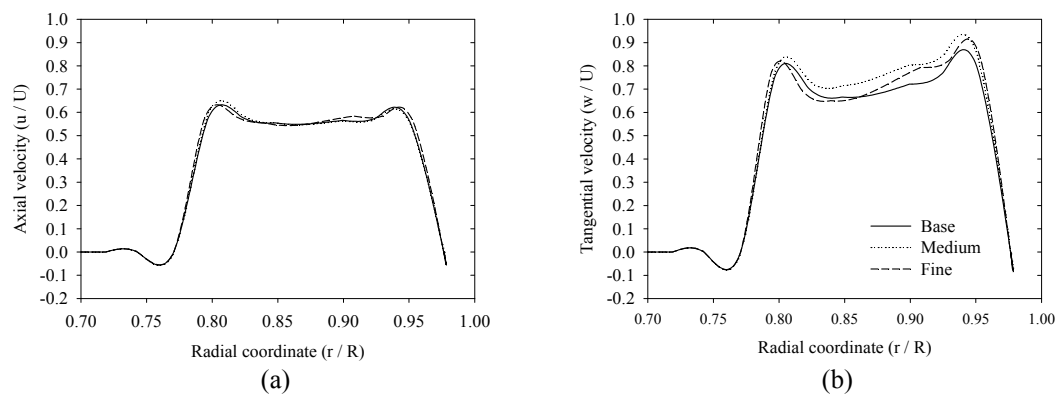


Figure 4.7: Radial profiles of the (a) axial and (b) tangential velocities at outlet of swirler for the three investigated meshes.

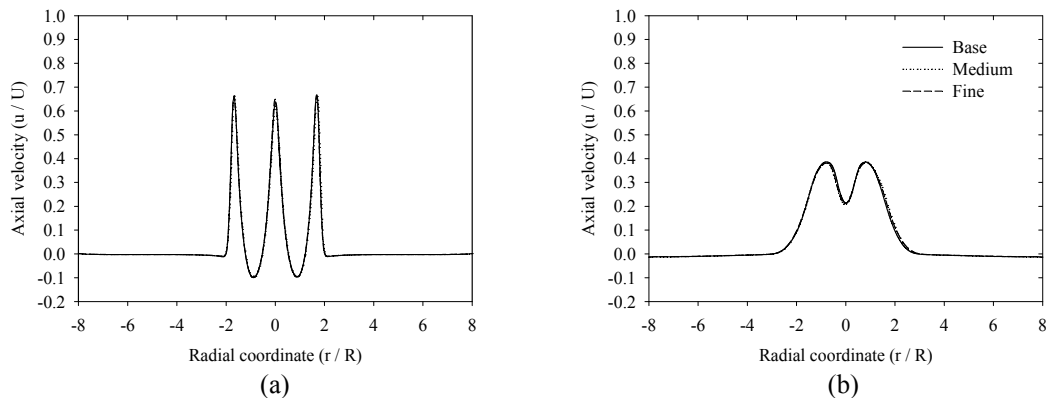


Figure 4.8: Radial profiles of the axial velocity for the three investigated meshes at (a) 0.050 m and (b) 0.355 m from the burner exit.

4.3.4.2 Effect of Vane Angles

The impact of swirler vane angles on the velocity profiles are presented in Figures 4.9-4.10. Because the predicted results show that the flow pattern is symmetric, only the half section of axial and tangential velocity profiles is depicted in the following plots. The analysis presented in this section uses air and a secondary/tertiary mass flow ratio of 0.40. At 0.100 m upstream of the origin (Figure 4.9), two distinct regions can be observed: a core region at the centerline due to the primary jet, and another at the outlet of the secondary jet, whose axial and tangential momentum depend on the vane angle used to induce rotation in the flow. As expected, by increasing the vane angle, the velocity profiles show an increase in the tangential velocity component in addition to the axial component of velocity encountered in non-swirling jets.

Axial and tangential profiles at 0.050 and 0.355 m axial downstream distances are depicted in Figure 4.10. The decay of maximum axial and tangential velocity components along the length of the jet and for various degrees of swirl is observed. In both plots, it is seen that the core region near the centerline and the mixing layer between the secondary and tertiary stream varies from one plane to another. At an axial distance of 0.050 m, the impact of axial momentum of the tertiary jet is clearly observed at $r/R = -2.00$. Since the secondary/tertiary flow ratio is kept unchanged, similar maximum axial velocities are predicted at this radial distance. Because of the lower confinement ratio, velocities in the outer recirculation zone ($r/R > 2.00$) are negligible. From Figure 4.10 (b), it is also observed that the reverse flow in the vicinity of the burner increases slightly in width with an increase of the vane angle. In addition, the maximum axial velocity of the core region is influenced by the internal reverse-flow zone created by the swirler, decreasing its axial velocity when the tangential momentum is increased. Interesting in both pictures is that the primary jet penetrates the IRZ to an extent

which depends on its axial momentum and on the level of swirl imparted to the flow. Consequently, higher axial velocities in the core region are obtained when swirlers with reduced vane angles are used. At this distance, the axial velocity profiles show velocity peaks at distinct radial distances by varying the vane angles. This is due to the centrifugal force induced by swirl, which pushes the flow towards the wall.

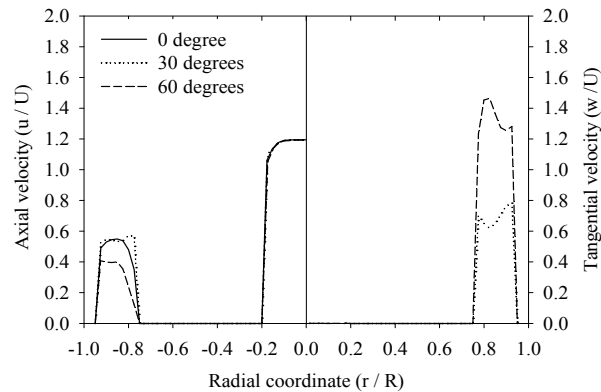


Figure 4.9: Radial profiles of the axial velocity for vane angles of 0, 30, and 60 degrees at the exit of the primary and secondary registers applying air and a 0.40 secondary/tertiary flow ratio.

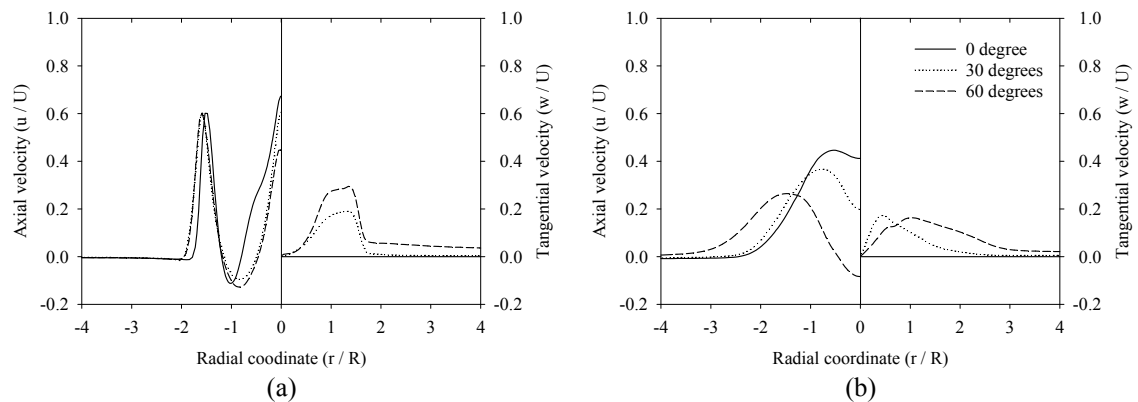


Figure 4.10: Radial profiles of the axial and tangential velocity for vane angles of 0, 30, and 60 degrees at (a) 0.050 m and (b) 0.355 m from the burner exit applying air and 0.40 secondary/tertiary flow ratio.

4.3.4.3 Effect of Feed Gas Distribution

Predicted gas flow patterns in the near burner region are also influenced by increasing the secondary/tertiary flow ratio. Results applying a swirler with 15 and 45 degree vane angles are presented in Figures 4.11 and 4.12. For both cases, higher axial and tangential velocities are obtained at an axial distance of -0.100 m

when the secondary/tertiary flow ratio is increased. On the other hand, results at axial distances of 0.050 and 0.355 m show clearly that maximum axial velocities at a radial distance $r/R = -2.00$ (outlet of tertiary stream) are reached for lower secondary/tertiary mass flow ratios. Because of a lower tangential momentum and a consequently less-pronounced IRZ when reduced flow rates are applied in the secondary stream, the primary jet penetrates completely the internal reverse flow zone for 0.70 and 1.00 flow ratios using a swirler with a 15 degree vane angle. In addition, due to viscosity dissipation, the tangential component decays along the axial direction, while the peak simultaneously shifts toward the furnace walls for both air and oxy-fuel cases.

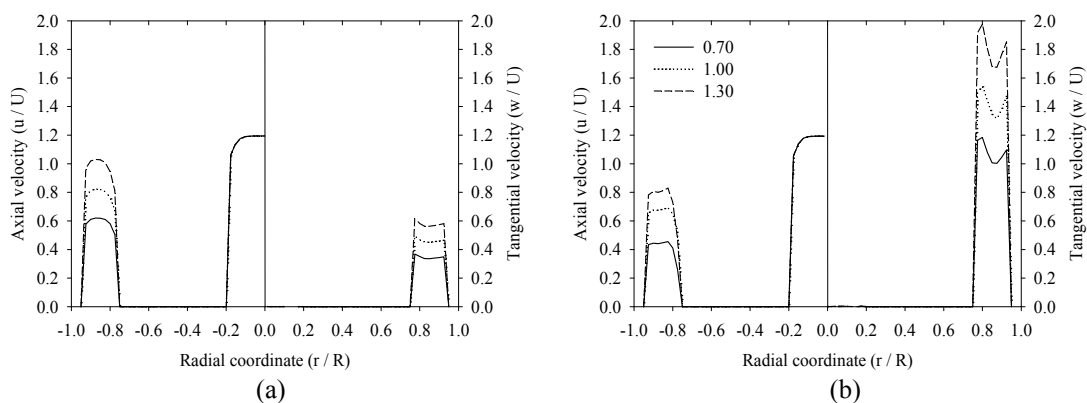


Figure 4.11: Radial profiles of the axial and tangential velocity at exit of primary and secondary registers (-0.100 m) for vane angles of (a) 15 degrees and (b) 45 degrees applying 0.70, 1.00, and 1.30 secondary/tertiary flow ratios.

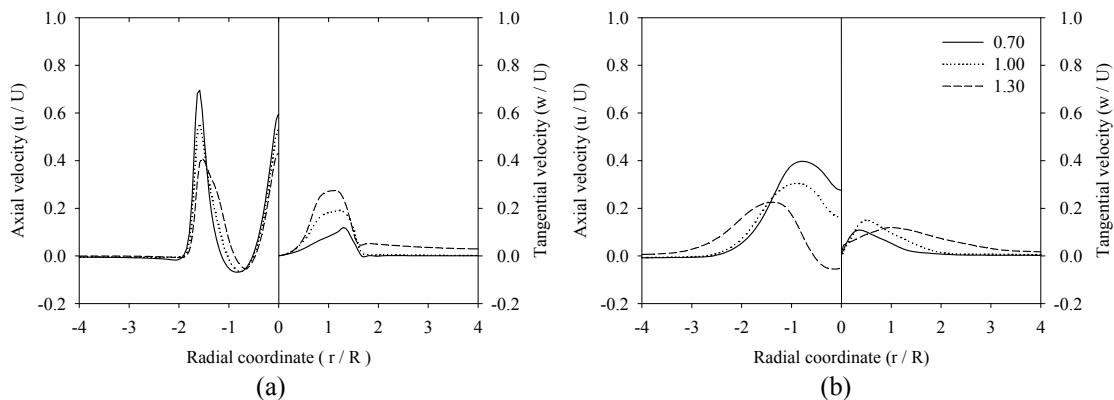


Figure 4.12: Radial profiles of the axial and tangential velocity at (a) 0.050 m and (b) 0.355 m from the burner exit for vane angles of 15 degrees and 0.70, 1.00, and 1.30 secondary/tertiary flow ratios.

4.3.4.4 Effect of Feed Gas Composition

Figure 4.13 illustrates the variation in the velocity profiles with the composition of the feed gas for swirlers with 30 and 60 degree vane angles. As expected, the maximum axial and tangential velocity components decay along the length of the jet and reverse mean velocities increase along with swirl strength for both cases. A substantial reduction in the axial and tangential velocities is evident in the oxy-fuel case due to the lower flow rates and higher density of the feed gas. Nevertheless, the maximum axial velocities in the core region downstream of the burner for air and oxy-fuel are quite similar when applying a secondary/tertiary mass flow ratio equal to 0.70.

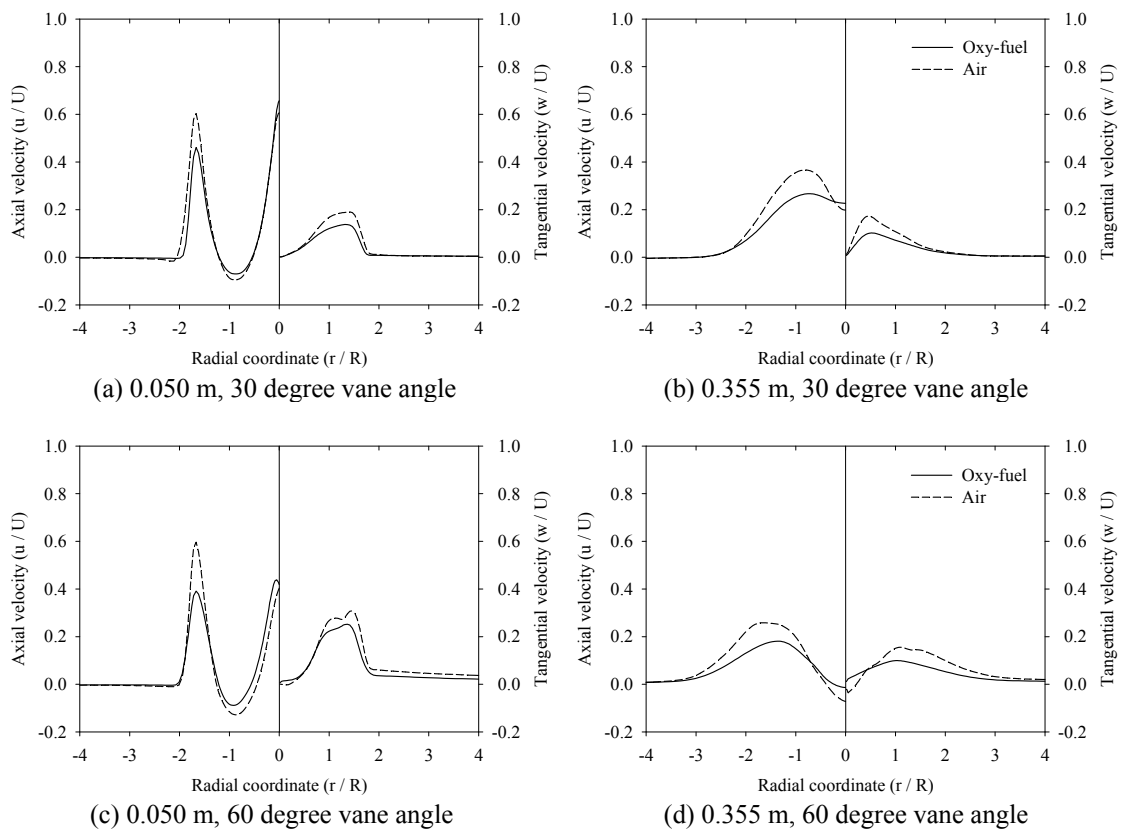


Figure 4.13: Comparison of velocity profiles for air and oxy-fuel for 30 and 60 degree vane angles applying a 0.70 secondary/tertiary flow ratio.

The main differences are observed in the maximum axial velocities in the core region when the secondary/tertiary mass flow ratio is increased (Figure 4.14). The general reduction in the feed gas flow rate in oxy-fuel cases generates slightly weaker IRZ and thereby increases the penetration depth of the non-swirling primary jet. In other words, the generated recirculation zone does not have sufficient strength relative to the primary jet to force an abrupt radial arc away from the centerline. The tangential velocity component imparted by the swirler in

oxy-fuel is lower than the baseline air case, which considerably influences the IRZ to determine the flow pattern. Peaks of the axial and tangential velocities in the baseline air cases are located at slightly longer radial distances, indicating a stronger centrifugal force imparted by the swirler.

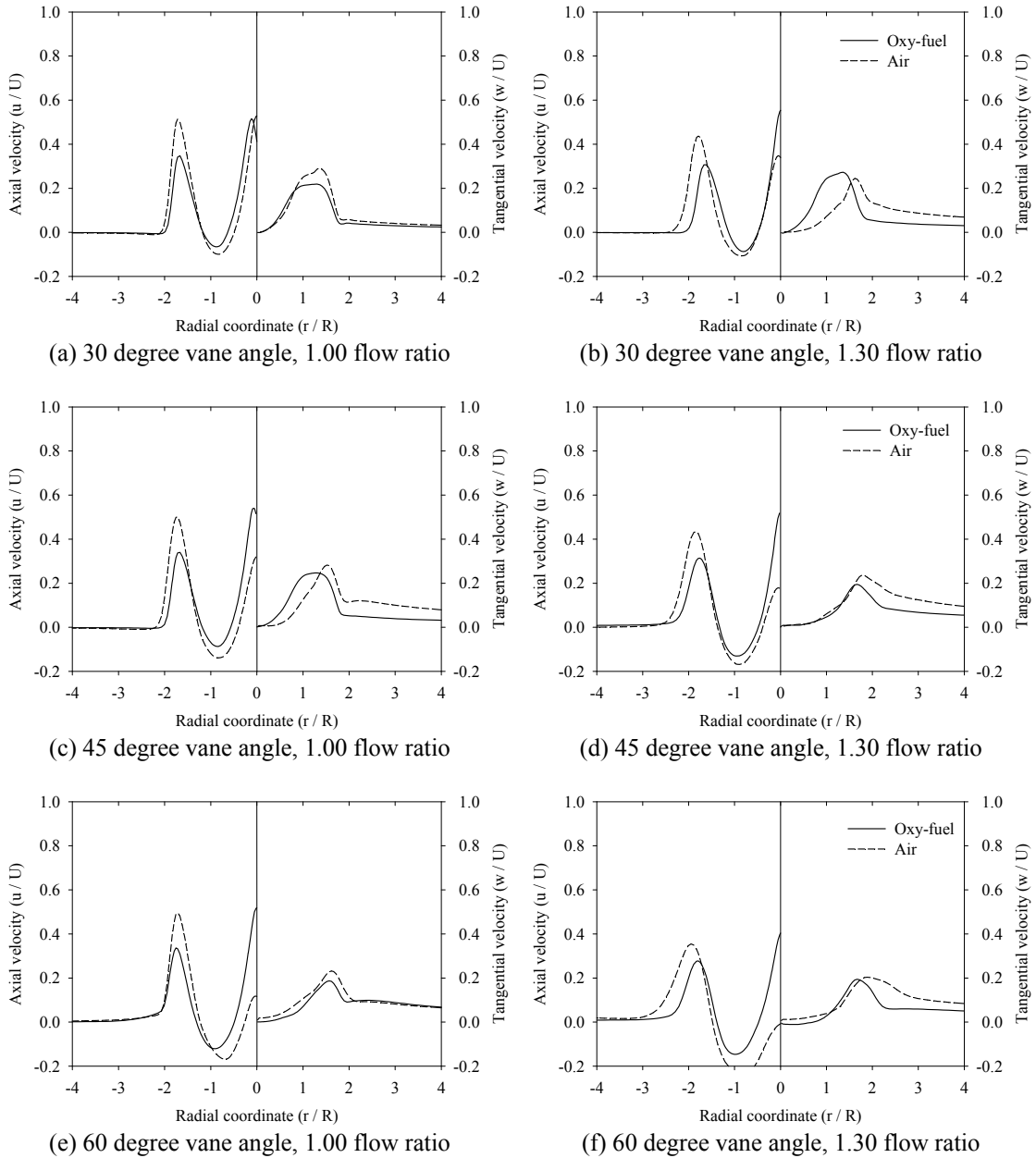
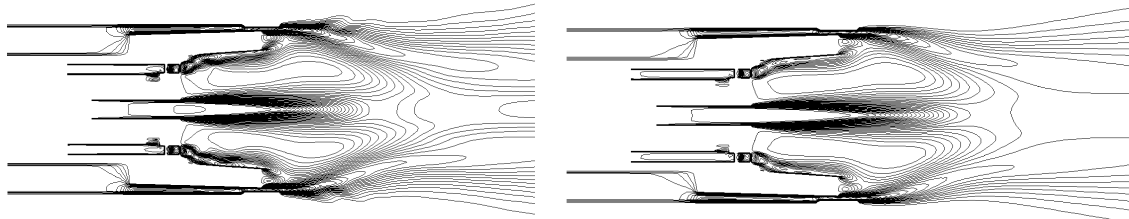


Figure 4.14: Comparison of velocity profiles for air and oxy-fuel at 0.050 m from the burner exit.

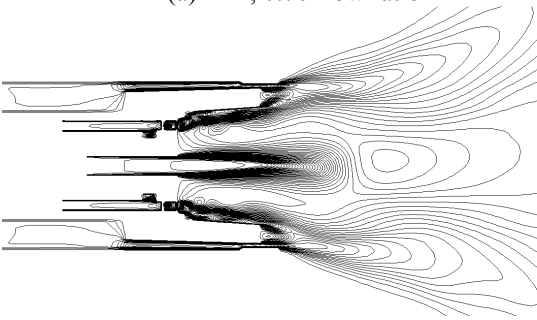
Axial velocity isolines of the average flow are depicted in the Figures 4.15-4.17 for air and oxy-fuel cases using swirlers with 30, 45, and 60 degree vane angles. From the results, it is clear that the velocity profiles emitted from the swirler may lead to differences in the flow patterns, even at same swirl strengths at the outlet of the secondary register. The strength of the swirl jet imparted by the swirler is discussed in detail in the next section. Generally, it is observed that the secondary swirling jet follows the slope of the burner quarl and thereby promoting divergent flow and intensifying the adverse pressure gradient on the symmetry axis. Such a divergent nozzle aids in swirling flow deceleration by increasing the existing reverse flow created by the swirler. It is also observed that by reducing the vane angle of swirler, a longer and narrower flow pattern is obtained, while an increase in the angle produces a shorter and wider flow structure. Additionally, an increase in swirl associated with an increase in the flow rate of the secondary jet seems initially to expand the recirculation zone in width. In cases of a 1.30 secondary/tertiary flow ratio, primary jet penetrated partially into the IRZ and then deflected radially for both air and oxy-fuel. In these cases where stronger recirculation zones are formed, the axial momentum of the tertiary jet is not strong enough to maintain the same flow envelope as when lower flow ratio distributions are applied.

Flow pattern predictions display differences in the flow structure for oxy-fuel, even when using the same vane angle of swirler and secondary/tertiary flow ratio. The main difference lies in the lower divergence angle of the flow pattern; the general tendency is for the primary jet to penetrate much more into recirculation zone forming an annular reverse flow region. An increase in the penetration depths of the primary jet into the IRZ may result in reduced residence times in the recirculation zone and suppressed burnout. From the results of velocity profiles at 0.050 m and flow patterns, it is clear that no full IRZ is formed in the burner front because of high axial momentum of the primary jet. It is worth pointing out that swirling annular flows with external and central non-swirling jets are of considerable practical importance. The optimization of the interaction between these three streams may lead to a better flame stabilization and a low-pollutant burner design. These aspects are evaluated in Chapter 6 when the experimental results are presented.

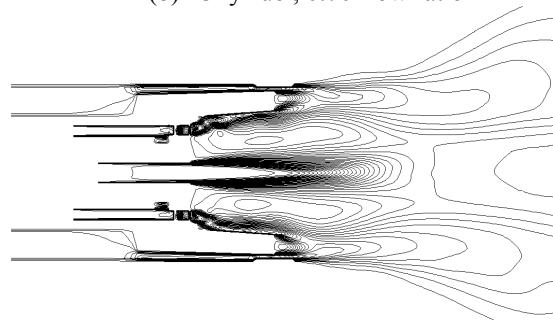


(a) Air, 0.70 flow ratio

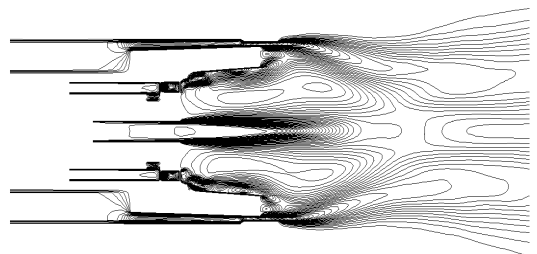
(b) Oxy-fuel, 0.70 flow ratio



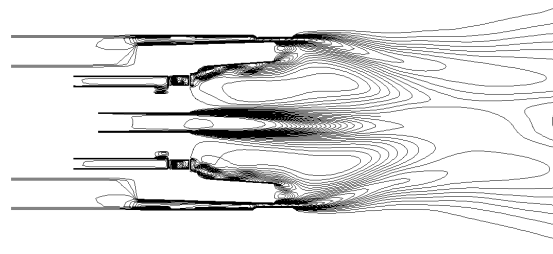
(c) Air, 1.30 flow ratio



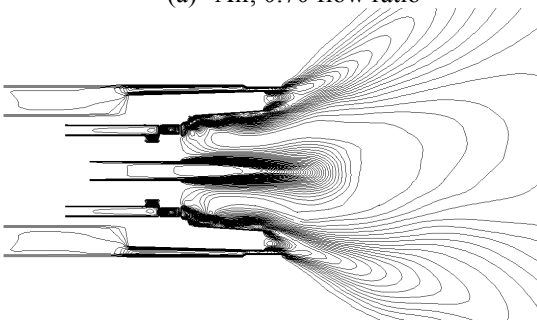
(d) Oxy-fuel, 1.30 flow ratio

Figure 4.15: Flow pattern generated by a swirler with 30 degree vane angle.

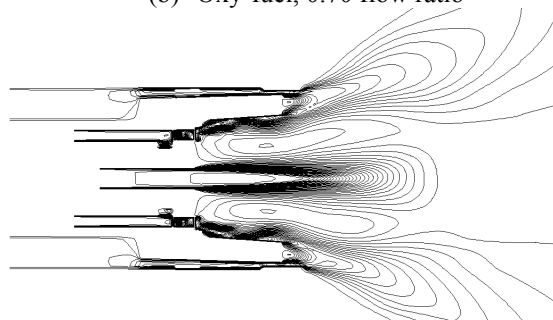
(a) Air, 0.70 flow ratio



(b) Oxy-fuel, 0.70 flow ratio



(c) Air, 1.30 flow ratio



(d) Oxy-fuel, 1.30 flow ratio

Figure 4.16: Flow pattern generated by a swirler with 45 degree vane angle.

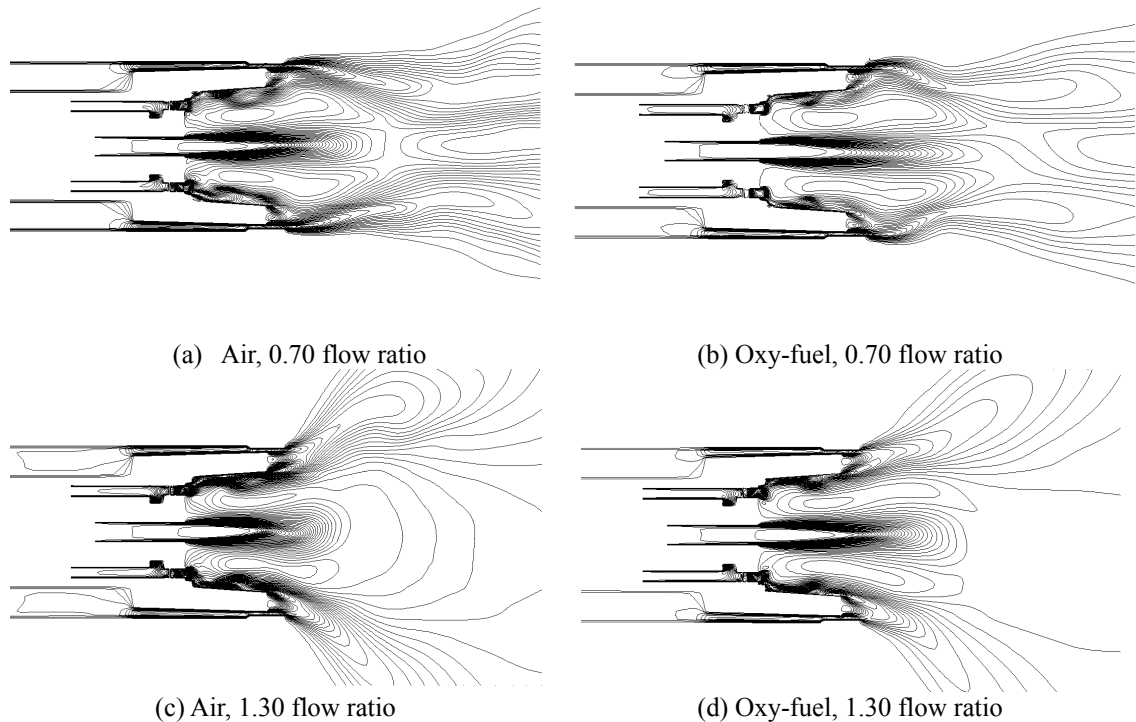


Figure 4.17: Flow pattern generated by a swirler with 60 degree vane angle.

The effect of feed gas composition on the strength of IRZ is presented in Figure 4.18. The strength of the IRZ is defined as the ratio of the reverse mass flow to the total inlet flow. From the plots, it is clear that the recirculated flow changes drastically from a zone extending far downstream into the furnace to a small zone contained fully within the quarl (<0.100 m). For air and oxy-fuel, the variation in the IRZ strength is similar for 30-45 degree swirler vane angles at 0.70 secondary/tertiary mass flow ratio. In general, the recirculated mass flow rates present an increase of swirl strength and secondary/tertiary flow ratios because of the imparted pressure gradients. The reduction in the IRZ strength in oxy-fuel, observed mainly downstream of burner quarl, is a result of the reduction of the flow rate in the secondary and tertiary registers associated with high axial momentum of the non-swirling primary jet. The more significant impact in the reduction of strength of the IRZ in oxy-fuel is apparent in cases where the secondary/tertiary flow ratio is higher than 1.00. In short, the tangential momentum imparted by the swirler in oxy-fuel cases is not enough to overcome the axial momentum and increase the recirculated gas flow rate in the near burner zone.

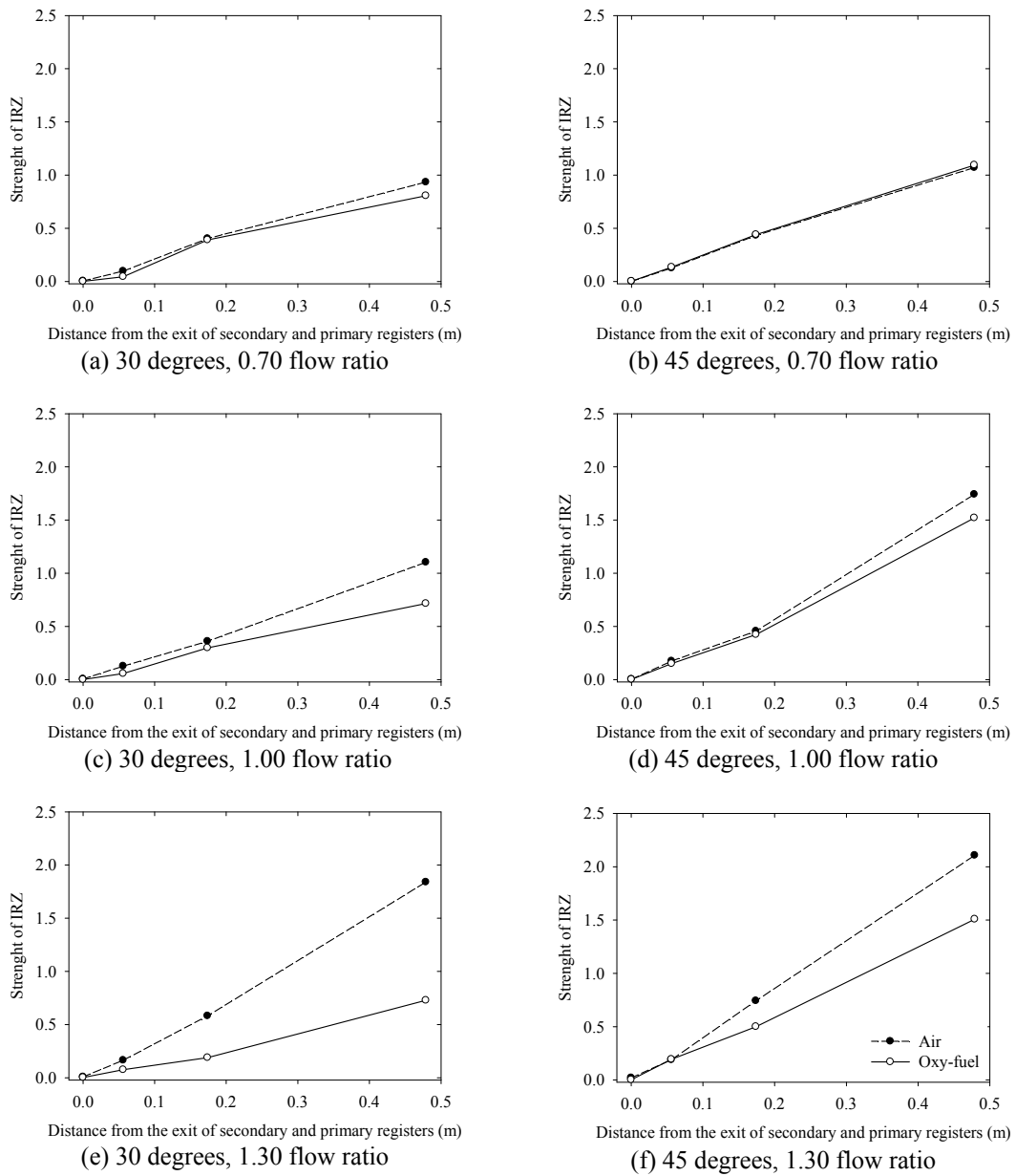


Figure 4.18: Comparison of the strength of IRZ for air and oxy-fuel.

4.3.4.5 Swirl Number

A dimensionless parameter to characterize the intensity of a swirling flow is needed to assess and convey the results to other different burner configurations. Beér and Chigier [134] proposed a dimensionless number defined as swirl intensity based on the ratio of angular momentum to axial momentum as

described in Equation 4.16. In this format, the swirl number is ideally conserved in a free and isothermal system and can be considered an appropriate similarity criterion for swirling jets, produced by geometrically similar swirlers [132]. However, the calculation of Equation 4.16 requires knowledge of the pressure profile, which is experimentally difficult to obtain. Later an alternative swirl number was defined without the pressure term to simplify the calculation and to eliminate the difficulties stemming from the static pressure variations. These two swirl numbers are used interchangeably in the literature. Nevertheless, in all recent publications the alternative swirl number is used and for this reason is applied in this work. Further details can be found elsewhere [134,137,145,146]. Because in this research the swirl number was calculated using the axial and tangential velocity contours at outlet of secondary annulus, the swirl number can be rewritten according to Equation 4.17.

$$S = \frac{\int \rho (wr) u 2\pi r dr}{R \int \rho u u 2\pi r dr + R \int P 2\pi r dr} \quad (4.16)$$

$$S = \frac{\int \rho (wr) u dA}{R \int \rho u u dA} \quad (4.17)$$

The swirl number calculated from the profiles of axial and tangential velocities at outlet of outer secondary register is plotted as function of vane angle of the solid-body swirler for the four investigated flow ratios. Figure 4.19 displays the results for air and oxy-fuel conditions. As expected, both atmospheres lead to same values for the swirl number in the range covered in this work, which prove to be independent of the velocity and feed gas composition. Thus, the intensity of swirl at outlet of secondary register is uniquely influenced by the geometry of the swirler.

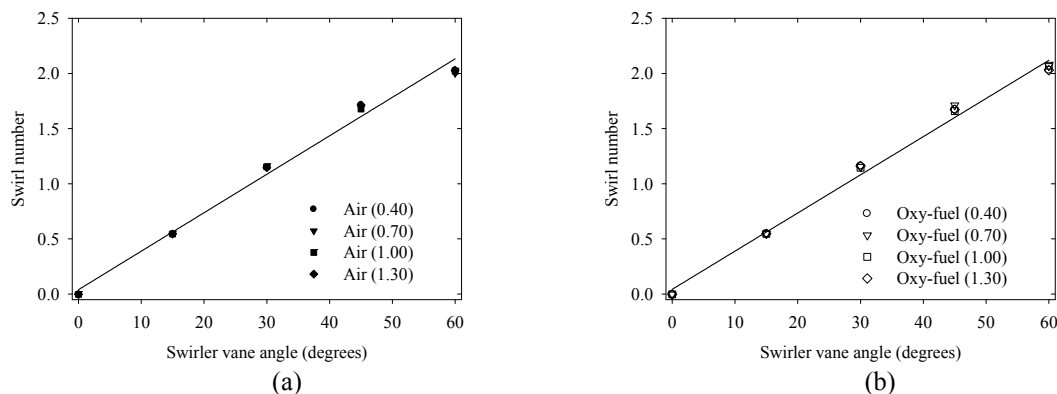


Figure 4.19: Calculated swirl number for (a) air and (b) oxy-fuel. Note: the values in parentheses indicate the secondary/tertiary flow ratio.

5 Experimental Results and Discussion

5.1 Introduction

In this section the experimental results are fully presented and discussed. A parametric study is firstly carried out to investigate the impacts of oxy-fired conditions on the overall combustion performance. Due to lack of information on the combustion behavior under various burner operating conditions, the feed gas distribution among the burner registers and strength of secondary swirling flow are the main parameters evaluated. Experimental data under air-fired conditions are also obtained and used as benchmark. Because the experiments contain many of the hostile features of actual furnaces (e.g. high particulate load and elevated temperatures) that limit measurements especially in the near burner zone for all cases, the conclusions from the parametric study are used for defining the burner settings appropriate for performing detailed in-flame measurements.

5.2 Operating Conditions

The objective of the first part of the experimental activities is to perform a parametric study through the evaluation of various burner operating settings on the overall combustion performance. Experimental runs include:

- i Composition of feed gas (i.e., air and oxy-fuel),
- ii Distribution of feed gas between the secondary and tertiary registers, and
- iii Strength of secondary swirl.

Average operating conditions during the tests, along with their expanded uncertainties are listed in Table 15. All experimental errors reported in this work are based on a coverage factor of a t-distribution for infinite degrees of freedom, which defines an interval estimated to have a level of confidence of 95.45%. The reader is referred to the Appendix A for further information on the determination of uncertainty of measurements.

The O₂ volumetric fraction upstream of the burner for the oxy-fuel runs was defined similarly to the theoretical adiabatic flame temperature to conventional air operation, i.e. 31 vol%. Because the O₂ concentration has already been thoroughly investigated in the past by several authors, only a few response variables are here discussed in terms of O₂ volumetric fraction. The coal feed rate was maintained at approximately 56 kg/h, while the feed gas flow rate was defined in order to keep a stoichiometric ratio of 1.17. The overall thermal input, including the sensible heat flow rate of the coal and feed gas varies because of differences in temperature and

volume flow rates between air-fired and oxy-fired conditions. The swirl number of the secondary feed gas, determined in the previous chapter with the help of isothermal simulations, was varied at three levels, i.e. 1.15, 1.65, and 2.05, corresponding to vane angles of 30, 45, and 60 degrees, respectively. Because a poor flame stability was observed during the commissioning using a swirl number of 1.15, experiments were not carried out with a smaller swirl number. The flow ratio of secondary to tertiary stream was varied between 0.40 and 2.00, while the mean axial momentum of the primary gas was maintained at 0.47 N for both air-fired and oxy-fired cases. Slightly lower recycle ratios are obtained in this work because the primary stream is supplied by CO₂ and O₂ storage vessels. As expected, the CO₂ volumetric fraction in the flue gas of all oxy-fired cases is approximately 90 vol% (dry), significantly higher than in air-fired cases (17 vol%, dry).

During the experiments, efforts were made to establish and maintain the same operating conditions in the furnace without large changes. The maximum variation about the mean for the experiments was less than $\pm 5\%$. Careful tests carried out with the fuel feed system during the parametric study showed that the maximum variation in the feed rate about the mean was $\pm 5\%$; the overall furnace mass balance was generally within $\pm 10\%$ of the flows at the burner inlet. In order to verify any change in the furnace operating condition, the flue gas was also continuously monitored throughout the measurements. The pressure within the furnace was maintained at near atmospheric pressure to reduce the contamination from air in-leakage. Air in-leakage is responsible for the presence of N₂ upstream of the burner to values lower than 7 vol%. During the parametric study, data were collected over a period of 45 minutes of stable operation; approximately 30 minutes were allowed for change over and stabilization between each evaluated case. Shorter time intervals resulted in huge variation and the determination of statistically significant trends became very difficult. The repeatability of the results was checked continuously during the tests and most experiments were replicated three times and on different days.

The composition of the coal characterized by proximate and ultimate analysis, heating value, particle size distribution, and ash melting point is given in Table 16. The bulk drying and grinding were carried out commercially. The mean particle size of the coal is approximately 200 μm with a size distribution displayed in Figure 5.1. Some variation in water content of the coal was noticeable over the course of experimentation, which led to difficulties in coal metering and flame stabilization. Indeed, it was observed that a few coal containers presented water content 10% higher and due to time constraints, this effect was not further investigated.

Table 15: Typical operating conditions during the parametric study.

Operating parameter	Air-firing	Oxy-firing
Coal feed rate (kg/h)	56 ±0.27	56 ±0.27
Volume flow rate of primary stream (m ³ /h, STP)	41 ±1.58	35 ±1.58
O ₂ fraction of primary stream (vol%, wet)	21 ±1.21	19 ±1.10
CO ₂ fraction of primary stream (vol%, wet) ¹	-	81
Temperature of primary stream (°C)	25 ±1.25	17 ±1.23
Velocity of primary stream at burner exit (m/s) ¹	28.30	23.01
Axial momentum of primary stream at burner exit (N) ¹	0.47	0.47
Volume flow rate of secondary and tertiary stream (m ³ /h, STP)	335 ±5.33	215 ±3.54
O ₂ fraction of secondary and tertiary stream (vol%, wet)	21 ±1.21	33 ±1.91
H ₂ O fraction of secondary and tertiary stream (vol%, wet) ¹	-	19
CO ₂ fraction of secondary and tertiary stream (vol%, wet) ¹	-	41.50
N ₂ fraction of secondary and tertiary stream (vol%, wet) ¹	79	6.50
Temperature of secondary and tertiary streams (°C)	190 ±1.84	155 ±1.69
Secondary/tertiary mass flow ratio ¹	0.40-1.30	0.70-2.00
Swirl number of secondary stream ¹	1.15, 1.65, 2.05	
Stoichiometric ratio ¹	1.17	1.17
Overall heat input (kW) ¹	355	332
Flue gas		
O ₂ (vol%, dry)	3.50 ±0.83	6.00 ±0.83
CO ₂ (vol%, dry)	17 ±1.05	88.50 ±1.05
N ₂ (vol%, dry) ¹	79.50	5.50
H ₂ O (vol% wet)	16 ±0.18	27 ±0.18
Volume flow rate at furnace exit (m ³ /h, STP)	410 ±4.96	304 ±5.34
Volume flow rate of recycled flue gas (m ³ /h, STP)	-	142 ±3.58
Temperature at furnace exit (°C)	500 ±3.43	500 ±3.43
Recycle ratio ¹	-	0.46
Outer wall surface temperature at the vertical section (°C)	195 ±1.84	
Inner surface temperature of the cylindrical section (°C)	890 ±4.28	

¹calculated value**Table 16:** Analysis of pre-dried lignite.

Proximate analysis (wt%, ar)		Ultimate analysis (wt%, daf)	
Moisture	10.12	Carbon	57.41
Volatiles	46.84	Hydrogen	4.52
Fixed carbon	37.65	Nitrogen	0.62
Ash	5.39	Sulfur	0.58
		Oxygen	21.36
D _{mean} (μm)	200	Lower heating value (kJ/kg)	21,200
D ₁₀ (μm)	11	Ash softening point (°C)	1266
D ₉₀ (μm)	750		

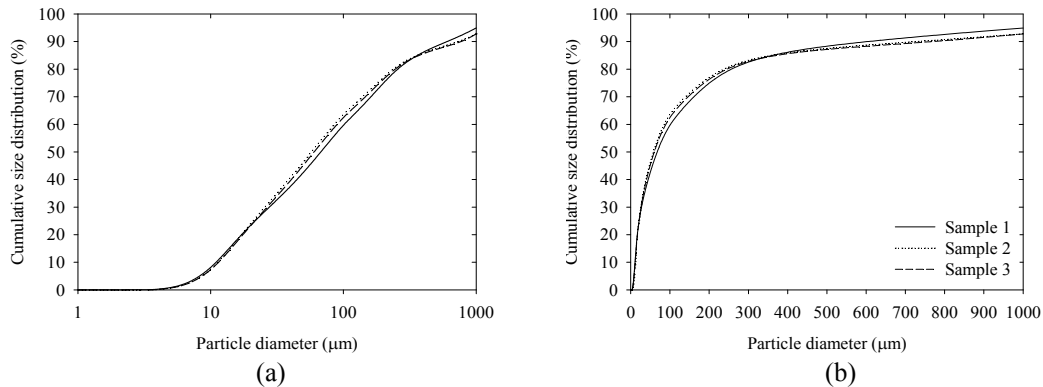


Figure 5.1: Cumulative particle size distribution of three samples using (a) logarithmic and (b) linear scale type.

To evaluate the overall impacts of oxy-fired conditions on the combustion performance, key parameters were defined and continuously monitored during the experiments. Table 17 summarizes the evaluated performance variables and the measurement techniques applied in the parametric study.

Table 17: Performance variables for the parametric study.

Response variable	Method	Position
Flame pattern	Flame images	Measurement port A and back wall
Peak flame temperatures	Non-intrusive digital imaging	-
Flame stability	Variation of feed gas distribution and swirl number	-
Burnout efficiency	Solid sampling	Measurement port H
Flame radiative heat flux	Ellipsoidal radiometer	Measurement port C
Local heat flux	Temperature difference	Water-cooled walls
Heat uptake	Thermodynamic balance	Boiler and economizer
NO, SO ₂ , and CO emissions	Gas sampling	Furnace exit and stack

5.3 Flame Pattern

Even though there are considerable variations in the geometry of pulverized coal burners, a classification of flames issuing from nozzles with divergent exits has been proposed by the IFRF [147] and for convenience is summarized here before the discussion of results. As depicted in Figure 5.2, a flame of type-0 is a long jet-flame used mostly in tangentially fired furnaces. The feed gas of this flame type is either not swirled or has a low inlet swirl. In burners operating with weak swirl, the axial pressure gradients are not sufficiently large to cause internal recirculation and the swirl has the effect of increasing the rate of entrainment and the rate of velocity decay [134]. The type-2 flame, typically achieved by industrial swirl burners, is usually short and intense. It is produced when a sufficient degree of

swirl is applied to the feed gas stream, and is accompanied by higher velocities of the swirling flow, which leads to a strong IRZ. The devolatilization process takes place at the boundary of this internal recirculation region and the flame ignites in the vicinity of the burner. The type-1 flame is a combination of the type-0 and type-2 flames and is encountered in low NO_x burners, which use the principle of internal feed gas staging. The swirl number is usually high but in contrast to the type-2 flame is accompanied by lower velocities in the secondary flow compared to high primary gas velocities. In this flame, the primary jet completely penetrates the IRZ, leaving a relatively small annular region of reverse flow. For all these flame types, the combustion in the near burner region is diffusion controlled, while the heat release downstream of the burner is governed by the heterogeneous oxidation process.

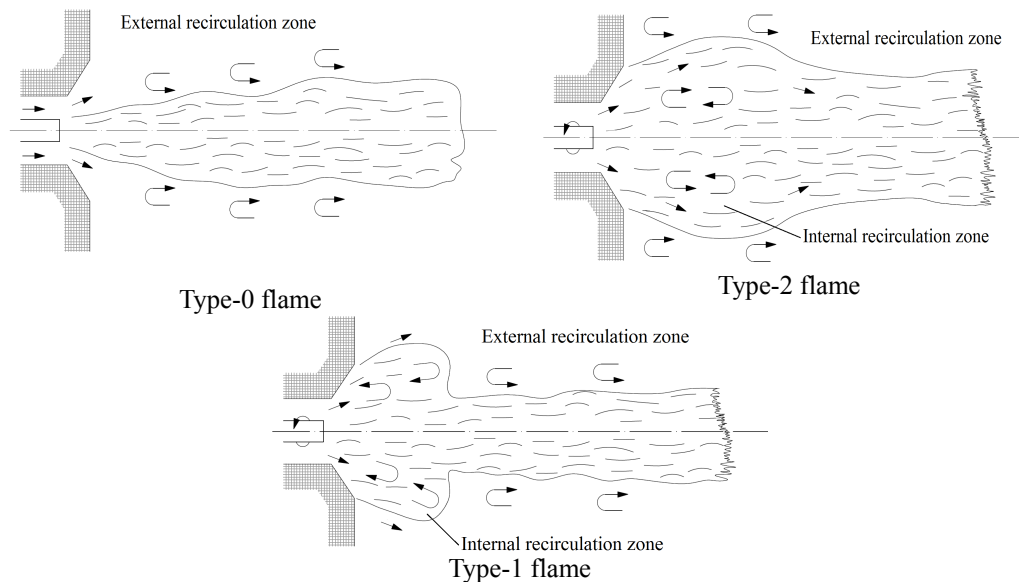


Figure 5.2: Classification of diffusion coal-flames according to IFRF. Adapted from [147].

Typical examples of photographic images of the flames visualized through the access port A at 0.050 m from the burner exit are shown in Figure 5.3. The aperture and shutter speed settings were identical for all photographs. The overall characteristics of the investigated flames are similar. Two regions are clearly identified: a darker region in center of the flame, which indicates the coal jet, and a more luminous yellow region surrounding the coal jet due to combustion of volatiles and particles. A wide and intense devolatilization and combustion start inside the quarl for both firing environments. In general, a bulbous combustion zone near the burner with a flame tail which resembles a type-1 flame is produced in all stabilized and anchored flames in the quarl. In these cases, the fuel jet penetrated completely the IRZ forming an annular doughnut reverse flow region. This is clearly observed in the post-processed images obtained from the CCD

camera installed at the furnace backwall (Figure 5.4). The primary jet penetrates the toroidal recirculation zone under both firing conditions and generates a stratified flame structure, with the center of the flame operating fuel rich and the annular operating fuel lean.

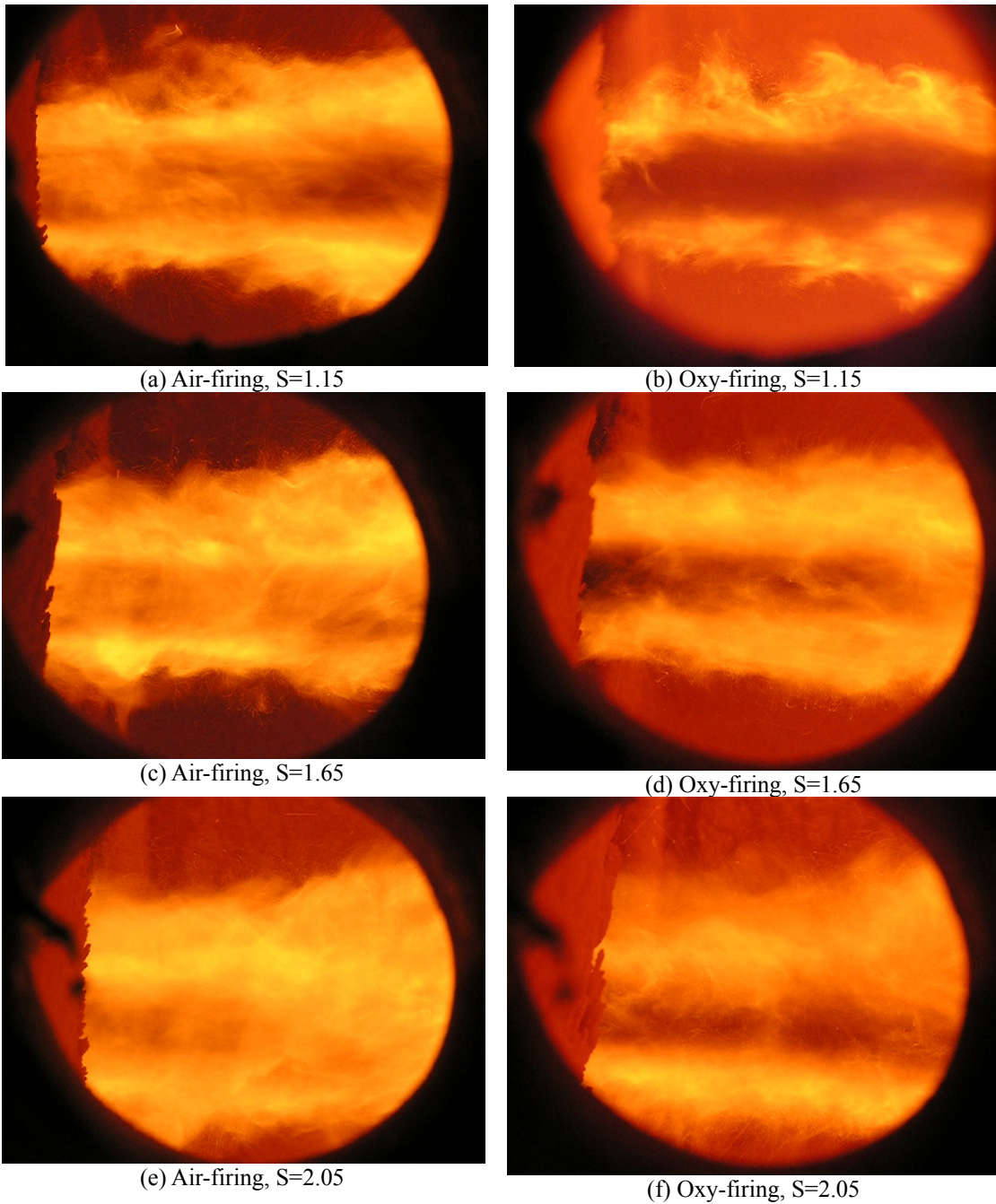


Figure 5.3: Photographs of the flames as seen through measurement port A. Note: the flame direction is from left to right.

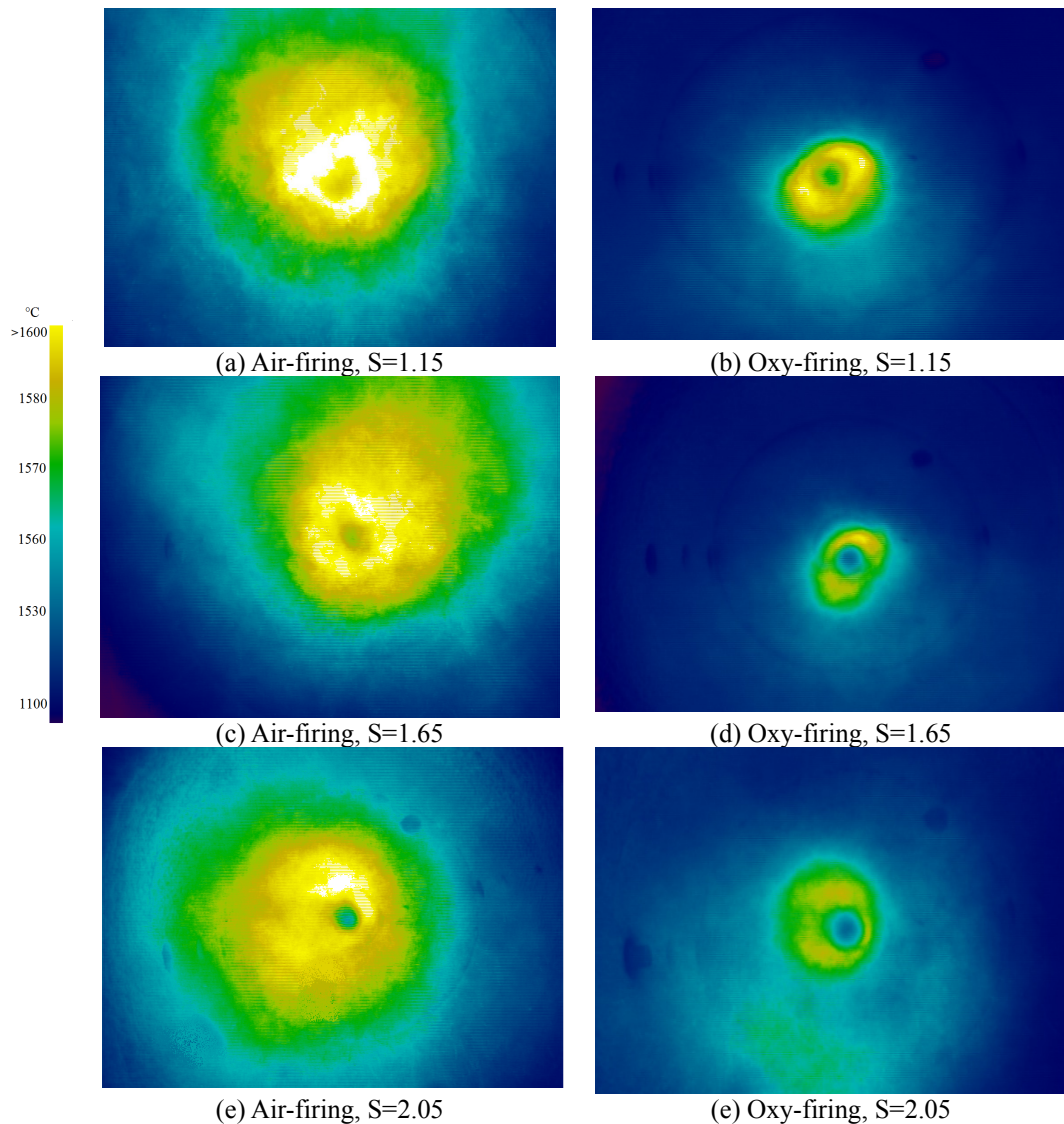


Figure 5.4: Post-processed flame images captured by the digital imaging system. Note: the secondary/tertiary flow ratio for air-firing and oxy-firing is kept equal to 1.30 and 1.50, respectively.

A conspicuous difference in the flame appearance clearly shows that the pulverized coal flame is very sensitive to the composition of feed gas. A coal jet is clearly observed in the photographs of oxy-fuel flames, whereas the air-fired flames are characterized by a slightly more intense flame which is stabilized by a stronger IRZ generated in front of the burner. The penetration depth of the primary jet is much more pronounced in oxy-fuel cases because of the lower flow rate of feed gas in the secondary and tertiary annulus. Since CO_2 and H_2O are not transparent to radiation and have much higher volume fractions in oxy-firing, they contribute to a slightly decrease in the luminosity of the oxy-fuel flames. Unless the flame is unstable or not anchored, the ignition point of the flame is

unfortunately not visible as the coal/oxidant mixture ignites inside the burner quarl. When the secondary/tertiary flow ratio exceeds a certain lower limit, depending on the strength of swirling flow, the ignition point is visible, indicating a delayed ignition of the flame as a result of the changed aerodynamic flow in the vicinity of the burner.

The observed combustion flow pattern differs from those predicted by the isothermal CFD simulations mainly in one aspect. The theoretical study indicated that in most cases the primary jet penetrates the IRZ only until a certain extent downstream of the burner, which depends on the feed gas composition, swirl number and feed gas distribution among the burner registers. On the other hand, flame images captured by the digital imaging system show a complete penetration of the fuel jet through the reverse region for all cases in which the flames were stabilized in the burner quarl. A previous study [137] investigated the effect of combustion on properties of swirl-induced IRZ and demonstrated that when the cold vortex is combustion accelerated, the IRZ strength and size are reduced. It was concluded that the combustion reduces the importance of the centrifugal forces relative to inertial forces of the swirling flow by increasing the latter substantially. Therefore, it is generally agreed that in a swirling flame the amount of reverse flow inside the IRZ is reduced if compared to a corresponding cold flow of identical swirl. This effect is qualitatively similar to a reduction in the IRZ when the inlet swirl of a cold flow is decreased [133,137].

5.4 Peak Flame Temperatures

The burner is operated to maintain a target temperature. As reviewed previously, the O₂ fraction in the feed gas plays an important role in determining the adiabatic flame temperature under oxy-fired conditions. However, no attention has been given in the existing literature to the fact that the feed gas distribution and strength of swirling flow may also influence the temperatures in the furnace. Figure 5.5 shows a comparison of peak flame temperature between air and oxy-fuel combustion taking into account the swirl number and feed gas distribution. The error bars represent the maximum and minimum variation in peak temperatures on the various testing days. The expanded uncertainty of measurement varies between ± 99 and ± 101 °C for a temperature range of 1500-1850 °C.

From the dynamic flow study, an increase in the swirl number associated with a higher flow rate of the secondary stream expands the flow/flame envelope in width. Axial and tangential velocities were smooth and their peaks moved towards the walls, which in turn changes the burning rates and affects the temperature distribution in the flame envelope. The experiments revealed that a decrease in the secondary feed gas flow rate increases the flame temperatures. Under these

conditions, the mixture between fuel and feed gas generates regions with higher temperatures, although the flame is still stratified in fuel-rich and fuel-lean zones.

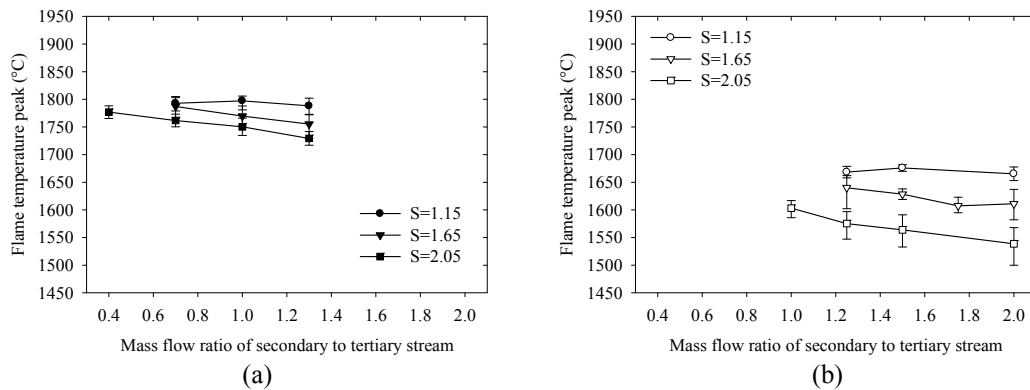


Figure 5.5: Peak flame temperatures in (a) air-fired and (b) oxy-fired environments.

Because of reduced volume flow rate, oxy-fired flames are much more influenced by the strength of secondary swirl number and feed gas distribution than conventional combustion in air. At the same swirl number, the average maximum flame temperature in air combustion was typically 120-180 °C higher than the oxy-fuel combustion. An overall reduction of peak flame temperature in oxy-fired environments is explained by the slightly lower temperatures of the feed gas and higher proportion of CO₂ and water vapor in the furnace. By comparing the physical properties of air and oxy-fuel environments, special attention is given to the volumetric heat capacity, which gives an indication of the amount of energy required to change the temperature per unit volume. The volumetric heat capacity at atmospheric pressure and temperature of 1500 °C under oxy-firing (based on FluidEXL property library [130]) is 15% higher than it is under air-firing. This indicates that more energy is required to reach thermal equilibrium at higher temperatures similar to air-firing.

The theoretical adiabatic flame temperatures are compared to the peak temperatures measured by the digital imaging system in Figure 5.6. Despite the inaccuracy caused by heat loss, the theoretical adiabatic flame temperature is useful in understanding burner performance and heat transfer within the furnace. Experimental results were obtained for both firing environments at an approximate secondary/primary flow ratio of 3.70. This value corresponds to a secondary/tertiary flow ratio of 1.00 and 2.00 under air-fired and oxy-fired conditions, respectively. As previously discussed, the choice of an O₂ fraction of 31 vol% in the feed gas was intended to provide similar adiabatic flame temperatures than that air-firing. Slightly reduced adiabatic flame temperatures are obtained under oxy-fired conditions because the temperature of feed gas cannot be precisely matched to air operation mode (see Table 15). The maximum average temperature of air-fired combustion was 200-250 °C lower than the

calculated adiabatic flame temperature; in the oxy-fired cases, the corresponding temperature difference was larger, varying between 270-400 °C.

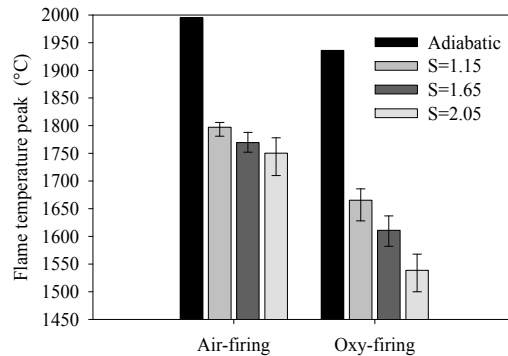


Figure 5.6: Flame temperature peaks in (a) air-fired and (b) oxy-fired environments for an approximate secondary/primary flow ratio of 3.70.

5.5 Flame Stability

Flame instability was a particular problem under low-load operation at outputs under 250 kW_{th}, necessitating a natural gas pilot flame to maintain stable combustion of pulverized coal. At firing rates of 300-400 kW_{th}, the luminous region of the flame was kept unaltered and no differences in the flame pattern and stability were observed. In these cases, all flames were stabilized without the aid of a pilot flame. The velocity of the primary stream was found to be one of the most important parameters for generating type-1 flames firmly attached to the burner quarl in both firing environments. It is known that the velocity must exceed an acceptable minimum value to prevent particle stratification in the pipeline, and to avoid any flashback of the flame. However, too much primary feed gas causes unstable ignition of the flame and complete flame detachment as illustrated in Figure 5.7.

During the commissioning, it was also observed that the introduction of pure CO₂ as a primary stream during the oxy-fuel tests yielded a cooling effect on the flame, leading to unstable flames. Stable combustion was possible only by increasing the O₂ concentration in the primary stream to levels similar to air; this seems to be crucial for stabilizing the flame. Because this burner configuration applies staging combustion techniques and does not use nozzles where the O₂ could be injected independently, the achievement of stable combustion becomes even more difficult in oxy-fired conditions. Therefore, the O₂ content in the primary stream is essential for initiating the combustion of volatiles within the burner quarl, which leads to stable and attached flames.

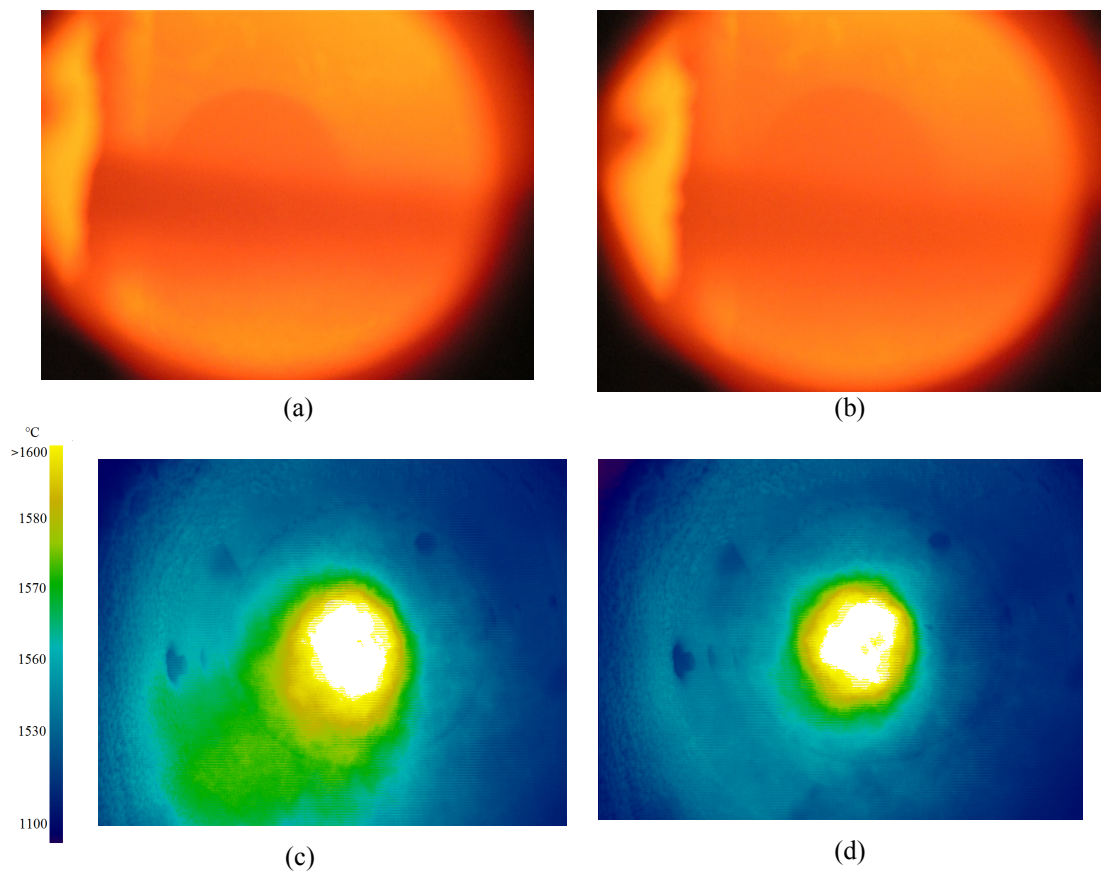


Figure 5.7: Photographs and post-processed images of detached flames for (a,c) air-firing and (b,d) oxy-firing at 1.15 swirl number.

Oxy-flames were observed to be more sensitive to variations in the primary stream velocity than conventional air-fired flames. By keeping a similar velocity as with conventional air combustion (28 m/s), the coal particles could not be ignited within the burner quarl and, because of reduced temperatures, it seemed that there was insufficient heat in the IRZ to liberate the minimum necessary amount of volatiles. In these cases, the flame was established well downstream of the burner quarl. Since CO_2 has a higher density than N_2 , a higher axial momentum is obtained at the burner outlet if the same velocity is maintained. Therefore, the strategy adopted during the oxy-fuel trials was to reduce the velocity of the primary stream until the axial momentum equaled that of the air-fired case; a similar strategy adopted previously by Fry and co-authors [71].

A diffusion flame has certain regions beyond which stable burning cannot occur. The flame stability limits were determined by decreasing the secondary/tertiary flow ratio while keeping all other conditions constant until flame lift-off was detected both visually and by fluctuations in the signal generated by the UV scanners. The results are evaluated as a function of swirl number and secondary/tertiary flow ratio as shown in Figure 5.8 (a); in Figure 5.8 (b) the

stability limits as a function of secondary/primary axial momentum ratio are plotted. In both graphs, the lower limit of the mass flow ratio and axial momentum ratio is the point at which a stable flame cannot be maintained leading to local lift-off as illustrated in Figure 5.9. The upper and lower error bars of the plots indicate the maximum and minimum values obtained on different test days, respectively.

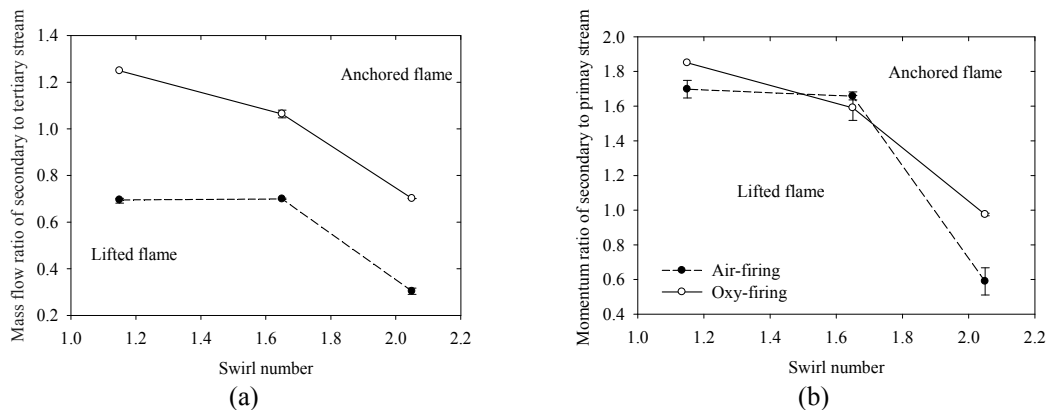


Figure 5.8: Stability performance as function of (a) secondary/tertiary flow ratio and (b) secondary/primary axial momentum ratio.

The results show that an increase in the swirl number improves the operating limits of the burner by decreasing both the secondary/tertiary mass flow ratio and the secondary/primary axial momentum ratio. In Figure 5.8 (a), the staged feed-gas burner operating with air produces a more stable flame for a lower secondary/tertiary flow ratio compared to the oxy-fuel case. When the secondary/primary axial momentum is compared, the stability curves remain practically unaffected by the feed gas composition.

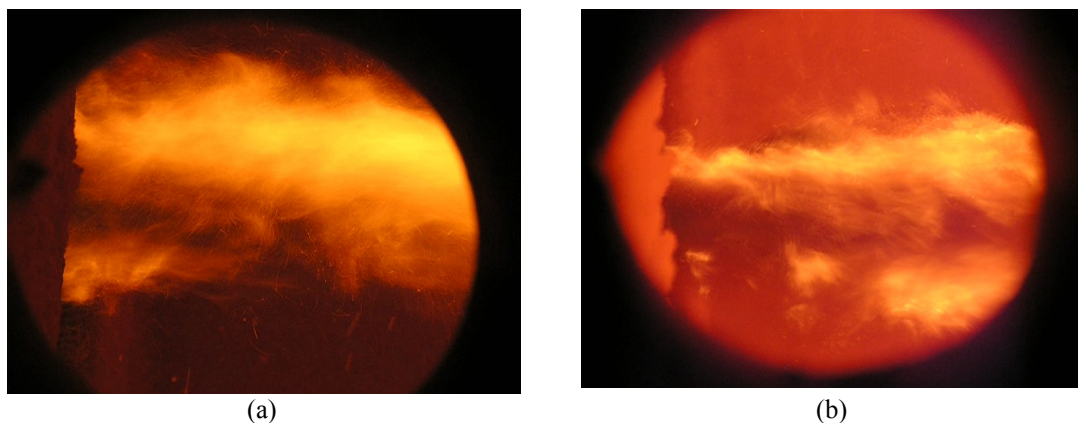


Figure 5.9: Photographs showing local lift-off for (a) air and (b) oxy-fuel flames at 1.15 swirl number.

Reducing the secondary/tertiary flow ratio, and the secondary/primary axial momentum ratio, decreases flame stability. This is a result of weaker IRZ generated in the vicinity of the burner as observed in the numerical cold flow study. Thus, the primary stream inertia is too high for the bulk of coal particles to be ignited in a short space of time. Although numerical simulations were performed in the absence of particles, it was shown that an increase in the secondary feed gas flow rate combined with higher swirl numbers improves the reverse flow. Under such conditions more hot combustion gases are recirculated from within the flame zone and, consequently, ensure more volatile release, stronger gas-phase combustion, and particle ignition inside the burner quarl.

5.6 Heat Transfer Performance

The primary objective of this section is to evaluate in greater detail the impacts of burner settings on heat transfer. Due to high temperatures in the furnace, the dominant mode of heat transfer is thermal radiation. During the parametric study, the ellipsoidal radiometer measured all incident radiation from a 2π steradian solid angle. The measurement procedure involved taking measurements at the inside of the furnace wall at 0.660 m distant from burner exit (measurement port C) in a region where the fire ball is located. The expanded uncertainty of the measurements varies between ± 9.84 and ± 12.21 kW/m² for a measurement range of radiative heat flux between 150 and 200 kW/m², respectively.

The effect of feed gas distribution and swirl number on the total radiative heat flux is represented by box plots in Figure 5.10. The experimental data indicate that the radiation emitted by oxy-fired flames at this position is very close to those of the air-fired case. Despite the lower temperature peaks found with oxy-firing, similar or even slightly higher values of radiation emitted by the flame are obtained. This behavior is caused by the higher concentration of triatomic gases (mainly CO₂ and water vapor), soot, and particles which yield an increase in flame emissivity. The results show no considerable evidence of the impacts of feed gas distribution and swirl intensity on the radiant incident heat flux at this position. Only for the oxy-fired case using the highest swirl number does a reduction of the secondary/tertiary flow ratio seem to lead to an increase in incident radiation. Nevertheless, measurements at various distances from the burner are still necessary to verify whether the changes in the near burner flow dynamics would affect the distribution of radiation intensity along the flame length. This aspect is discussed further in the following sections.

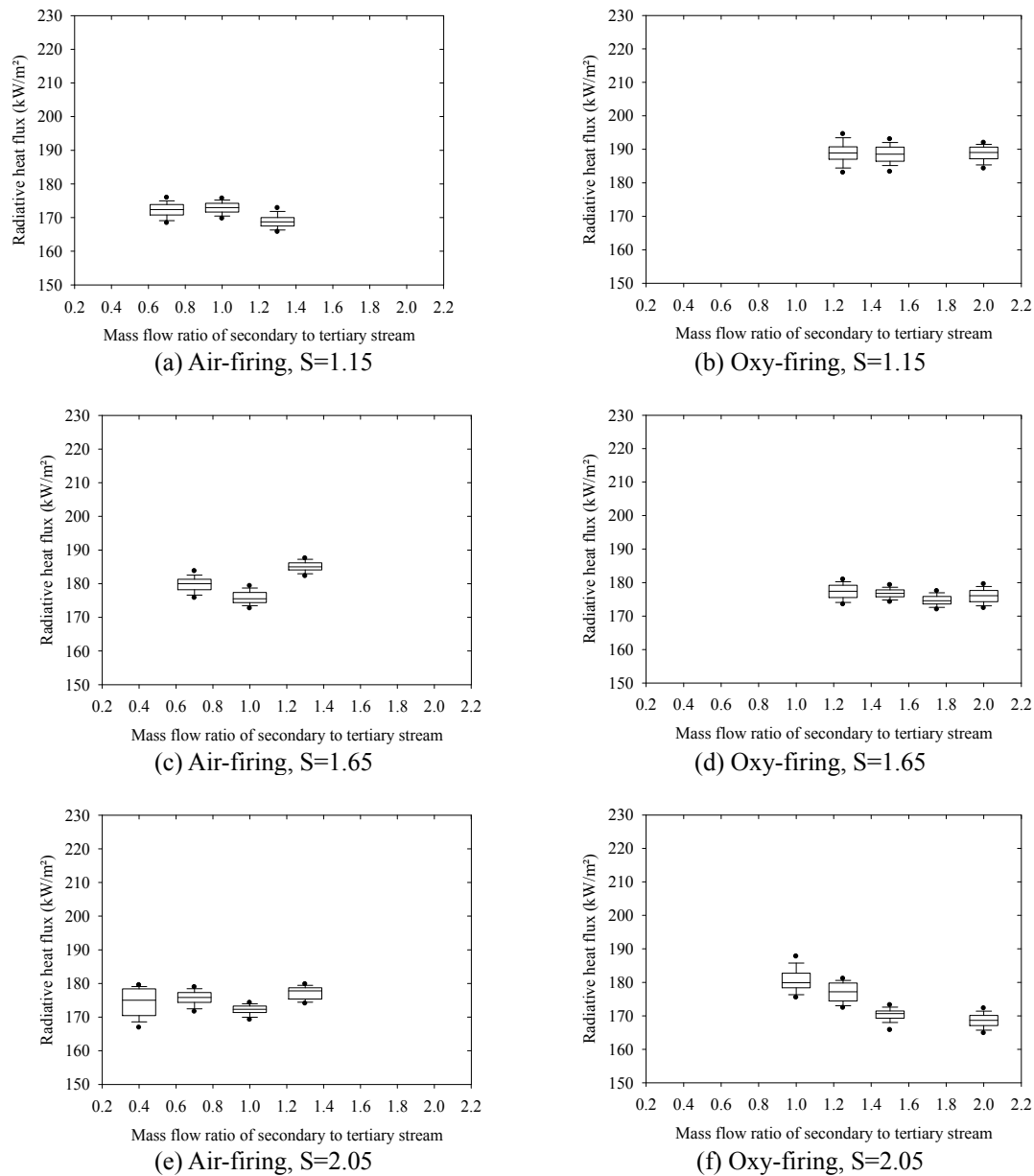


Figure 5.10: Box plots of total radiative heat flux at 0.660 m distant from burner.

From the evaluation of combustion-related parameters, it was seen that the adiabatic flame temperature can be easily manipulated by the O₂ fraction in the feed gas. Although the impact of the O₂ fraction or recycle ratio has been extensively investigated by other authors [27,67-70], this effect is quickly evaluated here for completeness. A series of tests was conducted for a swirl number of 1.65, while the secondary/tertiary flow ratio was kept at 2.00. Three different O₂ fractions were used in the secondary and tertiary streams to match an overall O₂ fraction of 29, 31, and 33 vol%, labeled as Oxy29, Oxy31, and Oxy33, respectively. All the experimental runs were performed at a stoichiometric ratio of

1.17. Figure 5.11 demonstrates the impact of feed gas composition on the average peak temperatures and incident radiation at the access port C. The error bars represent the expanded uncertainty of measurements.

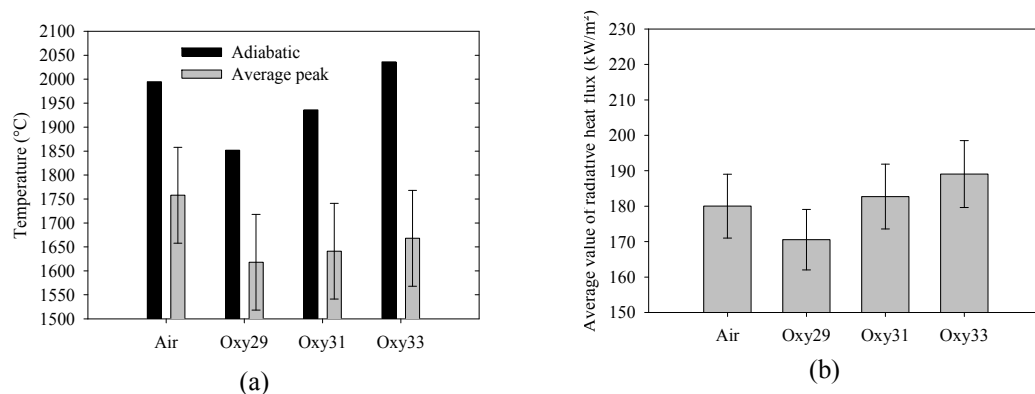


Figure 5.11: Comparison of (a) arithmetic mean flame temperature peaks and (b) total radiative heat flux for various O₂ concentrations in the feed gas.

For an O₂ fraction of 29 vol%, the oxy-coal flame was observed to be less luminous, indicating lower emissivity due to the higher feed gas flow rate. This reduces the concentrations of particulate in the flame envelope and consequently the temperatures as indicated in Figure 5.11(a). Although the adiabatic flame temperature is similar for both the air-fired and oxy-fired cases, the peak temperatures are considerably lower for oxy-firing, even at the highest O₂ fraction (33 vol%). Conversely, the radiative heat flux measurements indicate the possibility of matching similar values by varying the O₂ fraction in the feed gas. An increase in the overall O₂ fraction from 29 to 33 vol% corresponded to an increase in the radiative heat flux from approximately 170 to 190 kW/m².

Profiles of the local heat flux along the height of water-cooled walls monitored by the sensors detailed in the Section 3.2.6 are compared for swirl numbers of 1.15 and 2.05 (Figure 5.12). The results are also plotted for different test days, where error bars indicate the expanded uncertainty of measurement. The results indicate that the values of local heat flux decreased over the course of days of experimentation, caused by an increase of ash deposits on the upper section of the water-cooled walls. In overall, the local heat flux is reduced at the lower section of the furnace. This is caused by the lower thermal conductivity of the lining material, which reduces considerably the radiative heat transfer rate from the flame. Higher values of heat flux are obtained only at a height distance of 1.59 m from the burner axis. A significant difference in the peak heat flux between the two swirl numbers was observed for both firing conditions. This behavior occurs due to the differences in the flame length and temperatures generated by the various burner settings. Although the flame length cannot be precisely estimated, these results suggests that a decrease in the swirl strength moves the flame front towards the back wall and thereby increases the radiation view factor and

consequently the radiative heat transfer at the upper section of the furnace. Similarly, high values are obtained when the feed gas flow rate in the secondary register is reduced.

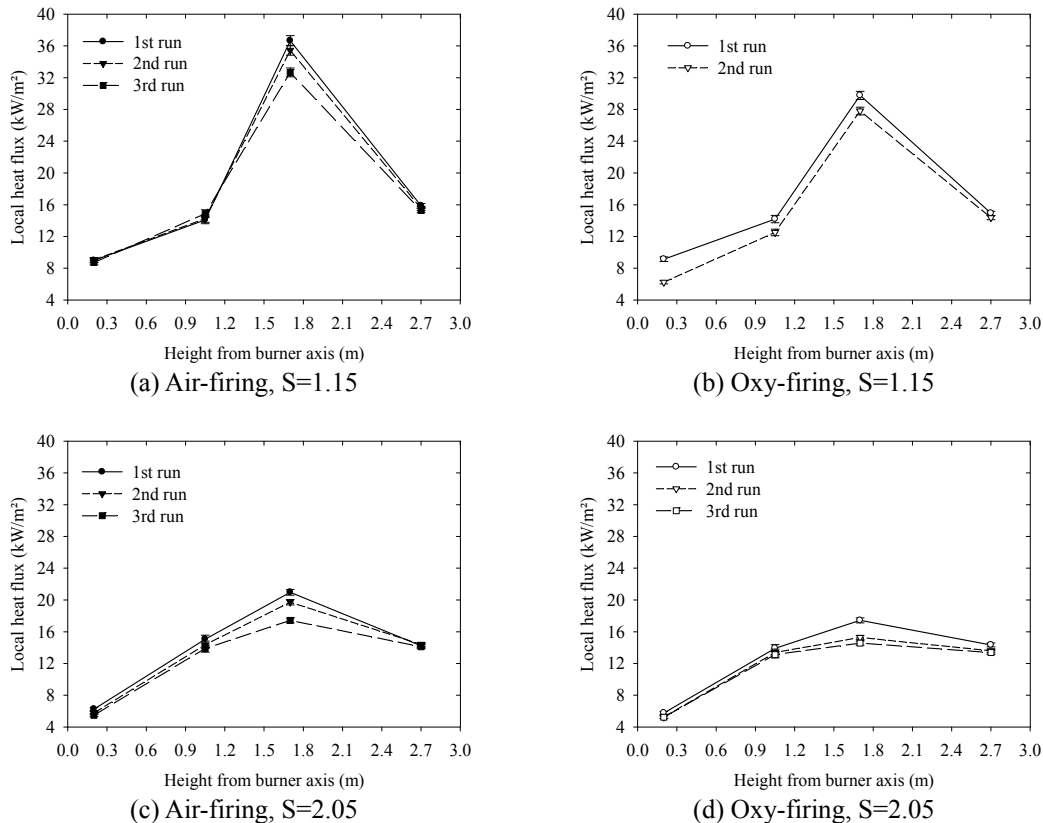


Figure 5.12: Profiles of absorbed heat flux along the back wall for (a,c) air-firing and (b,d) oxy-firing at a secondary/tertiary flow ratio of 1.30 and 2.00, respectively.

Values of average heat uptake at the boiler obtained on different days are compared in Figure 5.13. For completeness, a comparison of the values in the economizer is also included. The results are presented in terms of a secondary swirl number of 2.05 because of the possibility of obtaining stable flames for a wider range of feed gas flow ratios. The uncertainty of the calculated values of the heat transfer rate was estimated to vary between ± 1.07 and 4.28 kW/m² for 50-200 kW/m², respectively. Even though the adiabatic flame temperature of oxy-fired conditions does not match precisely that achieved by conventional air combustion (approximately 3% lower), similar values of heat extracted by the water-cooled walls is shown to be possible. The results indicate that as the flow ratio of secondary to tertiary decreases, the overall heat uptake increases. Again, this behavior occurs due to an increase in both flame length and radiative heat transfer in the vertical section of the furnace. Conversely, the feed gas distribution does not affect the heat transfer performance in the economizer because the dominant heat transfer mechanism is convection.

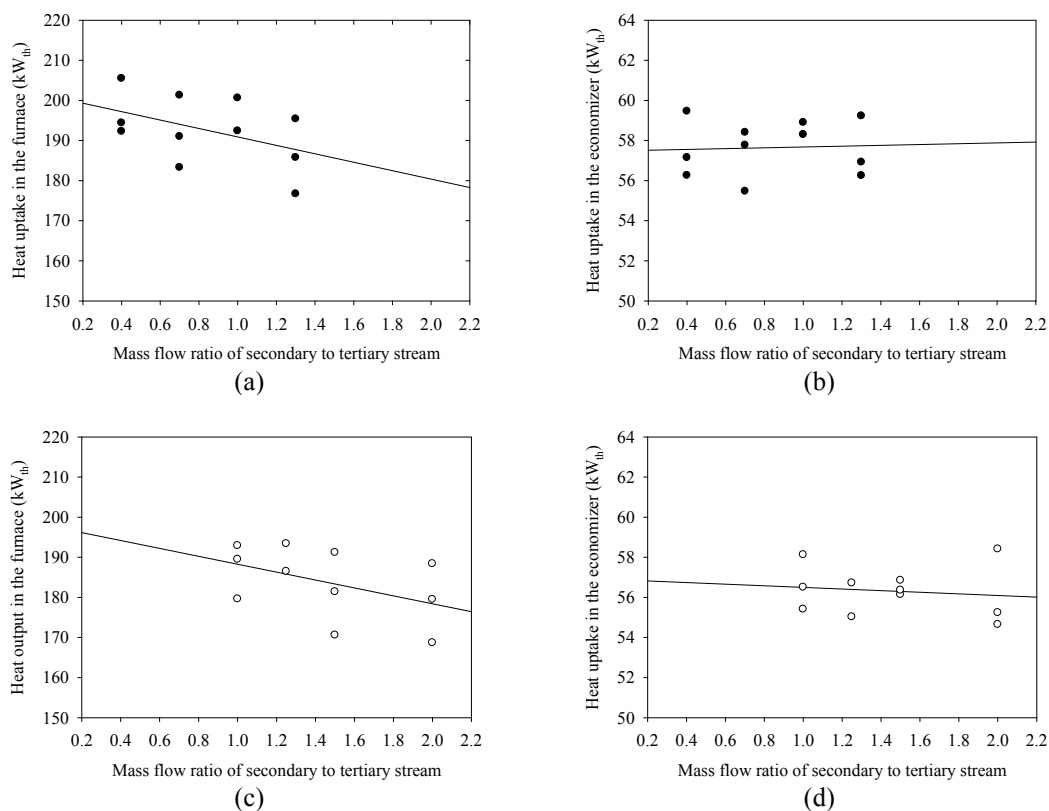


Figure 5.13: Heat uptake in the furnace and economizer under (a,b) air-fired and (c,d) oxy-fired conditions at 2.05 swirl number.

The heat uptake in the boiler and economizer normalized to air for the three swirl levels are given in Figure 5.14. The burner operating conditions were chosen to match a similar secondary/primary flow ratio. In case of a value of 3.70, it means that the secondary/tertiary flow ratio for air-firing and oxy-firing is 1.00 and 2.00, respectively; a value of 3.00 is for a secondary/tertiary flow ratio of 0.70 (air-firing) and 1.25 (oxy-firing). Under these conditions, the total amount of heat extracted in the furnace is slightly reduced under oxy-fired conditions. The results also indicate that the amount of heat transferred to the furnace is influenced not only by the feed gas distribution among the burner registers, but also by the strength of the swirl. Slightly differences are observed in the amount of heat transferred to the economizer, indicating that the convection mechanism is affected by the reduced volume flow rate of flue gas under oxy-firing. As discussed in Chapter 4, in order to obtain similar temperatures and heat uptake in the radiative section of the furnace, the recycled flue gas flow is reduced due to the necessary increase of the O₂ fraction in the feed gas. Nevertheless, it is expected that this problem can be easily overcome in full-scale power plants by optimizing the arrangement of tube bundles in the convective section in order to match a similar heat transfer rate.

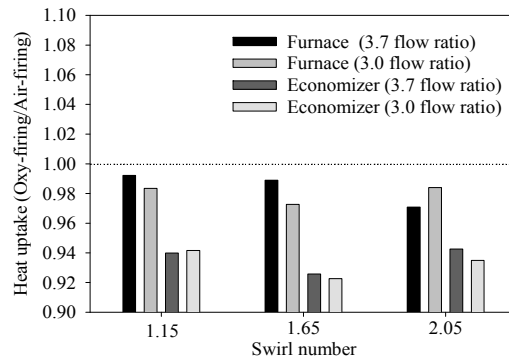


Figure 5.14: Heat uptake ratio from oxy-firing to air-firing as a function of swirl number and secondary/primary flow ratio.

5.7 Carbon Monoxide Emission and Burnout Efficiency

Under the conditions evaluated, the CO measured within the flue gas was lower than the minimum detectable limit of the gas analyzer for all experiments. In general, values smaller than 30 mg/m³ on dry basis were obtained, indicating a complete combustion for air-firing and oxy-firing. Furthermore, CO concentration in the flue gas proved to be unaffected by the feed gas composition, despite the many mechanisms which contribute to the increase in CO concentrations in the near burner region of oxy-fired flames as will be discussed in the following sections. The uncertainty of measurements of CO at furnace exit and stack are ± 2.26 and ± 3.74 mg/m³ (dry), respectively; both values are independent of the measurement range.

An analysis of burnout efficiency calculated by Equation 3.3 is presented in Figure 5.15 and also confirms that for both firing conditions the combustion of CO was completed before the furnace exit. However, the results do not provide a clear picture on the influence of both secondary stream swirl and feed gas distribution. Contrary to the results obtained by Smart et al [70], particle burnout is not enhanced under oxy-firing and the experimental data does show very similar values for both firing conditions. An increase in the O₂ concentration of the feed gas going into the furnace reduces the overall volumetric flow of gas and thus increase the residence time of the coal particles in the furnace. An estimate of particles' residence time assuming a plug flow reactor, as suggested by Smart et al [70], indicates that the residence time in oxy-fired cases is typically 1.30 times higher than with air-firing. However, no difference was observed. This is probably due to the higher reactivity of lignite or by differences in the burner settings.

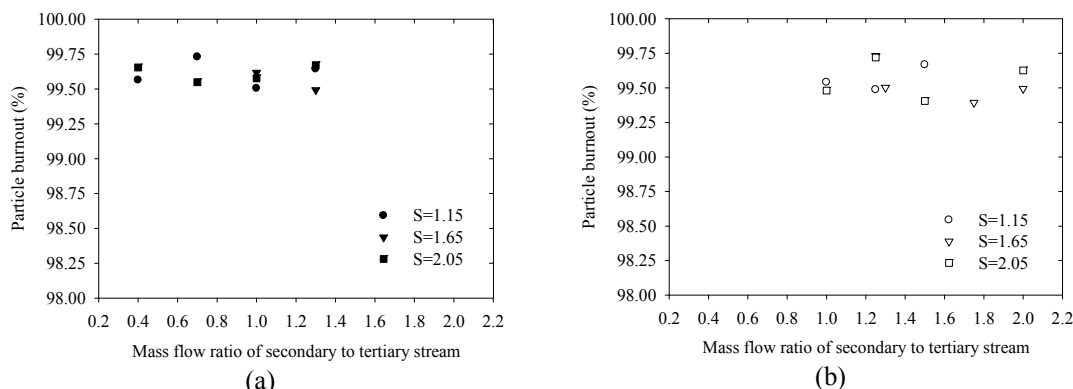


Figure 5.15: Particle burnout for (a) air-firing and (b) oxy-firing.

5.8 Nitric Oxide Emissions

As previously discussed, little information is available at present in the literature about the impact of burner settings on NO_x emissions under oxy-fired conditions. In the present work the NO_2 emissions were in average less than 10 and 25 mg/m^3 (dry) in air and oxy-fuel combustion, respectively. These values correspond to less than 3% in the total NO_x formed. For this reason, only NO emissions are considered in this study. The uncertainty of measurement of NO emission at furnace exit is ± 40.80 mg/m^3 (dry) and this value is independent of the measurement range. Box plots of the NO emissions from stable flames are presented in Figure 5.16. The highest NO concentrations occurred during oxy-fuel combustion. This is a result of the recycling of NO in the flue gas back to the burner and a reduction of the overall feed gas flow rate.

Experimental data does show that the resultant conversion to NO can be significantly altered by burner settings. A general tendency is that an increase in the secondary/tertiary flow ratio associated with higher swirl number can decrease the NO emission. To provide a clear understanding for such abatement, this aspect is discussed in detail in the following sections along with the in-flame measurements. Nevertheless, the NO formation and reduction mechanisms are already partially explained in the current literature. The stratified flame structure created by this burner, where a central core region deficient in O_2 is generated, allows a reduction of NO previously formed. In case of air-firing, because of reduced temperatures, the formation of NO by the Zeldovich mechanisms becomes less important. An interesting behavior observed during the experiments was the subtle increase of NO emissions when the flame was detached from the burner. NO peaked at 600 and 950 mg/m^3 (dry) independently of swirl number for air-fired and oxy-fired conditions, respectively. From Figure 5.7, it is clear that the stratified structure of the attached diffusion flame separated by an oxygen-lean

zone (central core) surrounded by swirling secondary feed gas was completely changed to a lifted, partially premixed flame. Consequently, this leads to secondary feed gas entrainment, which supplies O_2 into zones considered to be critical to NO formation.

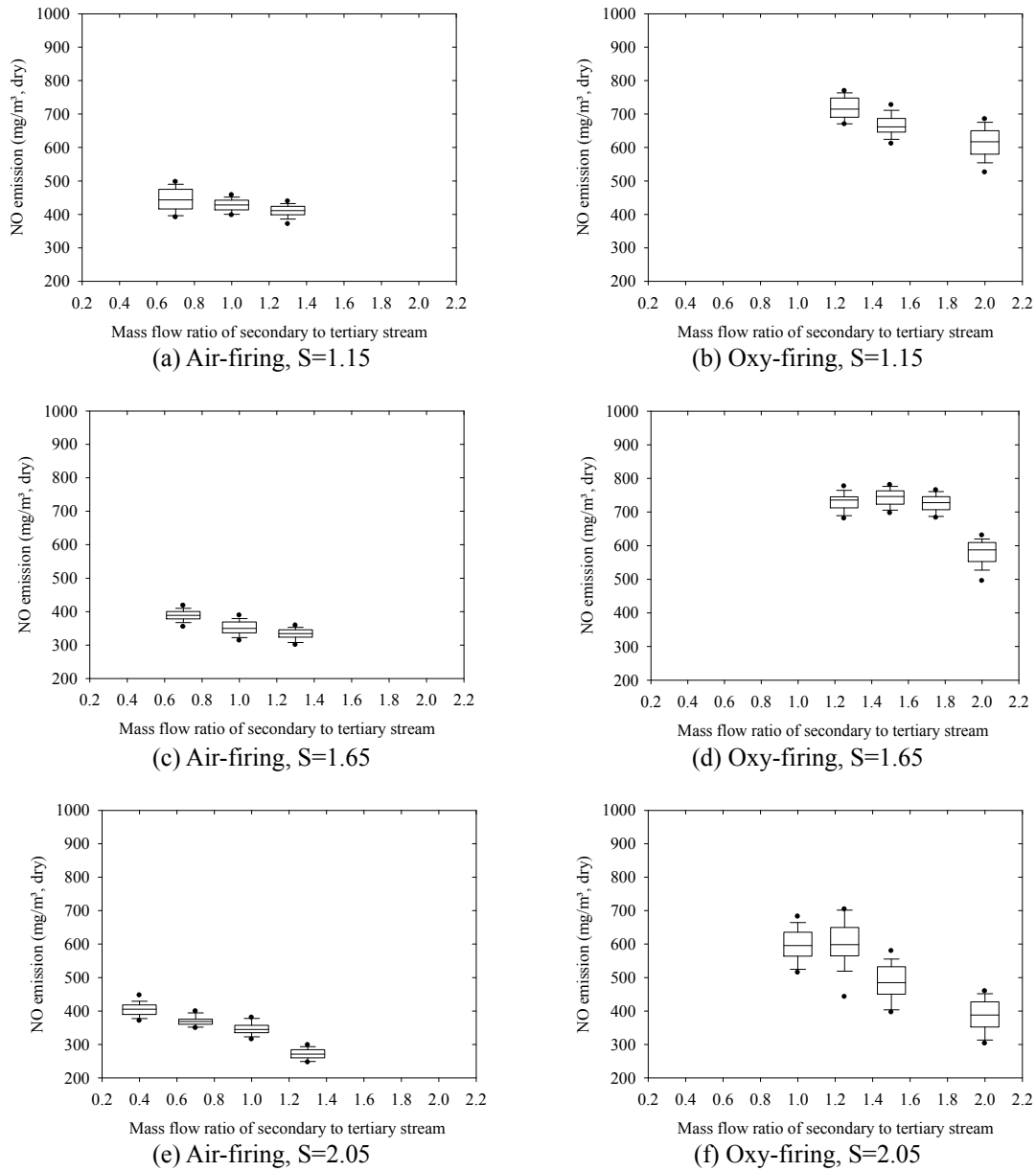


Figure 5.16: Box plots of NO emissions at furnace exit.

A series of experiments was also performed to evaluate the influence of the O_2 fraction in the feed gas and O_2 excess at the furnace exit. The experiments were carried out at a swirl number of 1.65, while the secondary/tertiary flow ratio was kept at 1.30 and 2.00 for air-fired and oxy-fired conditions, respectively. The

dependence of NO emission on the O₂ excess for the various feed gas compositions is illustrated in Figure 5.17. In these plots, the error bars represent the expanded uncertainty of measurement. There is a general linear relationship between the O₂ excess and the amount of NO formed. The results are very much the same for oxy-fired conditions using an overall O₂ concentration of 31 and 33 vol% upstream of the burner. Higher NO emissions in comparison to the case operating at 29 vol% O₂ are explained by the fact that higher O₂ fractions yield an increase in temperatures in the near burner region and thereby enhance the pyrolysis rate of nitrogen evolved in the early volatiles.

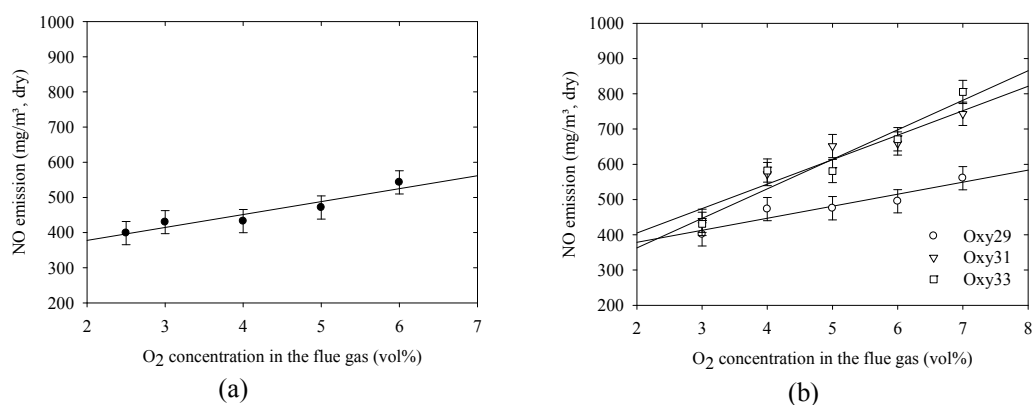


Figure 5.17: NO emission at furnace exit for (a) air-firing and (b) oxy-firing at 1.65 swirl number.

Although higher NO concentrations are obtained under oxy-fired conditions, results show the possibility to decrease the amount of NO formed per energy input (Figure 5.18). On average, a decrease between 22% and 38% in comparison to air for the same secondary swirl number are obtained. Likewise, lower values are also observed for the three levels of O₂ fraction in the feed gas for oxy-firing. In the case of the lowest O₂ fraction in the feed gas (Oxy29), the emissions are reduced to approximately 47%. Overall, this reduction under oxy-firing occurs, in parts, by the absence of thermal NO formation, since the N₂ concentration in the feed gas is much lower. As discussed in Chapter 2, the thermal component accounts for around 20% of the total NO produced in conventional air-fired combustion. An even more important mechanism for the reduction of NO in oxy-fired environments is reburning. Previous works also demonstrated that the reduction efficiency of NO through reburning is even higher for wet flue gas recirculation [148,149]. Additionally, previous studies showed that the small fractions of N₂ enable the Zeldovich mechanism to reduce NO at higher temperatures because the feed gas is oversaturated with NO [92,93]. Interesting is that the concentration of NO at the furnace exit and emission rates between the oxy-fired cases applying an overall O₂ fraction of 31 and 33 vol% were almost unchanged. Because at higher O₂ fractions the flame temperature is increased, it is speculated that for oxy-fuel case using 33 vol% O₂, higher temperatures are generated and enabling a NO reduction by the reverse Zeldovich mechanism.

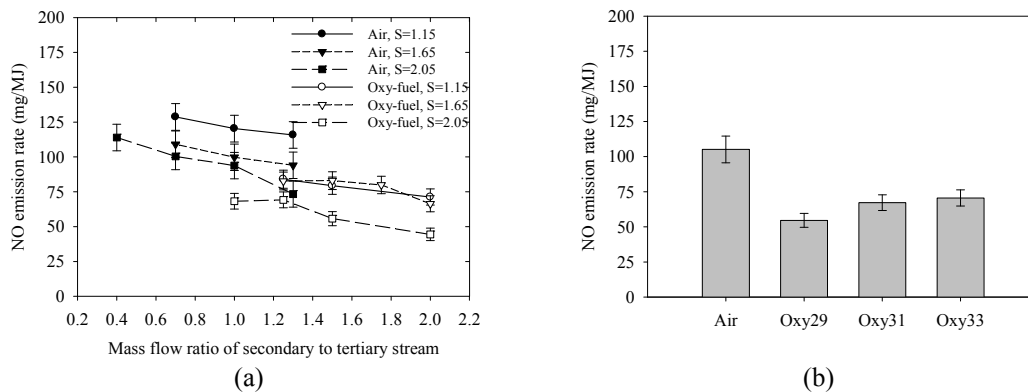


Figure 5.18: Values of NO emission rate at stack by varying (a) burner settings and (b) feed gas composition at 1.65 swirl number.

The effect of reduction mechanisms are approximated by comparing the conversion rate of fuel-N to NO (Figure 5.19). Under air-fired conditions there is the possibility of additional NO formation due to the thermal mechanism, which is not deducted from Equation 3.2. From the plots it is concluded that the conversion rate depends on the burner settings. In addition, the lower values of the percentage conversion in oxy-fired environments clearly suggest the presence of reduction mechanisms.

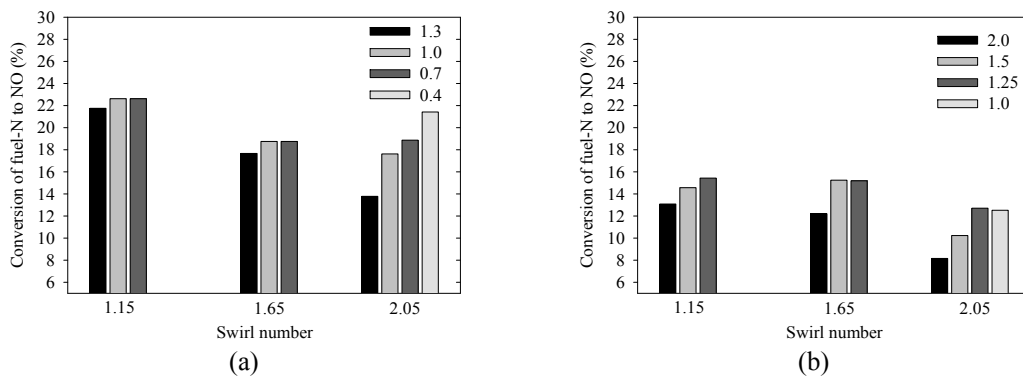


Figure 5.19: Conversion of fuel-N to NO in (a) air-firing and (b) oxy-firing as a function of swirl number and secondary/tertiary flow ratio.

The emission and conversion rates obtained in this work are compared with experimental data reported in the literature for Lusatian pre-dried lignite (Table 18). Several factors may contribute to the differences summarized in this table. In the experiments performed by Dhungel [91], the flue gas was not recirculated, while in the other works, the burner configuration and O₂ fraction in the feed gas play the most important role in the differences observed. NO emissions under conventional air combustion are much lower in the present work. This is explained by the feed gas staging techniques used in the burner, which reduce both fuel and thermal NO formation. In case of oxy-firing, the values obtained by Hjærtstam et al [67] and Andersson et al [93] using a burner without

staging measures, are very closer to the present work. This indicates that the reduction mechanisms might be, to a certain extent, even more important in determining the NO emission performance under oxy-fired conditions.

Table 18: Comparison of NO emission values of Lusatian pre-dried lignite.

First author	Thermal power (MW _{th})	O ₂ fraction (vol%)	NO emission (mg/MJ)		Conversion rate (%)	
			Air	Oxy-fuel	Air	Oxy-fuel
Present work	0.35	31	73-125	44-84	13-22	8-15
Hjærtstam [67] Andersson [93]	0.10	25-29	160	41-48	24	7-8
Wilhelm [86]	0.05	17-33	260	60-140	42	9-23
Dhungel [91] ¹	0.02	27	300	300	34	33

¹Results without staging.

5.9 Sulfur Dioxide Emissions

SO₂ concentrations in the flue gas were monitored at the furnace exit and stack. The uncertainty of SO₂ measurements at furnace exit and stack are ± 47.51 and ± 47.17 mg/m³ (dry), respectively; both values are independent of the measurement range. Because of flue gas desulfurization, emissions of SO₂ at the stack are considerably lower and usually no higher than 20 mg/m³ (dry). The direct SO₂ removal with NaOH showed similar desulfurization capacity in both operating modes with a scrubbing efficiency higher than 98%. Nevertheless, experiments carried out under oxy-fired conditions represented an increase in the consumption of the sorbent slurry to keep the sump at a constant PH level of 7.00. Much of this additional consumption is attributed to the higher partial pressure of CO₂ in the flue gas, which also reacts with NaOH to form NaHCO₃ (sodium bicarbonate).

Average SO₂ concentrations and emission rates at the furnace exit are presented in Figure 5.20. The error bars represent the expanded uncertainty of measurement. Oxy-fired conditions result in a higher concentration of SO₂ at the furnace exit. This is because of reduced dilution of SO₂ due to the volumetric change of the flue gas. In general, an increase by a factor of 1.40 is found in the experiments. When the emission rates are compared, the results clearly indicate that feed gas composition and burner operating settings do not necessarily affect the SO₂ formation, indicating that SO₂ emissions are exclusively dependent on the sulfur content of the coal. Because the SO₂ is scrubbed before the flue gas is recycled back to the furnace, much lower SO₂ concentrations are obtained in the present work in comparison to studies without SO₂ scrubbing [150,151]. The peak SO₂ emission rates at the stack for air and oxy-fuel were found to be lower than 10 mg/MJ.

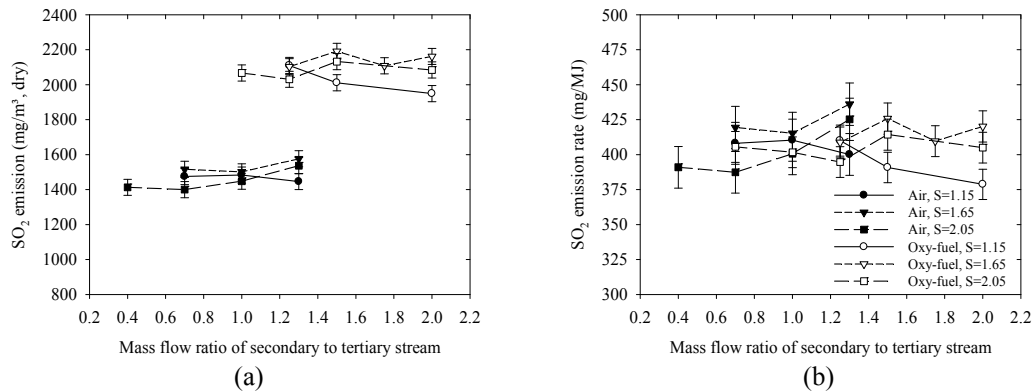


Figure 5.20: (a) Values of SO₂ emissions on dry basis and (b) emission rates at furnace exit.

A comparison of the conversion of fuel-S to SO₂ is presented in Figure 5.21. A conversion ratio of about 80% is observed for both firing conditions, indicating that the increased partial pressures of CO₂ and H₂O in the furnace does not affect the release of sulfur from the coal during combustion. Similar to values of SO₂ emissions, the strength of the secondary swirl and feed gas distribution do not have any effect on the conversion ratio. It is worthy of mention that analysis of fly ash samples collected under oxy-fired conditions indicated no sulfur retention.

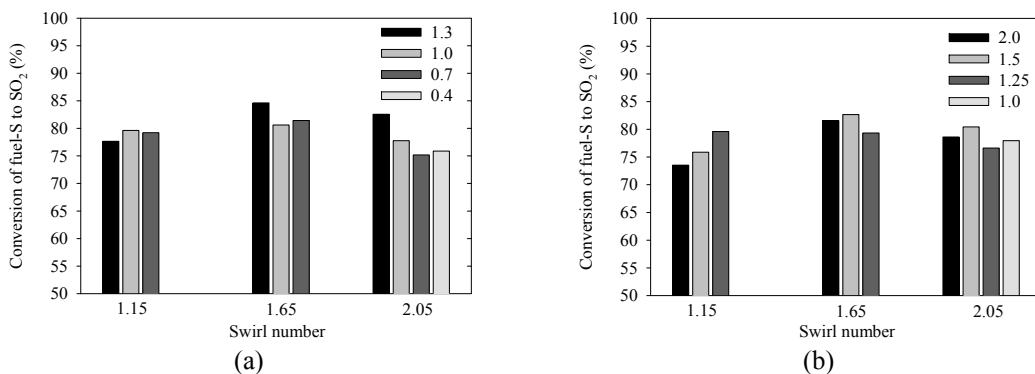


Figure 5.21: Conversion of fuel-S to SO₂ in (a) air-firing and (b) oxy-firing as a function of swirl number and secondary/tertiary flow ratio.

5.10 Detailed In-Flame Measurements

After recognizing in the parametric study that the secondary stream swirl number and feed gas distribution play an important role in flame stabilization, peak temperatures, heat transfer, and emission performance, the effect of both parameters was further explored through detailed measurements for selected flames. Measurements were conducted for five cases: four oxy-fired cases and one air-fired case. Table 19 summarizes the main burner settings of the flames evaluated in this section. Typical furnace operating conditions were already listed

in Table 15. For the reader interested in further analysis or modeling purposes, the detailed operating conditions are fully described in the Appendix B. The flue gas composition and furnace temperature consistency was monitored before starting the measurements and checked against the values obtained during the parametric study. Hourly spot checks of the furnace operating conditions were better than 5% of the mean. The symmetry of the flame was checked regularly with help of the digital imaging system. Deviations in the symmetric flow can be caused by slagging along the furnace walls or small misalignments of the swirler installed at the exit of the inner secondary register.

Table 19: Burner settings of selected flames.

Case	Overall O ₂ fraction (vol%)	Swirl number	Axial momentum of the primary jet (N)	Secondary/tertiary flow ratio
Air-flame	21	1.65	0.47	1.30
Oxy-flame 1	31	1.15	0.47	2.00
Oxy-flame 2	31	1.65	0.47	2.00
Oxy-flame 3	31	2.05	0.47	2.00
Oxy-flame 4	31	2.05	0.47	1.25

During the measurements, much emphasis was placed on the near burner field because of its importance to flame stability and pollutant emissions. Testing was done to obtain profiles of local mean gas phase temperature, species concentration, and total radiative heat flux. Each probe had to have access to the various access ports of the furnace at several distances from the burner exit to provide characteristic mappings and profiles as described in the Section 3.2.8. Beside the flame axis profiles using box plots, data are also reported along the entire transversal section of the furnace to allow for a direct comparison of the burner settings and to indicate the degree of symmetry. The lines presented in these plots represent only the trends of measurement and for a better visualization and comparison of the results provided by the different burner settings, error bars are not included in the transversal plots. The full set of data including mean values, standard deviations, percentiles, and uncertainty of measurements are fully reported in the Appendix B.

Only one probe was used in the furnace at a time so that upstream probes would not cause flow variations affecting the downstream measurements. Keeping the opening of the sampling probes clear from slag and coal particles was extremely difficult, especially when close to the burner. The tip of the suction pyrometer had to be changed or cleaned after every complete profile measurement due to clogging of the opening and depositions on the probe tip. However, tests showed that as long as the opening was not completely blocked, adequate flow through the suction tube was maintained.

As can be observed in Figure 5.22, the use of water-cooled probes brings about changes in the flame pattern and the mixing between the feed gas and coal

particles. In these cases, a radial momentum is imparted to the flow and affects pollutant formation and destruction mechanisms in zones close to the burner. This effect is even more remarkable in the measurements of NO during oxy-firing, because a great amount of NO is recirculated back to the furnace. Further details are discussed in the next sections.

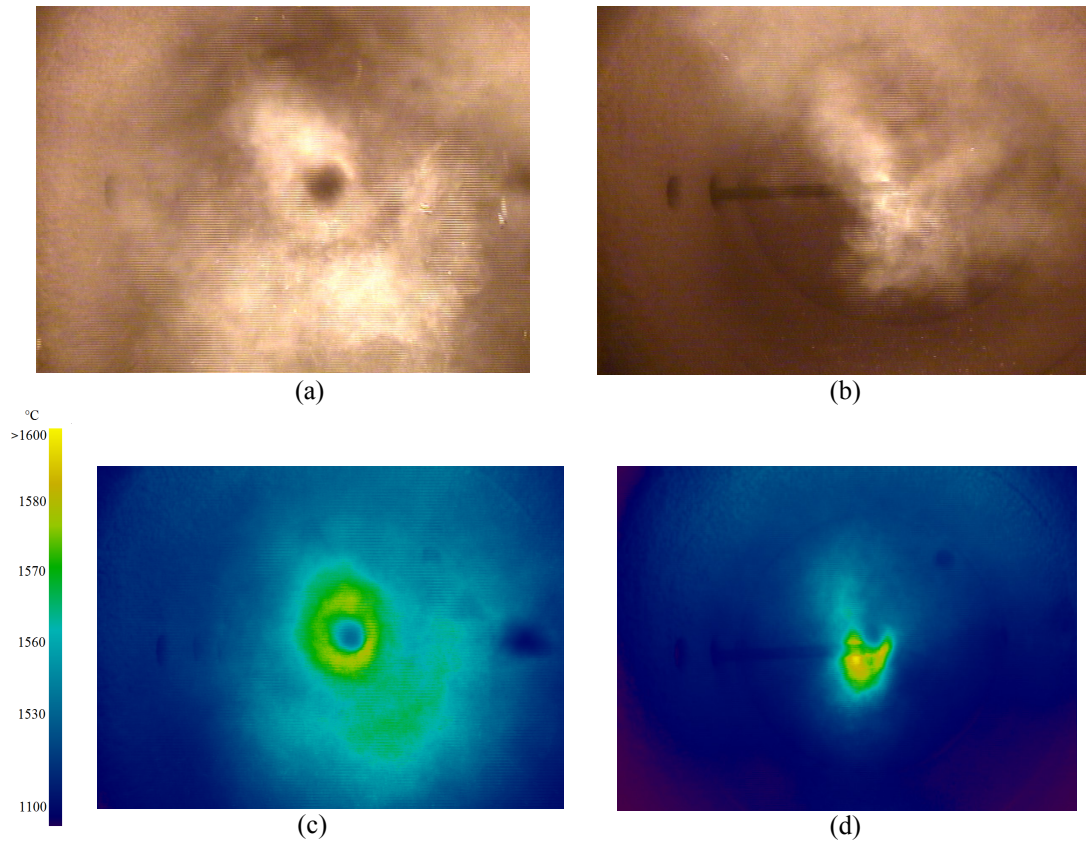


Figure 5.22: Example of change in the flame pattern caused by intrusive sampling.

5.10.1 Local Gas-Phase Temperature

Because of higher temperatures close to the burner (access ports A-C), measurements performed with a suction pyrometer were obtained using a calibrated ANSI type B thermocouple. At the other access ports, a type K thermocouple was applied. The expanded uncertainty of the suction pyrometer with a thermocouple type B for a temperature range of 500-1500 °C varies between ± 13 and ± 38 °C, respectively. In case of a type K thermocouple, an expanded uncertainty of ± 10 and ± 29 °C was calculated for a measuring range of 400-1200 °C, respectively. The spatial distribution of gas temperature obtained for the investigated flames is compared in Figure 5.23.

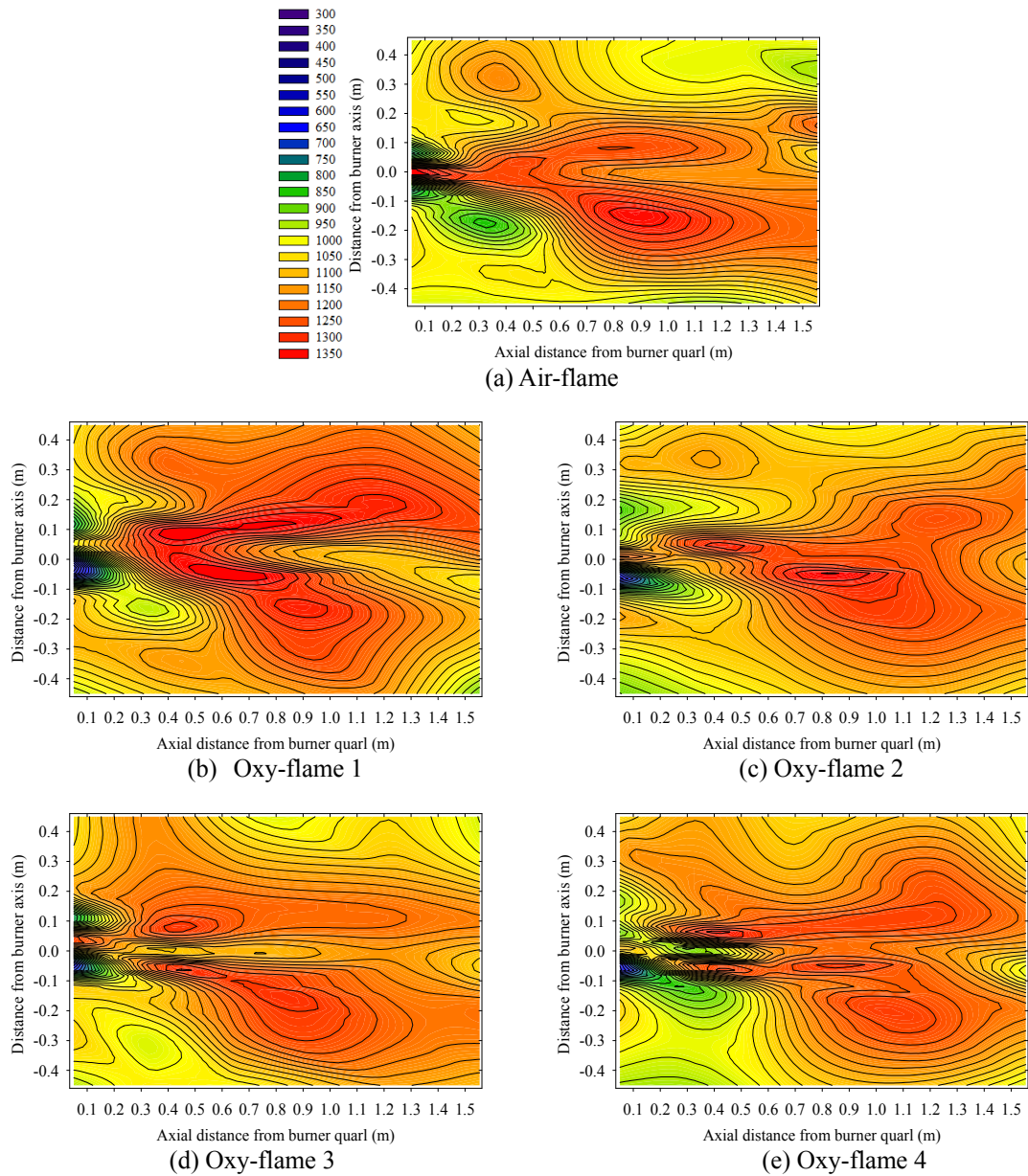


Figure 5.23: Spatial distribution of mean gas-phase temperature ($^{\circ}\text{C}$).

Even though the temperature distribution shows similarities for all investigated cases, the peak gas-phase temperatures are reduced in oxy-firing. Furthermore, the feed gas distribution among the burner registers and swirl number show a considerably influence on the gas peak temperatures. Similar trends were observed in the maximum values monitored continuously by the flame digital imaging system as discussed in Section 5.4. The peak gas temperatures of oxy-flames were found at axial distances from burner exit between 0.355 and 0.660 m; air-fired flame had peak temperatures closer to the burner (0.050 m). This indicates differences in the flame propagation due to changes in feed gas

properties. An increase in the secondary swirl number yielded a size reduction of the region with the highest temperatures found under oxy-firing. Overall, peak gas temperatures acquired by the suction pyrometer were 17-21% lower than those obtained by the flame digital imaging system. Several factors contribute to these differences. For instance, temperature measurements using thermometry are weighted towards higher values because the energy emitted is a function of temperature to the fourth power. In addition, there is the possibility that the peak temperature region cannot be precisely measured by the suction pyrometer because of limited number of access ports. Theoretical evidence and past experimental measurements also indicate that particles can attain temperatures appreciably higher than that of the gas around them [152]. Particles with initial size of 67 μm reached temperatures 370-1070 $^{\circ}\text{C}$ higher than the surrounding gas. The difference became negligible when the particles size fell to 4 μm .

Transversal profiles of mean gas-phase temperature at six measurement ports are given in Figure 5.24. The plots indicate that the temperature peaks coincide with the trajectories of the secondary and tertiary streams. Considerable differences in the temperature distribution among the investigated flames occur very close to the burner front and inside the shear layer. Due to the mixing region between the feed gas streams, the results show a sharp drop followed by a rapid increase of temperature at a transversal distance between -0.100 and 0.100 m from burner axis (Figure 5.24a).

At a distance of 0.050 m (measurement port A), oxy-flames presented lower temperatures. Possible explanations for this difference close to the burner are: excessively slow heating of the coal particles or an excessively slow devolatilization and consequently a slow combustion in the shear layer. Additionally, the average temperature of the secondary and tertiary stream entering the furnace was 150-170 $^{\circ}\text{C}$ as compared to approximately 200 $^{\circ}\text{C}$ for the air-flame. This is primarily a result of the lower heat transfer rate in the preheater due to reduced flue gas volume flow rate. The low temperature of the O_2 injected into the secondary and tertiary stream (15-20 $^{\circ}\text{C}$) also contributed to decrease the feed gas temperature. As discussed in the Chapter 2, the differences in feed gas composition considerably affect the combustion process by altering the flame propagation as well as the heat and mass transfer properties. At 0.050 m from burner exit, the oxy-flame 1 had the lowest temperatures as a result of cool, poor mixing between the coal particles and secondary feed gas stream due to reduced swirl strength. The experiments also showed that these differences can be overcome to some extent by increasing the swirl number. As observed in the temperature contours and profiles, combustion is shown to be more intense in the near burner region for the higher swirl numbers, with the flame spreading radially outwards at distances closer to the burner. Additionally, the distance between the burner and peak temperature location becomes shorter with increasing swirl numbers.

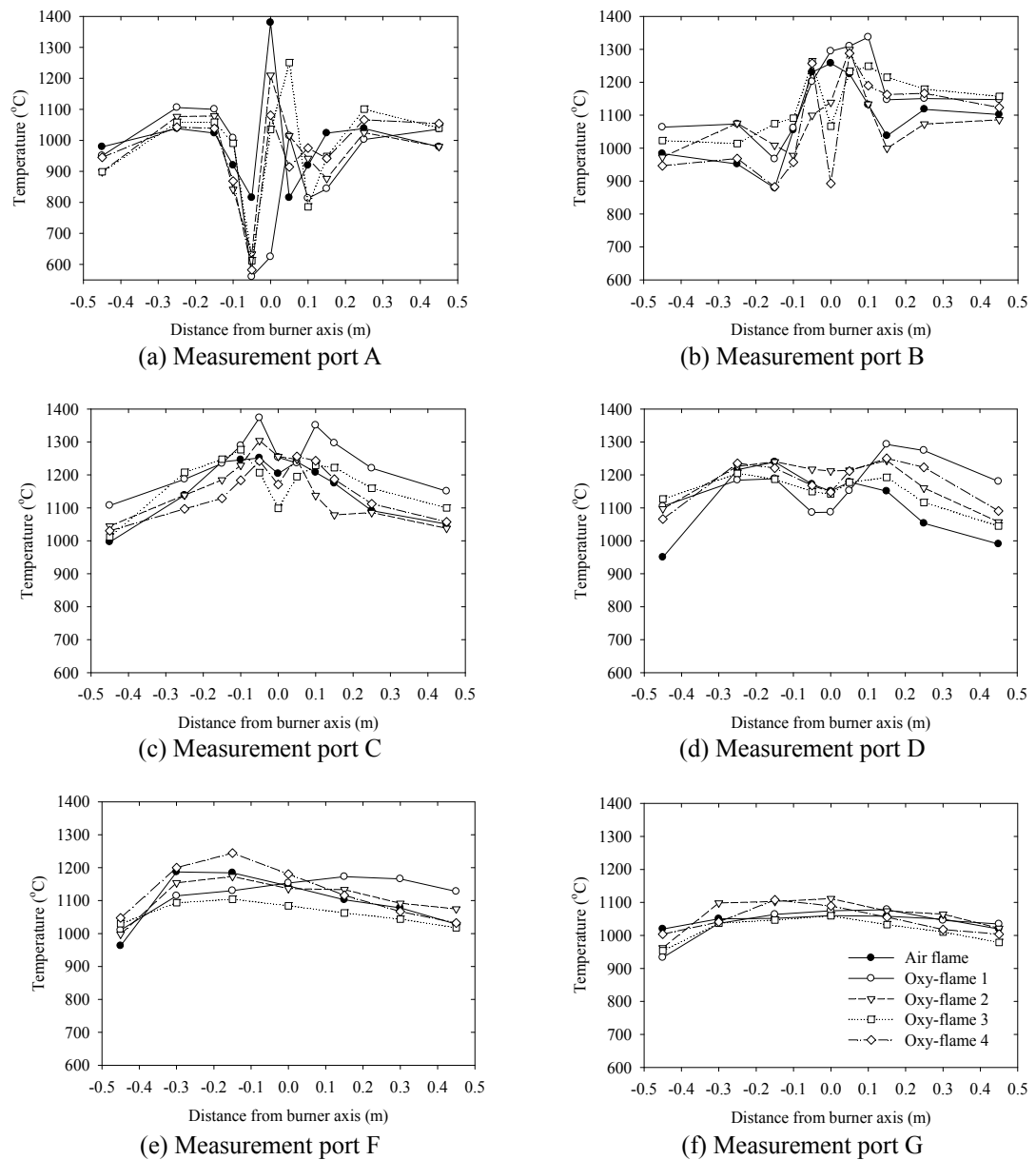


Figure 5.24: Transversal profiles of mean gas-phase temperature.

At the stations near to the burner and far from the axis, the reasonably flat gas temperature profiles are a consequence of the product-rich external recirculation zone. The transversal profiles taken at port C are very similar for all cases. This is because increasing distance downstream, the reaction zone spreads outwards until the fuel jet is consumed and then flattening the profiles. Profiles at access port F indicate that the flame front is slightly shifted to one side of the furnace. This is explained by the transition between the horizontal and vertical furnace sections. The flatness of the gas temperature profiles at access port G suggests that the

flame is being uniformly cooled by radiation losses to the water-cooled walls in the vertical section of the furnace.

From the temperature contours and transversal profiles, depressed temperatures near to the burner axis are clearly noted. The reduced temperature levels in the central core arise not only from the aerodynamic characteristics of penetration flames due to a high axial momentum of the carrier gas, but also due to combustion reaction mechanisms. The sensible heat required to raise the solid particles to their pyrolysis temperature need to be absorbed. Moreover, pyrolysis reactions resulting in devolatilization are endothermic. The release and subsequent diffusion-controlled combustion of volatile products of pyrolysis are manifested in the broadening of the radial temperature profiles near the flame axis. By comparing the decline of the temperature profiles in the radial direction of the furnace at ports B and C, it is seen that by increasing the swirl number, the structure of oxy-flames becomes more stratified and the temperature levels lower close to the axis. This indicates that the expansion of the flame envelope in width by an increase in swirl associated with higher secondary flow rates affects the extent of diffusion-controlled combustion of volatiles and temperature distribution.

Figure 5.25 shows the development of gas-phase temperature along the flame axis. Temperature measurements under air-firing indicate a decrease in on-axis temperature as the distance from the burner exit increases. On the other hand, oxy-fired cases show lower temperatures at port A and a flatter profile between the access ports D and G. Only under air-firing was the peak gas temperature found on the burner axis; this is because of intense mixing between the feed gas and coal particles. As previously discussed, the lower temperature at port A for the oxy-flame 1 is explained by the reduced strength of secondary swirl, which reduces the mixing between the secondary feed gas stream and coal particles. A lower axial temperature at port B for oxy-flame 4 is due to the flame shifting slightly to one side of the furnace. In general, the temperatures along the centerline in the near burner region are much lower in the oxy-fuel cases; this trend is enhanced by an increase in the secondary swirl number. Besides a reduction in the mixing between the feed gas and the coal under oxy-firing (due to a reduced flow rate) the higher amount of CO₂ and water vapor may also affect the char burnout and cool the particles in the oxygen-lean regions through the gasification reactions. Although this still requires further investigation, it is speculated that in the type-1 flame, the gasification reactions by CO₂ and water vapor could be more pronounced than in other flame patterns.

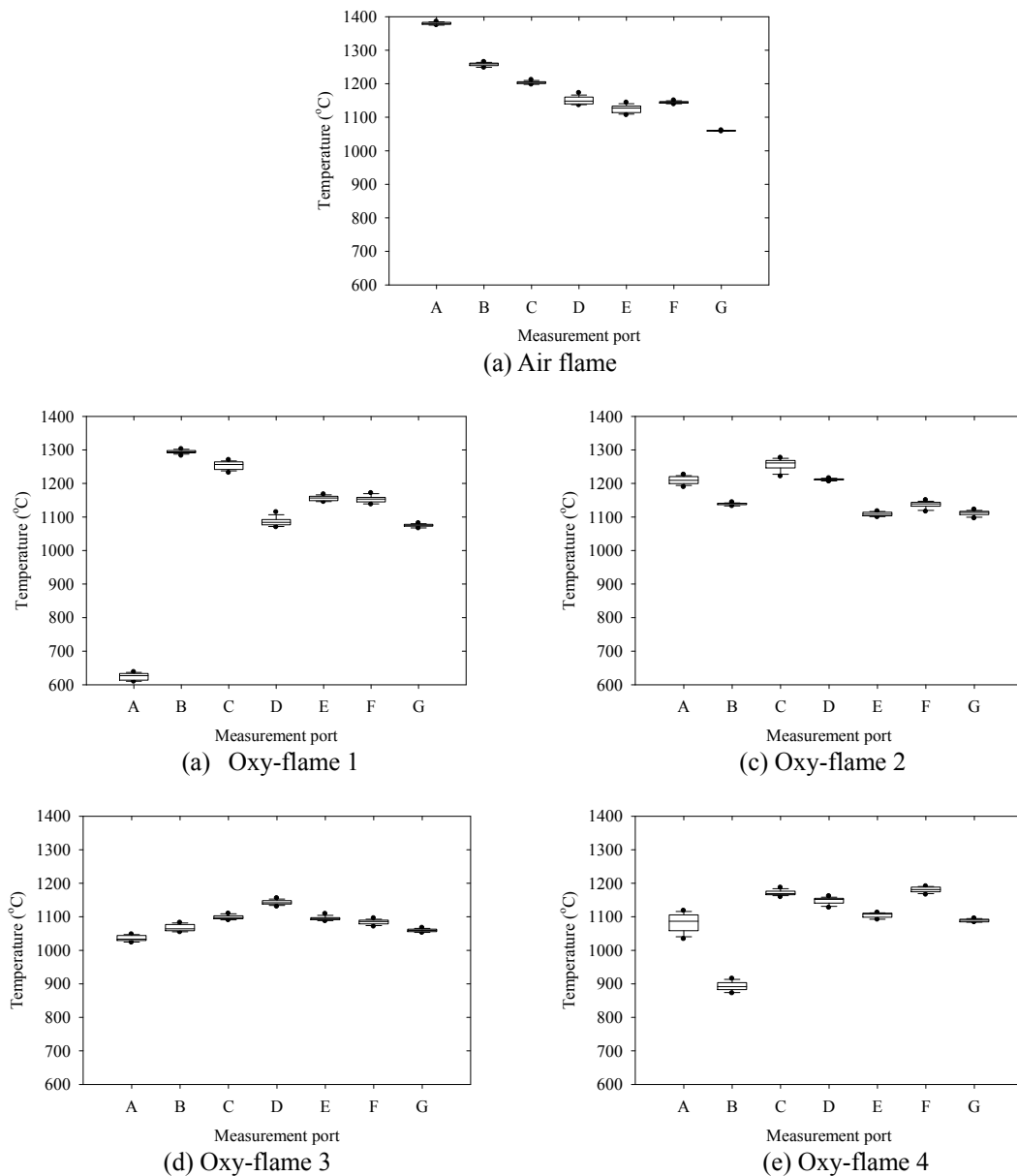


Figure 5.25: Box plots of gas-phase temperature along flame axis.

5.10.2 Local Oxygen and Carbon Dioxide Concentration

The contour maps of O_2 fractions presented in Figure 5.26 illustrate the important aerodynamic features of the stratified flames created by various burner settings. Even though the ignition point inside the burner quarl is not measured or visually monitored, an initial fuel-rich flame core is initiated there by the mixing between the fuel jet and the secondary stream. The O_2 contours reveal that the measured

fuel-rich region in oxy-fuel combustion is somewhat larger than conventional air combustion. This is because the reduced overall flow rate of the feed gas reduces the mixing with the coal. These contours also indicate that the flame is broadened and slightly shortened by increasing the secondary swirl number. Because of the lower tangential momentum, the oxy-flame for the lowest swirl number (oxy-flame 1) is much more symmetric compared to other cases. Despite some discrepancies in the data (mainly in the transition region of the furnace), all flames have acceptable symmetry.

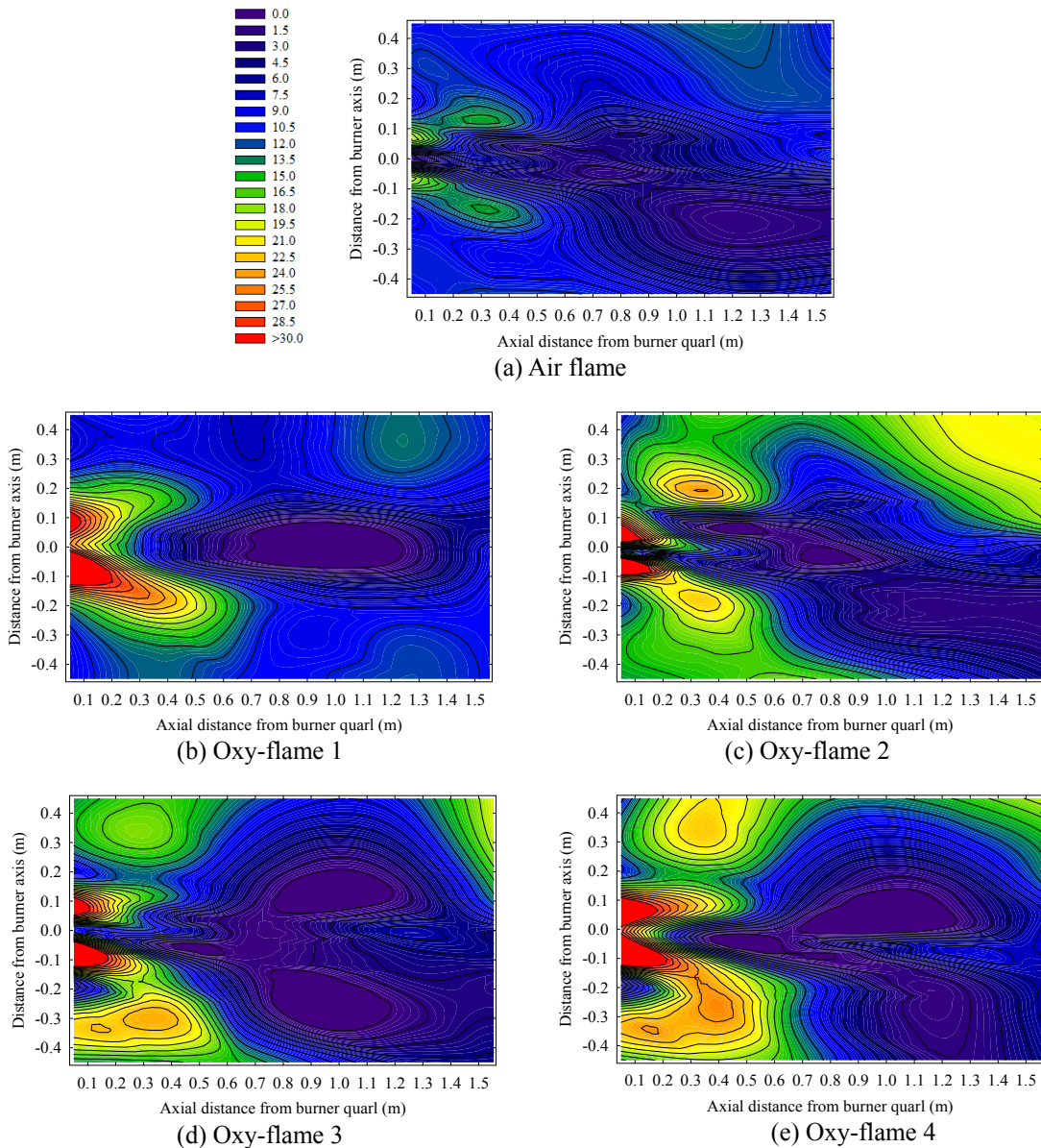


Figure 5.26: Spatial distribution of mean O_2 concentration (vol%, dry basis).

Figures 5.27 and 5.28 illustrate the transversal distribution of O₂ and CO₂ for the flames at six locations in the furnace. The uncertainty of O₂ and CO₂ measurements are independent of measuring range. In case of a standard deviation of the mean of 0.00-0.30 vol% (dry), the calculated expanded uncertainty for O₂ and CO₂ is ± 0.58 -0.84 vol% (dry) and ± 1.75 -1.85 vol% (dry), respectively. At access port A, the O₂ concentration peaks while CO₂ concentration sharply decreases at a distance of 0.100 and -0.100 m from flame axis; this is due to the tertiary jet, introduced through the radially displaced annulus surrounding the quarl. At the same access port, the profiles indicate that the combustion is in its initial stages, with the main reaction zone located near the axis as indicated by an O₂ decrease. Mixing in this zone is due to the strong shear between the central jet and the secondary stream. As the coal jet penetrates the IRZ, the O₂ concentration near to the flame axis drops. At 0.355 m from burner exit (measurement port B), the centerline O₂ concentration is in most cases higher than at 0.050 and -0.050 m. This clearly indicates that the coal particle combustion is initiated slightly off the axis in a relatively fuel-rich region between the outer periphery of the central jet and the inner boundary of the IRZ.

Away from axis, O₂ and CO₂ concentrations are much more uniform due to the presence of external non-reacting recirculation zones. Measurements taken at ports A and B show that at 0.450 m from the burner axis, the O₂ concentration appears to be slightly lower than opposite side (at -0.450 m). This is explained by the influence of the intrusive gas sampling, which results in a partial flow blockage, thereby radially spreading the particles. This also explains the slightly higher temperatures in this region. The gas temperature profiles are flatter than those of the O₂ concentration due to the smoothing effect of thermal radiation [153]. However, the temperature profiles are very consistent with those of concentrations discussed in this section.

Even though both the O₂ and CO₂ profiles display similar trends for all investigated cases, the profiles of oxy-flames can be considered more diffusive than that of the baseline air-fired case. This is immediately noticeable because the initiation of reaction zone, as typified by the minimum O₂ concentration, has shifted from 0.050 m in case of air-firing to 0.660 m for oxy-firing. This is clearly observed by comparing the O₂ concentration values on flame axis (Figure 5.29). Moreover, transversal profiles shown in Figure 5.28 indicate that the evolution of CO₂ is much more gradual. Under air-firing, the CO₂ profile at 0.660 m (access port C) is already flattened, whereas in the case of oxy-flames, the profiles become flat only at 1.274 m (access port D) from burner exit. This may be explained by the content of water vapor and CO₂, which are sufficiently high to reduce the thermal diffusivity of the homogenous mixture and consequently the O₂ consumption rate. Figures 5.27 and 5.28 also show the concentration profiles still farther downstream of the burner and; as expected, the O₂ and CO₂ profiles became progressively unchanged as the flame moves upwards in the vertical

section of the furnace. The relatively uniform O_2 concentration at the center of the furnace taken at inspection ports F and G (Figure 5.29) also confirm that the combustion is almost complete.

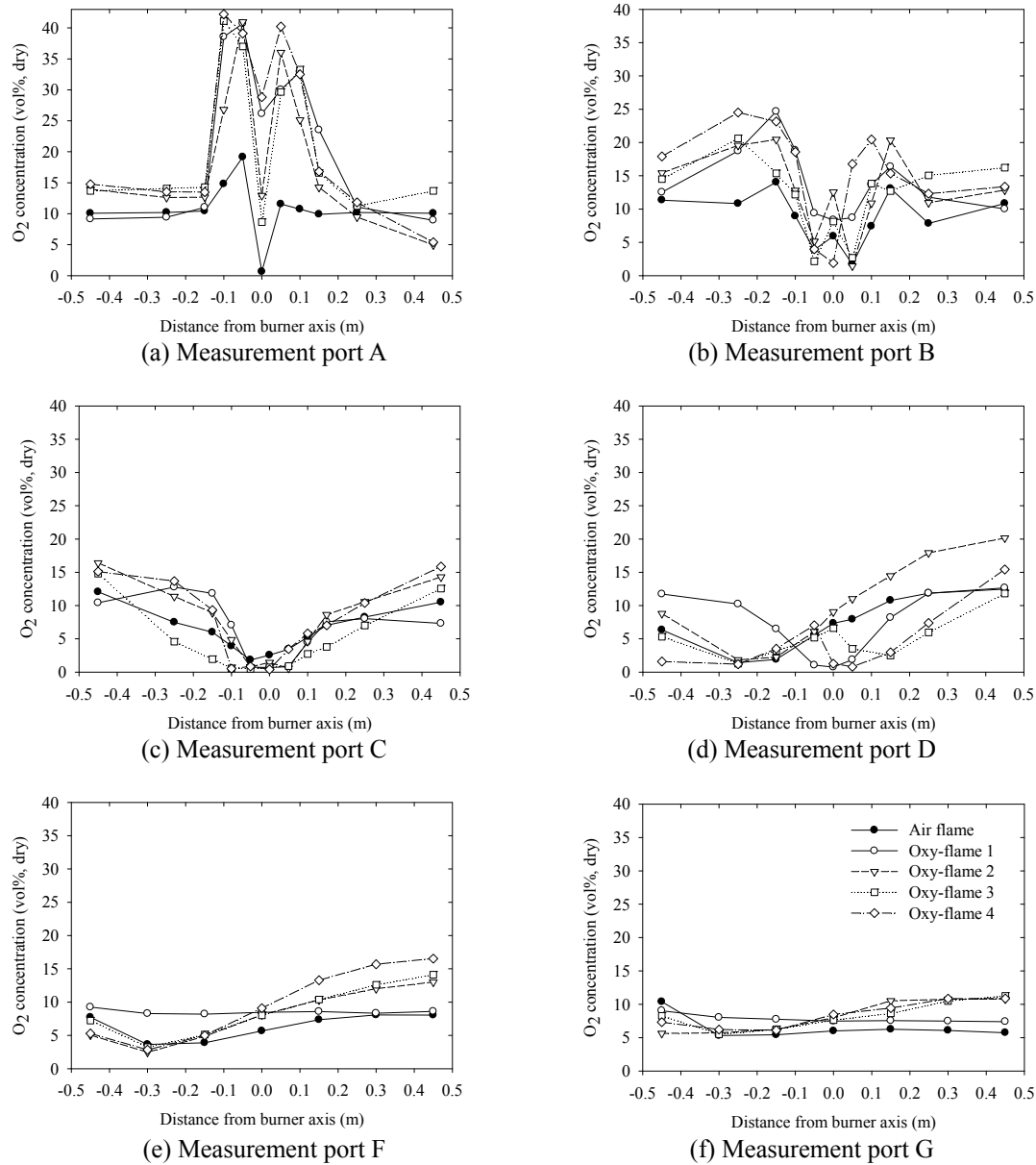


Figure 5.27: Transversal profiles of mean O_2 concentration.

The results show a conspicuous difference among the structures of oxy-fuel flames for the investigated swirl numbers. A much more intense fuel-rich region is obtained when the swirl strength of the secondary flow is increased. As discussed in the results obtained by the isothermal CFD predictions of the flow pattern, an increase in the swirl strength imparted to the secondary stream radially expands

the flow, thereby increases the O_2 concentration at radial distances closer to the furnace walls. A detailed comparison of the O_2 concentration values close to the axis measured at access port A indicates an enhanced combustion rate for the high swirl flame as a consequence of the intensified mixing between the feed gas and the coal particles. This also explains the results obtained when the mass flow ratio of secondary to tertiary stream was increased from 1.25 (oxy-flame 4) to 2.00 (oxy-flame 3).

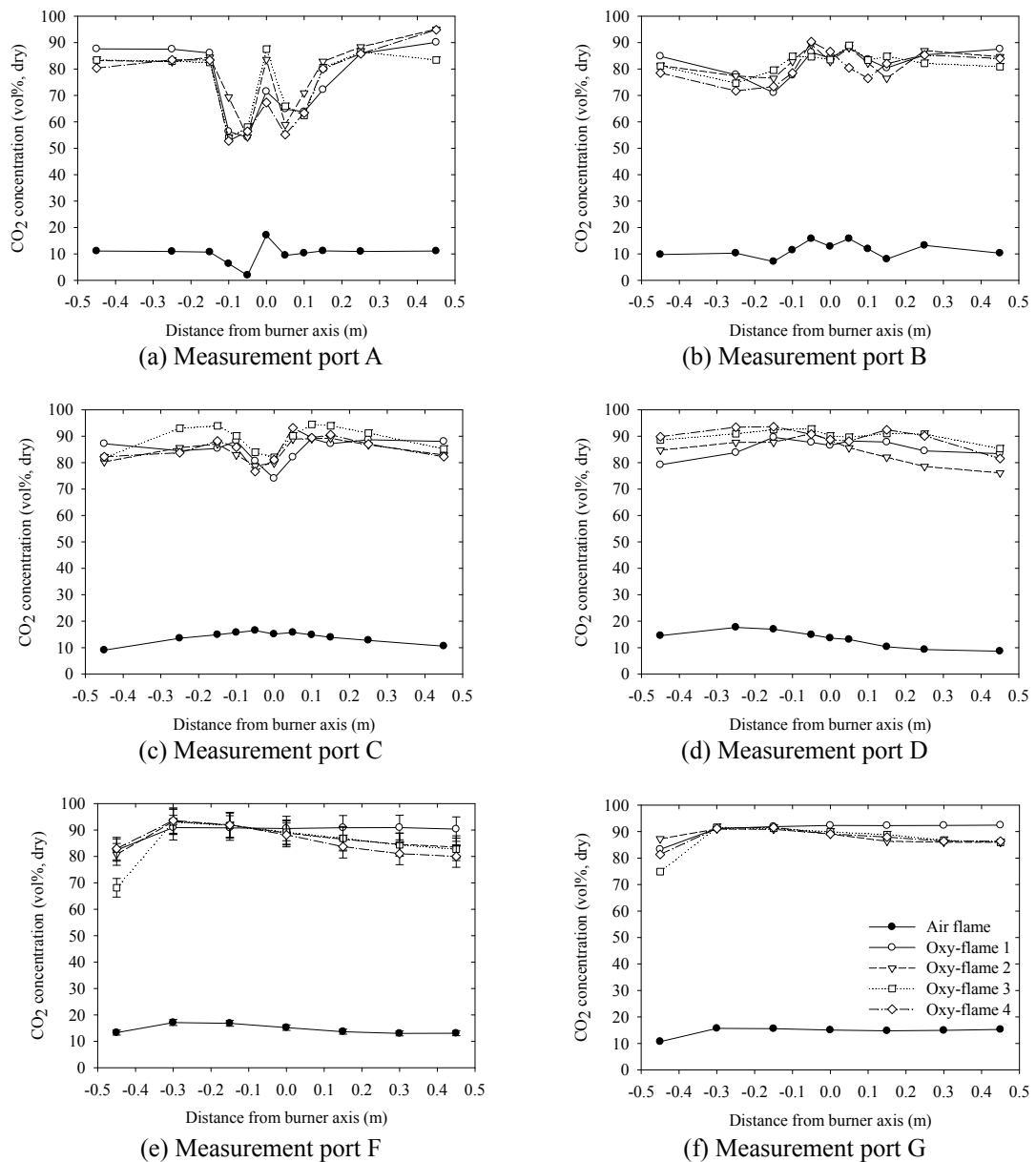


Figure 5.28: Transversal profiles of mean CO_2 concentration.

The stability of the investigated flames can be qualitatively evaluated by the small variations in O_2 concentrations near the burner as indicated by the box plots in Figure 5.29. The variation of the O_2 concentrations at the measurements ports near the burner is much lower in comparison to the measurement ports farther downstream. Higher deviations at these downstream ports are due to temporal fluctuations in the flow direction in the transition region of the furnace. More significant fluctuations observed during the measurements of oxy-flame 1 are due to poor mixing between the fuel jet and feed gas, which led to small flame instabilities in the central core.

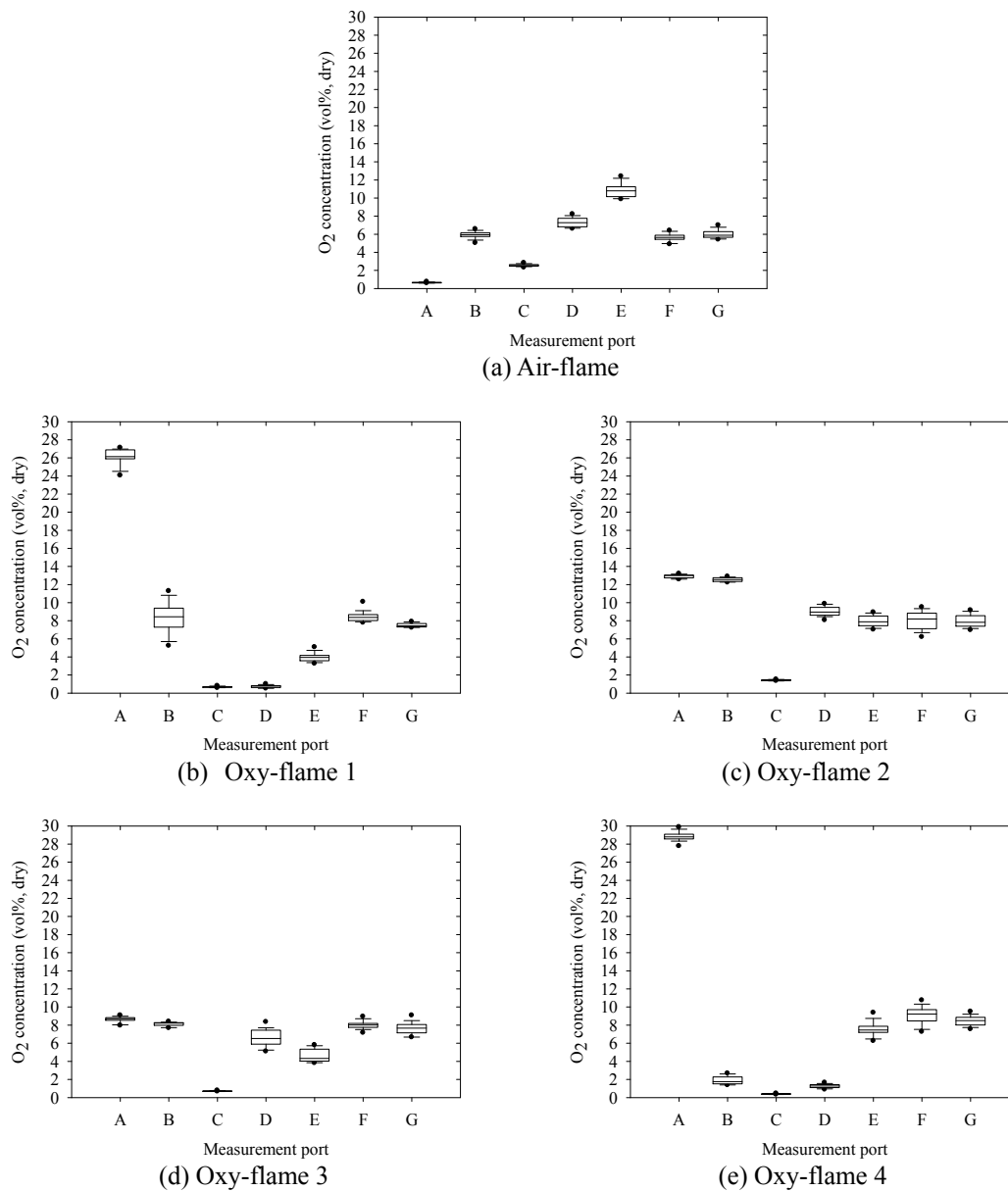


Figure 5.29: Box plots of O_2 concentration along flame axis.

5.10.3 Local Carbon Monoxide and Methane Concentration

Detailed measurements for CO and unburned hydrocarbons, expressed in terms of CH₄, were performed in order to see the evolution of volatile matter and the size of the reaction zone. CO is produced through the burning of volatiles near the burner and through char partial oxidation; CH₄ is the dominant constituent among the unburned hydrocarbons [154]. In addition, the CH₄ concentration is also important as an indicator of the presence of other hydrocarbon fragments such as CH, CH₂, and CH₃, which play an important role in the NO reburn mechanism. The uncertainty of measurement of CO and CH₄ is independent of measuring range. The expanded uncertainty of CO varies between ± 0.35 and ± 0.53 vol% (dry) for a standard deviation of the mean between 0.00 and 0.20 vol% (dry), respectively. In case of CH₄, the expanded uncertainty varies between ± 123.95 and ± 153.18 mg/m³ (dry) for a standard deviation of the mean between 0.00 and 45.00 mg/m³ (dry).

From the CO concentration distribution illustrated in Figure 5.30, the shear mixing layer for all flames can be identified by the peaks in CO concentrations confined to the near axis region. Corresponding temperature and O₂ profiles also confirm the oxidation of the coal particles in the region indicated by higher concentration of CO and reveal the presence of a zone of intense combustion. Similarly to previous studies [27,67], the CO concentrations under oxy-fired conditions are higher than the baseline air-fired case. As discussed in Chapter 2, higher CO concentrations may be due to CO₂ dissociation at high temperatures. In addition, as evidenced by the lower temperatures and lower O₂ concentration on the flame axis, it is suggested that the gasification reactions also contribute to enhancing the volumetric fraction of CO. Again, these reactions are believed to be enhanced by this flame pattern (type 1), where a larger region of the flame operating under fuel-rich region is created.

Transversal profiles of the CO and CH₄ concentrations are presented in Figures 5.31 and 5.32. By comparing the profiles of CH₄ with those of CO it is seen that the concentration behavior is broadly similar. The presence of CO and CH₄ near the flame axis (at an axial distance of 0.050 m) indicates that the pyrolysis is initiated upstream (within the burner quartz) along with intense combustion within the primary coal jet itself. This fact is consistent with the values of O₂ observed in this region. CO and CH₄ concentrations at measurement ports A-C were not detected away from the axis due to the presence of the non-reacting and product rich external recirculation zone.

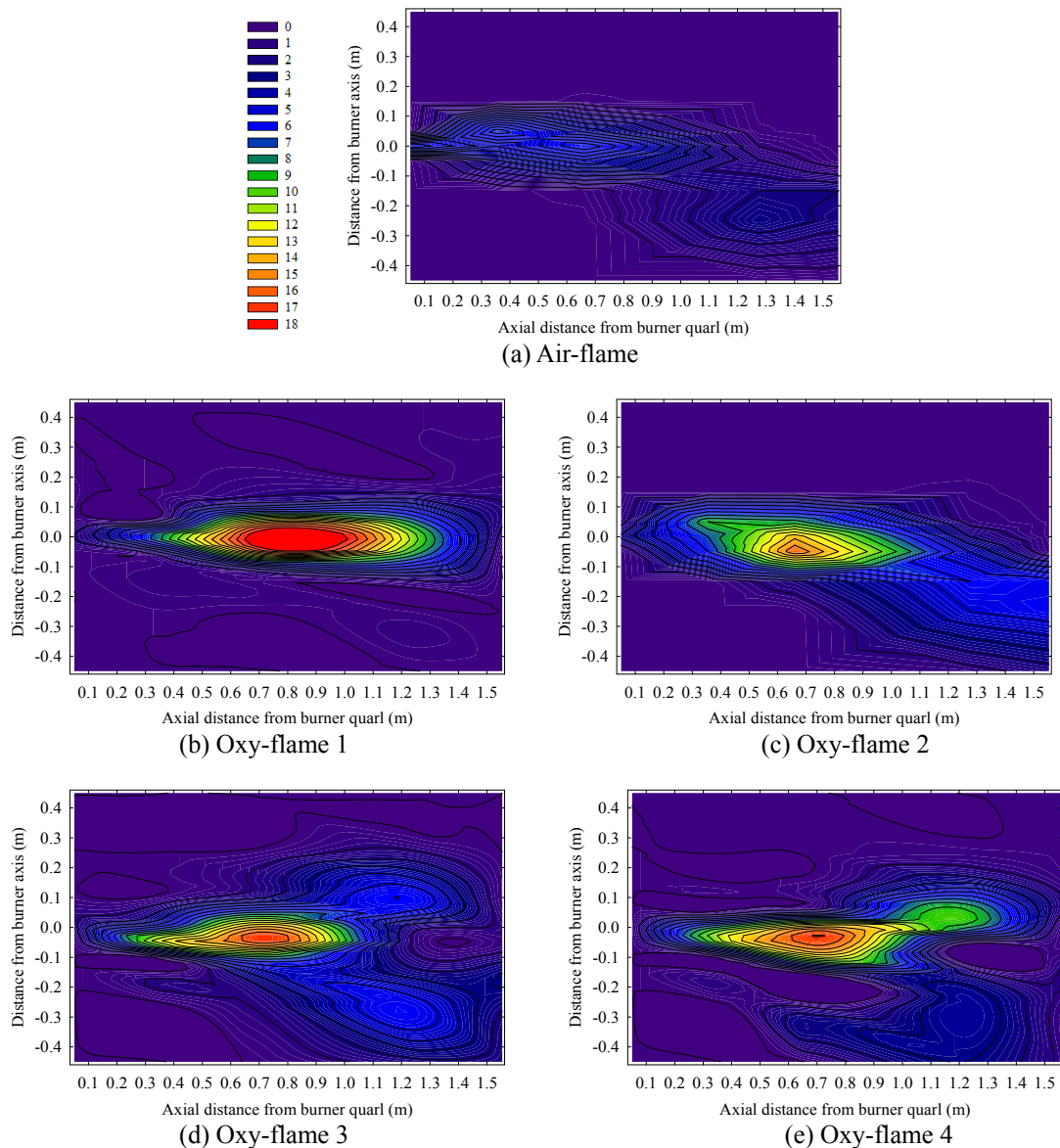


Figure 5.30: Spatial distribution of mean CO concentration (vol%, dry basis).

The initial production of CO under air-firing is considerably higher in comparison to the oxy-flames at 0.050 m from burner exit. An interesting comparison to assess this behavior can be done by means of analysis of the stoichiometric ratio at the burner registers. The stoichiometric ratio of the primary stream is approximately the same (0.13 in the case of the air-fired baseline and 0.10 in the oxy-flames), while the stoichiometric ratio of the secondary stream is increased from 0.55 (air-firing) case to 0.71 (oxy-firing). These results reinforce the conclusions obtained from small-scale combustion reactors, which show that the higher concentrations of CO_2 reduce the burning rates [25,48,49] and that the oxy-flames are more diffusive.

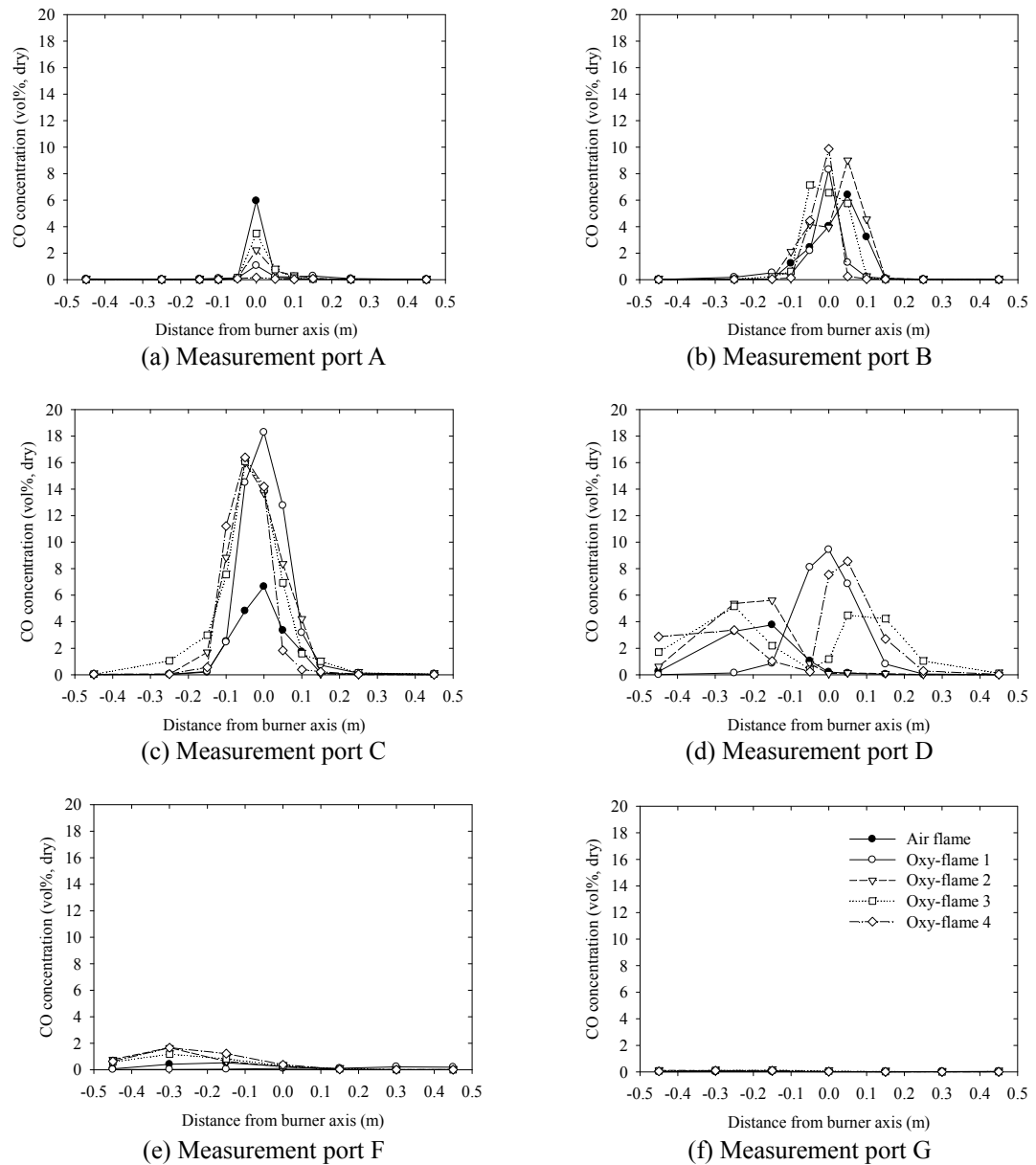


Figure 5.31: Transversal profiles of mean CO concentration.

CO measurements also confirm that a decrease in the swirl number suppresses the mixing of feed gas and fuel under oxy-fired conditions. Profiles taken at 0.050 m (measurement port A) indicate that for lower swirl intensity, combustion proceeds more slowly because of the poor mixing between the secondary feed gas and fuel jet. This also partly accounts for the lower temperatures in the vicinity of the burner. These trends are also seen in the on-axis profiles of CO and CH_4 using box plots (Figures 5.33 and 5.34). The axial distance where CO and CH_4 concentrations became significant for all investigated flames is located farther downstream at 0.660 m (measurement port C) due to the rapid heating in this

zone. However, from the transversal profiles, the zones with high CO concentrations appear slightly more intense and narrower for lower swirl numbers owing to the reduced expansion of the secondary and tertiary jets.

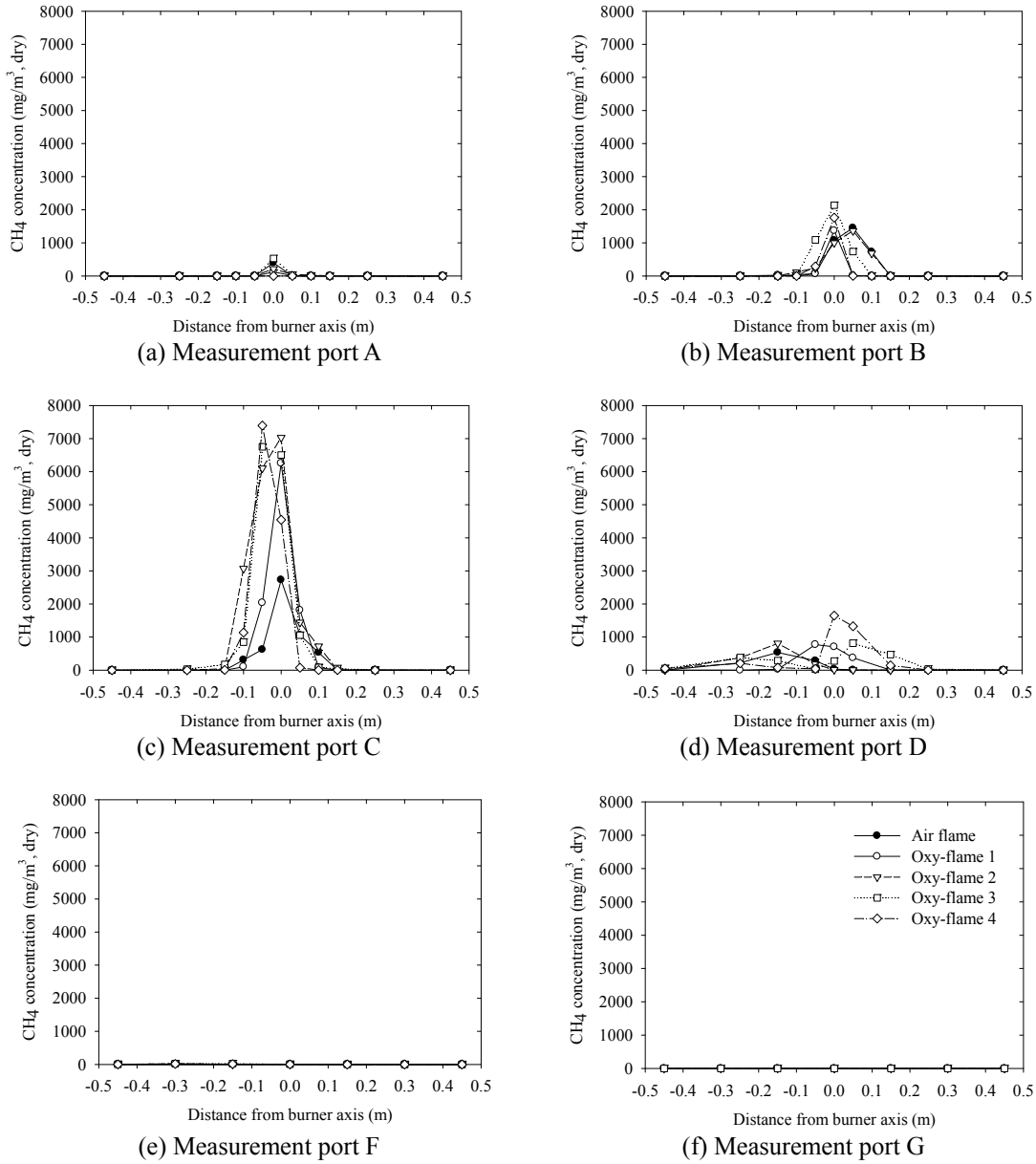


Figure 5.32: Transversal profiles of mean CH₄ concentration.

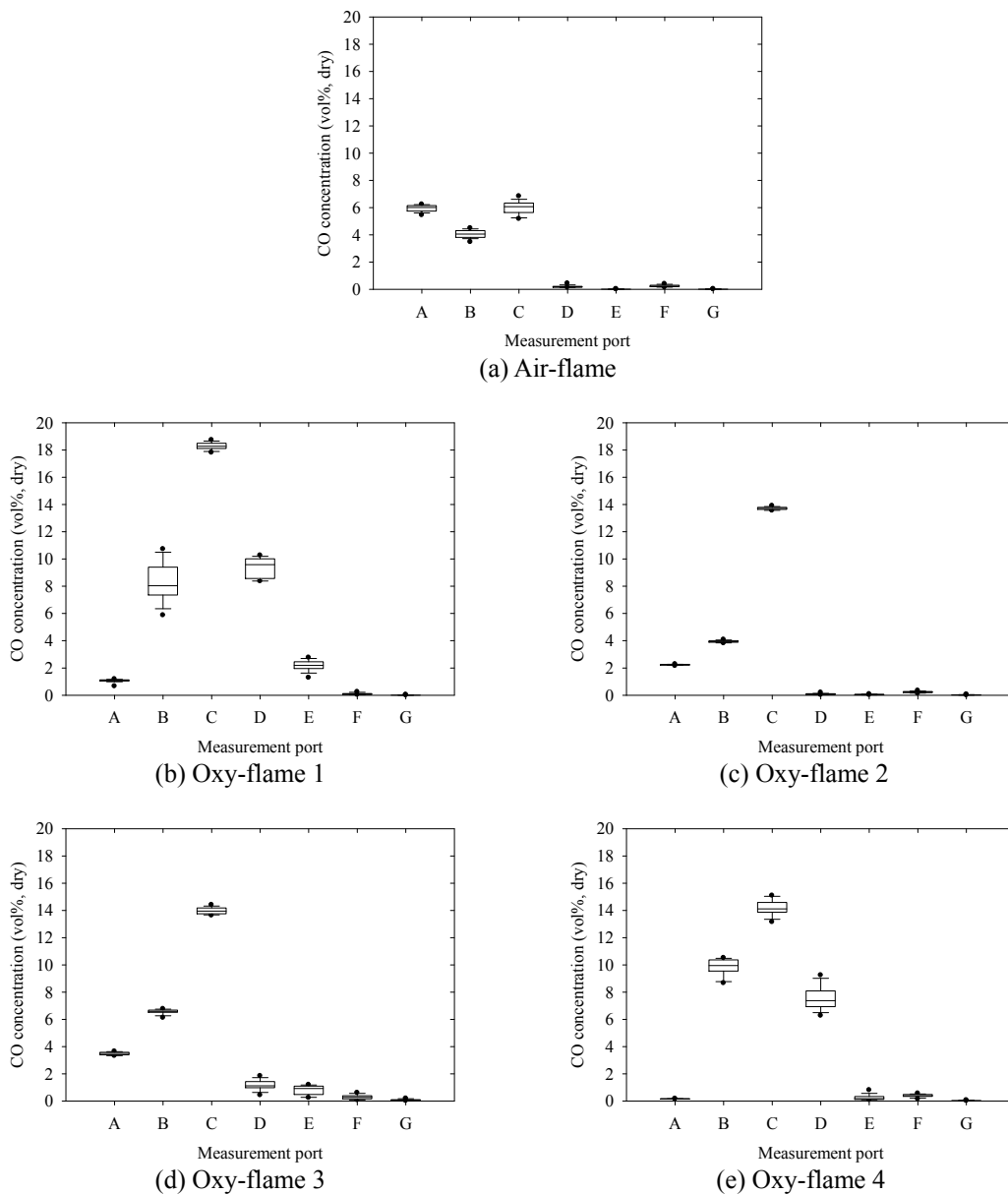


Figure 5.33: Box plots of CO concentration along the flame axis.

The CO and CH₄ concentrations at access port D (1.273 m) for oxy-flames 1 and 4 reveal that CO concentration slowly decreased for reduced swirl numbers and reduced secondary/tertiary flow ratio as a result of a longer reaction zone. At the measurement port F, CH₄ was not detected, indicating that the release of volatile matter is completed by this point. Nevertheless, the presence of CO at measurement port F reveals the continuation of heterogeneous reactions until the access port G, where the reactions appear to reach the final stages. The variation between the 95th and 5th percentiles of CO and CH₄ measurements at the stations closest to the burner may qualitatively indicate the degree of flame stability. From

the plots, a conspicuous variation in the values for the oxy-flame 1 and 4 suggests that a reduction in the swirl strength and secondary flow rate reduces marginally the stability of the combustion process due to a slow devolatilization and O₂ consumption rate.

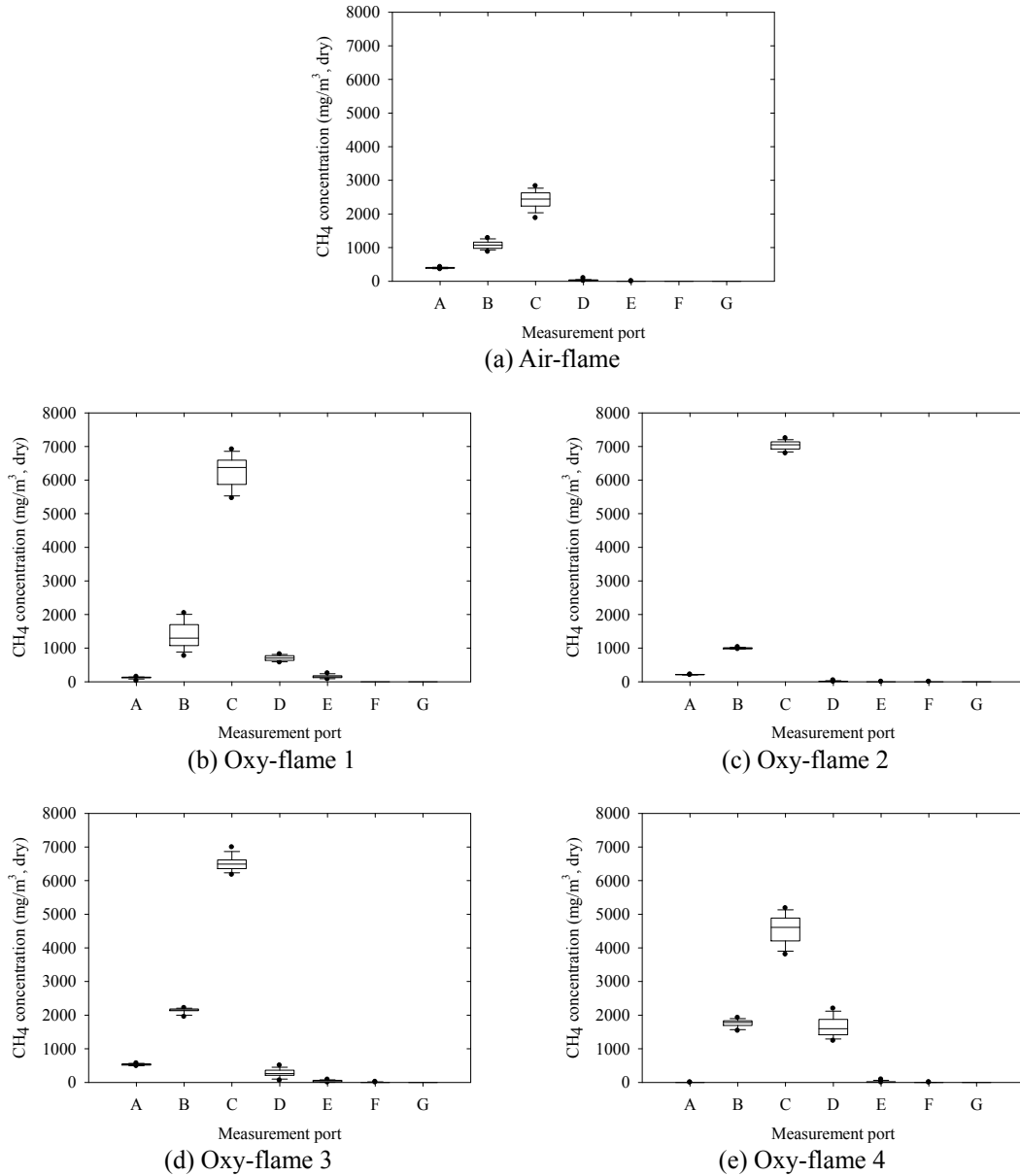


Figure 5.34: Box plots of CH₄ concentration along the flame axis.

5.10.4 Local Nitric Oxide Concentration

NO concentrations for the investigated flames are compared in Figure 5.35. As already mentioned, the intrusive measurements with water-cooled probes affect the flow pattern and consequently the pollutant formation and destruction. The contours of NO concentration display high values at transversal distances between the flame axis and 0.450 m; much more noticeable differences are observed mainly in the oxy-flame 3, where NO emissions increased from approximately 400 to 550 mg/m³ (dry). This increase is accounted not only by the presence of the water-cooled probe, but mostly by the flue gas recirculation in the oxy-fuel operating mode, which in turn contributes to increase the NO concentration. The uncertainty of NO concentration is independent of the measuring range and varies between ± 30.54 and ± 33.60 mg/m³ (dry) for a standard deviations of the mean of 0.00 and 7.00 mg/m³ (dry), respectively.

Transversal and axial profiles are compared in Figures 5.36 and 5.37. In practical conditions of pulverized flames, most NO is contributed by the volatiles through conversion of nitrogen species [155]. From the previous section, the devolatilization characteristics were shown to be affected by the burner settings. In general, measurements of CO and CH₄ indicated that the volatiles are predominantly evolved farther downstream of the burner exit in a fuel-rich region. Since the organically bound nitrogen is more refractory than other volatile elements [80-84] (with exception of sulfur), it is reasonable to speculate that the early released nitrogen-free volatiles consume the O₂ prior to significant nitrogen specie evolution [156].

The parametric study indicated that NO is suppressed at both high swirl numbers and high secondary/tertiary flow ratios. From the qualitative knowledge of the computed flow pattern and experimental species concentration data, the recirculation zone in front of the burner is expanded particularly in width under such conditions. This creates a radial flame stratification through an effective spatial separation of the fuel-rich core from the lean outer regions of the flame. In the air-flame, the formation of NO occurs very close to the burner. In this region, the devolatilized species, including the fuel-bound nitrogen, are oxidized mainly on the IRZ boundary, in a region of high O₂ concentration in the shear layer. The maximum flame temperatures are also located in this area, and thus, NO generation through the thermal route may also become significant. As expected, the peaks of NO concentration are lowest under air-firing owing to the higher flow rates of feed gas and absence of flue gas recirculation. A trend observed in oxy-flames is that the NO formation is apparent at higher distances from burner exit than air-firing. NO is formed in the regions of high O₂ availability; these regions are the predominant path of the secondary and tertiary streams and are consistent with O₂ profiles. A first region of NO formation is located at 0.355 m (measurement port B) close to the burner axis and a second region, at 0.660 m

(measurement port C) from the burner exit, but at transversal distances off from the axis. Only in case of oxy-flame 1, oxidation of fuel-N does not start at the station nearest the burner exit. These results are consistent with the O_2 and temperature plots (Figures 5.24 and 5.27).

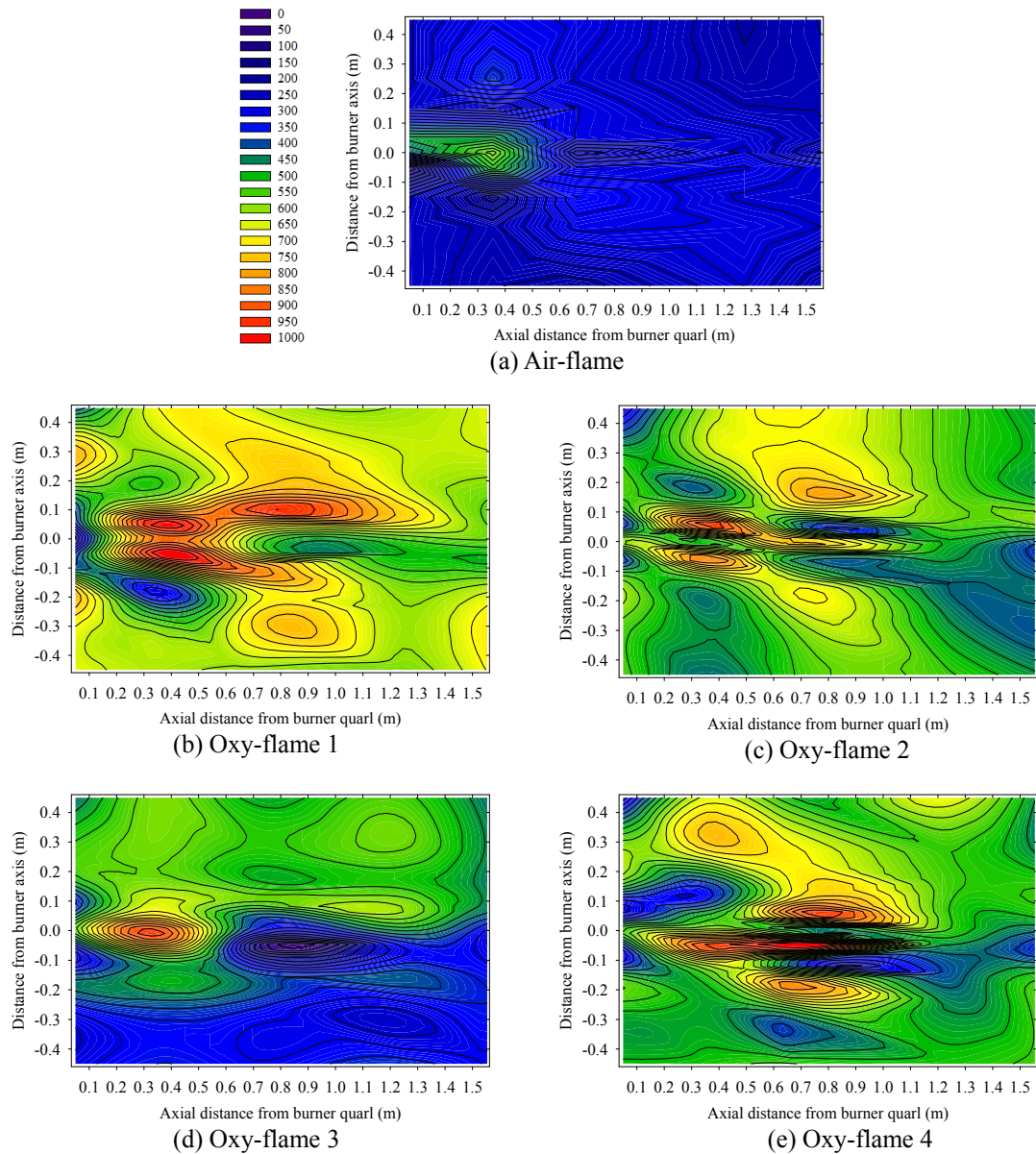


Figure 5.35: Spatial distribution of mean NO concentration (mg/m³, dry basis).

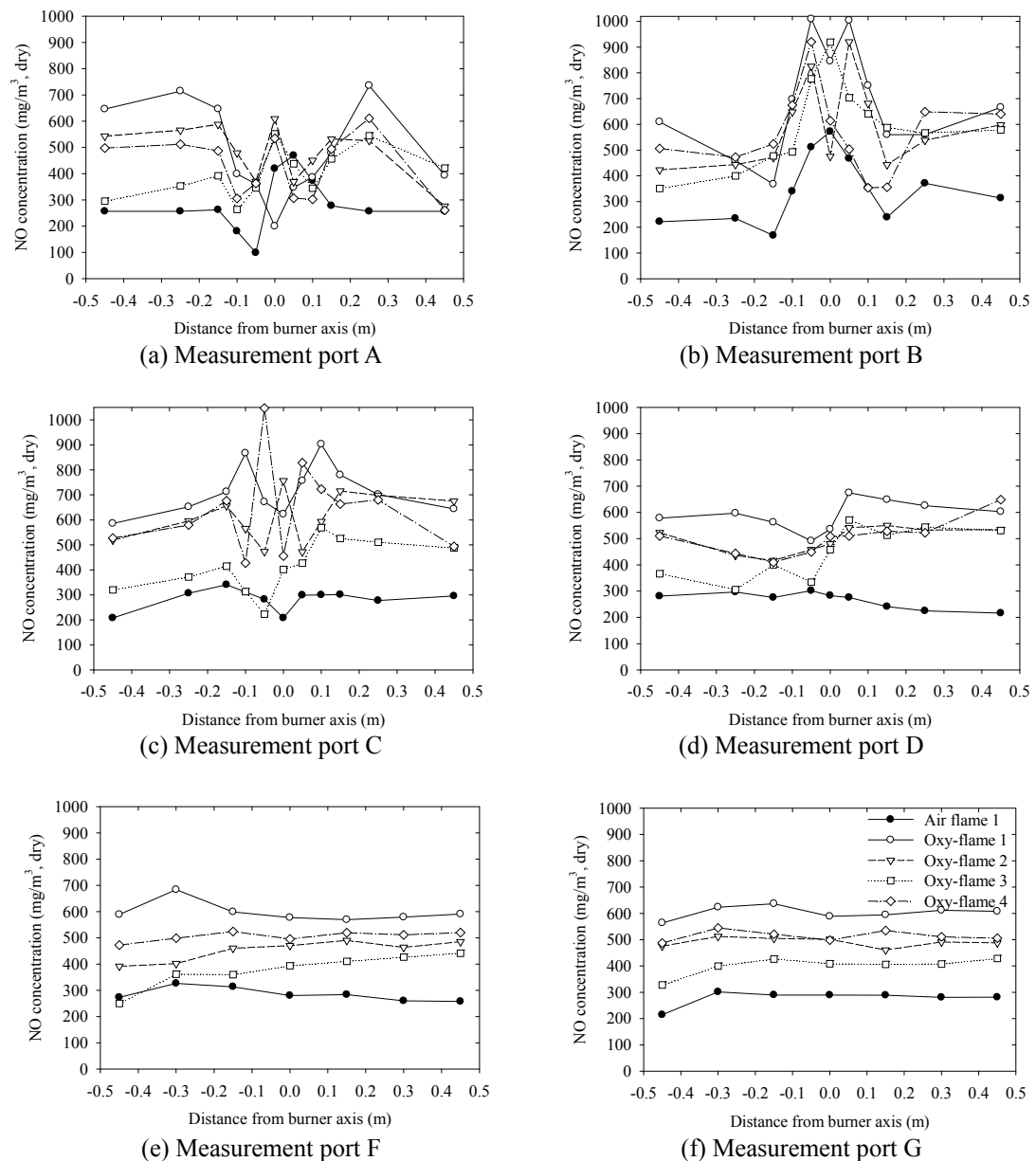


Figure 5.36: Transversal profiles of mean NO concentration.

For the lower swirl numbers, the NO formation region increased drastically in length, given the reduced O₂ admixing to the central fuel jet. In this case, the contact with available O₂ occurs in the region where the nitrogen species are evolved, which in turn allows significant fuel-NO formation. This also explains the NO peak at an axial distance of 0.660 m (access port C) where the secondary/tertiary flow ratio is reduced to 1.25 in the case of oxy-flame 4. Conversely, the lower availability of O₂ in front of the burner, created by an increase in the secondary/tertiary flow ratio and swirl number, inhibits the

formation of NO. In the case of oxy-flame 3, there is a conspicuous lack of available O_2 where the volatiles are evolved whereby fuel-N is pyrolyzed to form mostly N_2 . The large size of the fuel-rich region in the case of oxy-flame 3 also explains the lower NO concentrations at almost all points in the flame.

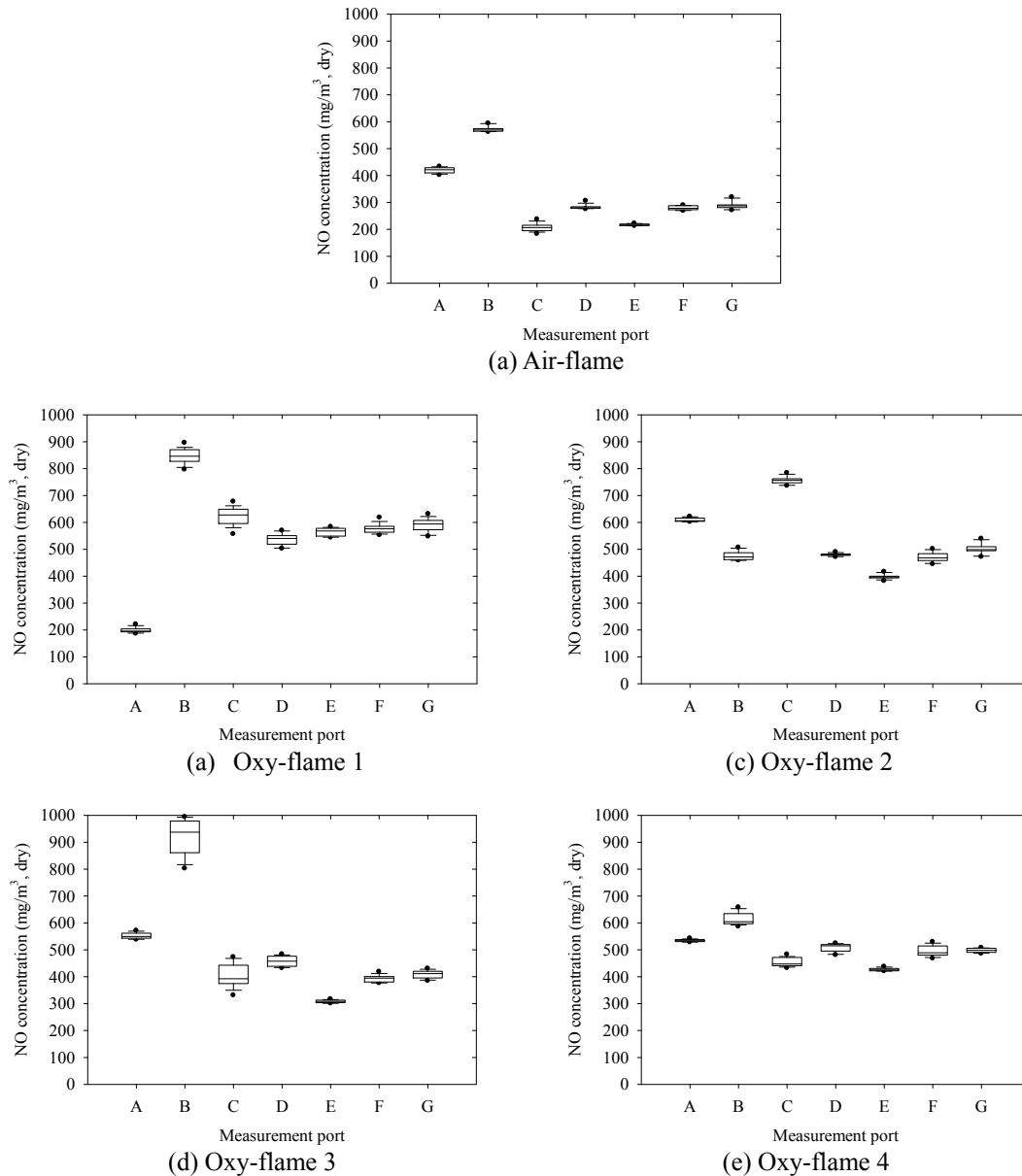


Figure 5.37: Box plots of NO concentration along the flame axis.

Transversal profiles indicate that the NO concentrations are suppressed close to the centerline at axial distances where the measurement ports C and F are located. Box plots of the axial NO concentrations show a general tendency for the NO concentration to decrease along the flame length. This is expected, since the conditions for NO reduction are met: high temperature and fuel-rich environment.

At high temperatures, the conversion of volatile-N proceeds towards N_2 faster than towards NO. Furthermore, high temperatures within fuel-rich zones increase the rate of NO destruction [15]. As discussed in Chapter 2, research has shown that reburning and reduction of the recycled NO with flue gas recirculation are important in reducing the previously formed NO under oxy-fired conditions. Rather than attempting to identify which of several mechanisms plays the most important role in reducing the previously formed NO, the present study seeks to determine those burner settings which best suppress and reduce NO emissions. Previous studies indicate that the reduction of NO by the reverse Zeldovich mechanism becomes important at temperatures over 1500 °C [15,92,93]. Because of the reduced gas-phase temperatures observed during the experiments (lower than 1400 °C), the contribution of this mechanism to the destruction of NO is considered negligible. Due to the type-1 flame pattern, all the investigated flames presented O_2 -deficient zones near the axis, which present high concentrations of CO and CH_4 . High concentrations of CO may act as an important catalyst for the reduction of NO (Equation 2.13). CH_4 is an important indicator of the presence of hydrocarbon fragments, which play a major role in the NO reburn mechanism (Equations 2.20-2.22). Furthermore, reduction of NO emissions could be achieved through homogeneous and heterogeneous reactions in the fuel-rich and coal dust core through Equations 2.14-2.19.

Farther downstream, the flattened profiles at measurement ports F and G indicate that the formation and reduction mechanisms achieved completion as observed previously by the low concentrations of O_2 , CO, and CH_4 . The NO concentration at both access ports are consistent with that measured at the furnace exit during the parametric study.

5.10.5 Total Radiative Heat Flux

In this section, the results using the ellipsoidal radiometer to measure the total radiative flux incoming from the flame at various distances from the burner are presented. This information is important in determining the distribution and magnitude of radiative heat transfer near the boundary of the combustion chamber as a function of burner settings. As discussed previously, during the parametric study, no significant differences were observed in the total hemispheric radiative heat flux monitored at access port C. At this distance from burner exit (0.660 m), the temperature profiles were very similar for all cases and explain this behavior.

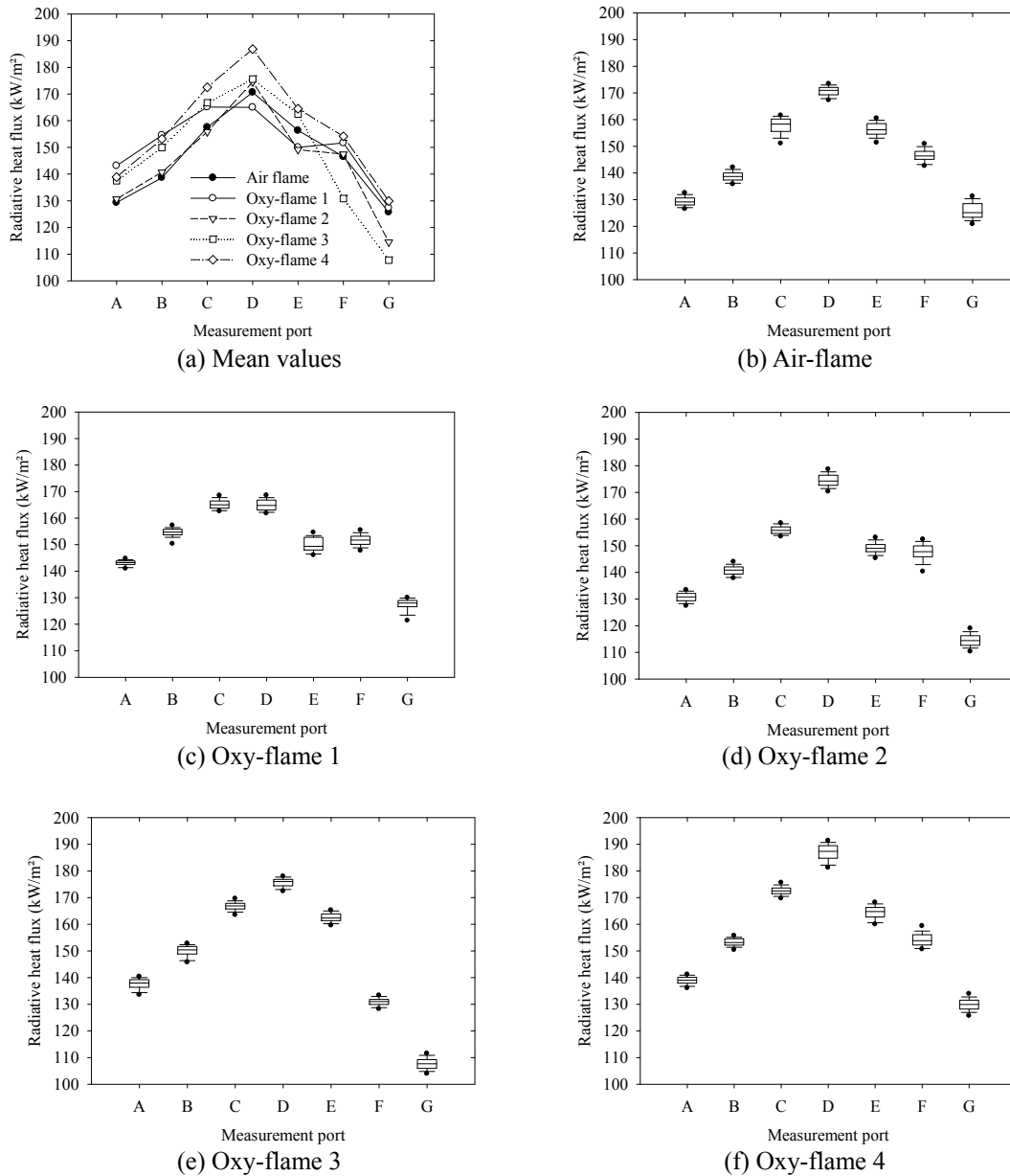


Figure 5.38: Profiles of incident wall radiative heat flux.

Profiles using mean values and box plots are presented in Figure 5.38. The measurement uncertainty for a range of 100-200 kW/m² was calculated at ± 7.45 -12.21 kW/m² in case of a standard deviation of the mean of 0.25 kW/m². Overall, the distribution of incident radiative heat flux is unlikely to be much altered among the studied cases and indicate that the choice of an O₂ fraction of 31 vol% upstream of the burner for the oxy-coal flames reaches successfully a similar radiative heat flux distribution to that of the air-fired case. For all investigated flames, the maximum values are obtained at access port D because a significant amount of the volatile combustion occurs farther away from the burner exit. The

oxy-flames present higher radiative heat flux at measurement ports closest to the burner (A and B). Although the air-fired case presented peak temperatures at the measurement port A, the higher fractions of CO₂ and water vapor under oxy-fired conditions yield an increase in the radiative heat flux in this zone.

As expected, the burner operating settings have an impact on the flame heat flux distribution. Oxy-flame 1 exhibits a higher level of radiation at the access ports A and B; this fact is consistent with the higher gas temperatures monitored close to the burner. Furthermore, oxy-flame 1 produces a much more uniform heat flux profile than oxy-flames with higher swirl. The high values of incident radiation flux at access port D occurred for the flames operating with the highest secondary swirl number (oxy-flames 3 and 4). This is because the flame becomes larger, thereby increasing the radiation intensity facing the tip of the radiometer at this position. Among the investigated flames, slightly higher values for the oxy-flame 4 are a result of the high peak temperatures. On the other hand, reduced values of incident wall radiation flux are obtained for the oxy-flames with higher secondary swirl number at access ports F and G. Such behavior is explained by the fact that an increase in the swirl number reduces the flame length. This observation is consistent with the values of local heat flux at the water-cooled walls and the total heat uptake in the boiler as discussed in the Section 5.6.

6 Conclusions and Recommendations

A number of issues arise in the transition from air-firing to oxy-firing. In situations where the furnace should be retrofitted for oxy-firing, the existing pulverized coal burners are designed and optimized for conventional air combustion. Thus, the adoption of oxy-fuel technology requires additional research to achieve optimal combustion. A survey of recent literature turned up very little detailed research on the characterization of pulverized oxy-coal flames generated by staged feed-gas burners. Most of the pulverized burner configurations studied by the researchers appear to be rather specialized, making a generalized interpretation of results very difficult. It is not surprising that the large number of experimental facilities used for oxy-coal studies has yielded wide variations in parametric effects and results. For this reason, one of the goals of this study was to identify common threads and characteristic parameters for the operation of test facilities and assessment of experimental results.

The experiments were conducted in a newly constructed test facility with a rated capacity of 0.40 MW_{th} fired by a staged feed-gas burner. This test facility was designed to study how switching from air-firing to oxy-firing affects the combustion performance of pulverized coal flames. The data obtained from this research enhance the present understanding of the effect of oxy-fired conditions on the combustion process of pre-dried lignite. The present work differs from that of other research in a number of ways. While previous studies focused on the impacts of recirculation rates and O₂ fraction upstream of the burner on pulverized coal flames, this work aims to investigate the impacts of various burner operating settings. Before any experiment was carried out, isothermal CFD simulations in the near burner region were performed to develop a greater fundamental understanding of the effect of the reduced feed gas flow rates on the flow pattern generated by a staged feed-gas burner. The axial and tangential profiles at the exit of the secondary annulus resulting from various swirler vane angles and feed gas distributions under air-fired and oxy-fired conditions were applied to calculate the swirl number. This approach is much more elegant than using rule-of-thumb or empirical approximations to predict the intensity of a swirling flow. The predictions of the flow pattern together with the dimensionless swirl number were successfully used to assess the experimental results.

The experimental activities were divided in two parts. First, a systematic parameter study was performed focusing on the burner operating at three levels of secondary swirl (i.e. 1.15, 1.65, and 2.05); the feed gas was divided between the secondary and tertiary registers applying flow ratios between 0.40 and 2.00. The parametric study measured the impact of oxy-firing on several combustion parameters, including: flame pattern, stability limits, peak temperature, heat transfer, burnout, and emission performance. The effects of the secondary swirl number and feed gas distribution were also further explored through in-flame

measurements for four selected oxy-fired flames and a baseline using air as a feed gas. Contour maps, transversal profiles, and centerline profiles of gas-phase temperature, species concentration, and total radiative heat flux were measured for three different swirl strengths, with special emphasis given to the near burner field. These measurements allowed exploring from a phenomenological viewpoint the effect of oxy-fired conditions and burner settings on the combustion mechanisms and pollutant formation and destruction. Another important aspect of this work is the presentation of experimental data together with statistical parameters and uncertainty of measurements. They are expected to contribute to the subsequent validation of numerical simulations of this laboratory furnace.

In the following sections, the main conclusions drawn from the theoretical and experimental studies are summarized along with suggestions for future investigations.

6.1 Summary and Major Findings from the Theoretical Study

- i Combustion-related parameters including oxygen-fuel ratio, adiabatic flame temperature, and main flue gas components were calculated based on theoretical chemical and energy balances. The results were an important tool in setting up the burner for the experimental investigations. Theoretical data indicated that a similar adiabatic flame temperature as air-firing is achieved only by increasing the O₂ fraction upstream of the burner to approximately 31 vol% under oxy-fired conditions. The results also demonstrated that the adiabatic flame temperature is strongly influenced by water vapor concentration, stoichiometric ratio, and feed gas temperature. An increase in the O₂ fraction causes a decrease in the feed gas flow rate flowing through the burner. In addition, it was observed that the O₂ excess exiting the furnace is increased by an increase in the O₂ fraction upstream of the burner for the same stoichiometric ratio.
- ii A number of isothermal flows in the near burner region were successfully simulated using a commercial CFD code. The simulations were performed using the Reynolds Stress Model (RSM) as a turbulence closure model. Five swirlers with vane angles varying from 0 to 60 degrees were examined. The feed gas distribution was varied using secondary/tertiary mass flow ratios of 0.40-1.30, all the while keeping the axial momentum of the primary jet at 0.47 N.
- iii The results indicated evidence of consistent radial flow stratification for the range of operating conditions investigated in this work. An increase in both the mass flow rate in the secondary annulus and the vane angle of the swirl expands the flow in width for air and oxy-fuel. It was especially important to observe the penetration depth of the non-swirling primary

stream into the reverse flow imparted by the swirler. Increased swirl intensity and mass flow ratio of secondary to tertiary stream promote a much more divergent flow and intensify the adverse pressure gradient in the vicinity of the burner, thereby reducing the penetration depth of the primary stream. Even though the velocity of the primary stream was reduced in the oxy-fuel cases, the main differences lie in the general tendency of the primary jet to penetrate much more into the IRZ. Velocity profiles and recirculated mass flow rates, evaluated at various distances from the burner exit, indicated that the overall reduction of the feed gas flow rate generates weaker recirculation zones under oxy-fired conditions.

- iv The swirl number at the exit of the secondary annulus was obtained by integrating the axial and tangential velocity profiles. This parameter serves as an important indication of the swirl magnitude and allows an easier comparison with several types of burner configurations. The swirl number calculated for the swirlers investigated in this work varied between 0.00 and 2.05. The values were shown to be independent of the feed gas composition and flow rates used in this work.

6.2 Summary and Major Findings from the Experimental Study

- i Diffusion coal flames with high axial momentum of the primary jet produced a bulbous combustion zone near the burner quarl with a flame tail for a wide range of operating conditions. Flame photographs and post-processed images obtained with a CCD camera indicated that the fuel jet penetrates the IRZ, forming an annular doughnut reverse flow region for both firing conditions and resembling a type-1 flame pattern. This flame pattern suggests low NO emissions because a stratified flame structure in fuel-rich and fuel-lean zones is generated. No attention was given to this flame structure in previous oxy-coal studies. Although the geometrical and luminous characteristics were similar between air-firing and oxy-firing operating with an overall O₂ fraction upstream of the burner of 31 vol%, flame images displayed a pronounced coal jet in oxy-fired conditions due to reduced feed gas flow rate; air flames were generally characterized by a more intense flame.
- ii Qualitative comparisons of the images of generated diffusion flames and flow patterns produced by the CFD simulations suggested that the main effect of combustion is to reduce the strength of the IRZ, which in turn allows the primary jet to penetrate the reverse flow. In the isothermal simulations, the primary jet only penetrates the IRZ to a certain extent downstream of the burner. This indicates that the combustion process reduces the importance of the tangential momentum imparted by the swirler at distances further downstream of the burner.

- iii The criteria for stabilizing diffusion type-1 flames under oxy-fired conditions were fully described. Keeping the axial velocity of the carrier gas similar to that of the air-fired case (28 m/s) led to an increase in the axial momentum of the primary jet and consequently the initiation of precursor events preceding the flame blow-off. The strategy was to reduce the velocity of the primary stream until a similar axial momentum to air-firing were achieved (approximately 0.47 N). Trials during the commissioning showed that the replacement of the primary stream by pure CO₂ caused a marked change in flame characteristics and loss of stability. This is because a lack of primary O₂ delays the particle ignition and volatile combustion until secondary feed gas mixing occurs. Stable combustion was achieved only by increasing the O₂ fraction in the primary stream to air-fired levels. Flame stabilization was shown to be strongly dependent on an appropriate distribution of the feed gas and strength of swirling flow in the burner front. A weak swirl or low secondary/tertiary flow ratio led to unstable operation, i.e. to flames which are lifted rather than anchored in the burner quarl. In these cases, the bulk of the coal particles punch through a relatively weak IRZ due to their high momentum.
- iv The stability limits were evaluated by slowly decreasing the flow ratio of secondary to tertiary stream until the flame lifted off. Results were correlated in terms of swirl number, secondary/tertiary flow ratio, and secondary/primary axial momentum. This is considered a very useful practice for comparing the stability limits of a burner operating with various feed gas compositions. The stability limit curves correlated in terms of secondary swirl number (between 1.15 and 2.05) and secondary/primary axial momentum ratio showed remarkable similarities between air-firing and oxy-firing at a 1.17 stoichiometric ratio. This indicates that the strength of swirling flow can overcome the differences in the feed gas properties.
- v The parametric study and detailed in-flame measurements suggest that the feed gas distribution among the burner registers control the maximum temperature in parallel with the swirl number for both air and oxy-fuel. Lower peak temperatures were obtained under oxy-firing as a result of the lower temperature of the feed gas and higher proportion of CO₂ and water vapor in the furnace. Even though some discrepancies were found between the peak temperatures monitored by the visual digital imaging system and the suction pyrometer, the results indicate that increasing the swirl number and the secondary/tertiary flow ratio suppresses the peak temperatures. In such cases, the temperature profiles indicate that the flame was spread radially outwards, reducing the temperatures close to the burner.
- vi Temperature measurements at the measurement port closest to the burner indicate that oxy-flames have lower temperatures. This is a result of a lower feed gas temperature and the differences in the thermophysical

properties of the feed gas which reduces the flame propagation and the mass transfer properties in the gas phase. By increasing the swirl strength imparted to the secondary stream, higher temperatures closer to the burner were obtained. The oxy-fuel cases exhibited markedly reduced temperatures on the flame axis. This difference in the core arises not just from the more pronounced penetration depth of the primary jet, but also due to reaction mechanisms including pyrolysis and gasification reactions at the higher concentrations of CO₂ and water vapor.

- vii Measurements of O₂ revealed that the fuel-rich region becomes more significant for the investigated oxy-flames than the air-fired baseline. In addition, a marked difference exists among the structure of oxy-flames using various swirl numbers and secondary/tertiary flow ratios. The CFD simulations showed that an increase in the swirl also expands the flow radially thereby increasing the O₂ concentration at distances closer to the wall. Transversal O₂ profiles at 0.050 m from the burner exit showed an enhanced combustion rate for the higher swirl flame (oxy-flame 3) as a consequence of the intensified mixing between the feed gas and coal particles. Similarly, an increase in the secondary/tertiary flow ratio improved the coal conversion rate as observed with oxy-flames 3 and 4. The transversal profiles also showed that the minimum O₂ concentration shifted from 0.050 m (baseline flame under air-firing) to 0.660 m for the oxy-flames. Additionally, the evolution of CO₂ was much more gradual under oxy-firing. Both O₂ and CO₂ profiles suggest that oxy-flames are much more diffusive than air-fired ones.
- viii Measurements of CH₄ and CO revealed the locations where volatiles are released and carbon content is oxidized. Overall, the CO and CH₄ trends were similar. The contour plots and transversal profiles showed that most volatile matter was released close to the axis and farther downstream of the burner exit (usually at 0.660 m). Measurements clearly showed much higher CO concentrations under oxy-firing, possibly a result of CO₂ dissociation and/or gasification by water vapor and CO₂. These reactions are expected to be enhanced by the generated flame pattern (type-1). The initial production of CO at 0.050 m from the burner was highest in the baseline air-flame. This backs up previous findings obtained in small-scale reactors which show a reduction in the burning rate for higher CO₂ concentrations. CO and CH₄ profiles also indicated that a decrease in the swirl number suppresses the mixing of feed gas and fuel.
- ix The CO concentration at the furnace exit was measured during the parametric study. The values remained below 30 mg/m³ (dry), indicating that complete combustion under oxy-fired conditions is possible at a 1.17 stoichiometric ratio. Particle burnout measurement showed that the char conversion in the furnace reached high values (typically 99.50 %); carbon in ash is not an obstacle for the use of staged feed-gas burner in oxy-coal

flames.

- x Experimental data obtained from the parameter study and in-flame measurements suggest great potential for NO abatement through flame aerodynamics for oxy-coal combustion. The experiments demonstrated that staging the feed gas in a burner is an effective technique in improving the flame stratification in fuel-rich and fuel-lean zones. In particular, combining high swirl and high secondary/tertiary flow ratio results in significant NO reduction.
- xi Higher NO concentrations were obtained during oxy-fuel combustion as a result of recycling NO with the flue gas and reducing the overall volume flow rate. The emission rates for oxy-firing varied between 40 and 85 mg/MJ; for air-firing, between 70 and 130 mg/MJ. For the same swirl number, the mass of NO formed per energy input decreased 22-38%. A series of experiments were also performed to evaluate the influence of the O₂ fraction in the feed gas (29, 31, and 33 vol%) and O₂ excess on NO emission. A linear relationship was observed between the O₂ excess and NO emission, i.e. as the O₂ excess increases, the total amount of NO formed also increases. Increasing the O₂ fraction from 29 to 31 vol% led to higher values of NO exiting the furnace. However, no noticeable differences between the 31 and 33 vol% cases were observed. NO₂ emissions were insignificant and did not exhibit any obvious relationship to those of NO.
- xii In the baseline air-flame, NO formed very close to the exit of the burner; in oxy-flames, the NO formed usually farther downstream and off the centerline (i.e. in the regions of high O₂ availability). The exception was oxy-flame 3, which operated with the highest swirl number and secondary/tertiary flow ratio, and displayed NO formation similar to the baseline. For oxy-flames operating with lowest secondary swirl number (oxy-flame 1), the NO formation region was wider and longer owing to the reduced O₂ admixing to the central fuel jet; the contact of O₂ occurred in critical regions where nitrogen species are evolved. This also explains the increased size of NO formation zones in case of the oxy-flame operating with reduced flow ratio of secondary to tertiary stream (oxy-flame 4). The measurements clearly identified high-temperature and oxygen-lean regions situated close to the axis at distances between 0.355 and 1.274 m. In these regions, the presence of higher amounts CO and CH₄ suggest the presence of NO reduction mechanisms.
- xiii SO₂ emissions were monitored at the furnace exit and downstream of the flue gas scrubber. Desulfurization capacity was similar for air-fired and oxy-fired cases and emissions of SO₂ were no higher than 20 mg/m³ (dry) at the stack. Nevertheless, oxy-fuel operation suffers from a higher consumption of sorbent slurry due to the higher concentration of CO₂. At the furnace exit, SO₂ increased by a factor of 1.40 under oxy-firing due to

the reduced volume flow rate of the flue gas. But these values are still considerably lower compared to other investigations carried in test facilities which do not apply SO₂ scrubbing techniques. SO₂ emission rates at the furnace exit were approximately 400 mg/MJ and fuel-S conversion was on average 75% under both firing conditions. These results show that oxy-fuel combustion does not affect the release of sulfur from the pre-dried lignite under the conditions evaluated in the present work.

- xiv Heat transfer data were correlated in terms of the swirl number and secondary/tertiary flow ratio. The results suggest the possibility of matching similar heat uptake in the furnace and economizer under air-fired and oxy-fired conditions. Due to the furnace geometry, the flame shape influences the heat flux distribution in the radiative section and consequently the heat transfer rate. For comparison purposes, the influence of the overall O₂ fraction of the feed gas on the heat transfer from oxy-flames was performed at three levels (29, 31, and 33 vol% O₂); the burner operating conditions were kept at a secondary swirl of 1.65 and a secondary/tertiary flow ratio of 2.05. Radiative heat flux measured at 0.660 m from the burner exit clearly shows the flexibility of oxy-fuel operation with varying O₂ fraction and shows that a closer value of radiative heat flux to air-firing is obtained using a O₂ fraction of 31 vol%.
- xv In-flame measurements indicated that the distribution of radiative heat flux along the flame length was unlikely much altered among the studied cases and reinforced that the choice of an O₂ fraction of 31 vol% upstream of the burner for the oxy-coal flames was appropriated for maintaining similar heat transfer characteristics as under air-fired conditions. This, together with the results obtained from the parametric study, supports the use of the adiabatic flame temperature as an indicator of radiative heat transfer in the combustion process for oxy-coal flames. Large changes were observed when the swirl intensity was reduced to 1.15 (oxy-flame 1), which produced a much more uniform distribution of incident radiation flux. In addition, this flame provided higher values of incident radiative heat flux farther downstream of the burner (at access ports F and G), indicating differences in the flame length.

6.3 Suggestions for Further Study

- i A suction pyrometer and gas sampling probe, which are sufficiently non-intrusive and do not also suffer from excessive building up of ash deposits, should be developed.
- ii Apart from the qualitative knowledge of the flow patterns obtained by CFD simulations, no quantitative velocity data were reported in this work. Experimental velocity data would be useful for a more accurate

interpretation of the results.

- iii Additional work is necessary to investigate the impact of coal particle size and water content of the pre-dried lignite on the overall combustion performance under oxy-fired conditions. In addition, the impact of feed gas temperature, stoichiometric ratio, and various O₂ distributions among the burner registers should be further explored.
- iv The influence of the inner secondary stream of the burner and feed gas staging ports located at several levels of the furnace on NO emissions would greatly increase the understanding of the impacts of control strategies under oxy-fired conditions.
- v In order to better assess the fate of the chemically bound nitrogen, additional measurements of HCN, NH₃, and char nitrogen are recommended.
- vi Future investigations should experiment with other burner configurations that generate new and different flame patterns.

7 References

- [1] International Energy Agency (IEA). World energy outlook 2011. Paris: IEA Publications; 2011. 696 p.
- [2] International Energy Agency (IEA). World energy outlook 2007: China and India Insights. Paris: IEA Publications; 2007. 670 p.
- [3] International Energy Agency (IEA). World energy outlook 2008. Paris: IEA Publications; 2008. 578 p.
- [4] World Coal Institute. Coal meeting the climate challenge: technology to reduce greenhouse gas emissions. Richmond (UK): World Coal Institute Publications; 2007. 48 p.
- [5] World Coal Institute. The coal resource: a comprehensive overview of coal. Richmond (UK): World Coal Institute Publications; 2005. 44 p.
- [6] Minchener AJ, McMullan JT. Sustainable clean coal power generation within a European context: the view in 2006. *Fuel*. 2007; 87(14): 2124-33.
- [7] Beér JM. Combustion technology developments in power generation in response to environmental challenges. *Progress in Energy and Combustion Science*. 2000; 26(4-6): 301-27.
- [8] Federal Ministry of Economics and Technology (BMWi). Recommendations by the COORETEC advisory council on support for research and development for low CO₂-emission power plant technologies and carbon capture and storage technologies. Berlin: BMWi; 2009. 12 p.
- [9] Wall TF. Combustion processes for carbon capture. *Proceedings of the Combustion Institute*. 2007; 31(1): 31-47.
- [10] Bachu S. CO₂ storage in geological media: role, means, status and barriers to deployment. *Progress in Energy and Combustion Science*. 2008; 34(2): 254-73.
- [11] Schilling S. Geological CO₂ storage: risk assessment and lessons learned. II International Workshop: Carbon Capture and Storage Technologies; 2009 Nov 10-11; Fortaleza, Brazil.
- [12] Song C. Global challenges and strategies for control, conversion and utilization of CO₂ for sustainable development involving energy catalysis, adsorption and chemical processing. *Catalysis Today*. 2006; 115: 2-32.
- [13] Buhre BJP, Elliott LK, Sheng CD, Gupta RP, Wall TF. Oxy-fuel combustion technology for coal-fired power generation. *Progress in Energy and Combustion Science*. 2005; 31(4): 283-307.
- [14] Gibbins J, Chalmers H. Carbon capture and storage. *Energy Policy*. 2008; 36(12): 4317-22.

- [15] Toftegaard MB, Brix J, Jensen PA, Glarborg P, Jensen AD. Oxy-fuel combustion of solid fuels. *Progress in Energy and Combustion Science*. 2010; 36(5): 581-625.
- [16] McDonald D, Tranier JP. Oxy-Coal is ready for demonstration. *Proceedings of the 35th Clearwater Clean Coal Conference*; 2010 Jun 6-10; Clearwater, USA.
- [17] Varagani RK, Châtel-Pélage F, Pranda P, Rostam-Abadi M., Lu Y, Bose AC. Performance simulation and cost assessment of oxy-combustion process for on carbon sequestration. *Proceedings of the Fourth Annual Conference on Carbon Sequestration*; 2005 May 2-5; Alexandria, USA .
- [18] Simmins M, Miracca I, Gerdes K. Oxy-fuel technologies for CO₂ capture: a techno-economic overview. *Proceedings of the 7th International Conference on Greenhouse Gas Control Technologies*; 2004 Sep 5-9; Vancouver, Canada.
- [19] Davison J. Performance and costs of power plants with capture and storage of CO₂. *Energy*. 2007; 32 (7): 1163-76.
- [20] Hill G. Implementing CCS in Europe: ZEP's vision of zero emissions power by 2020. *Proceedings of the 9th International Conference on Greenhouse Control Technologies*; 2008 Nov 16-20; Washington, USA.
- [21] Wall T, Lie Y, Spero C, Elliot L, Khare S, Rathnam R, et al. An overview on oxy-fuel coal combustion: state of the art research and technology development. *Chemical Engineering Research and Design*. 2009; 87(8): 1003-16.
- [22] Abraham BM, Asbury JG, Lynch EP, Teotia APS. Coal oxygen process provides CO₂ for enhanced oil recovery. *Oil and Gas Journal*. 1982; 80(11): 68-75.
- [23] Horn FL, Steinberg M. Control of carbon dioxide emissions from a power plant (and use in enhanced oil recovery). *Fuel*. 1982; 61(5): 415-22.
- [24] Kimura N, Omata K, Kiga T, Takano S, Shikisima S. The characteristics of pulverized coal combustion in O₂/CO₂ mixtures for CO₂ recovery. *Energy Conversion Management*. 1995; 36(6): 805-8.
- [25] Kiga T, Takano S, Kimura N, Omata K, Okawa M, Mori T, et al. Characteristics of pulverized-coal combustion in the system of oxygen/recycled flue gas combustion. *Energy Conversion and Management*. 1997; 38(Supplement): 129-34.
- [26] Nozaki T, Takano S, Kiga T, Omata K, Okawa M, Kimura N. Analysis of the flame formed during oxidation of pulverized coal by an O₂-CO₂ mixture. *Energy*. 1997; 22(2-3): 199-205.

- [27] Woycenko DL, Van de Kamo WL, Roberts PA. Combustion of pulverized coal in a mixture of oxygen and recycle flue gas. Ijmuiden (NL): International Flame Research Foundation; 1995 Oct. Report No.:F98/Y/4.
- [28] Kaß H, Krautz HJ. Verbrennung von Lausitzer Trockenbraunkohle unter Oxy-fuel-Prozessbedingungen in der 0,5 MW_{th}- Tangentialfeuerung. 23. Deutscher Flammentag, Berlin, 2007. German.
- [29] Kaß H, Krautz HJ. Verbrennung von Lausitzer Trockenbraunkohle unter Oxy-fuel - Prozeßbedingungen in der 0,5 MW_{th} – Tangentialfeuerung. 40. Kraftwerkstechnisches Kolloquium, 2008. German.
- [30] Kaß H, Tappe S, Krautz HJ. The combustion of dry lignite under oxy-fuel process conditions in a 0.5 MW_{th} test plant. Energy Procedia. 2009; 1(1): 423-30.
- [31] Strömberg L, Lindgren G, Jacoby J, Giering R, Anheden M, Burchardt U, Altmann H, et al. Update on Vattenfall's 30 MW_{th} oxy-fuel pilot plant in Schwarze Pumpe. Proceedings of the 9th International Conference on Greenhouse Control Technology; 2008 Nov 16-20; Washington, USA.
- [32] Strömberg L, Lindgren G, Jacoby J, Giering R, Anheden M, Burchardt U, et al. First test results from vattenfall's 30 MW_{th} oxy-fuel pilot plant in schwarze pumpe. Proceedings of the 34th Clearwater Clean Coal Conference; 2009 May 31-Jun 4; Clearwater, USA.
- [33] Levasseur A, Chapman PJ, Nsakala N, Kluger F, Alstom. Oxy-firing technology development and demonstration: near term CO₂ solutions. Proceedings of the 34th Clearwater Clean Coal Conference; 2009 May31-Jun 4; Clearwater, USA.
- [34] Kim S, Lee H. Korean oxy-fuel demonstration project. Proceedings of the 1st Oxy-fuel Combustion Conference; 2009 Sep 8-11; Cottbus, Germany.
- [35] Spero C. Australian Japanese co-operation on oxy-fuel pilot project for plant retrofit – Callide: a project. Inaugural workshop of the Oxy-fuel Combustion network; 2005; Cottbus, Germany.
- [36] Victor R, Bonaquist D, Sha M, Hack H, Leathers D, Martin J. Jamestown oxy-coal CFB Project. Proceedings of the 1st Oxy-fuel Combustion Conference; 2009 Sep 8-11; Cottbus, Germany.
- [37] Lupion M. OxyCFB300 Compostilla project: technological development. Proceedings of the 2nd Oxy-fuel Combustion Conference; 2011 Sep 12-16; Yeppoon, Australia.
- [38] Wall T, Yu J. Coal-fired oxy-fuel technology status and progress to deployment. Proceedings of the 34th Clearwater Clean Coal Conference; 2009 May 31-Jun 4; Clearwater, USA.

- [39] Wall T, Yu J, Santos S. Oxy-combustion for carbon capture and storage (CCS): status, prospects and roadmap to commercialization. Proceedings of the 1st Oxy-fuel Combustion Conference; 2009 Sep 8-11; Cottbus, Germany.
- [40] Chen L, Yong SZ, Ghoniem AF. Oxy-fuel combustion of pulverized coal: characterization, fundamentals, stabilization and CFD modeling. *Progress in Energy and Combustion Science*. 2012; 38(2): 156-214.
- [41] Smoot LD, Pratt DT. Pulverized-coal combustion and gasification: theory and Applications for continuous flow processes. New York: Plenum Press; 1979.
- [42] Smoot LD, Smith PJ. Coal combustion and gasification. New York: Plenum Press; 1985.
- [43] Lahaye J, Prado G. Fundamentals of the physical-chemistry of pulverized coal combustion. Dordrecht: Martinus Nijhoff Publishers; 1987.
- [44] Sarofim AF, Bartok W. Fossil fuel combustion: a source book. New York: John Wiley & Sons; 1991.
- [45] Jordal K, Anheden M, Yan J, Strömberg L. Oxy-fuel combustion for coal-fired power generation with CO₂ capture: opportunities and Challenges. Proceedings of the 7th Conference on Greenhouse Gas Control Technologies; 2004 Sep 5-9; Vancouver, Canada.
- [46] Dillon DJ, Panesar RS, Wall RA, Allam RJ, White V, Gibbins J, Haines MR. Oxy-combustion processes for CO₂ capture from advanced supercritical PG and NGCC power plant. Proceedings of the 7th International Conference on Greenhouse Gas Control Technologies; 2004 Sep 5-9; Vancouver, Canada.
- [47] McDonald D, Zadiraka A. Control of pulverized coal oxy-combustion. Proceedings of the 17th Annual Joint ISA POWID/EPRI Controls and Instrumentation Conference/ 50th Annual ISA Power Industry (POWID) Conference; 2007 Jun 5-7; Pittsburgh, USA.
- [48] Kluger F, Moenckert, P, Stamatelopoulos GN, Alstom. Oxy-combustion technology development: update on pilot plants operation. Proceedings of the 35th Clearwater Clean Coal Conference; 2010 Jun 6-10; Clearwater, USA.
- [49] Nakayama S, Noguchi Y, Kiga T, Miyamae S, Maeda U, Kawai M. Pulverized coal combustion in O₂/CO₂ mixtures on a power plant for CO₂ recovery. *Energy Conversion management*. 1992; 33(5-8): 379-386.
- [50] Dillon DJ, White V, Allan RJ, Wall RA, Gibbins J. Oxy-combustion processes for CO₂ capture from power plant. Engineering Investigation Report, 2005/9, IEA Greenhouse Gas Research and Development Programme; 2005.

- [51] Tan R, Corragio G, Santos S. Oxy-coal combustion with flue gas recycle for the power generation industry: a literature review. Velsen Noord (NL): International Flame Research Foundation; 2005 Oct. Report No.: G 23/y/1.
- [52] Molina A, Shaddix CR. Effect of O₂/CO₂-firing on coal particle ignition. Proceedings of the 22nd International Pittsburgh Coal Conference; 2005 Sep 12-15; Pittsburgh, USA.
- [53] Molina A, Hechts ES, Shaddix CR. Ignition of a group of coal particles in oxy-fuel combustion with CO₂ recirculation. Proceedings of the 34th Clearwater Clean Coal Conference; 2009 May 31-Jun 4; Clearwater, USA.
- [54] Shaddix CR, Molina A. Particle imaging of ignition and devolatilization of pulverized coal during oxy-fuel combustion. Proceedings of the Combustion Institute. 2009; 32(9): 2091-98.
- [55] Molina A, Shaddix CR. Ignition and devolatilization of pulverized bituminous coal particles during oxygen/carbon dioxide coal combustion. Proceedings of the Combustion Institute. 2007; 31(2): 1905-12.
- [56] Rathnam RK, Elliot LK, Wall TF, Liu Y, Moghtaderi B. Differences in reactivity of pulverized coal in air (O₂/N₂) and oxy-fuel (O₂/CO₂) conditions. Fuel Process Technology. 2009; 90(6): 797-802.
- [57] Al-Makhadmed L. Coal pyrolysis and char combustion under oxy-fuel conditions [PhD thesis]. Stuttgart: University of Stuttgart; 2009.
- [58] Brix J, Jensen PA, Jensen AD. Coal devolatilization and char conversion under suspension fired conditions in O₂/N₂ and O₂/CO₂ atmospheres. Fuel. 2010; 89(11): 3373-80.
- [59] Borrego AG, Alvarez D. Comparison of chars obtained under oxy-fuel and conventional pulverized coal combustion atmospheres. Energy & Fuels. 2007; 21(6): 3171-79.
- [60] Mulcahy MFR, Smith IW. Kinetics of combustion of pulverized fuel: a review of theory and experiment. Reviews of Pure and Applied Chemistry. 1969; 19: 81-108.
- [61] Mann AP, Kent JH. A computational study of heterogeneous char reactions in a full-scale furnace. Combustion and Flame. 1994; 99(1): 147-56.
- [62] Shaddix CR, Hecht ES, Geier M, Molina A, Haynes BS. Effect of gasification reactions on oxy-fuel combustion of pulverized coal char. Proceedings of the 35th Clearwater Clean Coal Conference; 2010 Jun 6-10; Clearwater, USA.
- [63] Tappe S. Gaspotentiometrische und Thermogravimetrische Abbranduntersuchungen von Braun- und Steinkohlen in Luft und O₂/CO₂-Atmosphäre [PhD thesis]. Cottbus: Brandenburg University of Technology; 2011. German.

- [64] Shaddix CR, Hecht ES, Jimenez S, Lee SM. Evaluation of rank effects and gas temperature on coal char burning rates during oxy-fuel combustion. Proceedings of the 34th Clearwater Clean Coal Conference; 2009 May 31-Jun 4; Clearwater, USA.
- [65] Tan Y, Croiset E, Douglas MA, Thambimuthu KV. Combustion characteristics of coal in a mixture of oxygen and recycled flue gas. *Fuel*. 2006; 85(4): 507-12.
- [66] Khare SP, Wall TF, Farida AZ, Liu Y, Moghtaderi B, Gupta RP. Factors influencing the ignition of flames from air-fired swirl pf burners retrofitted to oxyfuel. *Fuel*. 2008; 87(7): 1042-49.
- [67] Hjærtstam S, Andersson K, Johnsson F, Leckner B. Combustion characteristics of lignite-fired oxy-fuel flames. *Fuel*. 2009; 88(11):2216-24.
- [68] Smart JP, Riley GS. On the effects of firing semi-anthracite and bituminous coal under oxy-fuel firing conditions. *Fuel*. 2011; 90(8): 2812-16.
- [69] Smart J, Lu G, Yan Y, Riley G. Characterisation of an oxy-coal flame through digital imaging. *Combustion and Flame*. 2010; 157(6): 1132-39
- [70] Smart JP, O’Nions P, Riley GS. Radiation and convective heat transfer, and burnout in oxy-coal combustion. *Fuel*. 2010; 89(9): 2468-76.
- [71] Fry A, Adams B, Pschedag A, Kazalski, P, Carney C, Oryshchyn D, et al. Principles for retrofitting coal burners for oxy-combustion. *International Journal of Greenhouse Gas Control*. 2011; 5(1): 151-58.
- [72] Morris WJ, Yu D, Wendt JOL. Soot, unburned carbon and ultrafine particle emissions from air- and oxy-coal flames. Proceedings of the Combustion Institute. 33; 2012. p. 3415-21.
- [73] Glaborg P, Bentzen LLB. Chemical effects of high CO₂ concentrations in oxy-fuel combustion of methane. *Energy Fuels*. 2008; 22(1): 291-96.
- [74] Liu F, Guo H, Smallwood GJ. The chemical effect of CO₂ replacement of N₂ in air on the burning velocity of CH₄ and H₂ premixed flames. *Combustion and Flame*. 1998; 113(1-2):274-276.
- [75] Fenimore CP. Formation of nitric oxide in premixed hydrocarbon flames. Symposium (International) on Combustion. 1971; 13(1): 373-380.
- [76] Baukal Jr CE. Industrial combustion pollution control. 1st ed. New York: Marcel Dekker; 2003.
- [77] Pershing DW, Wendt JOL. Pulverized coal combustion: the influence of flame temperature and coal composition on thermal and fuel nitrogen oxides. Proceedings of the Combustion Institute. 1977; 16: 389-399.
- [78] Glaborg P, Jensen AD, Johnsson JE. Fuel nitrogen conversion in solid fuel fired systems. *Progress in Energy and Combustion Science*. 2003; 29(2): 89-113.

- [79] Jones JM, Patterson PM, Pourkashanian M, Williams A. Approaches to modeling heterogeneous char NO formation/destruction during pulverized coal combustion. *Carbon*. 1999; 37(10): 1545-52.
- [80] Haussmann GJ, Kruger CH. Evolution and reaction of coal fuel nitrogen during rapid oxidative pyrolysis and combustion. Symposium (International) on Combustion. 1991; 23(1): 1265-71.
- [81] Blair DW, Wendt JOL, Bartok W. Evolution of nitrogen and other species during controlled pyrolysis of coal. *Progress in Energy and Combustion Science*. 1977; 16(1): 475-89.
- [82] Wendt JOL, Pershing DW. Physical mechanisms governing the oxidation of volatile fuel nitrogen in pulverized coal flames. *Combustion Science and Technology*. 1977; 16(3-6): 111-21.
- [83] Zhang H, Fletcher TH. Nitrogen transformations during secondary coal pyrolysis. *Energy and Fuels*. 2001; 15(6): 1512-22.
- [84] Sarofim AF. Pollutant formation and destruction. In: Lahaye J, Prado G, editors. *Fundamentals of the physical-chemistry of pulverized coal combustion*. Dordrecht: Martinus Nijhoff Publishers; 1987. p. 245-268.
- [85] Moline A, Eddings EG, Pershing DW, Sarofim AF. Nitric oxide destruction during coal and char oxidation under pulverized-coal combustion conditions. *Combustion and Flame*. 2004; 136: 303-312.
- [86] Wilhelm R. *Bildung und Reduktion von Stickoxiden im Luft- und Oxyfuel-Betrieb* [PhD Thesis]. Dresden: Dresden University of Technology; 2010. German.
- [87] Hu YQ, Kobayashi N, Hasatani M. Effects of coal properties on recycled-NO_x reduction in coal combustion with O₂/recycled flue gas. *Energy conversion and management* 2003; 44(14): 2331-40.
- [88] Liu H, Zailani R, Gibbs BM. Pulverized coal combustion in air and in O₂/CO₂ mixtures with NO_x recycle. *Fuel*. 2005; 84(16): 2109-15.
- [89] Chui EH, Douglas MA, Tan Y. Modeling of oxy-fuel combustion for a western Canadian sub-bituminous coal. *Fuel*. 2003; 82(10): 1201-10.
- [90] Chui EH, Majeski AJ, Douglas MA, Tan Y, Thambimuthu KV. Numerical investigation of oxy-coal combustion to evaluate burner and combustor design concepts. *Energy*. 2004; 29 (9-10): 1285-96.
- [91] Dhungel B. *Experimental investigations on combustion and emission behavior during oxy-coal combustion* [PhD thesis]. Stuttgart: University of Stuttgart; 2010.
- [92] Normann F, Andersson K, Leckner B, Johnsson F. High-temperature reduction of nitrogen oxides in oxy-fuel combustion. *Fuel*. 2008; 87(17-18): 3579-85.

- [93] Andersson K, Normann F, Johnsson F, Leckner B. NO emission during oxy-fuel combustion of lignite. *Industrial and Engineering Chemical Research*. 2008; 47(6): 1835-45.
- [94] Nordin M, Merriam NW. NO_x emissions produced with combustion of powder river basin coal in a utility boiler. Technical report. Western Research Institute. Larami, Wyoming; 1997 April.
- [95] Wegerich S. Experimentelle Untersuchungen zum Verbrennungsverhalten und zur NO_x-Entstehung bei der Verbrennung von Kohlenstaub in einer O₂/CO₂-Atmosphäre [PhD Thesis]. Hamburg: Hamburg University of Technology; 2009. German.
- [96] Suuberg EM, Teng H, Calo JM. Studies on the kinetics and mechanism of the reaction of NO with carbon. *Symposium (International) on combustion*. 1991; 23(1): 1199-1205.
- [97] Tomita A. Suppression of nitrogen oxides emission by carbonaceous reductants. *Fuel processing technology*. 2001; 71: 53-70.
- [98] Miller BG. *Coal Energy Systems*. 1st ed. New York: Elsevier; 2005.
- [99] Bowman CT. Chemistry of gaseous pollutant formation and destruction. In Bartok W, Sarofim AF, editors. *Fossil fuel combustion: a source book*. New York: John Wiley; 1991.p. 215-260.
- [100] Stanger R, Wall T. Sulphur impacts during pulverised coal combustion in oxy-fuel technology for carbon capture and storage. *Progress in Energy and Combustion Science*. 2011; 37(1): 69-88.
- [101] Croiset E, Thambimuthu KV. NO_x and SO₂ emissions from O₂/CO₂ recycle coal combustion. *Fuel*. 2001; 80(14): 2117:21.
- [102] Hu Y, Naito S, Kobayashi N, Hasatani M. CO₂, NO_x and SO₂ emissions from the combustion of coal with high oxygen concentration gases. *Fuel*. 2000; 79 (15): 1925-32.
- [103] Sheng Ch, Xu M, Zhang J, Xu Y. Comparison of sulphur retention by coal ash in different types of combustors. *Fuel Processing Technology*. 2000; 64(1-3): 1-11.
- [104] Toporov D, Bocian P, Heil P, Kellermann A, Stadler H, Tschunko S, et al. Detailed investigation of pulverized fuel swirl flame in CO₂/O₂ atmosphere. *Combustion and Flame*. 2008; 155(4): 605-18.
- [105] Heil P, Toporov D, Staffle H, Tschunko S, Förster M, Kneer R. Development of an oxycoal swirl burner operating at low O₂ concentrations. *Fuel*. 2009; 88(7): 1269-74.
- [106] Habermel M, Toporov D. Experimental and numerical investigations on a swirl oxycoal flame. *Applied Thermal Engineering*; In press 2011.

- [107] Rehfeldt S, Kuhr C, Ehmman, M, Bergins C, Schefknecht, G, Maier, J, Wu S. Basic experiments and CFD calculations of air and oxyfuel firing of lignite and bituminous coals in 0.5 and 1 MW scale combustion test facilities. 2nd International Oxyfuel Combustion Conference; 2011 Sep 12-16; Yeppoon, Australia.
- [108] Baukal Jr CE. Heat transfer in industrial combustion. 1st ed. Florida: CRC Press; 2000.
- [109] Correa da Silva R. Arranjo instrumental para monitorar temperaturas de superfície em feixes tubulares de unidades geradoras de vapor [Master Thesis]. Florianópolis, Brazil: Department of Mechanical Engineering, Federal University of Santa Catarina; 2008. Portuguese.
- [110] ASTM Committee E-20 on Temperature Measurement. Manual on the use of thermocouple in temperature measurements. Philadelphia: American Society for Testing and Materials; 1974. 252 p.
- [111] Chedaille J, Braud Y. Measurements in flames (Industrial Flames Vol.1). 1st ed. London: Edward Arnold; 1972.
- [112] Fricker N. How do I measure local flame temperatures with the IFRF suction pyrometer? [Internet]. [Updated 2001 Nov 1] IFRF Doc No C76/y/1/17. Available from: <http://www.handbook.ifrf.net/handbook/cf.html?id=145>
- [113] Smoot LD. Fundamentals of coal combustion for clean and efficient use. Amsterdam: Elsevier; 1993.
- [114] Ribeirete A, Costa M. Impact of the air staging on the performance of a pulverized coal fired furnace. Proceedings of the Combustion Institute. 2009; 32(2): 2667-73.
- [115] Measurement equipment: ellipsoidal radiometer [Internet]. [Updated 2010 April] IFRF Doc No C76/y/1/3b. Available from: <http://www.ifrf.net>
- [116] Doebelin EO. Measurement systems: application and design. 4th ed. Minnesota: McGraw-Hill College; 1989.
- [117] Holman JP. Experimental methods for engineers. 6th ed. New York: McGraw-Hill; 1994.
- [118] Taler J, Duda P, Weglowski B, Zima W, Gradziel S, Sobota T, Taler D. Identification of local heat flux to membrane water-walls in steam boilers. Fuel. 2009; 88(2): 305-11.
- [119] Krüger S. Wärmestrommessung an Membranwänden von Dampferzeugern [PhD thesis]. Dresden: Dresden University of Technology; 2009. German.
- [120] Lu G, Ya Y, Cornwell S, Whitehouse M, Riley G. Impact of co-firing coal and biomass on flame characteristics and stability. Fuel. 2008; 87(7): 1133-40.

- [121] Lu G, Ya, Y, Colechin M, Hill R. Monitoring of oscillatory characteristics of pulverized coal flames through image processing and spectral analysis. *IEE Transactions on Instrumentation and Measurement*. 2006; 55(1): 226-31.
- [122] Lu G, Ya Y, Colechin M. A digital imaging based multifunctional flame monitoring system. *IEE Transactions on Instrumentation and Measurement*. 2004; 53(4): 1152-58.
- [123] Lu G, Ya Y, Colechin M. Monitoring and characterization of pulverized coal flames using digital imaging techniques. *Fuel*. 2002; 81(5): 647-56.
- [124] Jiang ZW, Luo ZX, Zhou HC. A simple measurement method of temperature and emissivity of coal-fired flames from visible radiation image and its application in a CFB boiler furnace. *Fuel*. 2009; 88(6): 980-87.
- [125] Rego-Barcena S, Saari R, Mani R, El-Batroukh S, Thomson MJ. Real time, non-intrusive measurement of particle emissivity and gas temperature in coal-fired power plants. *Measurement Science and technology*. 2007; 18(11): 3479-88.
- [126] Joint Committee for Guides in Metrology. Evaluation of measurement data: guide to the expression of uncertainty in measurement. 1st ed. JCGM; 2008.
- [127] Warnatz J, Maas U, Dibble RW. Combustion: physical and chemical fundamentals, modeling and simulation, experiments, pollutant formation. 4th ed. Berlin: Springer; 2006.
- [128] Bazzo E. Geração de Vapor. 2nd ed. Florianópolis: Editora da UFSC; 1995. Portuguese.
- [129] Strauß K. Kraftwerkstechnik: zur Nutzung fossiler, nuklearer und regenerativer Energiequellen. 5th ed. Berlin: Springer; 2006. German.
- [130] FluidEXL property library [Internet]. Zittau, Goerlitz: University of Applied Sciences; [updated 2012 July 21; cited 2012 July 21]. Available from: http://thermodynamik.hszi.gr.de/cmsfg/data/Flyer_Property_Libraries_Univ_Zittau.pdf
- [131] German AE, Mahmud T. Modelling of non-premixed swirl burner flows using Reynolds-stress turbulence closure. *Fuel*. 2005; 84(5): 583-94.
- [132] Sloan DG, Smith PJ, Smoot D. Modeling of swirl in turbulent flow systems. *Progress in Energy and Combustion Science*. 1986; 12(3): 163-250.
- [133] Syred N, Beér JM. Combustion in swirling flows: A review. *Combustion and Flame*. 1974; 23(2): 143-201.
- [134] Beér JM, Chigier NA. Combustion aerodynamics. 1st ed. London: Applied Science Publishers; 1972.
- [135] Weber R, Visser BM, Boysan, F. Assessment of turbulence modeling for engineering prediction of swirling vortices in the near burner zone. *International Journal of Heat and Fluid Flow*. 1990; 11(3): 225-35.

- [136] Baukal CE. Industrial burners: Handbook. 1st ed. New York: CRC Press LLC; 2003.
- [137] Weber R, Dugué J. Combustion accelerated swirling flows in high confinements. *Progress in Energy and Combustion Science*. 1992; 18(4): 349-67.
- [138] Khademi SK, Birouk M. Assessment of the performances of RANS models for simulating swirling flows in a can-combustor. *The Open Aerospace Engineering Journal*. 2008; 1(1): 8-27.
- [139] ANSYS Fluent. *Fluent User's Guide: Fluent 12.0 theory guide*; 2009.
- [140] Yaras MI, Grosvenor AD. Evaluation of one- and two-equation low-Re turbulence models. Part I-Axisymmetric separating and swirling flows. *International Journal of Numerical Methods in Fluids*. 1995; 42 (12): 1293-319.
- [141] Ritua A, Eiamsa-ard S, Promvong P. Numerical simulation of 3D turbulent isothermal flow in a vortex combustor. *International Communications in Heat and Mass Transfer*. 2007; 34(7): 860-69.
- [142] Leonard BP, Mokhtari S. ULTRA-SHARP Nonoscillatory Convection Schemes for High-Speed Steady Multidimensional Flow. NASA Technical Memorandum 102568 (ICOMP 90-12), NASA Lewis Research Center; 1990.
- [143] Patankar SV, Spalding DB. A calculation procedure for heat, mass and momentum transfer in three-dimensional parabolic flows. *International Journal of Heat and Mass Transfer*. 1972; 15(10): 1787-806.
- [144] Patankar SV. *Numerical heat transfer and fluid flow*. New York: McGraw-Hill; 1980.
- [145] Ricou FP, Spalding DB. Measurements of entrainment by axisymmetrical turbulent jets. *Journal of Fluid Mechanics*. 1961; 11(1): 21-32.
- [146] Tigges KD, Klauke F, Bergins C, Busekrus K, Niesbach J, Ehmann M, et al. Conversion of existing coal-fired power plants to oxyfuel combustion: case study with experimental results and CFD-simulations. *Energy Procedia*. 2009; 1(1): 549-56.
- [147] IFRF today [Internet]. Available from: http://www.ffrc.fi/Liekkipaiva_2006/Liekkipaiva2006_IFRF_Today_HUPA.pdf
- [148] Payne R, Chen SL, Wolsky AM, Richter WF. CO₂ recovery via coal combustion in mixtures of oxygen and recycled flue gas. *Combustion Science and Technology*. 1989;67(1): 1-16.
- [149] Nozaki T, Takano S, Kiga T, Omata K, Kimura N. Analysis of the flame formed during oxidation of pulverized coal by an O₂-CO₂ mixture. *Energy*. 1997; 22 (2-3): 199-205.

- [150] Fleig DA, Andersson K, Kühnemuth D, Normann F, Johnsson F, Leckner B. The sulfur mass balance in oxy-fuel combustion of lignite. 1st Oxy-fuel combustion conference; 2009; Cottbus, Germany.
- [151] Grathwohl S, Lemp O, Schnell U, Maier J, Scheffknecht G, Klugher, et al. Highly flexible burner concept for oxy-fuel combustion. 1st Oxy-fuel combustion conference; 2009; Cottbus, Germany.
- [152] Ayiling AB, Smith IW. Measured temperatures of burning pulverized-fuel particles, and the nature of the primary reaction product. *Combustion and flame*. 1972; 18(2): 173-184.
- [153] Costa M, Costen P, Lockwood FC, Mahmud T. Detailed measurement in and modelling of an industry-type pulverised-coal flame. *Symposium (International) on Combustion*. 1990; 23(1): 973-80.
- [154] Howar JB. Fundamentals of coal pyrolysis and hydrolysis. In: Elliott MA, editor. *Chemistry of coal utilization*. New York: John Wiley & Sons; 1981. p. 665-784.
- [155] Pohl J, Sarofim AF. Devolatilization and oxidation of coal nitrogen. *Symposium on Combustion*. 1977; 16(1): 491-501.
- [156] Wendt JOL, Pershing DW, Lee JW, Glass JW. Pulverized coal combustion: NO_x formation mechanisms under fuel rich and staged combustion conditions. *Symposium on Combustion*. 1979; 17(1): 77-87.
- [157] Bently RE, editor. *Temperature and humidity measurement*. 1st ed. Singapore: Springer; 1998.

Appendix A - Experimental Uncertainty Assessment

A.1 Introduction

The result of a measurement is only an approximation or estimate of the real value of the measurand and thus an experimental value of a variable is complete only when accompanied by the uncertainty of that estimate. The objective of this section is to assess the uncertainty of the experimental data obtained in this work. The method used is based on the Guide to the Expression of Uncertainty in Measurement (GUM) [126] developed by the Joint Committee for Guides in Metrology (JCGM). This method is first summarized in Section A.2, while the uncertainty of the various measuring techniques used during the experiments is then discussed in the following sections.

A.2 General Procedure for Determining Uncertainty

A.2.1 Modeling the Measurement

If a measurand (Y) is not measured directly, but is determined from (N) other quantities (X_N), a mathematical relationship between the estimate of measurand (y) and input estimates (x_N) can be expressed as

$$y=f(x_1,x_2,\dots,x_N) \quad (\text{A.1})$$

The input quantities upon which the output quantities depends, may themselves be viewed as measurands and may themselves depend on other quantities, including corrections and correction factors for systematic effects. The function (f) may be determined experimentally or exist only as an algorithm that must be evaluated numerically.

A.2.2 Evaluating Standard Uncertainty

Several references suggest that an error has two components: a random and a systematic component. Random errors arise from unpredictable or stochastic temporal and spatial variations which influence the measured values and give rise to variations between repeated observations of the measurement. Systematic error, like random error, cannot be eliminated but it can be quantified and corrected. The uncertainty is classified into one of two categories: type A and type B. Uncertainty of type A is characterized by the variance of a series or of repeated observations.

The arithmetic mean (average) and variance of the probability distribution of a quantity (q) that varies randomly under the same conditions and for which (n) independent observations have been obtained can be determined according to the following equations.

$$\bar{q} = \frac{1}{n} \sum_{k=1}^n q_k \quad (\text{A.2})$$

$$s^2(q_k) = \frac{1}{n-1} \sum_{j=1}^n (q_j - \bar{q})^2 \quad (\text{A.3})$$

Both experimental variance of the mean $s^2(\bar{q})$ and standard deviation of the mean $s(\bar{q})$ quantify how well the arithmetic mean estimated the expectation of (q):

$$s^2(\bar{q}) = \frac{s^2(q_k)}{n} \quad (\text{A.4})$$

$$s(\bar{q}) = \sqrt{\frac{s^2(q_k)}{n}} \quad (\text{A.5})$$

For an estimate x_i of an input quantity X_i that has not been obtained from repeated observations, the associate estimated variance $u^2(x_i)$ or the standard uncertainty $u(x_i)$ is evaluated by scientific judgment based on all of the available information on the possible variability of (X_i). This approach for obtaining statistic parameters is referred to as type B evaluation of uncertainty. It is important to recognize that a type B evaluation of uncertainty requires a deep insight into the measuring system but data obtained can be as reliable as type A, mainly where a type A evaluation is based on a comparatively small number of statistically independent observations.

Information for the type B evaluation of standard uncertainty can be obtained from several sources, e.g. previous measurement data, manufacturer's specification, data provided in calibration, and other certificates and uncertainties assigned to reference data taken from handbooks. The quoted uncertainty may state to be a particular multiple of standard deviation, thus, the standard uncertainty $u(x_i)$ is simply the quoted value divided by the multiplier and the estimated variance $u^2(x_i)$ is the square of that quotient. In some situations, it may be stated that the quoted uncertainty defines an interval having a 90, 95, and 99 percent level of confidence and unless otherwise indicated, one may assume that a normal distribution was applied to calculate the quoted uncertainty, and recover the standard uncertainty of x_i by dividing the quote uncertainty by the appropriate

factor for the normal distribution. In other cases, it may be possible to estimate only bounds (upper and lower limits) for the input quantities (X_i); in particular, to state that the probability that the value of X_i lies within the interval a_- to a_+ for all practical purposes is equal to one and the probability that X_i lies outside the interval is essentially zero. If there is no specific knowledge about the possible values of X_i within the interval, one can only assume that it is equally probable for X_i to lie anywhere within it and consequently a rectangular distribution. It is important to emphasize that there are other approaches recommended by the GUM to determine the type B uncertainties and further information can be found elsewhere [126].

A.2.3 Determining Combined Standard Uncertainty

The standard uncertainty of the estimate of measurand (y) is obtained after combining the standard uncertainties $u(x_i)$ of the input estimates (x_N) by the evaluation of type A or B uncertainties. The combined variance $u_c^2(y)$ and standard uncertainty $u_c(y)$ are given by

$$u_c^2(y) = \sum_{i=1}^N \left(\frac{\partial f}{\partial x_i} \right)^2 u^2(x_i) + 2 \sum_{i=1}^{N-1} \sum_{j=i+1}^N \frac{\partial f}{\partial x_i} \frac{\partial f}{\partial x_j} u(x_i, x_j) \quad (\text{A.6})$$

$$u_c(y) = \sqrt{u_c^2(y)} \quad (\text{A.7})$$

The last term on the right side of Equation A.6 estimates the covariance of x_i and x_j and can be eliminated if the two variables are assumed to be uncorrelated. The partial derivatives are called the sensitivity coefficients and describe how the output estimate (y) varies with changes in the input estimates. In case of correlated input quantities, the degree of correlation between x_i and x_j is characterized by the estimated correlation coefficient according to Equation A.8.

$$r(x_i, x_j) = \frac{u(x_i, x_j)}{u(x_i) u(x_j)} \quad (\text{A.8})$$

A.2.4 Determining Expanded Uncertainty

The parameter used for quantitatively expressing the uncertainty of a measurement is obtained by defining an interval which encompasses a large

fraction of the distribution of values obtainable by the measurand. This additional measure of uncertainty is termed expanded uncertainty (U) and is obtained by multiplying the combined standard uncertainty by a coverage factor (k).

$$U = k u_c(y) \quad (\text{A.9})$$

The coverage factor is chosen based on the level of confidence (p) required of interval ($y-U$) to ($y+U$). Whenever practicable, the level of confidence associated with the interval should be clearly stated. However, it should be recognized that the level of confidence is usually rather uncertain, not only because of limited knowledge of the probability distribution characterized by (y) and $u_c(y)$, but also because of the uncertainty of $u_c(y)$ itself. A simpler approach recommended by the GUM is often adequate in measurement situations where the probability distribution characterized by (y) and $u_c(y)$ can be described by well-behaved probability distributions such as the normal and rectangular distributions, and where the effective degrees of freedom (ν_{eff}) of $u_c(y)$ is of significant size. Under these circumstances, the probability distribution characterized by the measurement result and its combined standard uncertainty can be assumed to be normal because of the central limit theorem.

The degrees of freedom can be computed from the Welch-Satterthwaite formula as described in Equation A.10. If $u(x_i)$ is obtained from a type A evaluation, the degrees of freedom is equal to ($\nu_i = n - 1$) for a single quantity estimated by the arithmetic mean of independent observations (n). If n independent observations are used to determine both the slope and intercept of a straight line by the method of least squares, the degrees of freedom of their respective standard uncertainties is ($\nu_i = n - 2$). If $u(x_i)$ is obtained from a type B evaluation and if it can be treated as exactly known, which is often the case in practice, the degrees of freedom tends to infinity ($\nu_i \rightarrow \infty$).

$$\nu_{\text{eff}} = \frac{u_c^4(y)}{\sum_{i=1}^N \frac{u_i^4(y)}{\nu_i}} \quad (\text{A.10})$$

The coverage factor (k), assuming $k = t_p(\nu_{\text{eff}})$, is obtained for the desired level of confidence (p) from Table A.1. It is worthy of mention that all values of expanded uncertainties in the present work have been obtained assuming a normal distribution and using a 95.45 % confidence level that produces a coverage factor of 2.00 for infinite degrees of freedom.

Table A.1: Values of $t_p(v_{\text{eff}})$ from the t-distribution for degrees of freedom v that defined an interval $-t_p(v)$ to $t_p(v)$ that encompasses the fraction (p) of the distribution.

Degrees of freedom v_{eff}	Fraction p in percent					
	68.27	90.00	95.00	95.45	99.00	99.73
10	1.05	1.80	2.20	2.25	3.11	3.85
15	1.03	1.75	2.13	2.18	2.95	3.59
20	1.03	1.72	2.09	2.13	2.80	3.42
25	1.02	1.71	2.06	2.11	2.79	3.33
35	1.01	1.70	2.03	2.07	2.72	3.23
50	1.01	1.68	2.01	2.05	2.68	3.16
100	1.00	1.66	1.98	2.02	2.63	3.08
∞	1.00	1.64	1.96	2.00	2.58	3.00

A.3 Assessing Measurement Uncertainty of Input and Output Combustion Parameters

In this section, the uncertainties of input and output parameters (such as temperature, gas composition, and flow rate) are calculated. Because most analog devices and analytical instruments operate continuously and because the standard deviation of the results are negligible compared to the systematic errors, a type A evaluation is not included here; the only exception is in the case of coal feed rate. The sources of uncertainty for each parameter with their respective error and type of distribution are firstly summarized in a table and followed by a presentation of the standard and expanded uncertainties of the measurement.

A.3.1 Coal Feed Rate

The coal feed rate is continuously monitored by load cells installed under the container of the metering system. Because of the variations of the coal fluidized bed characteristics along the operation, an algorithm controls the mass loss over a certain time period and corrects the speed of the metering disk. For simplicity, the uncertainty of this algorithm is not considered in the evaluation of the experimental errors. The sources of systematic error are listed in Table A.2 and the standard and expanded uncertainties are compared in Figure A.1. A maximum operating mass of the container (i.e. 70 kg) is assumed in the calculation of error due to sensitivity. The expanded uncertainty, which includes random error of type A, is based on the values of standard deviation of the mean obtained during the commissioning of the test facility.

Table A.2: Sources of uncertainty for the measurement of coal feed rate.

Source of uncertainty	Error	Type of distribution	Divider	DF
Sensitivity	$\pm 0.10\%$ of value	Rectangular	1.732	∞
Hysteresis	$\pm 0.008\%$ of range	Rectangular	1.732	∞
Non-linearity	$\pm 0.017\%$ of range	Rectangular	1.732	∞
Temperature effect – zero balance	$\pm 0.014\%$ of range	Rectangular	1.732	∞
Temperature effect – sensitivity	$\pm 0.007\%$ of range	Rectangular	1.732	∞
Verification interval	$\pm 0.009\%$ of range	Rectangular	1.732	∞

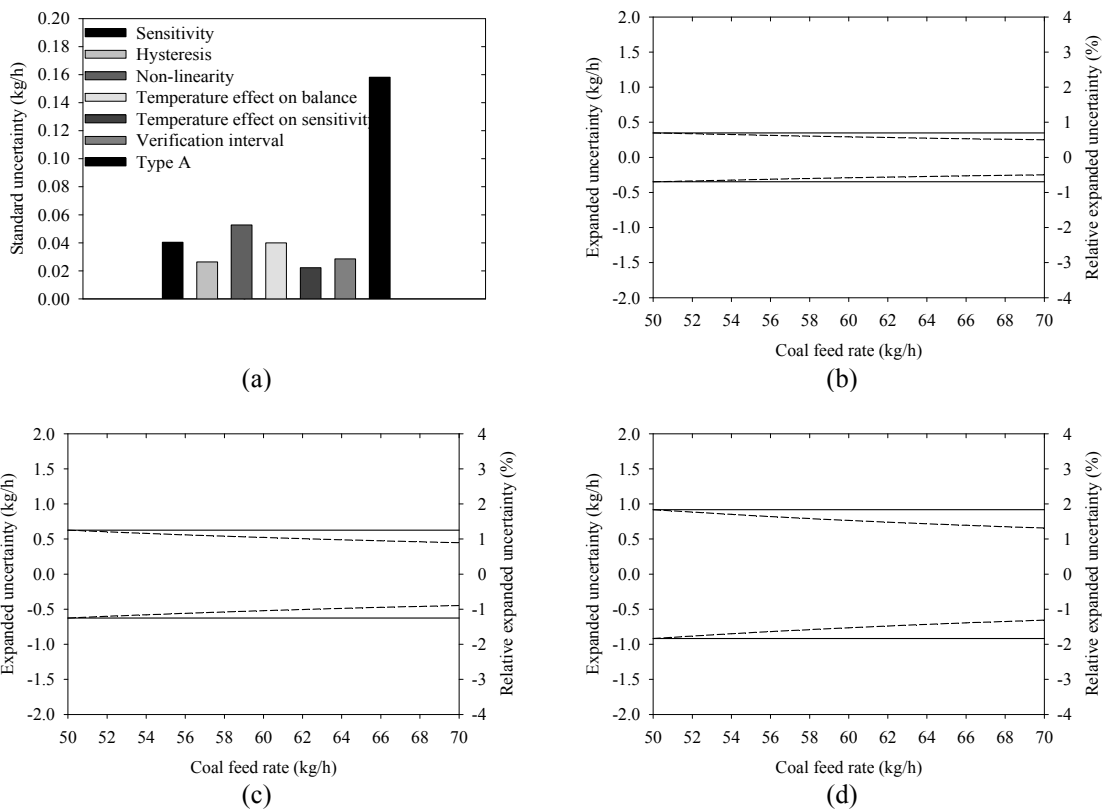


Figure A.1: (a) Comparison of standard uncertainty for a standard deviation of the mean of 0.16 kg/h; expanded uncertainty for the measurement of coal feed rate for standard deviations of the mean of (b) 0.16 kg/h, (c) 0.30 kg/h, and (d) 0.45 kg/h. Solid line: expanded uncertainty in kg/h; dashed line: relative expanded uncertainty.

A.3.2 Temperature of Feed Gas, Flue Gas, and Furnace Wall

The uncertainty analysis of temperature measurements in the feed gas, flue gas, and water cooling walls, monitored with standard resistance temperature detectors

(RTD), are summarized in Table A.3 and in Figure A.2. Inner surface temperatures at cylindrical section of the furnace are monitored with a thermocouple ANSI type B and the analysis of uncertainty is fully detailed in the Table A.4 and Figure A.3.

Table A.3: Sources of uncertainty for the measurement of temperature with RTD.

Source of uncertainty	Error	Type of distribution	Divider	DF
Accuracy of RTD	$\pm(0.15+0.002T)$	Normal	3.00	∞
Signal converter	± 0.20 °C	Rectangular	1.732	∞
Accuracy of reference temperature	± 0.50 °C	Rectangular	1.732	∞
Repeatability	$\pm 0.05\%$ of range	Rectangular	1.732	∞
Data acquisition	± 0.05 °C	Rectangular	1.732	∞

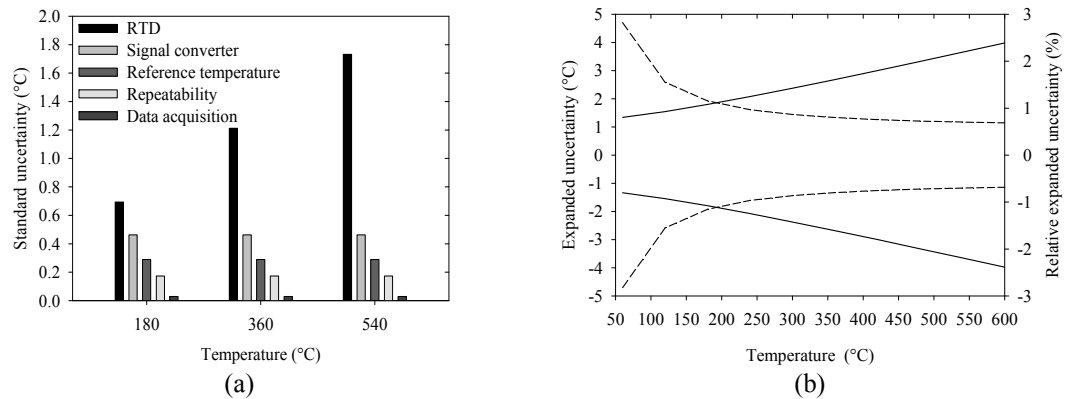


Figure A.2: (a) Comparison of standard uncertainty and (b) expanded uncertainty for the measurement of temperature with RTD. Solid line: expanded uncertainty in °C; dashed line: relative expanded uncertainty.

Table A.4: Sources of uncertainty for the measurement of temperature with thermocouple ANSI type B.

Source of uncertainty	Error	Type of distribution	Divider	DF
Accuracy of thermocouple	$\pm 0.0025T$	Rectangular	1.732	∞
Signal converter	$\pm(1+0.0003)T$	Rectangular	1.732	∞
Data acquisition	$\pm 0.00015 T$	Rectangular	1.732	∞

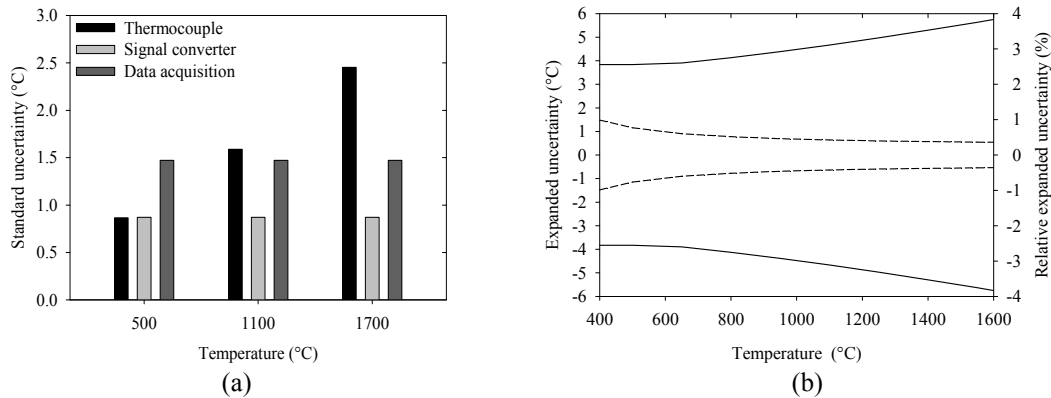


Figure A.3: (a) Comparison of standard uncertainty and (b) expanded uncertainty for the measurement of temperature with thermocouple type B. Solid line: expanded uncertainty in °C; dashed line: relative expanded uncertainty.

A.3.3 Flow Rate of the Primary Stream

The volumetric flow rate of the primary stream is measured using thermal mass flow meters. The sources of uncertainty along with standard and expanded uncertainty are presented in Table A.5 and in Figure A.4.

Table A.5: Sources of uncertainty for the measurement of primary flow rate.

Source of uncertainty	Error	Type of distribution	Divider	DF
Accuracy of transmitter	$\pm 3.00\%$ of range	Rectangular	1.732	∞
Repeatability of transmitter	$\pm 0.50\%$ of range	Rectangular	1.732	∞
Accuracy of data acquisition	$\pm 0.15\%$ of range	Rectangular	1.732	∞

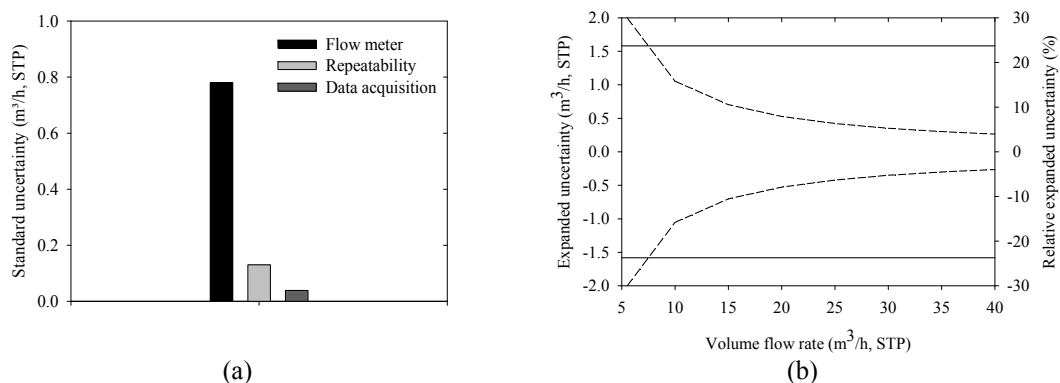


Figure A.4: (a) Comparison of standard uncertainty and (b) expanded uncertainty for the measurement of primary flow rate. Solid line: expanded uncertainty in m³/h; dashed line: relative expanded uncertainty.

A.3.4 Flow Rate of the Secondary, Tertiary and Flue Gas Streams

The flow rate of the secondary, tertiary, and flue gas streams are monitored continuously with orifice plates. For the calculation of the flow rate, temperature and pressure are also monitored. Because the flow rate is calculated as a function of the temperature, pressure, and differential pressure (Equation A.11), sensitivity coefficients are derived for the calculation of the combined uncertainty (Equations A.12-A.16). The sources of uncertainties are summarized in Table A.6 and the standard and expanded uncertainty of the volume flow rate based on STP conditions at several positions in the feed gas and flue gas path are compared in the Figures A.5-A.7. It is worthy of mention that the diameter of the orifice plate and pipe are assumed to be exactly know (without error). Because the influence of the gas composition is less significant, the expanded uncertainty is valid for both firing conditions. Furthermore, the temperature used in each orifice plate has only a negligible impact on the final expanded uncertainty; for this reason only the highest values of experimental errors are here summarized.

$$\dot{m} = \frac{C\varepsilon}{\sqrt{1-\beta^4}} \frac{\pi d^2}{4} \sqrt{2\Delta P \frac{MP}{RT}} \quad (\text{A.11})$$

$$\frac{\partial \dot{m}}{\partial C} = \frac{\varepsilon}{\sqrt{1-\beta^4}} \frac{\pi d^2}{4} \sqrt{2\Delta P \frac{MP}{RT}} \quad (\text{A.12})$$

$$\frac{\partial \dot{m}}{\partial \varepsilon} = \frac{C}{\sqrt{1-\beta^4}} \frac{\pi d^2}{4} \sqrt{2\Delta P \frac{MP}{RT}} \quad (\text{A.13})$$

$$\frac{\partial \dot{m}}{\partial \Delta P} = \frac{C}{2\sqrt{\Delta P(1-\beta^4)}} \frac{\pi d^2}{4} \sqrt{\frac{2MP}{RT}} \quad (\text{A.14})$$

$$\frac{\partial \dot{m}}{\partial P} = \frac{C}{2\sqrt{P(1-\beta^4)}} \frac{\pi d^2}{4} \sqrt{2\Delta P \frac{M}{RT}} \quad (\text{A.15})$$

$$\frac{\partial \dot{m}}{\partial T} = \frac{-C}{2T^{3/2} \sqrt{(1-\beta^4)}} \frac{\pi d^2}{4} \sqrt{2\Delta P \frac{MP}{R}} \quad (\text{A.16})$$

Table A.6: Sources of uncertainty for the measurement of flow rates with orifice plates.

	Source of uncertainty	Error	Type of distribution	Divider	DF
Temperature (T)	Accuracy of RTD	$\pm(0.15+0.002T)$	Normal	3.00	∞
	Signal converter	± 0.20 °C	Rectangular	1.732	∞
	Reference temperature	± 0.50 °C	Rectangular	1.732	∞
	Repeatability	$\pm 0.05\%$ of range	Rectangular	1.732	∞
	Data acquisition	± 0.05 °C	Rectangular	1.732	∞
Pressure (P)	Transmitter	$\pm 0.10\%$ of URV	Normal	3.00	∞
	Line pressure effect	$\pm 0.25\%$ of URL	Normal	3.00	∞
	Ambient temperature	$\pm(0.25\% \text{ URL} + 0.10\% \text{ URV})$	Normal	3.00	∞
	Data acquisition	$\pm 0.15\%$ of range	Rectangular	1.732	∞
Differential pressure (ΔP)	Long term stability	$\pm 0.15\%$ of URL	Rectangular	1.732	∞
	Thermal change of the zero output and the output span	$\text{URL}(0.31\text{TD} + 0.06)$	Rectangular	1.732	∞
	Operating pressure span	$\pm 0.14\%$ of URL	Rectangular	1.732	∞
	Accuracy of data acquisition	$\pm 0.15\%$ of range	Rectangular	1.732	∞
Model	Expansion coefficient (ϵ)	$\pm(1.67\beta - 0.50)\%$	Rectangular	1.732	∞
	Discharge coefficient (C)	$\pm(3.50 \Delta P / \kappa P_1)\%$	Rectangular	1.732	∞

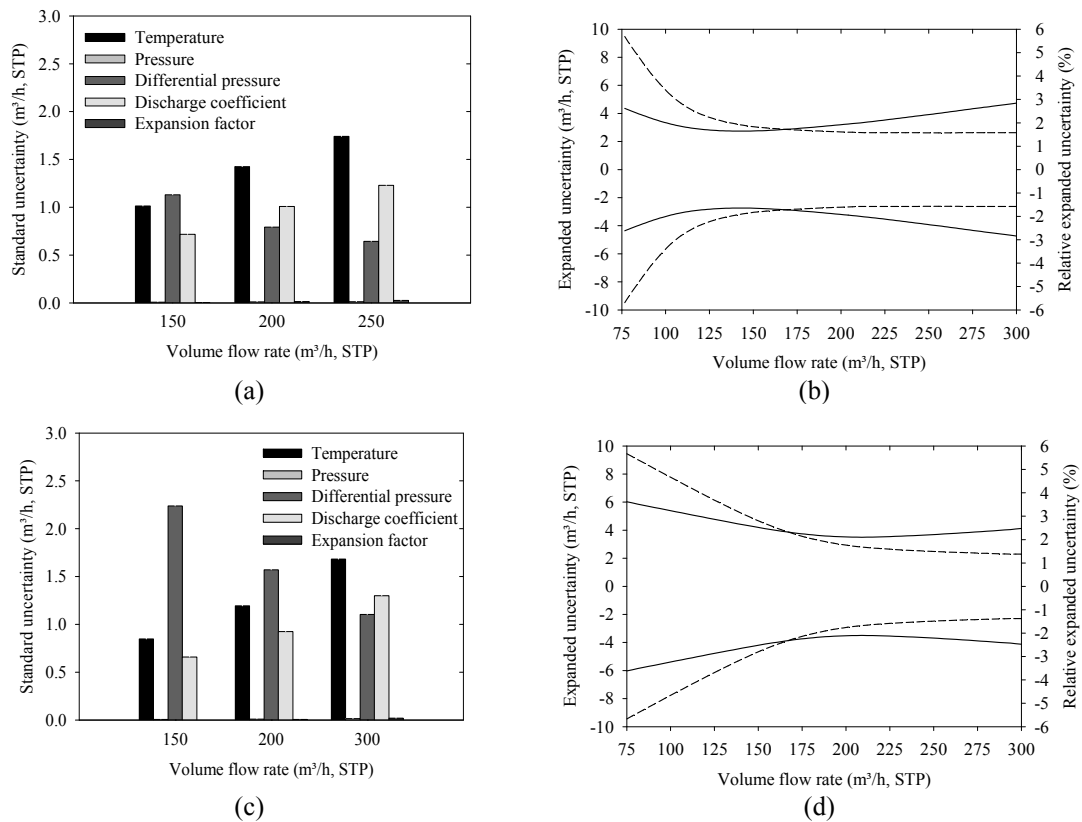


Figure A.5: Comparison of standard uncertainty and expanded uncertainty for the measurement of (a,b) secondary and (c,d) tertiary feed gas streams. Solid line: expanded uncertainty in m³/h; dashed line: relative expanded uncertainty.

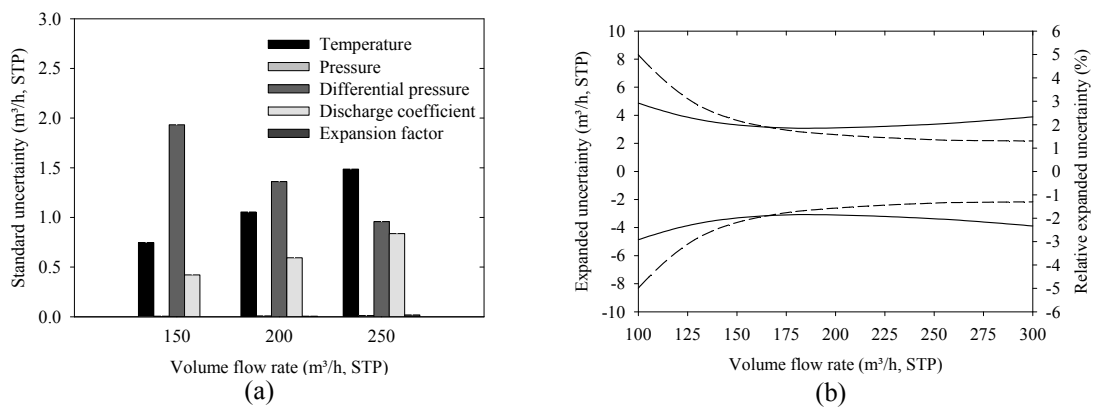


Figure A.6: (a) Comparison of standard uncertainty and (b) expanded uncertainty for the measurement of recirculated flue gas flow rate. Solid line: expanded uncertainty in m³/h; dashed line: relative expanded uncertainty.

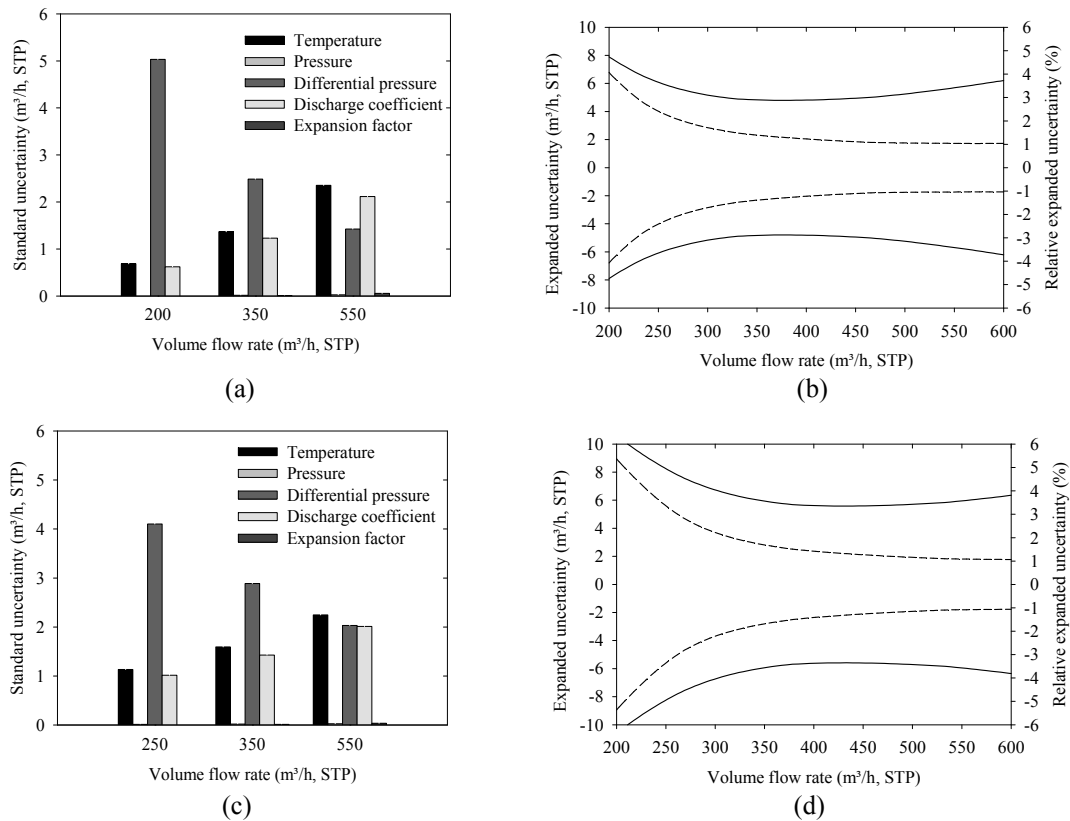


Figure A.7: Comparison of standard uncertainty and expanded uncertainty for the flue gas flow rate at the (a,b) furnace exit and (c,d) stack. Solid line: expanded uncertainty in m³/h; dashed line: relative expanded uncertainty.

A.3.5 Feed Gas and Flue Gas Composition

The O₂ concentration in the feed gas and the flue gas at exit of the furnace are measured on a wet basis via a gas-potentiometric analysis. The uncertainties of the experimental data are summarized in Table A.7 and Figure A.8. Volumetric fraction of water vapor in the flue gas is monitored continuously by a gas humidity analyzer. The measurement uncertainty is detailed in Table A.8 and in Figure A.9.

Table A.7: Sources of uncertainty for the measurement of O₂ concentration with gas-potentiometric analysis.

Source of uncertainty	Error	Type of distribution	Divider	DF
Accuracy of transmitter	±5.00% of value	Rectangular	1.732	∞
Accuracy of data acquisition	±0.15% of range	Rectangular	1.732	∞

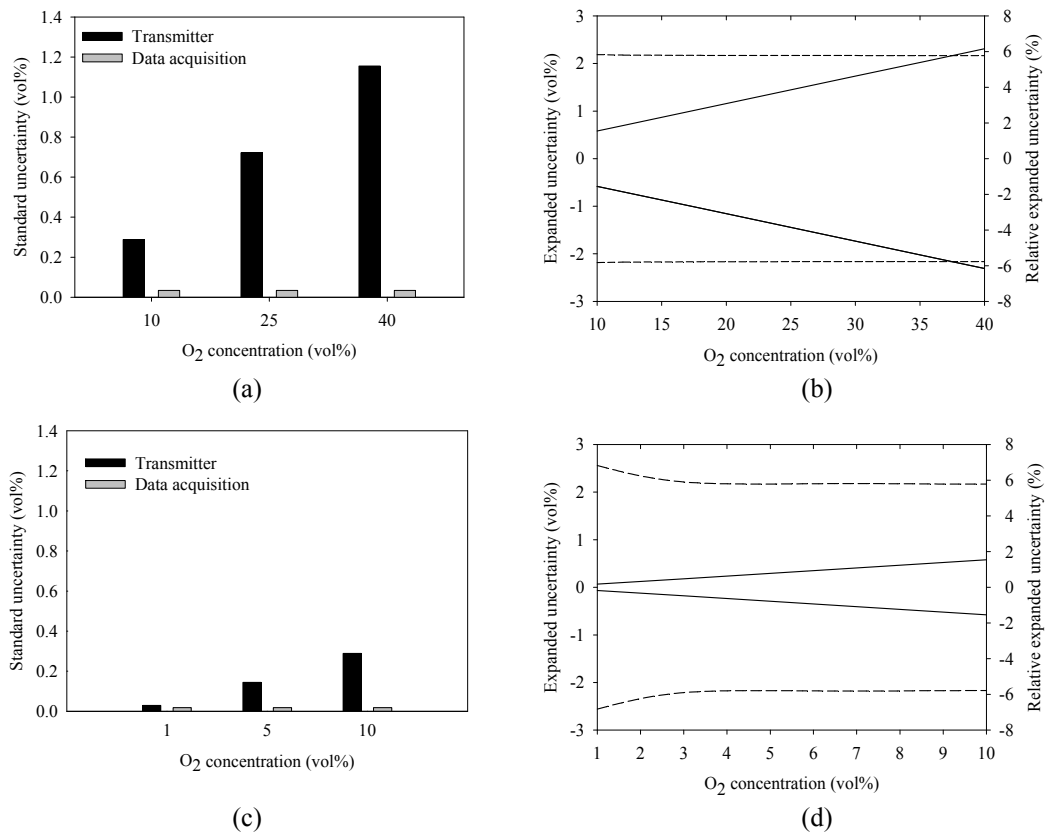


Figure A.8: Comparison of standard uncertainty and expanded uncertainty for the measurement of O₂ on wet basis in the (a,b) feed gas and (c,d) flue gas. Solid line: expanded uncertainty in vol%; dashed line: relative expanded uncertainty.

Table A.8: Sources of uncertainty for the measurement of water vapor concentration.

Source of uncertainty	Error	Type of distribution	Divider	DF
Accuracy of transmitter	$\pm 0.20\%$ of value	Rectangular	1.732	∞
Accuracy of data acquisition	$\pm 0.15\%$ of range	Rectangular	1.732	∞

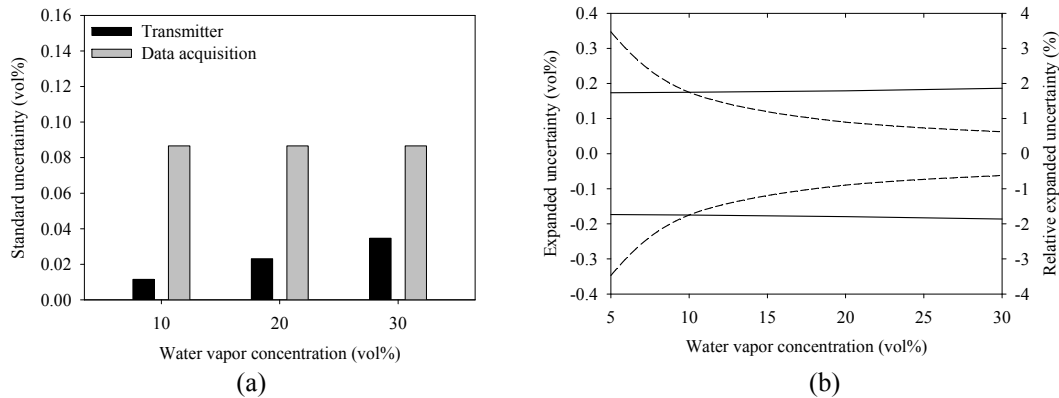


Figure A.9: (a) Comparison of standard uncertainty and (b) expanded uncertainty or the measurement of water vapor concentration. Solid line: expanded uncertainty in vol%; dashed line: relative expanded uncertainty.

The dry-basis concentration of O_2 at the exit of the furnace and stack is measured using magnetic pressure analyzers with a measurement range of 0-25 vol%. Analyzers based on non-dispersive infrared absorption measure the dry-basis concentration of CO (range: 0-300 mg/m³) and CO₂ (range: 0-100 vol%). A process photometer for measuring gas filter correlation determines the NO concentration (range of 0-3000 mg/m³), while wavelength comparison in an ultraviolet spectrum measures dry-basis SO₂ (range: 0-5000 mg/m³). The linearity and sensitivity of other substances were obtained during calibration procedures. Further sources of errors are summarized in the following Tables (A.9-A.13); the standard and expanded uncertainties are compared in the following Figures (A.10-A.14).

Table A.9: Sources of uncertainty for the measurement of O_2 concentration.

Source of uncertainty	Error at furnace exit	Error at stack	Type of distribution	Divider	DF
Linearity	±0.075 vol%	±0.075 vol%	Rectangular	1.732	∞
Sensitivity	±0.71 vol%	±0.26 vol%	Rectangular	1.732	∞
Output fluctuation	± 0.0025 vol%	± 0.0025 vol%	Normal	2.00	∞
Repeatability	± 0.0050 vol%	± 0.0050 vol%	Rectangular	1.732	∞
Detection limit	± 0.0050 vol%	± 0.0050 vol%	Normal	4.00	∞
Data acquisition	±0.15% of range	±0.15% of range	Rectangular	1.732	∞

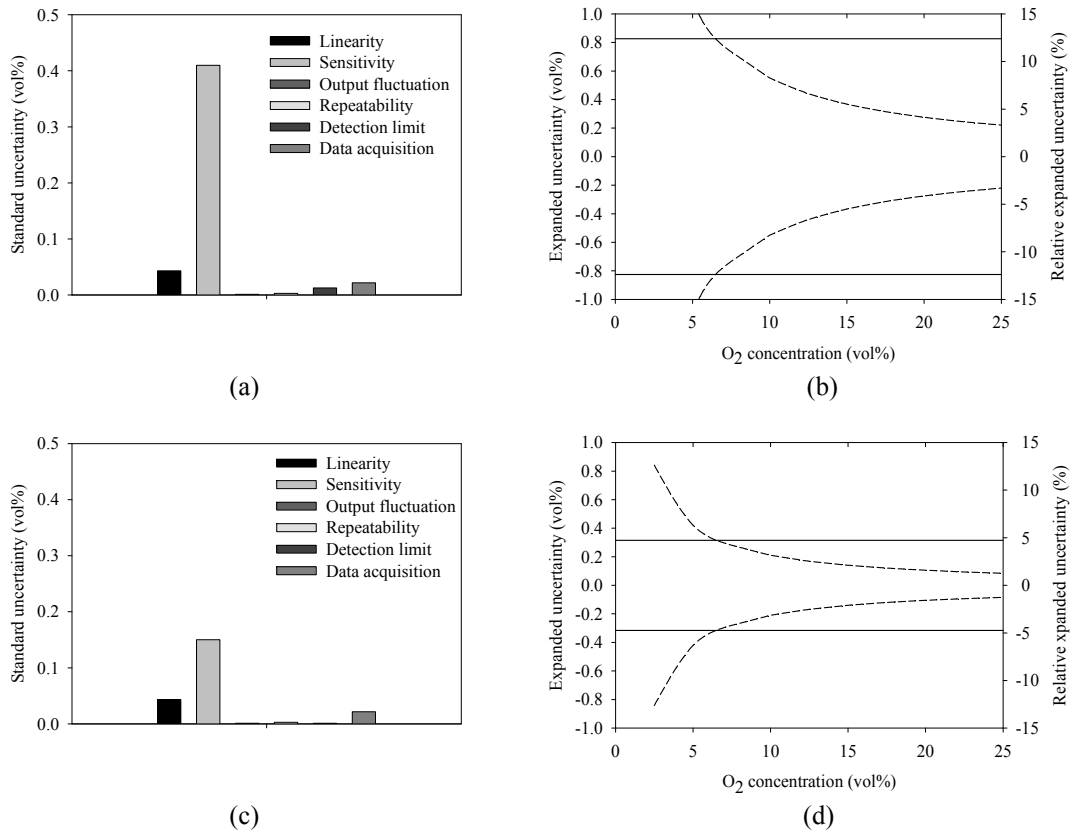


Figure A.10: Comparison of standard uncertainty and expanded uncertainty for the measurement of O₂ concentration on dry basis at (a,b) furnace exit and (c,d) stack. Solid line: expanded uncertainty in vol%; dashed line: relative expanded uncertainty.

Table A.10: Sources of uncertainty for the measurement of CO₂ concentration.

Source of uncertainty	Error at furnace exit	Error at stack	Type of distribution	Divider	DF
Linearity	±0.70 vol%	±0.30 vol%	Rectangular	1.732	∞
Sensitivity	±0.00 vol%	±0.00 vol%	Rectangular	1.732	∞
Output fluctuation	±0.20 vol%	±0.20 vol%	Normal	2.00	∞
Repeatability	±0.50 vol%	±0.50 vol%	Rectangular	1.732	
Detection limit	±0.40 vol%	±0.40 vol%	Normal	4.00	∞
Data acquisition	±0.15% of range	±0.15% of range	Rectangular	1.732	∞

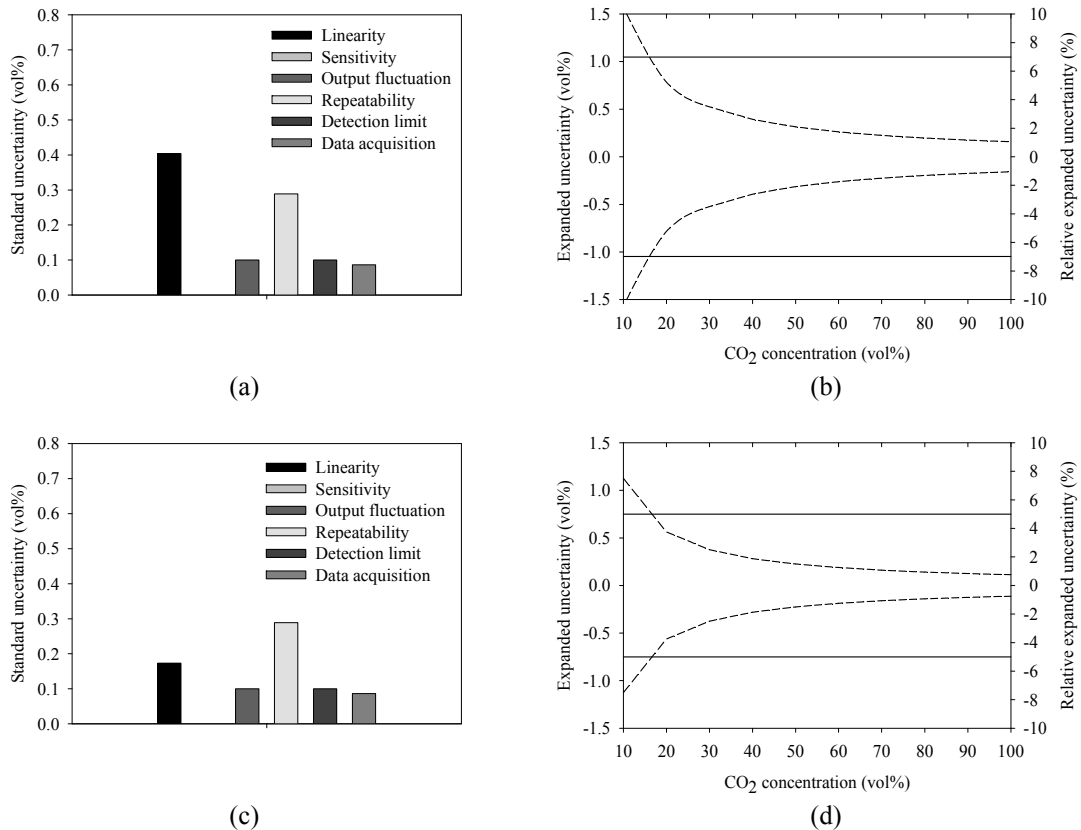


Figure A.11: Comparison of standard uncertainty and expanded uncertainty for the measurement of CO₂ concentration on dry basis at (a,b) furnace exit and (c,d) stack. Solid line: expanded uncertainty in vol%; dashed line: relative expanded uncertainty.

Table A.11: Sources of uncertainty for the measurement of CO concentration.

Source of uncertainty	Error at furnace exit	Error at stack	Type of distribution	Divider	DF
Linearity	$\pm 0.90 \text{ mg/m}^3$	$\pm 2.10 \text{ mg/m}^3$	Rectangular	1.732	∞
Sensitivity	$\pm 0.21 \text{ mg/m}^3$	$\pm 1.71 \text{ mg/m}^3$	Rectangular	1.732	∞
Output fluctuation	$\pm 0.60 \text{ mg/m}^3$	$\pm 0.60 \text{ mg/m}^3$	Normal	2.00	∞
Repeatability	$\pm 1.50 \text{ mg/m}^3$	$\pm 1.50 \text{ mg/m}^3$	Rectangular	1.732	∞
Detection limit	$\pm 1.20 \text{ mg/m}^3$	$\pm 1.50 \text{ mg/m}^3$	Normal	4.00	∞
Data acquisition	$\pm 0.15\%$ of scale	$\pm 0.15\%$ of scale	Rectangular	1.732	∞

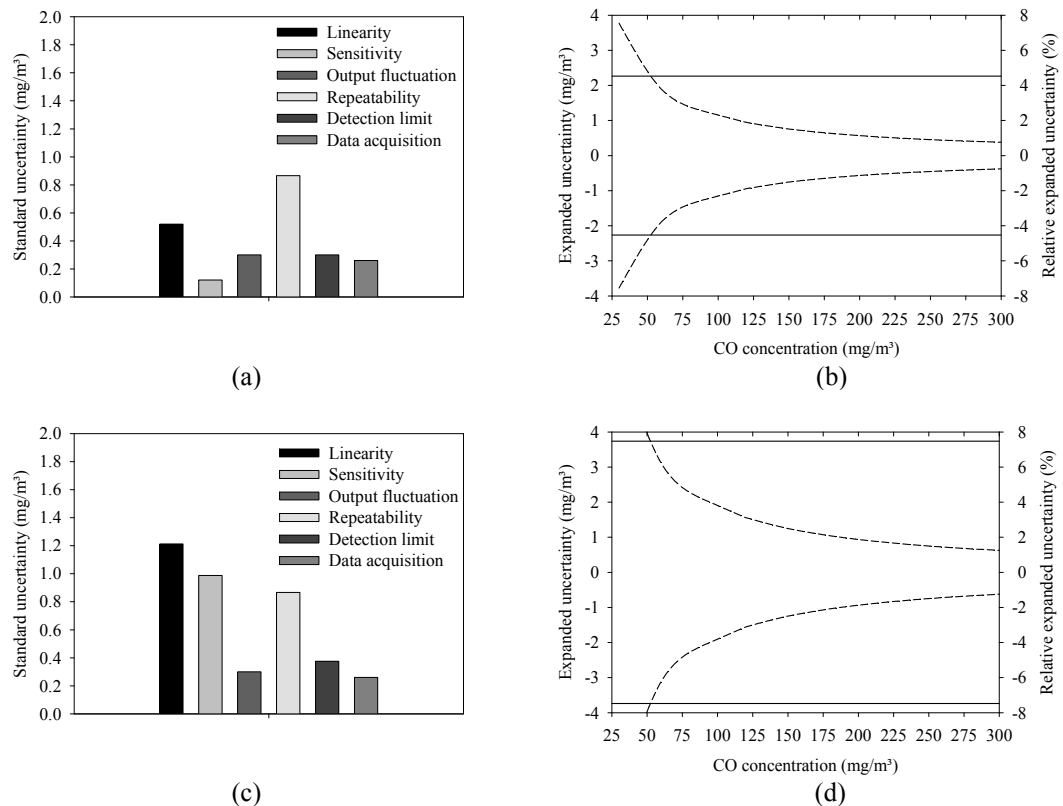


Figure A.12: Comparison of standard uncertainty and expanded uncertainty for the measurement of CO concentration on dry basis at (a,b) furnace exit and (c,d) stack. Solid line: expanded uncertainty in mg/m³; dashed line: relative expanded uncertainty.

Table A.12: Sources of uncertainty for the measurement of NO concentration.

Source of uncertainty	Error at furnace exit	Error at stack	Type of distribution	Divider	DF
Linearity	±21 mg/m ³	±6 mg/m ³	Rectangular	1.732	∞
Sensitivity	±15 mg/m ³	±9 mg/m ³	Rectangular	1.732	∞
Output fluctuation	±15 mg/m ³	±15 mg/m ³	Normal	2.00	∞
Repeatability	±15 mg/m ³	±15 mg/m ³	Rectangular	1.732	∞
Detection limit	±30 mg/m ³	±30 mg/m ³	Normal	4.00	∞
Data acquisition	±0.15% of range	±0.15% of range	Rectangular	1.732	∞

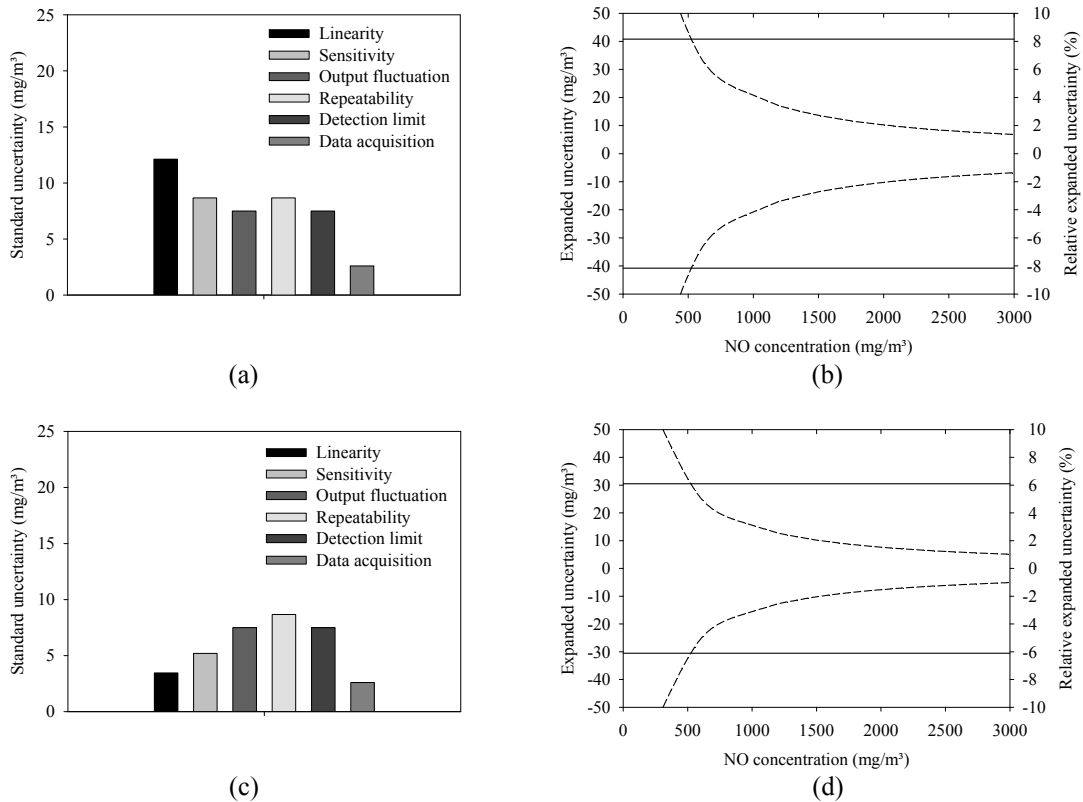


Figure A.13: Comparison of standard uncertainty and expanded uncertainty for the measurement of NO concentration on dry basis at (a,b) furnace exit and (c,d) stack. Solid line: expanded uncertainty in mg/m³; dashed line: relative expanded uncertainty.

Table A.13: Sources of uncertainty for the measurement of SO₂ concentration.

Source of uncertainty	Error at furnace exit	Error at stack	Distribution	Divider	DF
Linearity	±5 mg/m ³	±5 mg/m ³	Rectangular	1.732	∞
Sensitivity	± 7 mg/m ³	± 5 mg/m ³	Rectangular	1.732	∞
Output fluctuation	±25 mg/m ³	±25 mg/m ³	Normal	2.00	∞
Repeatability	±25 mg/m ³	±25 mg/m ³	Rectangular	1.732	∞
Detection limit	±50 mg/m ³	±50 mg/m ³	Normal	4.00	∞
Data acquisition	±0.15% of range	±0.15% of range	Rectangular	1.732	∞

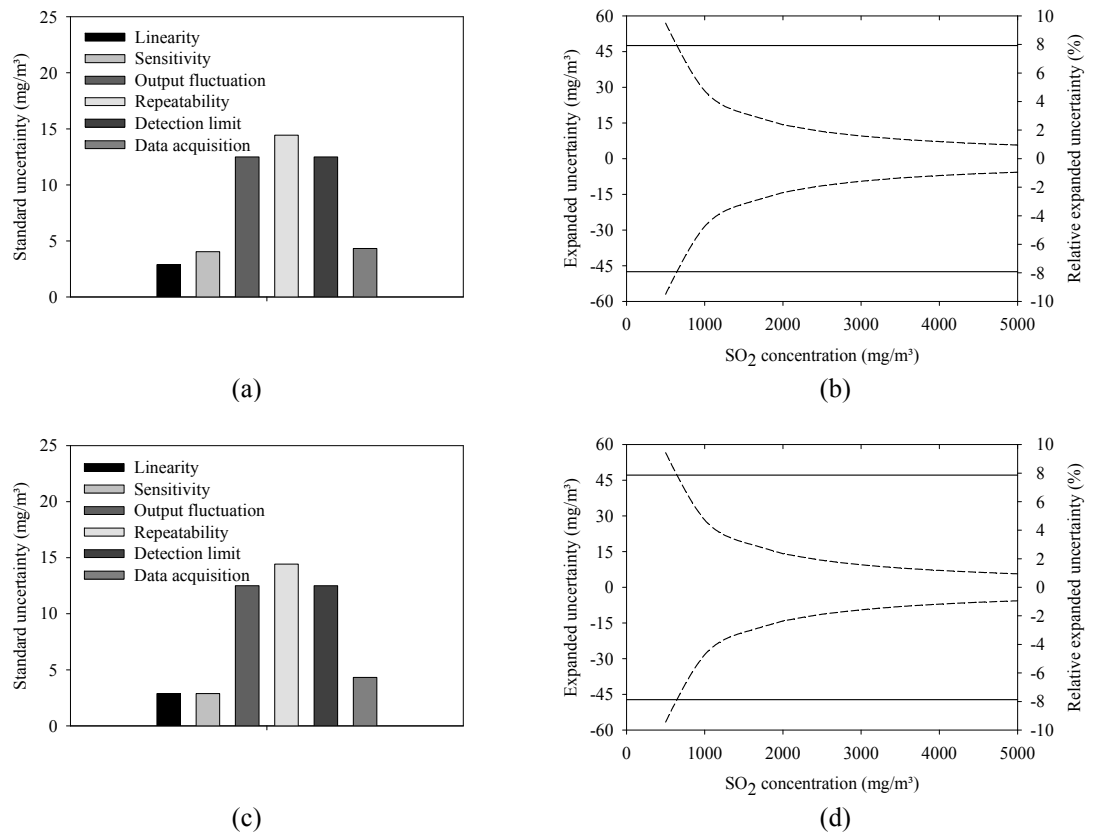


Figure A.14: Comparison of standard uncertainty and expanded uncertainty for the measurement of SO₂ concentration on dry basis at (a,b) furnace exit and (c,d) stack. Solid line: expanded uncertainty in mg/m³; dashed line: relative expanded uncertainty.

A.3.6 Emission Rates

For the evaluation of various combustion scenarios, emissions are presented in terms of the mass of emission per unit of input energy (Equation A.17). The uncertainty of emission rates are based on the measurement error of the parameters evaluated (i.e. volume flow rate of flue gas, gas species concentration, and coal feed rate). The sensitivity coefficients represented by the partial derivatives used in the calculation of combined standard uncertainties are fully described in Equations A.18-A.21. The expanded uncertainties for the emission rates of SO₂ and NO are presented in Figures A.15 and A.16. Expanded uncertainty was based on typical values of volume flow rate of flue gas and concentration of water vapor under air-fired and oxy-fired conditions.

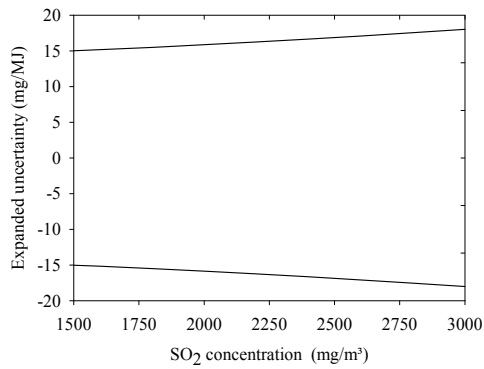
$$\varphi_i = \frac{1000 y_i \dot{V}_{\text{flue gas (STP)}}(1-x_{\text{H}_2\text{O}})}{\dot{m}_{\text{coal}} \text{LHV}} \quad (\text{A.17})$$

$$\frac{\partial \varphi_i}{\partial y_i} = \frac{1000 \dot{V}_{\text{flue gas (STP)}}(1-x_{\text{H}_2\text{O}})}{\dot{m}_{\text{coal}} \text{LHV}} \quad (\text{A.18})$$

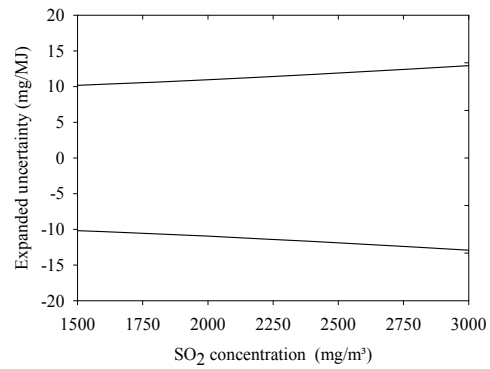
$$\frac{\partial \varphi_i}{\partial \dot{V}_{\text{flue gas (STP)}}} = \frac{1000 y_i(1-x_{\text{H}_2\text{O}})}{\dot{m}_{\text{coal}} \text{LHV}} \quad (\text{A.19})$$

$$\frac{\partial \varphi_i}{\partial x_{\text{H}_2\text{O}}} = \frac{-1000 y_i \dot{V}_{\text{flue gas (STP)}}}{\dot{m}_{\text{coal}} \text{LHV}} \quad (\text{A.20})$$

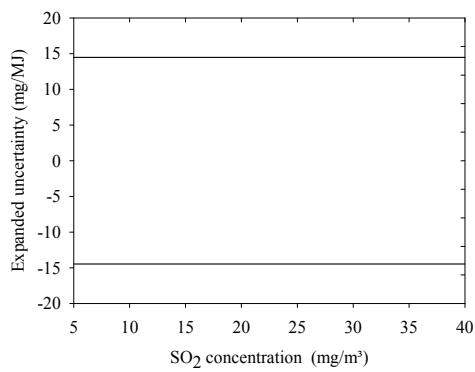
$$\frac{\partial \varphi_i}{\partial \dot{m}_{\text{coal}}} = \frac{-1000 y_i \dot{V}_{\text{flue gas (STP)}}(1-x_{\text{H}_2\text{O}})}{\dot{m}_{\text{coal}}^2 \text{LHV}} \quad (\text{A.21})$$



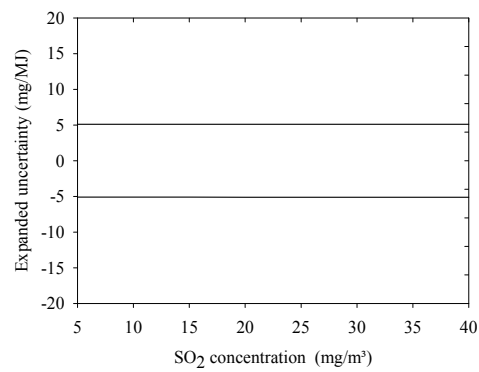
(a)



(b)



(c)



(d)

Figure A.15: Expanded uncertainty for the measurement of SO₂ emission rate at furnace exit and stack for (a,c) air-firing and (b,d) oxy-firing.

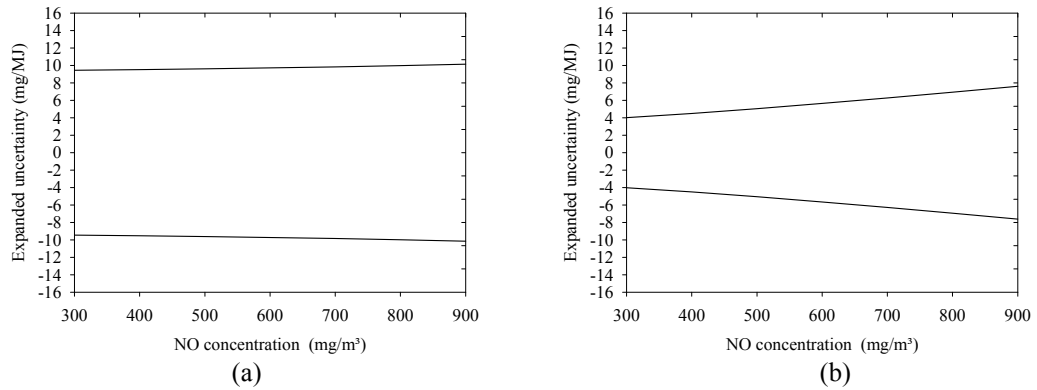


Figure A.16: Expanded uncertainty for the measurement of NO emission rate at stack for (a) air-firing and (b) oxy-firing.

A.3.7 Furnace Heat Transfer Rates

The uptake heat is calculated by Equation A.22, while the derived sensitivity coefficients are described by Equations A.23 and A.24. The water volume flow rate is monitored continuously by an orifice plate, whereas the temperatures are monitored with standard resistance thermometers. The sources of uncertainty are summarized in Table A.14; comparison of error sources and expanded uncertainty for various heat flow rates are presented in Figure A.17.

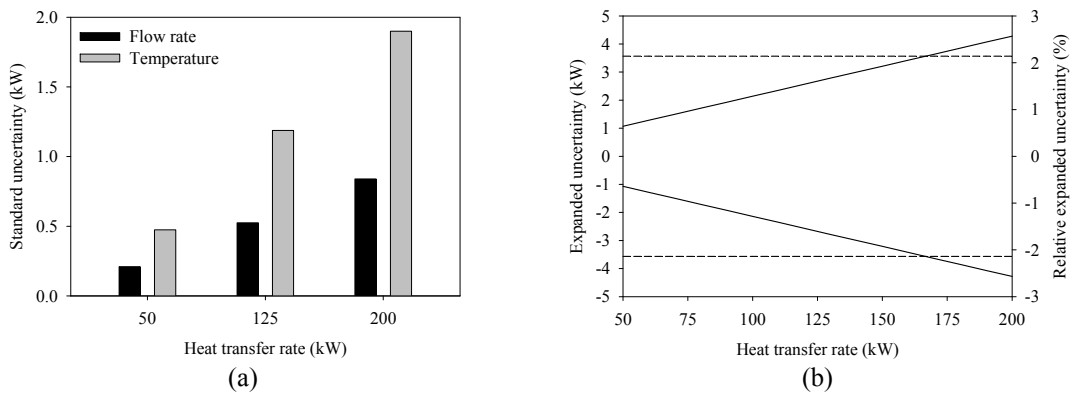
$$\dot{Q} = \frac{\dot{V} \rho c_p \Delta T}{3600} \quad (\text{A.22})$$

$$\frac{\partial \dot{V}}{\partial \dot{Q}} = \frac{\rho c_p \Delta T}{3600} \quad (\text{A.23})$$

$$\frac{\partial \Delta T}{\partial \dot{Q}} = \frac{\dot{V} \rho c_p}{3600} \quad (\text{A.24})$$

Table A.14: Sources of uncertainty for the measurement of heat transfer rate.

	Source of uncertainty	Error	Type of distribution	Divider	DF
Flow rate (\dot{V})	Orifice plate	$\pm(7.08E-05 \dot{V}^2 + 5.28E-03\dot{V} + 0.013289)$	Rectangular	1.732	∞
	Data acquisition	$\pm 0.15\%$ of range	Rectangular	1.732	∞
Temperature (T)	Accuracy of RTD	$\pm(0.15 + 0.002T)$	Normal	3.00	∞
	Signal converter	± 0.20 °C	Rectangular	1.732	∞
	Reference temperature	± 0.50 °C	Rectangular	1.732	∞
	Repeatability	$\pm 0.05\%$ of scale	Rectangular	1.732	∞
	Data acquisition	± 0.05 °C	Rectangular	1.732	∞

**Figure A.17:** (a) Comparison of standard uncertainty and (b) expanded uncertainty for the measurement of heat transfer rate. Solid line: expanded uncertainty in kW; dashed line: relative expanded uncertainty.

A.4 Assessing Measurement Uncertainty of Local Gas Temperature

Measurements of local temperature in the furnace are obtained using intrusive suction pyrometers equipped with ANSI type K and type B thermocouples. All thermocouples are calibrated with a reference temperature calibrator before each experimental run. The calibrator has an operating range of 150-1200 °C and an accuracy of ± 0.01 °C. The calibration temperatures are varied from 400 to 1200 °C in steps of 200 °C; standard deviations are based on 10 independent observations. The error due to extension cable and data acquisition; systematic source of errors, including variations in the gas velocity; and other environmental conditions are determined using the equations detailed by Chedaille and Braud [111]. The sources of uncertainty for the in-flame measurements with suction pyrometers are listed in Table A.15. Typical values for the standard deviation of

the mean obtained in the measurements are used in evaluating the type A uncertainty (Figure A.18 and A.19).

Table A.15: Sources of uncertainty for the measurement of local gas temperature with type K and type B thermocouples.

Source of uncertainty	Error	Type of distribution	Divider	DF
Calibration (type K)	$\pm (0.010T + 0.58) \text{ }^\circ\text{C}$	Normal	2.00	∞
Calibration (type B)	$\pm(3.21\text{E-}6 T^2 + 4.92\text{E-}3 T + 3.60) \text{ }^\circ\text{C}$	Normal	2.00	∞
Velocity error	$\pm 1.10 \text{ }^\circ\text{C}$	Rectangular	1.732	∞
Efficiency	$\pm 1.90\%$ of value	Rectangular	1.732	∞
Extension cable	$\pm 0.80 \text{ }^\circ\text{C}$	Rectangular	1.732	∞
Data acquisition	$\pm 0.10\%$ of range	Rectangular	1.732	∞

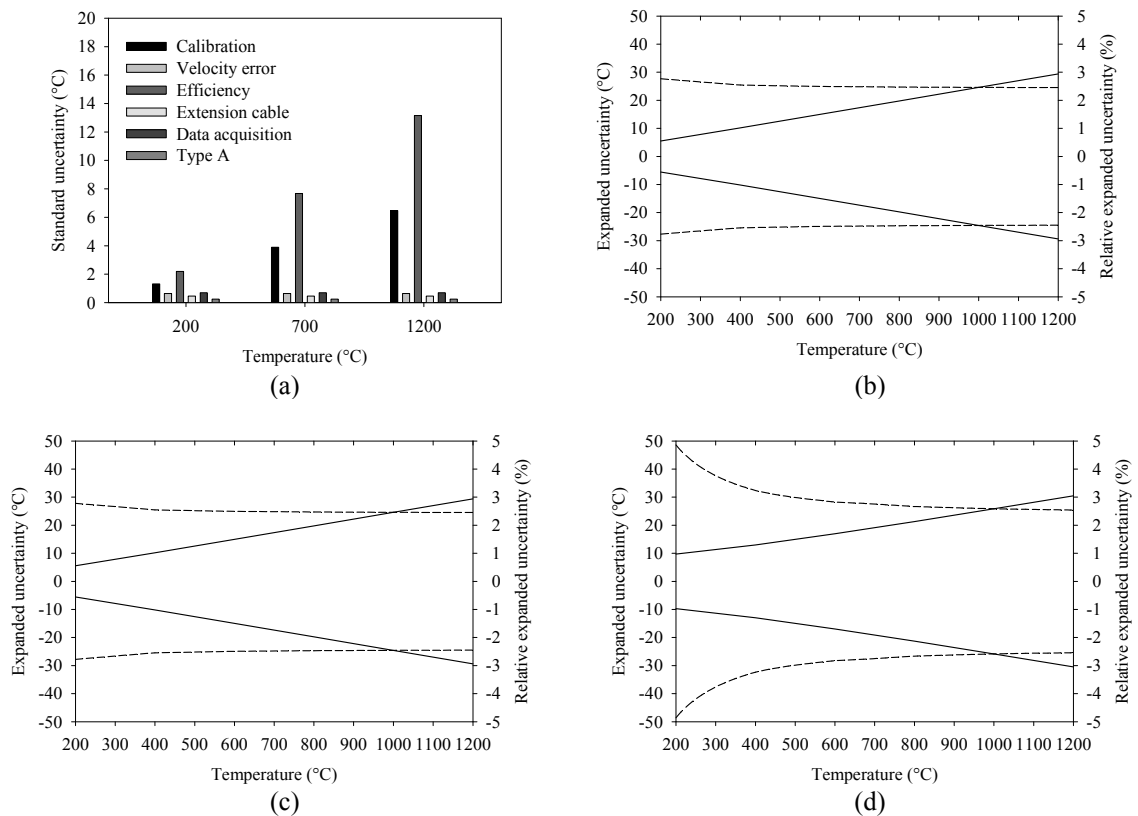


Figure A.18: (a) Comparison of standard uncertainty for the measurement of local gas temperature using a type K thermocouple for a standard deviation of the mean of 0.25 $^\circ\text{C}$; expanded uncertainty for standard deviations of the mean of (b) 0.00 $^\circ\text{C}$, (c) 0.25 $^\circ\text{C}$, and (d) 4.00 $^\circ\text{C}$. Solid line: expanded uncertainty in $^\circ\text{C}$; dashed line: relative expanded uncertainty.

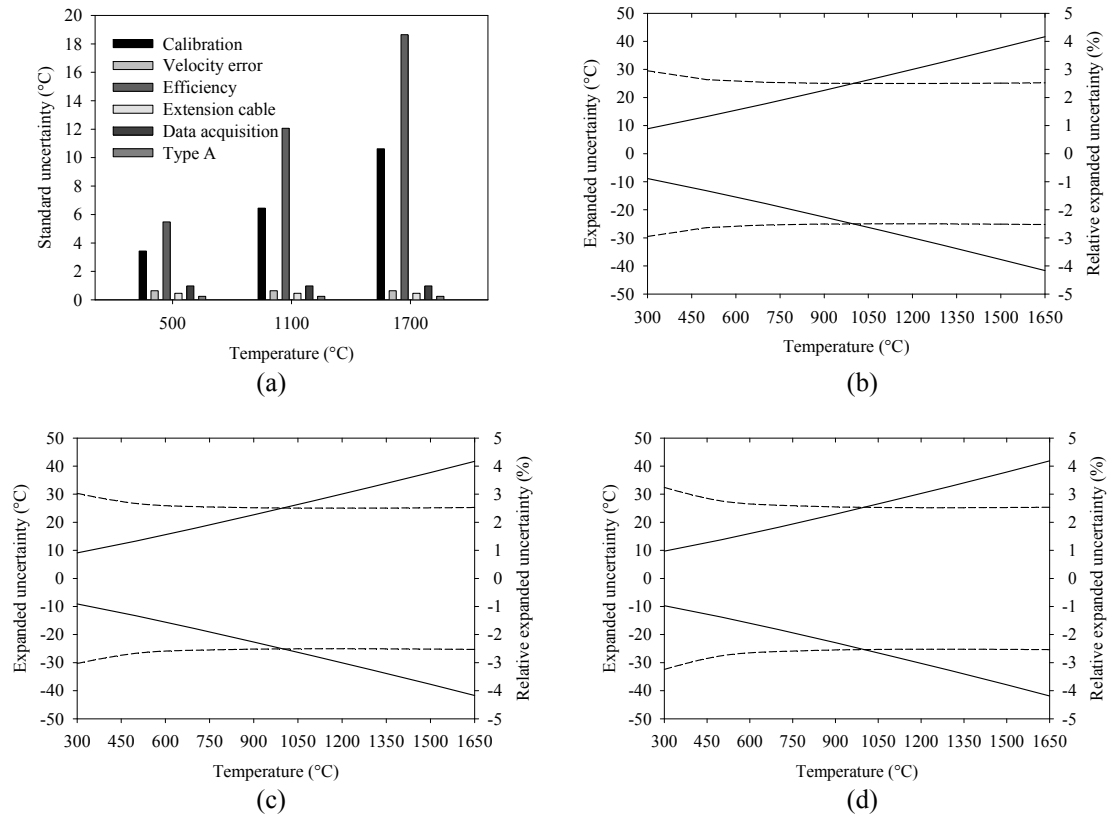


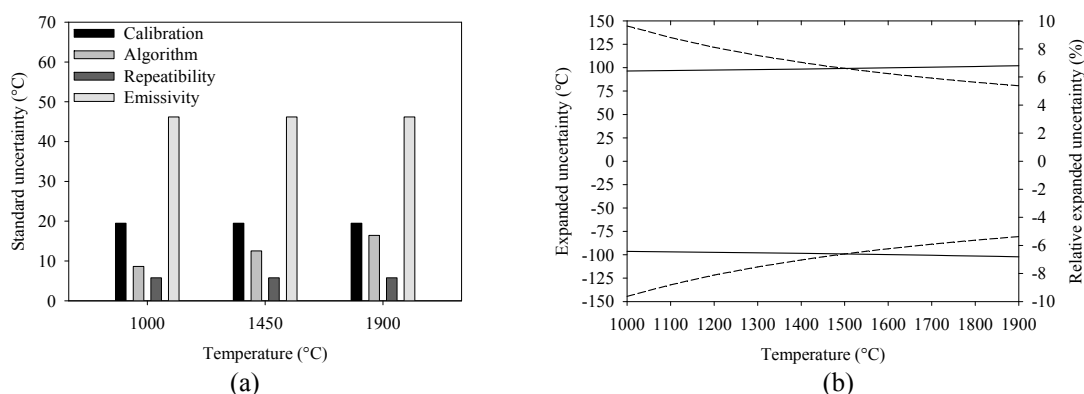
Figure A.19: (a) Comparison of standard uncertainty for the measurement of local gas temperature using a type B thermocouple for a standard deviation of the mean of 0.25 °C; expanded uncertainty for standard deviations of the mean of (b) 0.00 °C, (c) 0.25 °C, and (d) 4.00 °C. Solid line: expanded uncertainty in °C; dashed line: relative expanded uncertainty.

A.5 Assessing Measurement Uncertainty of Peak Flame Temperatures

One of central problems in radiation thermometry is that the emissivity of the target is not well enough known. A two-color Optix Q (PT70) pyrometer with an accuracy of 1% is used to calibrate the peak flame temperatures. The main advantage of two color pyrometers is the independence of emissivity [157]. During the calibration tests, a variation of emissivity between 0.80 and 1.00 represented a maximum variation of 78 °C for the peak temperature in both air-fired and oxy-fired flames. The maximum deviation of the measured peak values under various parameters was 30 °C. Sources of error are detailed in Table A.16, while the calculated standard and expanded uncertainty are depicted in Table A.16 and Figure A.20.

Table A.16: Sources of uncertainty for the measurement of maximum particles cloud temperature.

Source of uncertainty	Error	Type of distribution	Divider	DF
Calibration	± 30 °C	Rectangular	1.732	∞
Algorithm	$\pm 1.50\%$	Rectangular	1.732	∞
Repeatability	$\pm 1.00\%$	Rectangular	1.732	∞
Emissivity	± 78 °C	Rectangular	1.732	∞

**Figure A.20:** (a) Comparison of standard uncertainty and (b) expanded uncertainty for the measurement of maximum particles cloud temperature. Solid line: expanded uncertainty in °C; dashed line: relative expanded uncertainty.

A.6 Assessing Uncertainty in Local Gas Species Measurement

Dry-basis gas species are measured at several positions within the furnace. The amount of O₂ is measured with a magnetic pressure analyzer (range: 0-100 vol%); analyzers using non-dispersive infrared absorption measure levels of CO₂ (range: 0-100 vol%), CO (range: 0-20 vol%), and CH₄ (range: 0-7000 mg/m³). A photometer analyzer using gas filter correlation is applied for the measurement of NO (range: 0-3000 mg/m³). The type A uncertainty is based on typical maximum values of the standard deviation of the mean. The comparison of various sources of error and of standard and expanded uncertainties is presented in the following Tables (A.17-A.21) and Figures (A.21-A.25).

Table A.17: Sources of uncertainty for the measurement of local O₂ concentration

Source of uncertainty	Error	Type of distribution	Divider	DF
Linearity	±0.50 vol%	Rectangular	1.732	∞
Sensitivity	±0.10 vol%	Rectangular	1.732	∞
Output fluctuation	±0.0025 vol%	Normal	2.00	∞
Repeatability	±0.0050 vol%	Rectangular	1.732	∞
Detection limit	±0.0050 vol%	Normal	4.00	∞
Data acquisition	±0.01 % of range	Rectangular	$\sqrt{3}$	∞

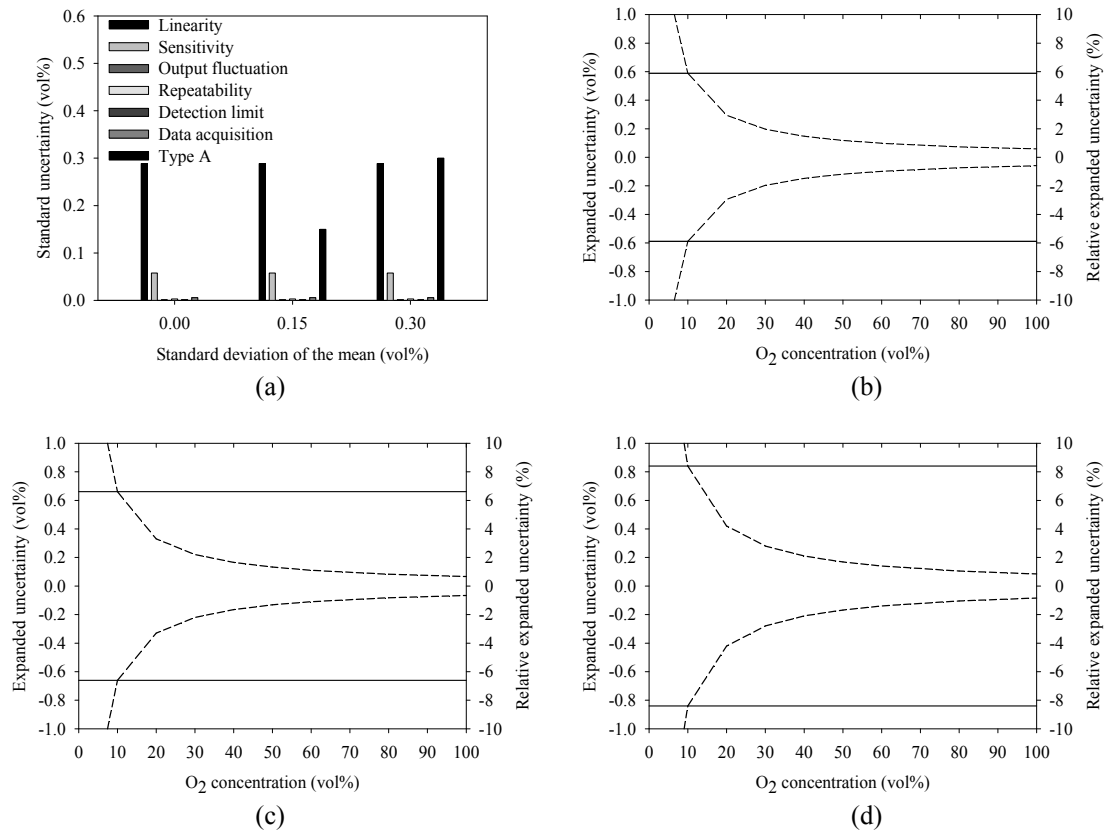
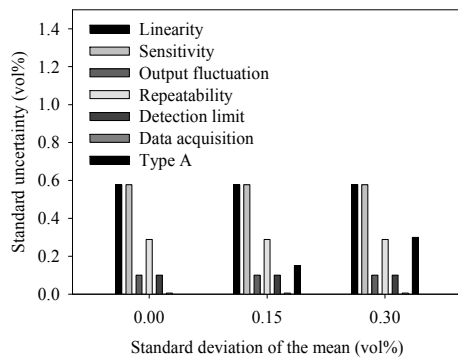
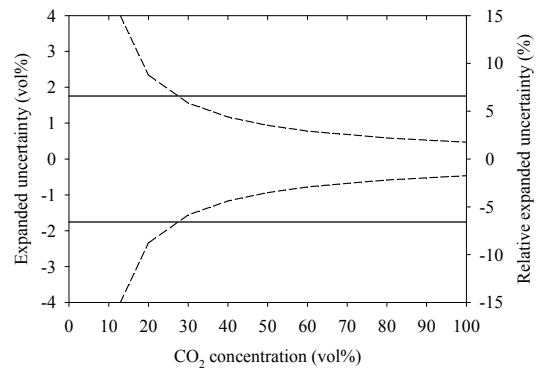
**Figure A.21:** (a) Comparison of standard uncertainty for the measurement of local O₂ concentration on dry basis and expanded uncertainty for standard deviations of the mean of (b) 0.00 vol%, (c) 0.15 vol%, and (d) 0.30 vol%. Solid line: expanded uncertainty in vol%; dashed line: relative expanded uncertainty.

Table A.18: Sources of uncertainty for the measurement of local CO₂ concentration.

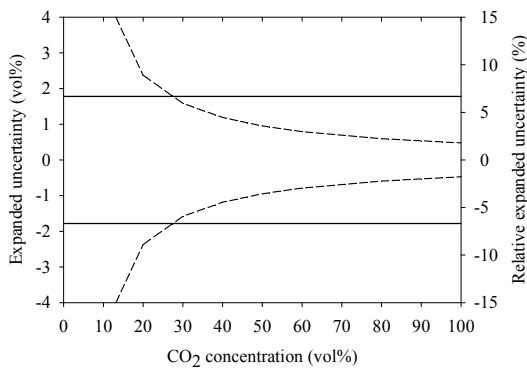
Source of uncertainty	Error	Type of distribution	Divider	DF
Linearity	± 1.00 vol%	Rectangular	1.732	∞
Sensitivity	± 1.00 vol%	Rectangular	1.732	∞
Output fluctuation	± 0.20 vol%	Normal	2.00	∞
Repeatability	± 0.50 vol%	Rectangular	1.732	∞
Detection limit	± 0.40 vol%	Normal	4.00	∞
Data acquisition	± 0.01 % of range	Rectangular	1.732	∞



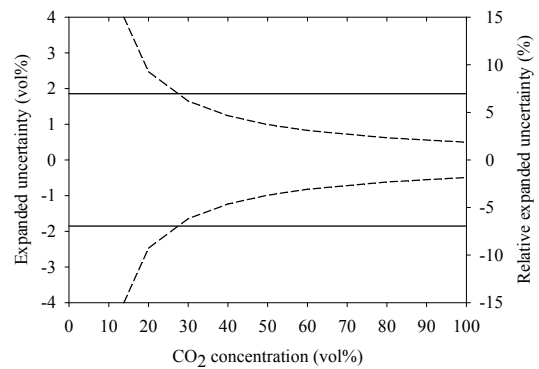
(a)



(b)



(c)



(d)

Figure A.22: (a) Comparison of standard uncertainty for the measurement of local CO₂ concentration on dry basis and expanded uncertainty for standard deviations of the mean of (b) 0.00 vol%, (c) 0.15 vol%, and (d) 0.30 vol%. Solid line: expanded uncertainty in vol%; dashed line: relative expanded uncertainty.

Table A.19: Sources of uncertainty for the measurement of local CO concentration.

Source of uncertainty	Error	Type of distribution	Divider	DF
Linearity	± 0.20 vol%	Rectangular	1.732	∞
Sensitivity	± 0.20 vol%	Rectangular	1.732	∞
Output fluctuation	± 0.04 vol%	Normal	2.00	∞
Repeatability	± 0.10 vol%	Rectangular	1.732	∞
Detection limit	± 0.08 vol%	Normal	4.00	∞
Data acquisition	$\pm 0.01\%$ of range	Rectangular	1.732	∞

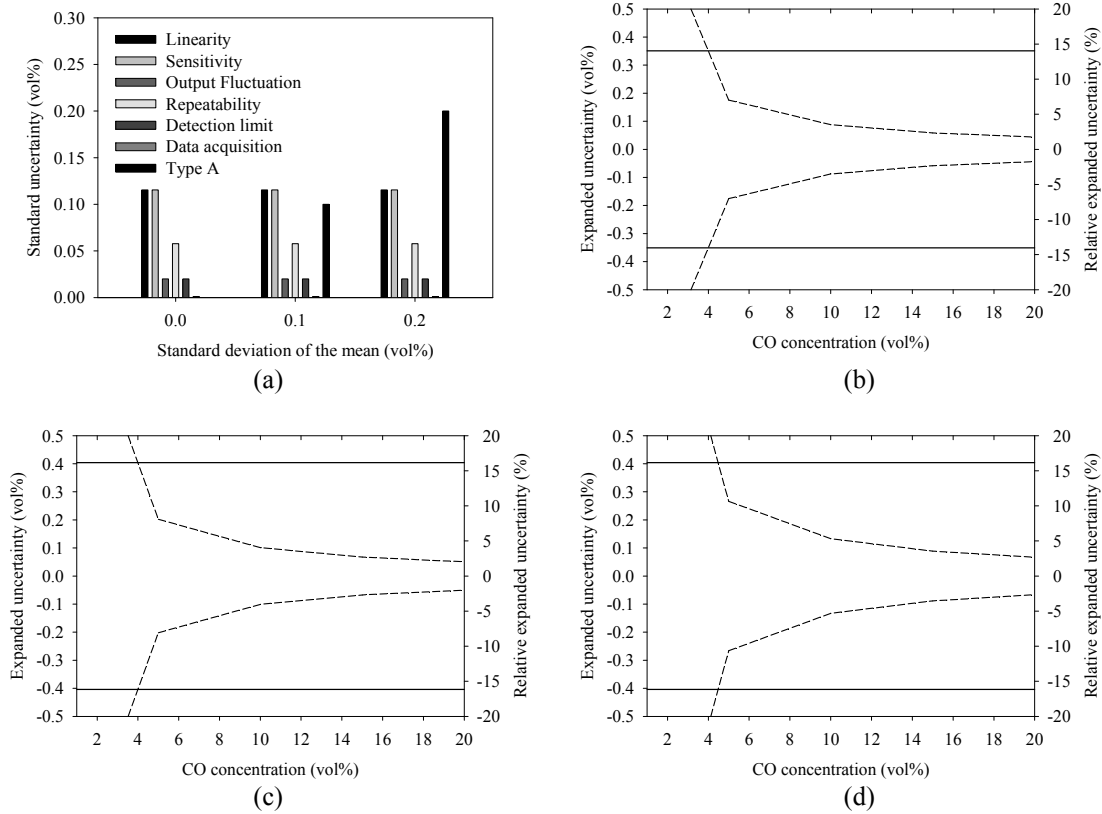


Figure A.23: (a) Comparison of standard uncertainty for the measurement of local CO concentration on dry basis and expanded uncertainty for standard deviations of the mean of (b) 0.00 vol%, (c) 0.10 vol%, and (d) 0.20 vol%. Solid line: expanded uncertainty in vol%; dashed line: relative expanded uncertainty.

Table A.20: Sources of uncertainty for the measurement of local CH₄ concentration.

Source of uncertainty	Error	Type of distribution	Divider	DF
Linearity	$\pm 70.63 \text{ mg/m}^3$	Rectangular	1.732	∞
Sensitivity	$\pm 70.63 \text{ mg/m}^3$	Rectangular	1.732	∞
Output fluctuation	$\pm 14.13 \text{ mg/m}^3$	Normal	2.00	∞
Repeatability	$\pm 35.32 \text{ mg/m}^3$	Rectangular	1.732	∞
Detection limit	$\pm 28.25 \text{ mg/m}^3$	Normal	4.00	∞
Data acquisition	$\pm 0.01 \%$ of range	Rectangular	1.732	∞

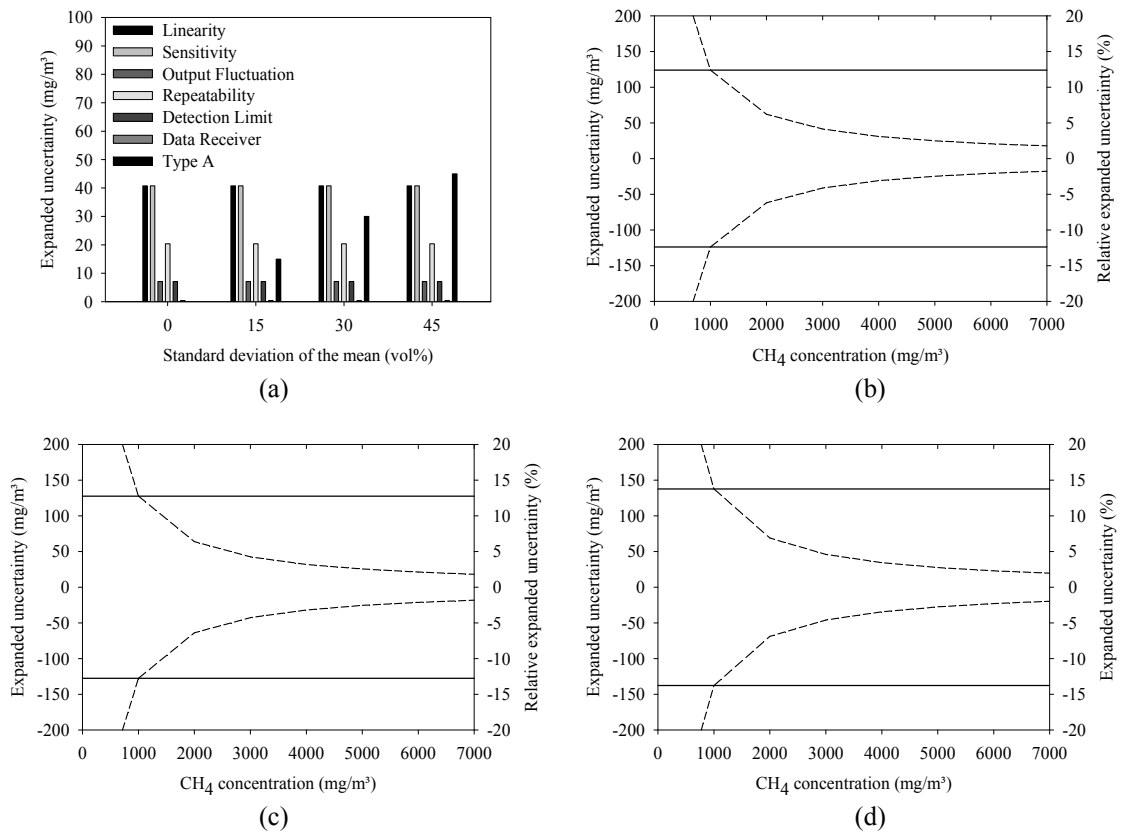
**Figure A.24:** (a) Comparison of standard uncertainty for the measurement of local CH₄ concentration on dry basis and expanded uncertainty for standard deviations of the mean of (a) 0 mg/m³, (b) 15 mg/m³, and (c) 30 mg/m³. Solid line: expanded uncertainty in vol%; dashed line: relative expanded uncertainty.

Table A.21: Sources of uncertainty for the measurement of local NO concentration.

Source of uncertainty	Error	Type of distribution	Divider	DF
Calibration of linearity	$\pm 6 \text{ mg/m}^3$	Rectangular	1.732	∞
Calibration of sensitivity	$\pm 9 \text{ mg/m}^3$	Rectangular	1.732	∞
Output fluctuation	$\pm 15 \text{ mg/m}^3$	Normal	2.00	∞
Repeatability	$\pm 15 \text{ mg/m}^3$	Rectangular	1.732	∞
Detection limit	$\pm 30 \text{ mg/m}^3$	Normal	4.00	∞
Data acquisition	$\pm 0.15\%$ of range	Rectangular	1.732	∞

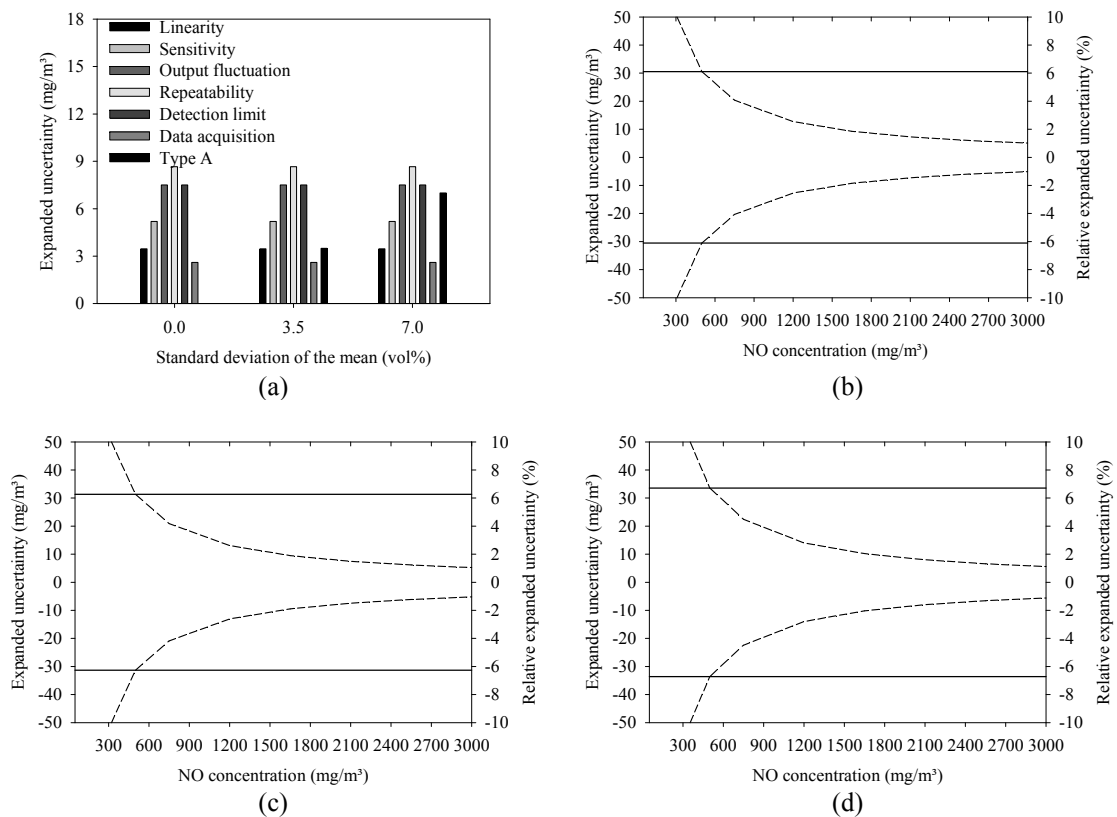


Figure A.25: (a) Comparison of standard uncertainty for the measurement of local NO concentration on dry basis and expanded uncertainty for standard deviations of the mean of (a) 0.00 mg/m³, (b) 3.50 mg/m³, and (c) 7.00 mg/m³. Solid line: expanded uncertainty in mg/m³; dashed line: relative expanded uncertainty.

A.7 Assessing Measurement Uncertainty of Total Radiative Heat Flux

Because the ellipsoidal heat flow meter does not provide an absolute indication of heat flux, it must be calibrated by subjecting it to the radiation of a blackbody of known temperature [111]. For this reason, a cylindrical furnace heated by resistance elements was adapted in order to create a source which emits a known energy by radiation only. A blackbody with an internal diameter of 0.05 m and 0.35 m length was constructed in silicon carbide. Since the internal area is much larger compared with that of the opening, the radiation is reflected internally numerous times and exits practically unchanged. The effective emissivity of the blackbody can be theoretically approximated by Gouffé's equation:

$$\varepsilon_0 = \frac{(1-\varepsilon) \left(\frac{A_o}{A_i} - \sin 2\theta \right)}{1 + \frac{A_o}{A_i} \left(\frac{1-\varepsilon}{\varepsilon} \right)} \quad (\text{A.25})$$

For a material emissivity of 0.85, the calculated emissivity of the blackbody is 0.978. The influence of the furnace blackbody radiation on the thermopile signal (in mV) during one calibration procedure is presented in Figure A.26. The dashed lines represent the expanded uncertainty of calibration due to the error of material emissivity, temperature measurement with thermocouples, and non-uniform temperature distribution in the blackbody. The latter was evaluated by measurements of temperature along the blackbody. The average temperature within the blackbody varied by approximately 5 °C. The pooled experimental expanded uncertainty characterizing the mean electric tension (mV) was obtained by over 100 independent observations. With knowledge of the blackbody temperature, the corresponding radiation fluxes were determined by Stefan-Boltzmann's law (Equation A.26).

$$P = \varepsilon_0 \sigma T^4 \quad (\text{A.26})$$

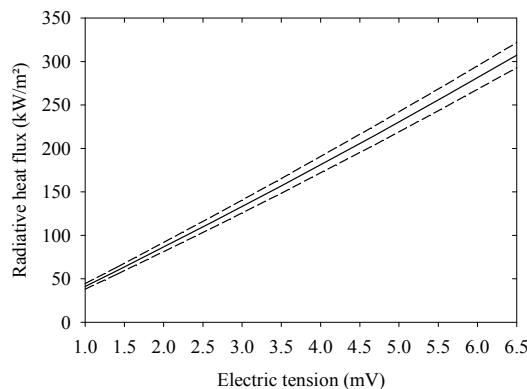


Figure A.26: Calibration curve of radiometer against the blackbody.

The sources of uncertainty for the measurement with the ellipsoidal radiometer are summarized in Table A.22. Besides the error due to the calibration, the electric voltage generated by the thermopile is influenced by variations in the N₂ purging. This source of error was investigated by varying the N₂ purging flow rate from 0 to 100 l/h at intervals of 20 l/h. A maximum variation obtained in the heat flux was found to be 0.68 kW/m². A comparison of standard and expanded uncertainty for typical values of standard deviations of the mean is presented in Figure A.27.

Table A.22: Sources of uncertainty for the measurement of total radiative heat flux.

Source of uncertainty	Error	Type of distribution	Divider	DF
Calibration	$\pm (-2.42E-5 q''^2 + 5.71E-2 q'' + 1.40)$ kW/m ²	Normal	2.00	∞
N ₂ purging	± 0.68 kW/m ²	Rectangular	1.732	∞
Data acquisition	± 0.01 % of range	Rectangular	1.732	∞

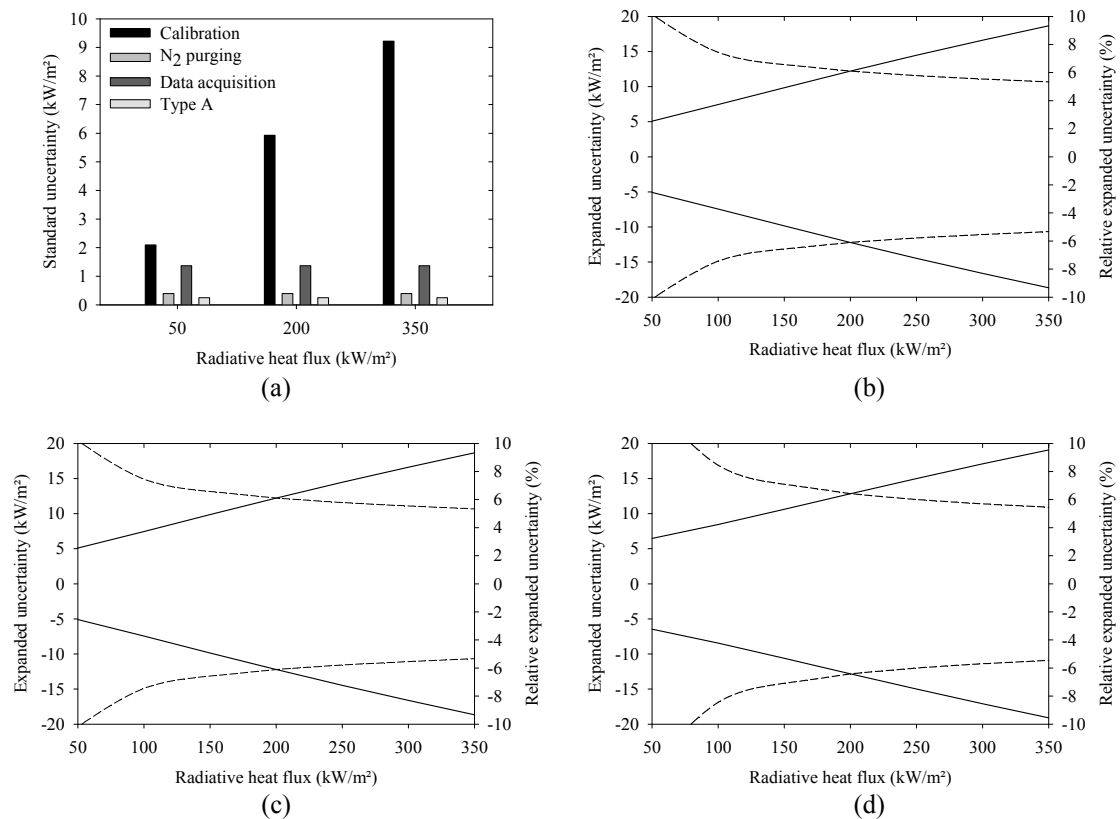


Figure A.27: (a) Comparison of standard uncertainty for the measurement of total radiative heat for a standard deviation of the mean of 0.25 kW/m²; expanded uncertainty for the standard deviations of the mean of (b) 0.00 kW/m², (c) 0.25 kW/m², and (d) 2.00 kW/m². Solid line: expanded uncertainty in kW/m²; dashed line: relative expanded uncertainty.

A.8 Assessing Measurement Uncertainty of Local Heat Flux at the Water-Cooled Walls

The correlation between the temperature difference at two characteristic points (tube and fin) and the heat flux was established using numerical simulations carried out in cooperation with the sensor manufacturer (Figure A.28). It is important to note that the lower section of the furnace is lined with refractory material and variations of lining thickness and thermal conductivity bring about changes in the linear correlation between heat flux and temperature difference. Both aspects are evaluated using values between 0.04-0.05 m for the refractory lining thickness; the thermal conductivity is evaluated using values between 0.90 and 3.00 W/mK. The non-linearity of the mathematical correlation between heat flux and temperature difference is estimated at 0.015 °C [119]. The sources of error and the values of standard and expanded uncertainty are compared in Table A.23 and Figures A.29 and A.30.

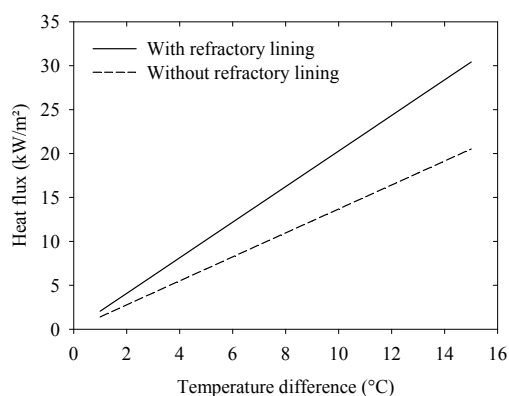


Figure A.28: Heat flux at water-cooled walls as a function of temperature difference between tube and fin.

Table A.23: Sources of uncertainty for the measurement of local heat flux at water-cooled walls.

Source of uncertainty	Error	Type of distribution	Divider	DF
Accuracy of thermocouple	$\pm (0.15 T)$	Rectangular	1.732	∞
Refractory lining thickness	$\pm(0.0213\Delta T+0.0016)$	Rectangular	1.732	∞
Thermal conductivity	$\pm(0.0116\Delta T- 0.0047)$	Rectangular	1.732	∞
Linearity	± 0.0015 °C	Rectangular	1.732	∞
Data acquisition	$\pm 0.01\%$ of range	Rectangular	1.732	∞

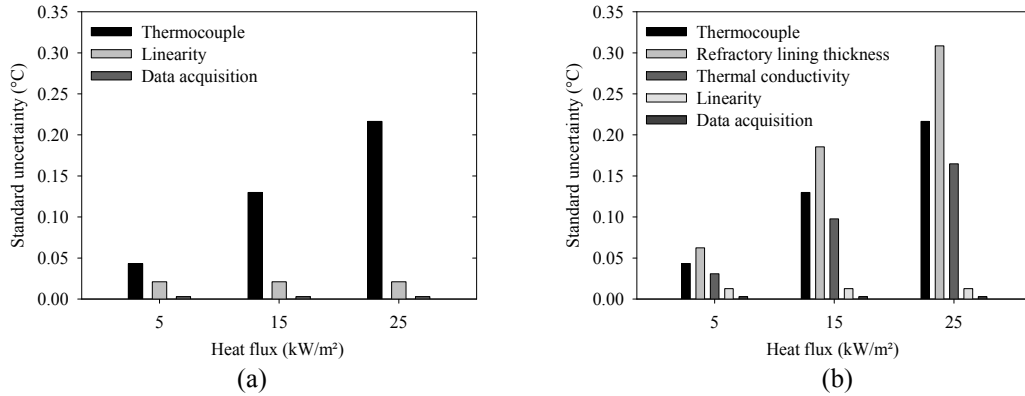


Figure A.29: Comparison of standard uncertainty for the measurement of local heat flux at the section of water-cooled wall (a) without and (b) with refractory lining.

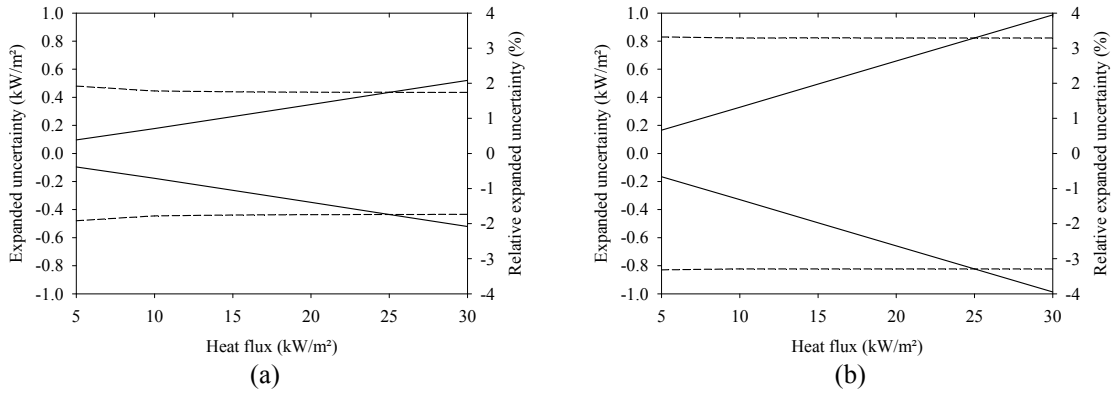


Figure A.30: Comparison of expanded uncertainty for the measurement of local heat flux at the section of water-cooled wall (a) without and (b) with refractory lining. Solid line: expanded uncertainty in kW/m²; dashed line: relative expanded uncertainty.

Appendix B - Experimental Data Sets

B.1 Air-Flame

B.1.1 Furnace Operating Conditions

Operating parameter	
Coal feed rate (kg/h)	56.88 ±0.24
Volume flow rate of primary stream (m ³ /h, STP)	41.07 ±1.58
O ₂ fraction of primary stream (vol%, wet)	21 ±1.21
CO ₂ fraction of primary stream (vol%, wet) ¹	-
Temperature of primary stream (°C)	29.52 ±1.26
Velocity of primary stream at burner exit (m/s) ¹	28.32
Axial momentum of primary stream at burner exit (N) ¹	0.47
Volume flow rate of secondary stream (m ³ /h, STP)	188 ±3.11
Volume flow rate of tertiary stream (m ³ /h, STP)	145 ±4.36
O ₂ fraction of secondary and tertiary stream (vol%, wet)	21 ±1.21
H ₂ O fraction of secondary and tertiary stream (vol%, wet) ¹	-
CO ₂ fraction of secondary and tertiary stream (vol%, wet) ¹	-
N ₂ fraction of secondary and tertiary stream (vol%, wet) ¹	79
Temperature of secondary and tertiary streams (°C)	199 ±1.89
Secondary/tertiary mass flow ratio ¹	1.30
Swirl number of secondary stream ¹	1.65
Stoichiometric ratio ¹	1.17
Overall heat input (kW) ¹	356.40
Sensible heat input (kW) ¹	21.40
Flue gas	
O ₂ (vol%, dry)	3.80 ±0.83
CO ₂ (vol%, dry)	16.89 ±1.05
N ₂ (vol%, dry) ¹	79.31
H ₂ O (vol% wet)	16.50 ±0.18
Volume flow rate at furnace exit (m ³ /h, STP)	405.70 ±4.96
Volume flow rate of recycled flue gas (m ³ /h, STP)	-
Temperature at furnace exit (°C)	505 ±3.46
Recycle ratio ¹	-
Outer wall surface temperature at the vertical section (°C)	199.85 ±1.86
Inner surface temperature of the cylindrical section (°C)	931 ±4.35

¹calculated value

B.1.2 Local Gas Temperature

Temperature (°C)	Measurement port A - Transversal distance (m)										
	-0.45	-0.25	-0.15	-0.10	-0.05	0	0.05	0.10	0.15	0.25	0.45
Mean	979	1038	1023	919	815	1380	815	919	1023	1038	979
Std. deviation	3.71	3.26	3.79	3.69	3.59	3.40	3.59	3.69	3.79	3.26	3.71
Uncertainty	24.51	25.95	25.59	23.06	20.53	34.58	20.53	23.06	25.59	25.95	24.51
5 th percentile	973	1031	1016	912	808	1374	808	912	1016	1031	973
25 th percentile	977	1037	1020	917	813	1377	813	917	1020	1037	977
50 th percentile	980	1038	1023	919	816	1380	816	919	1023	1038	980
75 th percentile	982	1041	1026	922	818	1383	818	922	1026	1041	982
95 th percentile	984	1043	1029	925	821	1385	821	925	1029	1043	984
Temperature (°C)	Measurement port B - Transversal distance (m)										
	-0.45	-0.25	-0.15	-0.10	-0.05	0	0.05	0.10	0.15	0.25	0.45
Mean	983	951	879	1055	1230	1257	1225	1131	1037	1118	1102
Std. deviation	4.43	4.99	5.92	6.95	7.97	5.23	10.02	7.91	5.80	3.44	3.38
Uncertainty	24.61	23.84	22.09	26.43	30.78	31.45	30.67	28.31	25.95	27.93	27.53
5 th percentile	975	944	867	1043	1220	1248	1212	1120	1028	1112	1097
25 th percentile	981	947	876	1050	1224	1254	1217	1125	1033	1116	1100
50 th percentile	984	951	880	1054	1229	1259	1224	1130	1037	1118	1102
75 th percentile	986	956	883	1060	1237	1261	1230	1136	1043	1121	1104
95 th percentile	990	959	888	1065	1242	1264	1244	1145	1047	1123	1106
Temperature (°C)	Measurement port C - Transversal distance (m)										
	-0.45	-0.25	-0.15	-0.10	-0.05	0	0.05	0.10	0.15	0.25	0.45
Mean	996	1138	1240	1246	1251	1204	1241	1208	1175	1091	1051
Std. deviation	3.79	6.15	9.22	7.31	5.41	4.37	5.35	5.13	4.92	5.09	2.95
Uncertainty	24.93	28.44	31.04	31.17	31.30	30.09	31.03	30.20	29.37	27.28	26.26
5 th percentile	990	1126	1224	1234	1243	1198	1232	1200	1167	1083	1045
25 th percentile	994	1134	1234	1241	1248	1201	1238	1205	1172	1087	1048
50 th percentile	996	1138	1239	1245	1251	1204	1241	1207	1174	1092	1051
75 th percentile	999	1142	1246	1251	1256	1206	1244	1211	1178	1095	1053
95 th percentile	1001	1147	1256	1258	1260	1211	1251	1218	1184	1099	1055
Temperature (°C)	Measurement port D - Transversal distance (m)										
	-0.45	-0.25	-0.15	-0.10	-0.05	0	0.05	0.10	0.15	0.25	0.45
Mean	950	1216	1239	-	1172	1151	1178	-	1151	1053	990
Std. deviation	5.52	3.45	3.46	-	6.41	11.48	5.36	-	6.76	6.31	2.09
Uncertainty	23.41	29.80	30.37	-	28.78	28.37	28.91	-	28.27	25.90	24.35
5 th percentile	941	1211	1233	-	1163	1136	1171	-	1143	1043	987
25 th percentile	946	1212	1237	-	1166	1140	1174	-	1147	1048	989
50 th percentile	949	1216	1239	-	1173	1148	1177	-	1149	1052	991
75 th percentile	954	1218	1241	-	1175	1160	1182	-	1153	1059	992
95 th percentile	959	1221	1245	-	1180	1170	1188	-	1163	1062	994

Temperature (°C)	Measurement port E - Transversal distance (m)										
	-0.45	-0.25	-0.15	-0.10	-0.05	0	0.05	0.10	0.15	0.25	0.45
Mean	1052	1201	1204	-	1169	1126	1053	-	1227	1050	1000
Std. deviation	8.72	7.50	10.45	-	13.05	11.73	6.10	-	3.44	3.96	2.19
Uncertainty	25.88	29.47	29.57	-	28.77	27.72	25.90	-	30.07	25.81	24.57
5 th percentile	1036	1190	1185	-	1144	1108	1045	-	1221	1044	996
25 th percentile	1047	1196	1196	-	1162	1115	1048	-	1225	1047	998
50 th percentile	1054	1202	1207	-	1170	1127	1052	-	1227	1050	1000
75 th percentile	1058	1206	1213	-	1178	1134	1055	-	1229	1053	1001
95 th percentile	1063	1214	1216	-	1189	1143	1067	-	1233	1057	1004
Temperature (°C)	Measurement port F - Transversal distance (m)										
	-0.45	-0.30	-0.15	-0.10	-0.05	0	0.05	0.10	0.15	0.30	0.45
Mean	963	1187	1184	-	-	1144	-	-	1102	1078	1028
Std. deviation	3.52	3.23	3.95	-	-	3.30	-	-	3.70	3.12	2.38
Uncertainty	23.69	29.10	29.03	-	-	28.07	-	-	27.06	26.47	25.27
5 th percentile	958	1182	1177	-	-	1139	-	-	1096	1073	1025
25 th percentile	960	1185	1181	-	-	1142	-	-	1101	1076	1027
50 th percentile	962	1187	1185	-	-	1144	-	-	1103	1078	1028
75 th percentile	965	1190	1187	-	-	1147	-	-	1104	1080	1030
95 th percentile	968	1192	1189	-	-	1150	-	-	1107	1083	1033
Temperature (°C)	Measurement port G - Transversal distance (m)										
	-0.45	-0.30	-0.15	-0.10	-0.05	0	0.05	0.10	0.15	0.30	0.45
Mean	1019	1050	1051	-	-	1060	-	-	1058	1050	1019
Std. deviation	1.42	0.98	1.77	-	-	0.83	-	-	2.22	1.15	1.42
Uncertainty	25.05	25.79	25.82	-	-	26.02	-	-	25.98	25.78	25.05
5 th percentile	1017	1048	1049	-	-	1058	-	-	1055	1047	1017
25 th percentile	1018	1050	1050	-	-	1059	-	-	1056	1049	1018
50 th percentile	1019	1050	1052	-	-	1060	-	-	1058	1050	1019
75 th percentile	1020	1051	1053	-	-	1060	-	-	1060	1050	1020
95 th percentile	1022	1052	1054	-	-	1061	-	-	1061	1051	1022

B.1.3 Local Oxygen Concentration

O ₂ (vol%, dry)	Measurement port A - Transversal distance (m)										
	-0.45	-0.25	-0.15	-0.10	-0.05	0	0.05	0.10	0.15	0.25	0.45
Mean	10.07	10.20	10.45	14.80	19.15	0.65	11.56	10.73	9.91	10.20	10.07
Std. deviation	0.33	0.51	0.64	0.33	0.01	0.04	0.24	0.24	0.24	0.51	0.33
Uncertainty	0.59	0.59	0.60	0.59	0.59	0.59	0.59	0.59	0.59	0.59	0.59
5 th percentile	9.62	9.32	9.53	14.33	19.13	0.59	11.22	10.31	9.41	9.32	9.62
25 th percentile	9.76	9.83	9.90	14.52	19.14	0.61	11.40	10.58	9.77	9.83	9.76
50 th percentile	10.08	10.25	10.43	14.79	19.15	0.63	11.55	10.77	9.98	10.25	10.08
75 th percentile	10.30	10.57	10.96	15.06	19.16	0.68	11.71	10.89	10.07	10.57	10.30
95 th percentile	10.60	11.02	11.41	15.29	19.17	0.73	11.96	11.10	10.23	11.02	10.60
O ₂ (vol%, dry)	Measurement port B - Transversal distance (m)										
	-0.45	-0.25	-0.15	-0.10	-0.05	0	0.05	0.10	0.15	0.25	0.45
Mean	11.35	10.83	14.04	8.95	3.86	5.93	1.72	7.41	13.10	7.83	10.84
Std. deviation	0.48	0.20	0.11	0.58	1.04	0.40	0.04	0.14	0.24	0.39	0.14
Uncertainty	0.60	0.59	0.59	0.61	0.63	0.59	0.59	0.59	0.59	0.59	0.59
5 th percentile	10.69	10.47	13.83	8.04	2.25	5.03	1.63	7.18	12.73	7.28	10.60
25 th percentile	10.92	10.69	13.95	8.61	3.28	5.75	1.71	7.32	12.93	7.48	10.76
50 th percentile	11.30	10.90	14.08	8.88	3.68	5.94	1.73	7.41	13.09	7.78	10.85
75 th percentile	11.83	11.00	14.11	9.30	4.50	6.15	1.75	7.52	13.30	8.23	10.94
95 th percentile	12.09	11.03	14.20	10.04	5.87	6.56	1.76	7.61	13.46	8.42	11.04
O ₂ (vol%, dry)	Measurement port C - Transversal distance (m)										
	-0.45	-0.25	-0.15	-0.10	-0.05	0	0.05	0.10	0.15	0.25	0.45
Mean	12.07	7.49	6.01	3.92	1.83	2.56	3.43	5.24	7.04	8.25	10.51
Std. deviation	0.30	0.48	0.72	0.46	0.19	0.13	0.26	0.40	0.54	0.86	0.38
Uncertainty	0.59	0.60	0.60	0.60	0.59	0.59	0.59	0.59	0.60	0.61	0.59
5 th percentile	11.58	6.48	4.75	3.16	1.57	2.33	2.98	4.65	6.33	6.97	9.94
25 th percentile	11.78	7.30	5.45	3.56	1.67	2.47	3.21	4.91	6.61	7.43	10.25
50 th percentile	12.16	7.58	6.04	3.95	1.85	2.54	3.44	5.18	6.91	8.31	10.47
75 th percentile	12.28	7.82	6.40	4.17	1.93	2.64	3.65	5.60	7.56	8.99	10.95
95 th percentile	12.47	8.22	7.42	4.78	2.14	2.82	3.83	5.88	7.93	9.46	11.06
O ₂ (vol%, dry)	Measurement port D - Transversal distance (m)										
	-0.45	-0.25	-0.15	-0.10	-0.05	0	0.05	0.10	0.15	0.25	0.45
Mean	6.34	1.43	1.91	-	5.55	7.33	7.94	-	10.78	11.85	12.46
Std. deviation	0.41	0.19	0.33	-	0.47	0.52	0.31	-	0.28	0.15	0.15
Uncertainty	0.59	0.59	0.59	-	0.60	0.60	0.59	-	0.59	0.59	0.59
5 th percentile	5.56	1.18	1.44	-	4.72	6.62	7.50	-	10.29	11.60	12.22
25 th percentile	6.22	1.27	1.68	-	5.30	6.83	7.69	-	10.53	11.74	12.36
50 th percentile	6.50	1.39	1.88	-	5.53	7.28	7.88	-	10.83	11.88	12.48
75 th percentile	6.58	1.60	2.10	-	5.69	7.76	8.19	-	11.01	11.97	12.57
95 th percentile	6.76	1.78	2.49	-	6.39	8.21	8.50	-	11.20	12.10	12.75

O ₂ (vol%, dry)	Measurement port E - Transversal distance (m)										
	-0.45	-0.25	-0.15	-0.10	-0.05	0	0.05	0.10	0.15	0.25	0.45
Mean	7.18	1.96	2.16	-	6.73	10.84	9.29	-	10.92	11.25	10.27
Std. deviation	0.44	0.40	0.44	-	0.53	0.76	0.67	-	0.25	0.14	0.53
Uncertainty	0.59	0.59	0.59	-	0.59	0.61	0.60	-	0.59	0.59	0.59
5 th percentile	6.43	1.37	1.27	-	5.93	9.87	8.44	-	10.41	11.04	9.64
25 th percentile	6.88	1.71	1.90	-	6.35	10.18	8.79	-	10.77	11.14	9.71
50 th percentile	7.23	1.86	2.25	-	6.67	10.79	9.24	-	10.92	11.24	10.24
75 th percentile	7.55	2.18	2.48	-	7.07	11.25	9.52	-	11.09	11.37	10.69
95 th percentile	7.80	2.76	2.65	-	7.63	12.40	10.78	-	11.33	11.49	11.17
O ₂ (vol%, dry)	Measurement port F - Transversal distance (m)										
	-0.45	-0.30	-0.15	-0.10	-0.05	0	0.05	0.10	0.15	0.30	0.45
Mean	7.71	3.64	3.89	-	-	5.66	-	-	7.36	8.06	8.05
Std. deviation	0.40	0.30	0.29	-	-	0.42	-	-	0.26	0.36	0.77
Uncertainty	0.59	0.59	0.59	-	-	0.59	-	-	0.59	0.59	0.61
5 th percentile	6.93	3.17	3.52	-	-	4.88	-	-	6.94	7.49	6.91
25 th percentile	7.58	3.41	3.63	-	-	5.43	-	-	7.13	7.74	7.27
50 th percentile	7.69	3.62	3.95	-	-	5.65	-	-	7.39	8.09	8.30
75 th percentile	8.02	3.89	4.08	-	-	5.89	-	-	7.54	8.32	8.73
95 th percentile	8.27	4.11	4.34	-	-	6.39	-	-	7.71	8.70	9.06
O ₂ (vol%, dry)	Measurement port G - Transversal distance (m)										
	-0.45	-0.30	-0.15	-0.10	-0.05	0	0.05	0.10	0.15	0.30	0.45
Mean	10.39	5.32	5.43	-	-	6.00	-	-	6.26	6.09	5.75
Std. deviation	0.43	0.38	0.41	-	-	0.46	-	-	0.32	0.21	0.38
Uncertainty	0.59	0.59	0.59	-	-	0.59	-	-	0.59	0.59	0.59
5 th percentile	9.66	4.79	4.89	-	-	5.40	-	-	5.64	5.74	5.16
25 th percentile	9.99	5.04	5.06	-	-	5.67	-	-	6.04	5.88	5.54
50 th percentile	10.54	5.33	5.39	-	-	5.89	-	-	6.32	6.16	5.74
75 th percentile	10.72	5.47	5.76	-	-	6.28	-	-	6.54	6.25	5.92
95 th percentile	10.96	6.21	6.13	-	-	6.99	-	-	6.70	6.35	6.55

B.1.4 Local Carbon Dioxide Concentration

CO ₂ (vol%, dry)	Measurement port A - Transversal distance (m)										
	-0.45	-0.25	-0.15	-0.10	-0.05	0	0.05	0.10	0.15	0.25	0.45
Mean	11.04	10.90	10.66	6.27	1.89	17.06	9.41	10.26	11.10	10.90	11.04
Std. deviation	0.34	0.52	0.65	0.33	0.01	0.09	0.25	0.25	0.25	0.52	0.34
Uncertainty	1.33	1.33	1.33	1.33	1.32	1.34	1.33	1.33	1.33	1.33	1.33
5 th percentile	10.48	10.06	9.68	5.77	1.87	16.94	8.94	9.86	10.78	10.06	10.48
25 th percentile	10.77	10.53	10.09	5.98	1.88	16.98	9.26	10.09	10.92	10.53	10.77
50 th percentile	11.08	10.86	10.71	6.30	1.89	17.04	9.41	10.24	11.06	10.86	11.08
75 th percentile	11.34	11.23	11.19	6.55	1.90	17.11	9.58	10.41	11.24	11.23	11.34
95 th percentile	11.47	11.80	11.58	6.74	1.91	17.23	9.78	10.70	11.63	11.80	11.47
CO ₂ (vol%, dry)	Measurement port B - Transversal distance (m)										
	-0.45	-0.25	-0.15	-0.10	-0.05	0	0.05	0.10	0.15	0.25	0.45
Mean	9.76	10.28	7.08	11.41	15.74	12.78	15.75	11.87	7.99	13.21	10.26
Std. deviation	0.50	0.22	0.12	0.50	0.88	0.34	0.08	0.16	0.24	0.39	0.14
Uncertainty	1.33	1.33	1.32	1.34	1.35	1.33	1.33	1.33	1.33	1.33	1.33
5 th percentile	8.97	10.04	6.89	10.42	13.96	12.25	15.67	11.65	7.63	12.60	10.05
25 th percentile	9.31	10.10	7.00	11.12	15.24	12.56	15.70	11.74	7.78	12.82	10.16
50 th percentile	9.82	10.20	7.04	11.45	15.86	12.75	15.72	11.86	8.00	13.24	10.26
75 th percentile	10.18	10.49	7.16	11.70	16.24	12.98	15.80	11.99	8.18	13.58	10.35
95 th percentile	10.47	10.64	7.26	12.14	17.01	13.46	15.89	12.13	8.38	13.74	10.51
CO ₂ (vol%, dry)	Measurement port C - Transversal distance (m)										
	-0.45	-0.25	-0.15	-0.10	-0.05	0	0.05	0.10	0.15	0.25	0.45
Mean	9.04	13.54	14.88	15.69	16.50	15.10	15.74	14.82	13.90	12.77	10.57
Std. deviation	0.31	0.48	0.68	0.44	0.19	0.38	0.17	0.35	0.53	0.85	0.38
Uncertainty	1.33	1.33	1.34	1.34	1.34	1.33	1.33	1.33	1.33	1.34	1.33
5 th percentile	8.60	12.86	13.49	14.82	16.15	14.46	15.43	14.24	13.04	11.61	10.00
25 th percentile	8.83	13.23	14.53	15.45	16.36	14.81	15.63	14.53	13.43	11.96	10.13
50 th percentile	8.94	13.45	14.83	15.68	16.53	15.15	15.76	14.93	14.09	12.76	10.62
75 th percentile	9.32	13.71	15.44	16.04	16.63	15.39	15.89	15.11	14.33	13.51	10.80
95 th percentile	9.51	14.53	15.98	16.39	16.79	15.64	16.01	15.30	14.59	14.05	11.15
CO ₂ (vol%, dry)	Measurement port D - Transversal distance (m)										
	-0.45	-0.25	-0.15	-0.10	-0.05	0	0.05	0.10	0.15	0.25	0.45
Mean	14.53	17.68	16.94	-	14.86	13.60	13.06	-	10.30	9.26	8.65
Std. deviation	0.39	0.19	0.24	-	0.39	0.50	0.32	-	0.28	0.16	0.16
Uncertainty	1.33	1.34	1.34	-	1.33	1.33	1.33	-	1.33	1.33	1.33
5 th percentile	14.11	17.39	16.53	-	14.07	12.74	12.53	-	9.87	9.00	8.35
25 th percentile	14.30	17.56	16.82	-	14.73	13.22	12.80	-	10.07	9.15	8.56
50 th percentile	14.38	17.67	16.96	-	14.90	13.68	13.14	-	10.27	9.24	8.65
75 th percentile	14.61	17.88	17.12	-	15.08	14.10	13.32	-	10.53	9.37	8.76
95 th percentile	15.29	17.98	17.25	-	15.52	14.31	13.45	-	10.80	9.56	8.92

CO ₂ (vol%, dry)	Measurement port E - Transversal distance (m)										
	-0.45	-0.25	-0.15	-0.10	-0.05	0	0.05	0.10	0.15	0.25	0.45
Mean	13.67	17.58	17.10	-	14.20	10.26	11.76	-	10.18	9.85	10.83
Std. deviation	0.43	0.21	0.25	-	0.51	0.79	0.68	-	0.26	0.15	0.55
Uncertainty	1.33	1.34	1.34	-	1.33	1.33	1.33	-	1.33	1.33	1.33
5 th percentile	13.03	17.16	16.70	-	13.32	8.69	10.26	-	9.76	9.62	9.88
25 th percentile	13.37	17.48	16.97	-	13.85	9.75	11.52	-	10.00	9.72	10.38
50 th percentile	13.61	17.64	17.12	-	14.32	10.31	11.77	-	10.19	9.87	10.87
75 th percentile	14.01	17.71	17.28	-	14.57	10.93	12.26	-	10.34	9.98	11.38
95 th percentile	14.37	17.86	17.52	-	14.92	11.31	12.69	-	10.66	10.06	11.49
CO ₂ (vol%, dry)	Measurement port F - Transversal distance (m)										
	-0.45	-0.30	-0.15	-0.10	-0.05	0	0.05	0.10	0.15	0.30	0.45
Mean	13.28	17.08	16.77	-	-	15.18	-	-	13.65	12.98	13.05
Std. deviation	0.41	0.26	0.26	-	-	0.42	-	-	0.28	0.37	0.76
Uncertainty	1.33	1.34	1.34	-	-	1.34	-	-	1.33	1.33	1.34
5 th percentile	12.70	16.65	16.36	-	-	14.51	-	-	13.20	12.25	12.03
25 th percentile	12.94	16.89	16.59	-	-	14.92	-	-	13.46	12.77	12.35
50 th percentile	13.28	17.12	16.73	-	-	15.16	-	-	13.63	12.93	12.84
75 th percentile	13.42	17.27	17.01	-	-	15.50	-	-	13.90	13.31	13.83
95 th percentile	14.14	17.47	17.15	-	-	15.89	-	-	14.11	13.53	14.25
CO ₂ (vol%, dry)	Measurement port G - Transversal distance (m)										
	-0.45	-0.30	-0.15	-0.10	-0.05	0	0.05	0.10	0.15	0.30	0.45
Mean	10.66	15.65	15.54	-	-	15.01	-	-	14.74	14.91	15.24
Std. deviation	0.42	0.39	0.41	-	-	0.46	-	-	0.32	0.21	0.41
Uncertainty	1.33	1.34	1.34	-	-	1.34	-	-	1.33	1.33	1.34
5 th percentile	10.10	14.84	14.83	-	-	14.05	-	-	14.25	14.64	14.42
25 th percentile	10.35	15.48	15.23	-	-	14.78	-	-	14.45	14.73	15.04
50 th percentile	10.52	15.67	15.53	-	-	15.07	-	-	14.71	14.84	15.25
75 th percentile	11.04	15.95	15.89	-	-	15.35	-	-	14.93	15.12	15.45
95 th percentile	11.39	16.21	16.08	-	-	15.61	-	-	15.33	15.27	15.94

B.1.5 Local Carbon Monoxide Concentration

CO (vol%, dry)	Measurement port A - Transversal distance (m)										
	-0.45	-0.25	-0.15	-0.10	-0.05	0	0.05	0.10	0.15	0.25	0.45
Mean	0.00	0.00	0.00	0.04	0.08	5.94	0.17	0.10	0.02	0.00	0.00
Std. deviation	0.00	0.00	0.00	0.00	0.00	0.24	0.01	0.01	0.00	0.00	0.00
Uncertainty	0.35	0.35	0.35	0.35	0.35	0.36	0.35	0.35	0.35	0.35	0.35
5 th percentile	0.00	0.00	0.00	0.04	0.07	5.56	0.16	0.09	0.02	0.00	0.00
25 th percentile	0.00	0.00	0.00	0.04	0.08	5.75	0.16	0.09	0.02	0.00	0.00
50 th percentile	0.00	0.00	0.00	0.04	0.08	6.01	0.17	0.10	0.02	0.00	0.00
75 th percentile	0.00	0.00	0.00	0.04	0.08	6.13	0.18	0.10	0.02	0.00	0.00
95 th percentile	0.01	0.00	0.00	0.04	0.08	6.23	0.19	0.11	0.02	0.00	0.01
CO (vol%, dry)	Measurement port B - Transversal distance (m)										
	-0.45	-0.25	-0.15	-0.10	-0.05	0	0.05	0.10	0.15	0.25	0.45
Mean	0.00	0.01	0.03	1.23	2.43	4.03	6.39	3.22	0.05	0.01	0.00
Std. deviation	0.00	0.00	0.00	0.17	0.34	0.29	0.19	0.10	0.00	0.00	0.00
Uncertainty	0.35	0.35	0.35	0.35	0.36	0.36	0.35	0.35	0.35	0.35	0.35
5 th percentile	0.00	0.00	0.03	0.92	1.81	3.56	6.09	3.07	0.04	0.01	0.00
25 th percentile	0.00	0.01	0.03	1.12	2.21	3.85	6.26	3.15	0.04	0.01	0.00
50 th percentile	0.00	0.01	0.03	1.24	2.44	4.05	6.42	3.23	0.05	0.01	0.00
75 th percentile	0.01	0.01	0.03	1.35	2.67	4.31	6.51	3.28	0.05	0.01	0.00
95 th percentile	0.01	0.01	0.04	1.50	2.97	4.48	6.68	3.37	0.05	0.01	0.01
CO (vol%, dry)	Measurement port C - Transversal distance (m)										
	-0.45	-0.25	-0.15	-0.10	-0.05	0	0.05	0.10	0.15	0.25	0.45
Mean	0.00	0.02	0.20	2.51	4.81	6.64	3.34	1.73	0.12	0.04	0.00
Std. deviation	0.00	0.01	0.07	0.34	0.61	1.07	0.43	0.24	0.05	0.02	0.00
Uncertainty	0.35	0.35	0.35	0.36	0.37	0.40	0.36	0.36	0.35	0.35	0.35
5 th percentile	0.00	0.01	0.11	2.00	3.89	5.19	2.71	1.37	0.03	0.01	0.00
25 th percentile	0.00	0.01	0.15	2.25	4.35	5.87	3.08	1.58	0.08	0.02	0.00
50 th percentile	0.00	0.02	0.19	2.43	4.66	6.33	3.28	1.71	0.13	0.03	0.00
75 th percentile	0.01	0.02	0.24	2.77	5.30	7.31	3.64	1.90	0.16	0.05	0.00
95 th percentile	0.01	0.03	0.33	3.11	5.89	8.67	4.00	2.10	0.21	0.08	0.01
CO (vol%, dry)	Measurement port D - Transversal distance (m)										
	-0.45	-0.25	-0.15	-0.10	-0.05	0	0.05	0.10	0.15	0.25	0.45
Mean	0.24	3.28	3.75	-	1.05	0.20	0.12	-	0.03	0.00	0.00
Std. deviation	0.04	0.37	0.52	-	0.20	0.09	0.05	-	0.01	0.00	0.00
Uncertainty	0.35	0.36	0.36	-	0.35	0.35	0.35	-	0.35	0.35	0.35
5 th percentile	0.19	2.51	2.79	-	0.80	0.13	0.06	-	0.01	0.00	0.00
25 th percentile	0.22	3.10	3.46	-	0.85	0.14	0.09	-	0.02	0.00	0.00
50 th percentile	0.24	3.24	3.73	-	1.02	0.17	0.12	-	0.03	0.00	0.00
75 th percentile	0.27	3.55	4.11	-	1.18	0.21	0.15	-	0.04	0.00	0.00
95 th percentile	0.31	3.88	4.51	-	1.41	0.43	0.23	-	0.05	0.00	0.00

CO (vol%, dry)	Measurement port E - Transversal distance (m)										
	-0.45	-0.25	-0.15	-0.10	-0.05	0	0.05	0.10	0.15	0.25	0.45
Mean	0.29	2.46	2.88	-	0.13	0.01	0.01	-	0.01	0.00	0.00
Std. deviation	0.06	0.44	0.61	-	0.07	0.00	0.01	-	0.01	0.00	0.00
Uncertainty	0.35	0.36	0.36	-	0.35	0.35	0.35	-	0.35	0.35	0.35
5 th percentile	0.21	1.72	1.98	-	0.05	0.00	0.00	-	0.00	0.00	0.00
25 th percentile	0.24	2.15	2.48	-	0.08	0.00	0.01	-	0.01	0.00	0.00
50 th percentile	0.28	2.53	2.86	-	0.11	0.01	0.01	-	0.01	0.00	0.00
75 th percentile	0.31	2.77	3.18	-	0.18	0.01	0.01	-	0.01	0.00	0.01
95 th percentile	0.43	3.19	4.13	-	0.28	0.01	0.05	-	0.02	0.00	0.01
CO (vol%, dry)	Measurement port F - Transversal distance (m)										
	-0.45	-0.30	-0.15	-0.10	-0.05	0	0.05	0.10	0.15	0.30	0.45
Mean	0.07	0.41	0.53	-	-	0.25	-	-	0.03	0.01	0.02
Std. deviation	0.02	0.09	0.09	-	-	0.07	-	-	0.02	0.00	0.01
Uncertainty	0.35	0.35	0.35	-	-	0.35	-	-	0.35	0.35	0.35
5 th percentile	0.03	0.30	0.40	-	-	0.14	-	-	0.01	0.00	0.01
25 th percentile	0.05	0.33	0.47	-	-	0.19	-	-	0.01	0.00	0.01
50 th percentile	0.06	0.41	0.52	-	-	0.23	-	-	0.02	0.01	0.01
75 th percentile	0.08	0.47	0.59	-	-	0.30	-	-	0.04	0.01	0.02
95 th percentile	0.10	0.57	0.70	-	-	0.39	-	-	0.07	0.02	0.04
CO (vol%, dry)	Measurement port G - Transversal distance (m)										
	-0.45	-0.30	-0.15	-0.10	-0.05	0	0.05	0.10	0.15	0.30	0.45
Mean	0.01	0.02	0.03	-	-	0.01	-	-	0.00	0.02	0.03
Std. deviation	0.01	0.01	0.01	-	-	0.01	-	-	0.00	0.01	0.01
Uncertainty	0.35	0.35	0.35	-	-	0.35	-	-	0.35	0.35	0.35
5 th percentile	0.00	0.01	0.01	-	-	0.00	-	-	0.00	0.00	0.01
25 th percentile	0.00	0.01	0.02	-	-	0.00	-	-	0.00	0.01	0.01
50 th percentile	0.01	0.02	0.02	-	-	0.01	-	-	0.00	0.02	0.02
75 th percentile	0.01	0.02	0.04	-	-	0.01	-	-	0.01	0.03	0.04
95 th percentile	0.02	0.03	0.05	-	-	0.02	-	-	0.01	0.03	0.06

B.1.6 Local Methane Concentration

CH4 (mg/m ³ , dry)	Measurement port A - Transversal distance (m)										
	-0.45	-0.25	-0.15	-0.10	-0.05	0	0.05	0.10	0.15	0.25	0.45
Mean	0.00	0.00	0.00	0.17	0.33	394.05	0.00	0.00	0.00	0.00	0.00
Std. deviation	0.00	0.00	0.00	0.19	0.38	18.39	0.00	0.00	0.00	0.00	0.00
Uncertainty	123.96	123.96	123.96	123.96	123.96	124.05	123.96	123.96	123.96	123.96	123.96
5 th percentile	0.00	0.00	0.00	0.00	0.00	358.47	0.00	0.00	0.00	0.00	0.00
25 th percentile	0.00	0.00	0.00	0.00	0.00	384.71	0.00	0.00	0.00	0.00	0.00
50 th percentile	0.00	0.00	0.00	0.12	0.25	394.09	0.00	0.00	0.00	0.00	0.00
75 th percentile	0.00	0.00	0.00	0.25	0.50	408.47	0.00	0.00	0.00	0.00	0.00
95 th percentile	0.00	0.00	0.00	0.64	1.27	422.49	0.00	0.00	0.00	0.00	0.00
CH4 (mg/m ³ , dry)	Measurement port B - Transversal distance (m)										
	-0.45	-0.25	-0.15	-0.10	-0.05	0	0.05	0.10	0.15	0.25	0.45
Mean	0.00	0.00	0.00	35.74	71.48	1076.07	1451.51	725.75	0.00	0.00	0.00
Std. deviation	0.00	0.00	0.00	7.22	14.43	120.87	62.55	31.27	0.00	0.00	0.00
Uncertainty	123.96	123.96	123.96	123.98	124.00	125.91	125.01	124.48	123.96	123.96	123.96
5 th percentile	0.00	0.00	0.00	22.85	45.69	879.17	1356.70	678.35	0.00	0.00	0.00
25 th percentile	0.00	0.00	0.00	30.98	61.95	976.27	1406.03	703.02	0.00	0.00	0.00
50 th percentile	0.00	0.00	0.00	35.61	71.22	1073.41	1467.68	733.84	0.00	0.00	0.00
75 th percentile	0.00	0.00	0.00	42.38	84.76	1158.98	1495.55	747.78	0.00	0.00	0.00
95 th percentile	0.00	0.00	0.00	46.41	92.81	1278.50	1537.86	768.93	0.00	0.00	0.00
CH4 (mg/m ³ , dry)	Measurement port C - Transversal distance (m)										
	-0.45	-0.25	-0.15	-0.10	-0.05	0	0.05	0.10	0.15	0.25	0.45
Mean	0.00	0.00	0.00	310.20	620.39	2728.91	1061.45	531.04	0.63	0.00	0.00
Std. deviation	0.00	0.00	0.00	52.83	105.67	487.39	167.68	84.49	1.29	0.00	0.00
Uncertainty	123.96	123.96	123.96	124.70	125.45	154.19	127.68	125.82	123.96	123.96	123.96
5 th percentile	0.00	0.00	0.00	234.71	469.41	2004.59	786.27	393.13	0.00	0.00	0.00
25 th percentile	0.00	0.00	0.00	270.93	541.86	2392.12	950.26	475.13	0.00	0.00	0.00
50 th percentile	0.00	0.00	0.00	305.24	610.48	2694.25	1048.29	524.14	0.00	0.00	0.00
75 th percentile	0.00	0.00	0.00	345.70	691.39	3039.05	1182.38	591.54	0.69	0.00	0.00
95 th percentile	0.00	0.00	0.00	405.33	810.66	3638.22	1329.50	666.77	4.04	0.00	0.00
CH4 (mg/m ³ , dry)	Measurement port D - Transversal distance (m)										
	-0.45	-0.25	-0.15	-0.10	-0.05	0	0.05	0.10	0.15	0.25	0.45
Mean	0.00	219.72	533.79	-	284.40	30.49	6.26	-	0.00	0.00	0.00
Std. deviation	0.00	44.99	101.86	-	76.41	22.21	5.86	-	0.00	0.00	0.00
Uncertainty	123.96	124.23	124.88	-	124.74	124.02	123.96	-	123.96	123.96	123.96
5 th percentile	0.00	144.87	351.86	-	198.64	10.26	0.00	-	0.00	0.00	0.00
25 th percentile	0.00	196.32	478.81	-	222.33	15.40	2.33	-	0.00	0.00	0.00
50 th percentile	0.00	208.24	523.78	-	253.78	24.72	5.09	-	0.00	0.00	0.00
75 th percentile	0.00	249.98	594.61	-	338.44	37.41	8.25	-	0.00	0.00	0.00
95 th percentile	0.00	293.17	701.18	-	434.14	92.37	16.95	-	0.00	0.00	0.00

CH4 (mg/m ³ , dry)	Measurement port E - Transversal distance (m)										
	-0.45	-0.25	-0.15	-0.10	-0.05	0	0.05	0.10	0.15	0.25	0.45
Mean	0.00	128.17	243.87	-	3.19	0.00	0.02	-	0.00	0.00	0.00
Std. deviation	0.00	34.06	72.44	-	6.96	0.00	0.13	-	0.00	0.00	0.00
Uncertainty	123.96	124.11	124.43	-	123.96	123.96	123.96	-	123.96	123.96	123.96
5 th percentile	0.00	73.48	144.91	-	0.00	0.00	0.00	-	0.00	0.00	0.00
25 th percentile	0.00	105.03	201.09	-	0.00	0.00	0.00	-	0.00	0.00	0.00
50 th percentile	0.00	127.95	231.20	-	0.00	0.00	0.00	-	0.00	0.00	0.00
75 th percentile	0.00	147.44	275.62	-	2.82	0.00	0.00	-	0.00	0.00	0.00
95 th percentile	0.00	187.48	396.93	-	19.40	0.00	0.00	-	0.00	0.00	0.00
CH4 (mg/m ³ , dry)	Measurement port F - Transversal distance (m)										
	-0.45	-0.30	-0.15	-0.10	-0.05	0	0.05	0.10	0.15	0.30	0.45
Mean	0.00	0.00	0.00	-	-	0.00	-	-	0.00	0.00	0.00
Std. deviation	0.00	0.00	0.00	-	-	0.00	-	-	0.00	0.00	0.00
Uncertainty	123.96	123.96	123.96	-	-	123.96	-	-	123.96	123.96	123.96
5 th percentile	0.00	0.00	0.00	-	-	0.00	-	-	0.00	0.00	0.00
25 th percentile	0.00	0.00	0.00	-	-	0.00	-	-	0.00	0.00	0.00
50 th percentile	0.00	0.00	0.00	-	-	0.00	-	-	0.00	0.00	0.00
75 th percentile	0.00	0.00	0.00	-	-	0.00	-	-	0.00	0.00	0.00
95 th percentile	0.00	0.00	0.00	-	-	0.00	-	-	0.00	0.00	0.00
CH4 (mg/m ³ , dry)	Measurement port G - Transversal distance (m)										
	-0.45	-0.30	-0.15	-0.10	-0.05	0	0.05	0.10	0.15	0.30	0.45
Mean	0.00	0.00	0.00	-	-	0.00	-	-	0.00	0.00	0.00
Std. deviation	0.00	0.00	0.00	-	-	0.00	-	-	0.00	0.00	0.00
Uncertainty	123.96	123.96	123.96	-	-	123.96	-	-	123.96	123.96	123.96
5 th percentile	0.00	0.00	0.00	-	-	0.00	-	-	0.00	0.00	0.00
25 th percentile	0.00	0.00	0.00	-	-	0.00	-	-	0.00	0.00	0.00
50 th percentile	0.00	0.00	0.00	-	-	0.00	-	-	0.00	0.00	0.00
75 th percentile	0.00	0.00	0.00	-	-	0.00	-	-	0.00	0.00	0.00
95 th percentile	0.00	0.00	0.00	-	-	0.00	-	-	0.00	0.00	0.00

B.1.7 Local Nitric Oxide Concentration

NO (mg/m ³ , dry)	Measurement port A - Transversal distance (m)										
	-0.45	-0.25	-0.15	-0.10	-0.05	0	0.05	0.10	0.15	0.25	0.45
Mean	256.72	256.34	262.16	180.32	98.48	419.22	469.13	373.38	277.63	256.34	256.72
Std. deviation	4.13	9.61	8.31	13.12	17.94	10.30	7.72	17.78	27.84	9.61	4.13
Uncertainty	30.56	30.58	30.58	30.74	30.89	30.66	30.61	30.79	30.97	30.58	30.56
5 th percentile	249.37	240.91	248.58	167.33	86.07	402.08	460.00	357.50	255.01	240.91	249.37
25 th percentile	253.52	247.85	254.72	170.70	86.68	409.70	464.15	361.92	259.69	247.85	253.52
50 th percentile	257.95	256.60	264.03	176.72	89.40	421.29	467.42	366.94	266.47	256.60	257.95
75 th percentile	259.63	264.27	269.31	186.15	102.99	428.37	470.48	377.46	284.44	264.27	259.63
95 th percentile	261.91	271.02	273.05	205.10	137.15	433.12	486.00	412.62	339.24	271.02	261.91
NO (mg/m ³ , dry)	Measurement port B - Transversal distance (m)										
	-0.45	-0.25	-0.15	-0.10	-0.05	0	0.05	0.10	0.15	0.25	0.45
Mean	221.75	234.45	168.42	339.83	511.23	572.32	467.38	353.04	238.71	370.94	313.36
Std. deviation	5.13	2.81	1.35	10.12	18.88	9.92	18.25	11.77	5.29	3.84	2.38
Uncertainty	30.57	30.55	30.55	30.68	30.80	30.60	30.91	30.74	30.57	30.55	30.55
5 th percentile	211.67	230.02	166.82	320.39	473.96	562.22	451.58	340.29	229.01	363.07	310.38
25 th percentile	217.88	231.69	167.19	334.95	502.72	565.11	452.20	343.23	234.26	368.46	312.24
50 th percentile	222.76	235.60	168.44	340.69	512.95	569.24	461.13	350.63	240.14	371.97	312.67
75 th percentile	225.93	236.42	169.21	348.14	527.07	574.23	475.39	359.12	242.84	373.34	313.94
95 th percentile	227.63	238.50	171.19	353.03	534.87	593.36	508.66	376.83	245.00	375.62	318.82
NO (mg/m ³ , dry)	Measurement port C - Transversal distance (m)										
	-0.45	-0.25	-0.15	-0.10	-0.05	0	0.05	0.10	0.15	0.25	0.45
Mean	207.67	306.47	340.67	311.38	282.10	207.66	298.84	299.94	301.04	277.22	295.34
Std. deviation	2.09	6.21	3.14	10.93	18.72	15.53	11.38	8.56	5.75	6.65	3.15
Uncertainty	30.55	30.57	30.55	30.64	30.74	30.68	30.62	30.59	30.56	30.57	30.55
5 th percentile	205.09	296.94	335.17	290.34	245.50	184.49	282.98	287.94	292.89	264.80	291.29
25 th percentile	206.46	299.17	338.67	304.74	270.81	194.96	287.91	292.15	296.40	272.26	292.41
50 th percentile	207.35	308.88	340.85	312.64	284.42	206.67	299.62	300.33	301.05	277.41	295.01
75 th percentile	208.46	311.55	343.23	318.27	293.31	214.91	306.90	306.06	305.22	283.70	297.03
95 th percentile	211.84	314.98	344.96	331.54	318.13	237.43	319.25	315.04	310.82	284.59	301.74
NO (mg/m ³ , dry)	Measurement port D - Transversal distance (m)										
	-0.45	-0.25	-0.15	-0.10	-0.05	0	0.05	0.10	0.15	0.25	0.45
Mean	280.59	296.48	275.96	-	301.93	283.07	275.76	-	241.33	224.65	216.40
Std. deviation	12.49	17.60	10.82	-	16.73	8.72	1.29	-	4.32	2.36	1.92
Uncertainty	30.63	30.71	30.59	-	30.70	30.59	30.55	-	30.56	30.55	30.55
5 th percentile	264.23	263.22	262.42	-	263.17	274.96	273.97	-	235.92	222.12	213.59
25 th percentile	270.45	288.01	267.74	-	298.56	278.41	274.69	-	237.48	222.82	215.15
50 th percentile	276.77	294.83	275.98	-	307.24	279.66	275.55	-	240.89	224.01	216.25
75 th percentile	292.29	309.08	280.27	-	313.62	283.61	276.66	-	244.45	225.68	217.92
95 th percentile	300.53	322.90	300.15	-	319.76	305.68	277.98	-	249.26	229.99	219.34

NO (mg/m ³ , dry)	Measurement port E - Transversal distance (m)										
	-0.45	-0.25	-0.15	-0.10	-0.05	0	0.05	0.10	0.15	0.25	0.45
Mean	221.32	280.03	269.19	-	273.25	216.85	244.34	-	238.35	236.16	241.11
Std. deviation	2.79	6.83	13.35	-	2.28	3.14	2.08	-	3.44	1.24	3.53
Uncertainty	30.55	30.57	30.61	-	30.55	30.55	30.55	-	30.55	30.55	30.55
5 th percentile	216.72	269.38	235.44	-	269.26	212.88	240.86	-	232.34	233.99	235.92
25 th percentile	219.97	273.78	266.59	-	271.62	214.43	242.93	-	235.98	235.14	239.14
50 th percentile	221.51	280.77	272.22	-	273.44	215.86	244.58	-	238.28	236.28	240.18
75 th percentile	223.50	285.56	276.98	-	275.32	219.97	245.87	-	240.50	236.85	243.51
95 th percentile	225.48	290.36	285.14	-	276.77	221.98	246.96	-	244.39	238.00	246.23
NO (mg/m ³ , dry)	Measurement port F - Transversal distance (m)										
	-0.45	-0.30	-0.15	-0.10	-0.05	0	0.05	0.10	0.15	0.30	0.45
Mean	272.87	326.19	313.22	-	-	279.84	-	-	283.49	259.44	257.29
Std. deviation	12.01	11.41	4.07	-	-	7.46	-	-	3.73	4.07	3.47
Uncertainty	30.62	30.62	30.55	-	-	30.58	-	-	30.55	30.55	30.55
5 th percentile	254.20	309.88	306.88	-	-	268.60	-	-	276.69	254.37	252.05
25 th percentile	259.76	315.53	310.22	-	-	273.15	-	-	280.68	256.70	254.34
50 th percentile	277.70	324.40	314.00	-	-	278.20	-	-	283.67	258.63	256.67
75 th percentile	283.08	336.03	316.62	-	-	287.85	-	-	286.10	260.60	260.60
95 th percentile	287.42	343.80	318.40	-	-	289.21	-	-	289.07	267.20	262.18
NO (mg/m ³ , dry)	Measurement port G - Transversal distance (m)										
	-0.45	-0.30	-0.15	-0.10	-0.05	0	0.05	0.10	0.15	0.30	0.45
Mean	214.04	301.55	289.59	-	-	289.18	-	-	288.62	280.67	281.41
Std. deviation	5.49	5.83	6.88	-	-	13.63	-	-	4.95	10.21	5.91
Uncertainty	30.56	30.56	30.57	-	-	30.65	-	-	30.56	30.60	30.56
5 th percentile	205.02	293.15	280.72	-	-	271.57	-	-	280.56	267.40	272.61
25 th percentile	210.96	296.04	285.04	-	-	281.36	-	-	286.06	272.62	276.19
50 th percentile	213.25	301.94	288.32	-	-	287.32	-	-	287.67	276.94	280.95
75 th percentile	217.18	305.38	296.04	-	-	290.89	-	-	290.57	290.10	286.78
95 th percentile	224.23	312.18	299.91	-	-	317.97	-	-	298.40	297.24	290.43

B.1.8 Total Radiative Heat Flux

Heat flux (kW/m ²)	Measurement						
	A	B	C	D	E	F	G
Mean	129.34	138.67	157.54	170.64	156.31	146.56	125.75
Std. deviation	1.77	1.98	3.28	1.92	2.65	2.47	3.16
Uncertainty	8.86	9.31	10.21	10.83	10.16	9.69	8.69
5 th percentile	126.55	135.75	151.15	167.26	152.38	142.71	120.81
25 th percentile	127.98	137.32	155.54	169.32	154.53	145.16	123.37
50 th percentile	129.14	138.68	158.30	170.96	156.20	146.36	125.07
75 th percentile	130.52	139.96	160.19	172.04	158.48	148.10	128.40
95 th percentile	132.35	141.89	161.53	173.36	160.27	150.85	131.03

B.2 Oxy-Flame 1

B.2.1 Furnace Operating Conditions

Operating parameter	
Coal feed rate (kg/h)	57.15 ±0.26
Volume flow rate of primary stream (m ³ /h, STP)	34.82 ±1.58
O ₂ fraction of primary stream (vol%, wet)	19.40 ±1.12
CO ₂ fraction of primary stream (vol%, wet) ¹	81.60
Temperature of primary stream (°C)	16.83 ±1.23
Velocity of primary stream at burner exit (m/s) ¹	23
Axial momentum of primary stream at burner exit (N) ¹	0.47
Volume flow rate of secondary stream (m ³ /h, STP)	144 ±2.80
Volume flow rate of tertiary stream (m ³ /h, STP)	72 ±7.05
O ₂ fraction of secondary and tertiary stream (vol%, wet)	33 ±1.91
H ₂ O fraction of secondary and tertiary stream (vol%, wet) ¹	20.84
CO ₂ fraction of secondary and tertiary stream (vol%, wet) ¹	42.82
N ₂ fraction of secondary and tertiary stream (vol%, wet) ¹	3.22
Temperature of secondary and tertiary streams (°C)	155.60 ±1.70
Secondary/tertiary mass flow ratio ¹	2.00
Swirl number of secondary stream ¹	1.15
Stoichiometric ratio ¹	1.16
Overall heat input (kW) ¹	350.10
Sensible heat input (kW) ¹	13.70
Flue gas	
O ₂ (vol%, dry)	6.24 ±0.83
CO ₂ (vol%, dry)	87.21 ±1.05
N ₂ (vol%, dry) ¹	6.55
H ₂ O (vol% wet)	29.80 ±0.19
Volume flow rate at furnace exit (m ³ /h, STP)	309.80 ±5.25
Volume flow rate of recycled flue gas (m ³ /h, STP)	142.60 ±3.57
Temperature at furnace exit (°C)	501.90 ±3.44
Recycle ratio ¹	0.46
Outer wall surface temperature at the vertical section (°C)	196.39 ±1.84
Inner surface temperature of the cylindrical section (°C)	920.61 ±4.33

¹calculated value

B.2.2 Local Gas Temperature

Temperature (°C)	Measurement port A - Transversal distance (m)										
	-0.45	-0.25	-0.15	-0.10	-0.05	0	0.05	0.10	0.15	0.25	0.45
Mean	950	1106	1100	1008	560	625	1014	813	844	1003	1036
Std. deviation	2.67	7.06	2.33	8.18	11.12	10.14	9.00	9.28	3.68	10.17	3.30
Uncertainty	23.80	27.67	27.49	25.28	14.73	16.23	25.50	20.54	21.22	25.26	25.91
5 th percentile	945	1094	1096	994	545	610	996	802	837	987	1031
25 th percentile	949	1099	1099	1000	549	614	1012	805	842	995	1034
50 th percentile	951	1109	1100	1010	559	627	1018	811	844	1003	1037
75 th percentile	952	1112	1102	1012	568	633	1021	823	846	1012	1039
95 th percentile	954	1114	1104	1022	578	638	1024	828	850	1016	1040
Temperature (°C)	Measurement port B - Transversal distance (m)										
	-0.45	-0.25	-0.15	-0.10	-0.05	0	0.05	0.10	0.15	0.25	0.45
Mean	1063	1073	967	1061	1202	1294	1310	1337	1147	1151	1147
Std. deviation	2.93	3.77	4.94	4.40	5.43	5.24	13.27	4.34	9.55	4.77	2.85
Uncertainty	26.58	26.83	24.23	26.53	30.06	32.40	32.86	33.48	28.72	28.75	28.66
5 th percentile	1057	1067	961	1052	1191	1285	1288	1328	1136	1144	1143
25 th percentile	1062	1071	964	1058	1198	1291	1295	1334	1138	1146	1144
50 th percentile	1063	1074	966	1061	1204	1294	1314	1338	1144	1152	1148
75 th percentile	1066	1076	970	1064	1205	1298	1320	1339	1157	1155	1149
95 th percentile	1067	1078	976	1067	1208	1302	1325	1342	1162	1157	1151
Temperature (°C)	Measurement port C - Transversal distance (m)										
	-0.45	-0.25	-0.15	-0.10	-0.05	0	0.05	0.10	0.15	0.25	0.45
Mean	1107	1187	1235	1289	1373	1253	1236	1351	1297	1220	1151
Std. deviation	3.16	4.29	4.46	8.09	4.35	12.32	7.69	5.90	3.62	6.79	3.61
Uncertainty	27.67	29.67	30.87	32.27	34.42	31.42	30.94	33.85	32.45	30.51	28.75
5 th percentile	1102	1176	1227	1275	1364	1233	1226	1341	1291	1208	1144
25 th percentile	1105	1184	1232	1283	1371	1242	1230	1345	1294	1216	1148
50 th percentile	1108	1187	1235	1288	1375	1257	1234	1351	1296	1221	1151
75 th percentile	1109	1190	1237	1296	1376	1264	1241	1355	1300	1225	1153
95 th percentile	1112	1192	1242	1300	1378	1270	1250	1360	1302	1230	1156
Temperature (°C)	Measurement port D - Transversal distance (m)										
	-0.45	-0.25	-0.15	-0.10	-0.05	0	0.05	0.10	0.15	0.25	0.45
Mean	1105	1184	1189	-	1086	1087	1152	-	1293	1274	1180
Std. deviation	7.88	15.55	15.08	-	16.07	13.35	20.62	-	10.97	7.85	8.98
Uncertainty	27.15	29.12	29.26	-	26.79	26.78	28.50	-	31.73	31.23	28.98
5 th percentile	1090	1161	1165	-	1067	1070	1120	-	1269	1262	1165
25 th percentile	1099	1172	1177	-	1074	1077	1141	-	1288	1268	1175
50 th percentile	1105	1184	1186	-	1081	1084	1149	-	1294	1275	1181
75 th percentile	1110	1193	1203	-	1094	1092	1168	-	1302	1279	1187
95 th percentile	1116	1210	1213	-	1119	1114	1188	-	1304	1286	1195

Temperature (°C)	Measurement port E - Transversal distance (m)										
	-0.45	-0.25	-0.15	-0.10	-0.05	0	0.05	0.10	0.15	0.25	0.45
Mean	901	1094	1092	-	1050	1156	1225	-	1250	1207	1100
Std. deviation	9.35	6.34	3.31	-	5.16	7.48	5.98	-	5.76	9.08	6.31
Uncertainty	22.33	26.87	26.80	-	25.80	28.38	30.04	-	30.65	29.62	27.01
5 th percentile	885	1085	1087	-	1042	1145	1215	-	1240	1190	1090
25 th percentile	893	1088	1088	-	1047	1149	1221	-	1247	1201	1095
50 th percentile	904	1096	1092	-	1049	1157	1225	-	1249	1209	1100
75 th percentile	907	1100	1093	-	1053	1162	1231	-	1254	1214	1104
95 th percentile	917	1102	1098	-	1060	1167	1233	-	1260	1222	1111
Temperature (°C)	Measurement port F - Transversal distance (m)										
	-0.45	-0.30	-0.15	-0.10	-0.05	0	0.05	0.10	0.15	0.30	0.45
Mean	1010	1114	1130	-	-	1153	-	-	1172	1166	1128
Std. deviation	1.39	11.80	7.52	-	-	10.09	-	-	11.28	15.52	14.13
Uncertainty	24.83	27.46	27.75	-	-	28.40	-	-	28.89	28.72	27.78
5 th percentile	1007	1089	1119	-	-	1138	-	-	1158	1133	1103
25 th percentile	1010	1108	1123	-	-	1146	-	-	1164	1157	1120
50 th percentile	1010	1117	1128	-	-	1153	-	-	1170	1167	1128
75 th percentile	1011	1123	1136	-	-	1158	-	-	1179	1175	1136
95 th percentile	1012	1129	1143	-	-	1171	-	-	1192	1190	1150
Temperature (°C)	Measurement port G - Transversal distance (m)										
	-0.45	-0.30	-0.15	-0.10	-0.05	0	0.05	0.10	0.15	0.30	0.45
Mean	933	1036	1063	-	-	1075	-	-	1078	1045	1034
Std. deviation	15.40	10.44	3.65	-	-	4.26	-	-	5.48	9.69	6.71
Uncertainty	23.08	25.53	26.12	-	-	26.40	-	-	26.48	25.74	25.44
5 th percentile	908	1019	1057	-	-	1066	-	-	1070	1028	1025
25 th percentile	916	1031	1061	-	-	1073	-	-	1075	1039	1030
50 th percentile	939	1034	1063	-	-	1075	-	-	1078	1046	1034
75 th percentile	946	1047	1066	-	-	1078	-	-	1082	1051	1037
95 th percentile	952	1053	1069	-	-	1081	-	-	1090	1061	1048

B.2.3 Local Oxygen Concentration

O ₂ (vol%, dry)	Measurement port A - Transversal distance (m)										
	-0.45	-0.25	-0.15	-0.10	-0.05	0	0.05	0.10	0.15	0.25	0.45
Mean	9.15	9.42	11.03	38.57	40.71	26.15	30.02	32.92	23.52	11.09	8.93
Std. deviation	0.56	0.60	0.95	0.70	0.28	0.88	0.69	2.81	0.66	1.10	1.11
Uncertainty	0.60	0.60	0.61	0.60	0.59	0.61	0.60	0.78	0.60	0.62	0.62
5 th percentile	8.37	8.28	9.89	37.52	40.29	24.06	29.00	28.67	22.16	9.45	7.29
25 th percentile	8.78	9.06	10.35	37.87	40.55	25.90	29.52	30.73	23.00	10.21	8.18
50 th percentile	9.01	9.52	10.77	38.62	40.64	26.14	29.98	32.72	23.65	11.22	8.81
75 th percentile	9.62	9.76	11.47	39.30	40.87	26.88	30.29	36.10	23.98	11.83	9.35
95 th percentile	10.26	10.32	13.05	39.41	41.24	27.11	30.85	36.76	24.41	12.96	11.15
O ₂ (vol%, dry)	Measurement port B - Transversal distance (m)										
	-0.45	-0.25	-0.15	-0.10	-0.05	0	0.05	0.10	0.15	0.25	0.45
Mean	12.53	18.72	24.67	18.83	9.38	8.36	8.70	13.70	16.37	11.80	10.00
Std. deviation	0.42	0.40	0.65	0.38	0.89	1.66	0.53	1.69	1.12	0.85	0.99
Uncertainty	0.59	0.59	0.60	0.59	0.61	0.64	0.60	0.66	0.62	0.61	0.61
5 th percentile	11.98	18.22	23.70	18.40	8.02	5.24	8.00	11.08	15.00	10.28	8.53
25 th percentile	12.15	18.37	24.17	18.53	8.81	7.32	8.40	11.97	15.29	11.11	9.00
50 th percentile	12.51	18.64	24.58	18.75	9.23	8.44	8.59	13.89	16.19	11.86	10.03
75 th percentile	12.91	19.01	25.07	19.06	9.82	9.38	8.87	15.10	17.29	12.52	10.86
95 th percentile	13.13	19.45	25.88	19.41	11.23	11.24	10.02	16.42	18.31	13.14	11.50
O ₂ (vol%, dry)	Measurement port C - Transversal distance (m)										
	-0.45	-0.25	-0.15	-0.10	-0.05	0	0.05	0.10	0.15	0.25	0.45
Mean	10.41	12.77	11.82	7.07	0.77	0.68	0.83	4.47	7.58	8.04	7.31
Std. deviation	0.78	0.66	0.68	0.54	0.08	0.06	0.15	0.50	0.52	0.58	0.61
Uncertainty	0.60	0.60	0.60	0.60	0.59	0.59	0.59	0.59	0.60	0.60	0.60
5 th percentile	9.29	11.83	10.62	6.19	0.65	0.58	0.71	3.76	6.85	7.02	6.20
25 th percentile	9.88	12.29	11.37	6.51	0.70	0.64	0.74	4.06	7.20	7.73	6.85
50 th percentile	10.15	12.63	11.79	7.09	0.76	0.67	0.77	4.35	7.51	8.06	7.44
75 th percentile	10.98	13.39	12.17	7.56	0.83	0.71	0.84	4.78	7.83	8.44	7.73
95 th percentile	11.75	13.94	13.07	7.76	0.89	0.79	1.22	5.39	8.57	8.94	8.36
O ₂ (vol%, dry)	Access port D - Transversal distance (m)										
	-0.45	-0.25	-0.15	-0.10	-0.05	0	0.05	0.10	0.15	0.25	0.45
Mean	11.73	10.22	6.48	-	1.05	0.74	1.86	-	8.20	11.86	12.65
Std. deviation	0.77	0.51	1.22	-	0.35	0.15	0.26	-	0.86	0.44	0.89
Uncertainty	0.61	0.59	0.63	-	0.59	0.59	0.59	-	0.60	0.59	0.60
5 th percentile	10.49	8.93	4.51	-	0.52	0.51	1.43	-	6.66	11.18	11.16
25 th percentile	11.19	10.03	5.51	-	0.85	0.61	1.68	-	7.63	11.51	11.91
50 th percentile	11.82	10.32	6.39	-	1.00	0.77	1.84	-	8.11	11.90	12.95
75 th percentile	12.20	10.55	7.72	-	1.16	0.83	1.97	-	8.73	12.15	13.36
95 th percentile	13.27	10.80	8.20	-	1.87	0.99	2.39	-	9.66	12.55	13.88

O ₂ (vol%, dry)	Measurement port E - Transversal distance (m)										
	-0.45	-0.25	-0.15	-0.10	-0.05	0	0.05	0.10	0.15	0.25	0.45
Mean	10.22	10.16	9.90	-	8.74	3.95	6.09	-	6.85	9.60	10.41
Std. deviation	0.44	0.76	0.43	-	0.71	0.49	0.76	-	0.58	0.81	0.86
Uncertainty	0.60	0.60	0.59	-	0.60	0.59	0.61	-	0.60	0.60	0.61
5 th percentile	9.52	9.05	9.23	-	7.59	3.26	4.71	-	5.75	8.21	9.16
25 th percentile	9.84	9.54	9.51	-	8.12	3.59	5.71	-	6.54	9.18	9.53
50 th percentile	10.17	10.21	9.96	-	8.80	3.94	6.17	-	6.88	9.63	10.59
75 th percentile	10.70	10.45	10.28	-	9.40	4.17	6.57	-	7.32	10.19	11.10
95 th percentile	10.81	11.68	10.55	-	9.67	5.08	7.28	-	7.70	10.84	11.69
O ₂ (vol%, dry)	Measurement port F - Transversal distance (m)										
	-0.45	-0.30	-0.15	-0.10	-0.05	0	0.05	0.10	0.15	0.30	0.45
Mean	9.25	8.28	8.20	-	-	8.47	-	-	8.59	8.33	8.61
Std. deviation	0.53	0.39	0.47	-	-	0.67	-	-	0.56	0.66	0.73
Uncertainty	0.59	0.59	0.59	-	-	0.60	-	-	0.59	0.60	0.60
5 th percentile	8.57	7.59	7.33	-	-	7.79	-	-	7.45	7.00	7.24
25 th percentile	8.92	8.04	7.93	-	-	8.03	-	-	8.31	7.83	8.18
50 th percentile	9.20	8.27	8.20	-	-	8.37	-	-	8.64	8.44	8.69
75 th percentile	9.68	8.50	8.49	-	-	8.67	-	-	9.05	8.84	9.11
95 th percentile	10.11	9.01	8.95	-	-	10.08	-	-	9.30	9.24	9.66
O ₂ (vol%, dry)	Measurement port G - Transversal distance (m)										
	-0.45	-0.30	-0.15	-0.10	-0.05	0	0.05	0.10	0.15	0.30	0.45
Mean	9.04	8.03	7.76	-	-	7.50	-	-	7.55	7.47	7.40
Std. deviation	0.46	0.27	0.21	-	-	0.22	-	-	0.28	0.28	0.47
Uncertainty	0.59	0.59	0.59	-	-	0.59	-	-	0.59	0.59	0.59
5 th percentile	8.20	7.60	7.42	-	-	7.24	-	-	7.22	6.96	6.55
25 th percentile	8.68	7.84	7.65	-	-	7.32	-	-	7.33	7.24	7.15
50 th percentile	9.11	7.99	7.70	-	-	7.43	-	-	7.56	7.48	7.39
75 th percentile	9.42	8.21	7.88	-	-	7.69	-	-	7.74	7.74	7.77
95 th percentile	9.70	8.58	8.16	-	-	7.88	-	-	8.08	7.84	8.14

B.2.4 Local Carbon Dioxide Concentration

CO ₂ (vol%, dry)	Measurement port A - Transversal distance (m)										
	-0.45	-0.25	-0.15	-0.10	-0.05	0	0.05	0.10	0.15	0.25	0.45
Mean	87.59	87.47	86.01	56.34	54.15	71.43	64.84	63.76	72.14	85.86	90.07
Std. deviation	0.67	0.73	1.09	0.77	0.27	0.82	0.83	2.13	0.80	1.24	1.21
Uncertainty	1.67	1.67	1.67	1.48	1.46	1.57	1.53	1.58	1.57	1.67	1.70
5 th percentile	86.39	86.32	83.57	55.43	53.65	70.49	63.60	60.69	71.05	83.66	88.06
25 th percentile	87.23	87.08	85.52	55.59	54.01	70.76	64.57	62.51	71.57	85.06	89.18
50 th percentile	87.50	87.32	86.29	56.18	54.20	71.36	64.91	63.60	72.04	85.96	90.06
75 th percentile	87.91	87.97	86.77	57.24	54.31	71.75	65.41	65.27	72.60	86.69	90.95
95 th percentile	88.71	88.90	87.37	57.48	54.55	73.34	65.96	66.98	73.76	87.80	92.17
CO ₂ (vol%, dry)	Measurement port B - Transversal distance (m)										
	-0.45	-0.25	-0.15	-0.10	-0.05	0	0.05	0.10	0.15	0.25	0.45
Mean	84.78	77.78	71.00	77.59	86.30	84.05	88.09	83.62	80.39	85.27	87.54
Std. deviation	0.52	0.45	0.69	0.45	1.17	0.80	0.51	1.94	1.38	1.05	1.15
Uncertainty	1.65	1.60	1.56	1.60	1.67	1.64	1.67	1.67	1.63	1.66	1.67
5 th percentile	84.01	76.91	69.75	76.87	84.16	82.53	86.81	80.74	78.03	83.65	85.81
25 th percentile	84.34	77.47	70.58	77.26	85.57	83.65	88.02	81.97	79.25	84.50	86.50
50 th percentile	84.81	77.86	71.08	77.72	86.41	84.23	88.15	83.46	80.74	85.18	87.42
75 th percentile	85.23	78.14	71.49	78.00	87.00	84.67	88.25	85.51	81.65	86.11	88.65
95 th percentile	85.45	78.38	72.02	78.12	88.18	85.06	88.82	86.62	82.05	87.15	89.24
CO ₂ (vol%, dry)	Measurement port C - Transversal distance (m)										
	-0.45	-0.25	-0.15	-0.10	-0.05	0	0.05	0.10	0.15	0.25	0.45
Mean	87.16	84.49	85.35	88.20	80.57	74.01	82.08	89.10	87.12	88.68	88.01
Std. deviation	0.95	0.75	0.77	0.49	1.07	0.45	0.59	0.50	0.67	0.69	0.79
Uncertainty	1.67	1.65	1.65	1.67	1.62	1.57	1.63	1.68	1.67	1.68	1.67
5 th percentile	85.47	83.23	83.88	87.55	79.14	73.28	81.18	88.12	85.94	87.59	86.56
25 th percentile	86.53	83.84	85.06	87.83	79.65	73.67	81.67	88.76	86.62	88.22	87.64
50 th percentile	87.42	84.56	85.40	88.08	80.48	74.01	82.00	89.21	87.12	88.62	87.97
75 th percentile	87.79	85.04	85.84	88.56	81.41	74.29	82.52	89.44	87.46	89.20	88.57
95 th percentile	88.52	85.62	86.59	89.13	82.63	74.90	83.08	89.85	88.29	89.89	89.51
CO ₂ (vol%, dry)	Measurement port D - Transversal distance (m)										
	-0.45	-0.25	-0.15	-0.10	-0.05	0	0.05	0.10	0.15	0.25	0.45
Mean	79.15	83.79	89.55	-	87.67	86.49	88.19	-	87.77	84.42	83.42
Std. deviation	1.29	1.05	1.03	-	1.17	0.66	0.42	-	0.68	0.47	1.03
Uncertainty	1.62	1.65	1.69	-	1.67	1.67	1.67	-	1.67	1.64	1.64
5 th percentile	76.94	82.45	88.13	-	85.81	85.69	87.61	-	86.57	83.71	81.94
25 th percentile	78.37	83.05	88.74	-	86.90	85.99	87.88	-	87.34	84.08	82.57
50 th percentile	79.06	83.70	89.48	-	87.59	86.30	88.09	-	87.87	84.40	83.19
75 th percentile	79.53	84.36	89.93	-	88.41	87.28	88.41	-	88.19	84.75	84.29
95 th percentile	81.61	86.22	91.43	-	89.75	87.54	89.08	-	88.99	85.19	85.11

CO ₂ (vol%, dry)	Measurement port E - Transversal distance (m)										
	-0.45	-0.25	-0.15	-0.10	-0.05	0	0.05	0.10	0.15	0.25	0.45
Mean	81.51	84.31	84.82	-	87.40	90.61	88.84	-	88.49	85.19	85.43
Std. deviation	0.60	0.93	1.46	-	0.80	0.40	0.64	-	0.51	0.83	0.88
Uncertainty	1.63	1.65	1.66	-	1.67	1.69	1.68	-	1.67	1.65	1.66
5 th percentile	80.55	82.48	80.83	-	86.29	89.97	87.98	-	87.75	83.91	84.03
25 th percentile	81.11	83.85	84.88	-	86.61	90.29	88.44	-	88.10	84.70	84.65
50 th percentile	81.56	84.16	85.30	-	87.42	90.68	88.75	-	88.50	85.11	85.41
75 th percentile	81.85	85.14	85.62	-	87.94	90.92	89.16	-	88.77	85.57	86.25
95 th percentile	82.40	85.69	86.02	-	88.72	91.18	90.15	-	89.42	86.63	86.60
CO ₂ (vol%, dry)	Measurement port F - Transversal distance (m)										
	-0.45	-0.30	-0.15	-0.10	-0.05	0	0.05	0.10	0.15	0.30	0.45
Mean	82.40	90.87	90.76	-	-	90.54	-	-	90.81	90.91	90.30
Std. deviation	1.72	0.51	0.57	-	-	0.72	-	-	0.66	0.73	1.05
Uncertainty	1.65	1.69	1.69	-	-	1.69	-	-	1.69	1.69	1.69
5 th percentile	79.15	89.68	89.94	-	-	88.81	-	-	90.00	89.97	88.23
25 th percentile	81.50	90.61	90.37	-	-	90.35	-	-	90.24	90.39	89.72
50 th percentile	82.58	90.95	90.73	-	-	90.64	-	-	90.74	90.70	90.46
75 th percentile	83.73	91.24	91.12	-	-	90.96	-	-	91.15	91.39	90.86
95 th percentile	84.80	91.58	91.80	-	-	91.28	-	-	92.19	92.43	92.07
CO ₂ (vol%, dry)	Measurement port G - Transversal distance (m)										
	-0.45	-0.30	-0.15	-0.10	-0.05	0	0.05	0.10	0.15	0.30	0.45
Mean	83.27	91.18	91.87	-	-	92.34	-	-	92.25	92.30	92.42
Std. deviation	1.96	0.35	0.26	-	-	0.27	-	-	0.32	0.35	0.57
Uncertainty	1.65	1.69	1.70	-	-	1.70	-	-	1.70	1.70	1.70
5 th percentile	80.11	90.52	91.39	-	-	91.84	-	-	91.61	91.81	91.44
25 th percentile	82.08	90.99	91.72	-	-	92.09	-	-	92.06	91.99	92.06
50 th percentile	83.13	91.16	91.89	-	-	92.42	-	-	92.29	92.31	92.46
75 th percentile	84.54	91.43	92.10	-	-	92.56	-	-	92.51	92.61	92.74
95 th percentile	86.45	91.74	92.24	-	-	92.64	-	-	92.70	92.91	93.42

B.2.5 Local Carbon Monoxide Concentration

CO (vol%, dry)	Measurement port A - Transversal distance (m)										
	-0.45	-0.25	-0.15	-0.10	-0.05	0	0.05	0.10	0.15	0.25	0.45
Mean	0.05	0.02	0.05	0.10	0.12	1.05	0.22	0.21	0.27	0.08	0.02
Std. deviation	0.02	0.00	0.01	0.01	0.01	0.14	0.21	0.02	0.01	0.03	0.00
Uncertainty	0.35	0.35	0.35	0.35	0.35	0.35	0.35	0.35	0.35	0.35	0.35
5 th percentile	0.03	0.02	0.04	0.09	0.11	0.75	0.06	0.17	0.25	0.05	0.02
25 th percentile	0.03	0.02	0.05	0.10	0.12	1.04	0.09	0.18	0.26	0.06	0.02
50 th percentile	0.04	0.02	0.05	0.10	0.12	1.07	0.17	0.22	0.27	0.07	0.02
75 th percentile	0.06	0.02	0.06	0.11	0.13	1.12	0.23	0.23	0.28	0.10	0.02
95 th percentile	0.07	0.02	0.06	0.11	0.13	1.17	0.81	0.24	0.29	0.15	0.03
CO (vol%, dry)	Measurement port B - Transversal distance (m)										
	-0.45	-0.25	-0.15	-0.10	-0.05	0	0.05	0.10	0.15	0.25	0.45
Mean	0.01	0.18	0.51	0.41	2.18	8.30	1.28	0.19	0.10	0.02	0.01
Std. deviation	0.00	0.02	0.05	0.03	0.25	1.46	0.18	0.02	0.02	0.00	0.00
Uncertainty	0.35	0.35	0.35	0.35	0.35	0.39	0.35	0.35	0.35	0.35	0.35
5 th percentile	0.00	0.13	0.43	0.38	1.66	6.00	0.96	0.17	0.08	0.02	0.01
25 th percentile	0.01	0.16	0.47	0.39	2.06	7.40	1.16	0.18	0.09	0.02	0.01
50 th percentile	0.01	0.18	0.51	0.41	2.19	8.04	1.27	0.19	0.10	0.02	0.01
75 th percentile	0.01	0.20	0.55	0.44	2.29	9.40	1.38	0.20	0.12	0.03	0.01
95 th percentile	0.01	0.21	0.59	0.46	2.57	10.68	1.63	0.24	0.13	0.03	0.01
CO (vol%, dry)	Measurement port C - Transversal distance (m)										
	-0.45	-0.25	-0.15	-0.10	-0.05	0	0.05	0.10	0.15	0.25	0.45
Mean	0.03	0.03	0.25	2.46	14.50	18.29	12.76	3.17	0.72	0.12	0.06
Std. deviation	0.05	0.02	0.10	0.52	0.92	0.28	0.59	0.32	0.13	0.03	0.02
Uncertainty	0.35	0.35	0.35	0.36	0.38	0.35	0.37	0.35	0.35	0.35	0.35
5 th percentile	0.01	0.02	0.14	1.72	12.71	17.81	11.56	2.61	0.50	0.07	0.03
25 th percentile	0.01	0.02	0.16	2.10	13.89	18.12	12.37	2.98	0.62	0.11	0.04
50 th percentile	0.01	0.03	0.23	2.30	14.56	18.28	12.92	3.15	0.73	0.12	0.05
75 th percentile	0.03	0.04	0.32	2.86	15.31	18.49	13.21	3.35	0.81	0.14	0.07
95 th percentile	0.12	0.06	0.45	3.49	15.77	18.73	13.52	3.70	0.91	0.16	0.11
CO (vol%, dry)	Measurement port D - Transversal distance (m)										
	-0.45	-0.25	-0.15	-0.10	-0.05	0	0.05	0.10	0.15	0.25	0.45
Mean	0.00	0.13	0.85	-	8.11	9.43	6.85	-	0.80	0.06	0.01
Std. deviation	0.00	0.05	0.48	-	1.29	0.68	0.52	-	0.31	0.03	0.01
Uncertainty	0.35	0.35	0.36	-	0.39	0.39	0.36	-	0.35	0.35	0.35
5 th percentile	0.00	0.06	0.24	-	5.70	8.36	5.69	-	0.29	0.03	0.00
25 th percentile	0.00	0.09	0.39	-	7.26	8.57	6.60	-	0.55	0.04	0.00
50 th percentile	0.00	0.12	0.73	-	8.25	9.59	6.93	-	0.87	0.05	0.00
75 th percentile	0.01	0.16	1.30	-	8.88	10.00	7.24	-	1.02	0.07	0.01
95 th percentile	0.01	0.22	1.63	-	10.22	10.21	7.49	-	1.34	0.11	0.03

CO (vol%, dry)	Measurement port E - Transversal distance (m)										
	-0.45	-0.25	-0.15	-0.10	-0.05	0	0.05	0.10	0.15	0.25	0.45
Mean	0.00	0.01	0.01	-	0.08	2.17	1.18	-	0.72	0.32	0.09
Std. deviation	0.00	0.01	0.01	-	0.10	0.41	0.32	-	0.21	0.11	0.05
Uncertainty	0.35	0.35	0.35	-	0.35	0.36	0.36	-	0.35	0.35	0.35
5 th percentile	0.00	0.00	0.00	-	0.01	1.28	0.69	-	0.44	0.16	0.04
25 th percentile	0.00	0.00	0.00	-	0.01	1.98	0.98	-	0.54	0.25	0.05
50 th percentile	0.00	0.01	0.01	-	0.03	2.19	1.18	-	0.64	0.32	0.07
75 th percentile	0.00	0.01	0.01	-	0.12	2.45	1.42	-	0.91	0.38	0.10
95 th percentile	0.00	0.03	0.02	-	0.32	2.75	1.76	-	1.06	0.52	0.20
CO (vol%, dry)	Measurement port F - Transversal distance (m)										
	-0.45	-0.30	-0.15	-0.10	-0.05	0	0.05	0.10	0.15	0.30	0.45
Mean	0.01	0.02	0.04	-	-	0.10	-	-	0.11	0.22	0.18
Std. deviation	0.01	0.02	0.02	-	-	0.06	-	-	0.04	0.09	0.13
Uncertainty	0.35	0.35	0.35	-	-	0.35	-	-	0.35	0.35	0.35
5 th percentile	0.00	0.00	0.01	-	-	0.03	-	-	0.04	0.07	0.03
25 th percentile	0.01	0.01	0.02	-	-	0.06	-	-	0.08	0.16	0.09
50 th percentile	0.01	0.01	0.03	-	-	0.08	-	-	0.10	0.22	0.15
75 th percentile	0.02	0.02	0.05	-	-	0.12	-	-	0.13	0.28	0.26
95 th percentile	0.05	0.08	0.09	-	-	0.24	-	-	0.19	0.36	0.46
CO (vol%, dry)	Measurement port G - Transversal distance (m)										
	-0.45	-0.30	-0.15	-0.10	-0.05	0	0.05	0.10	0.15	0.30	0.45
Mean	0.01	0.00	0.00	-	-	0.01	-	-	0.01	0.02	0.02
Std. deviation	0.01	0.00	0.00	-	-	0.01	-	-	0.00	0.02	0.01
Uncertainty	0.35	0.35	0.35	-	-	0.35	-	-	0.35	0.35	0.35
5 th percentile	0.00	0.00	0.00	-	-	0.00	-	-	0.00	0.00	0.00
25 th percentile	0.00	0.00	0.00	-	-	0.00	-	-	0.00	0.01	0.01
50 th percentile	0.00	0.00	0.00	-	-	0.01	-	-	0.01	0.01	0.02
75 th percentile	0.01	0.01	0.01	-	-	0.01	-	-	0.01	0.03	0.02
95 th percentile	0.04	0.01	0.01	-	-	0.02	-	-	0.01	0.07	0.05

B.2.6 Local Methane Concentration

CH ₄ (mg/m ³ , dry)	Measurement port A - Transversal distance (m)										
	-0.45	-0.25	-0.15	-0.10	-0.05	0	0.05	0.10	0.15	0.25	0.45
Mean	0.00	0.00	0.00	0.00	0.00	120.38	11.90	0.00	0.00	0.00	0.00
Std. deviation	0.00	0.00	0.00	0.00	0.00	32.31	25.73	0.00	0.00	0.00	0.00
Uncertainty	123.96	123.96	123.96	123.96	123.96	124.10	124.05	123.96	123.96	123.96	123.96
5 th percentile	0.00	0.00	0.00	0.00	0.00	32.00	0.00	0.00	0.00	0.00	0.00
25 th percentile	0.00	0.00	0.00	0.00	0.00	119.78	0.00	0.00	0.00	0.00	0.00
50 th percentile	0.00	0.00	0.00	0.00	0.00	128.62	0.00	0.00	0.00	0.00	0.00
75 th percentile	0.00	0.00	0.00	0.00	0.00	139.11	8.60	0.00	0.00	0.00	0.00
95 th percentile	0.00	0.00	0.00	0.00	0.00	143.80	85.21	0.00	0.00	0.00	0.00
CH ₄ (mg/m ³ , dry)	Measurement port B - Transversal distance (m)										
	-0.45	-0.25	-0.15	-0.10	-0.05	0	0.05	0.10	0.15	0.25	0.45
Mean	0.00	0.35	21.87	3.98	68.09	1371.24	13.74	0.00	0.00	0.00	0.00
Std. deviation	0.00	0.55	3.68	1.50	21.39	401.11	10.46	0.00	0.00	0.00	0.00
Uncertainty	123.96	123.96	123.96	123.96	124.02	132.33	123.97	123.96	123.96	123.96	123.96
5 th percentile	0.00	0.00	16.49	1.34	25.70	779.54	2.55	0.00	0.00	0.00	0.00
25 th percentile	0.00	0.00	19.12	3.40	49.37	1076.81	9.20	0.00	0.00	0.00	0.00
50 th percentile	0.00	0.00	21.51	3.75	73.69	1296.76	11.34	0.00	0.00	0.00	0.00
75 th percentile	0.00	0.65	24.64	5.04	82.36	1702.18	15.49	0.00	0.00	0.00	0.00
95 th percentile	0.00	1.45	27.98	6.53	94.85	2042.03	25.86	0.00	0.00	0.00	0.00
CH ₄ (mg/m ³ , dry)	Measurement port C - Transversal distance (m)										
	-0.45	-0.25	-0.15	-0.10	-0.05	0	0.05	0.10	0.15	0.25	0.45
Mean	0.00	0.00	0.00	102.17	2036.32	6253.99	1814.77	75.08	0.56	3.48	0.00
Std. deviation	0.00	0.00	0.00	40.93	246.38	465.07	122.64	16.19	0.84	1.76	0.00
Uncertainty	123.96	123.96	123.96	124.16	129.20	135.09	125.96	123.98	123.96	123.96	123.96
5 th percentile	0.00	0.00	0.00	53.22	1582.75	5476.68	1571.95	51.21	0.00	0.60	0.00
25 th percentile	0.00	0.00	0.00	73.22	1866.60	5870.46	1723.76	59.85	0.00	1.55	0.00
50 th percentile	0.00	0.00	0.00	86.43	2055.00	6374.68	1833.28	74.35	0.13	4.33	0.00
75 th percentile	0.00	0.00	0.00	140.83	2213.37	6588.59	1904.40	88.29	0.70	4.89	0.00
95 th percentile	0.00	0.00	0.00	187.71	2419.92	6910.22	1982.26	100.45	2.36	5.56	0.00
CH ₄ (mg/m ³ , dry)	Measurement port D - Transversal distance (m)										
	-0.45	-0.25	-0.15	-0.10	-0.05	0	0.05	0.10	0.15	0.25	0.45
Mean	0.00	0.00	27.02	-	771.99	704.33	371.79	-	4.52	0.00	0.00
Std. deviation	0.00	0.00	28.08	-	249.57	77.90	62.69	-	6.16	0.00	0.00
Uncertainty	123.96	123.96	124.06	-	128.08	125.58	124.31	-	123.96	123.96	123.96
5 th percentile	0.00	0.00	0.00	-	356.90	583.76	247.57	-	0.00	0.00	0.00
25 th percentile	0.00	0.00	0.00	-	613.85	639.94	329.87	-	0.00	0.00	0.00
50 th percentile	0.00	0.00	15.91	-	750.09	707.68	363.97	-	2.23	0.00	0.00
75 th percentile	0.00	0.00	54.87	-	929.02	771.49	425.42	-	5.59	0.00	0.00
95 th percentile	0.00	0.00	78.39	-	1219.33	816.37	469.94	-	20.29	0.00	0.00

CH ₄ (mg/m ³ , dry)	Measurement port E - Transversal distance (m)										
	-0.45	-0.25	-0.15	-0.10	-0.05	0	0.05	0.10	0.15	0.25	0.45
Mean	0.00	0.00	0.00	-	2.27	153.64	33.89	-	0.01	0.00	0.00
Std. deviation	0.00	0.00	0.00	-	6.18	49.77	23.12	-	0.06	0.00	0.00
Uncertainty	123.96	123.96	123.96	-	123.96	124.18	124.03	-	123.96	123.96	123.96
5 th percentile	0.00	0.00	0.00	-	0.00	75.73	8.89	-	0.00	0.00	0.00
25 th percentile	0.00	0.00	0.00	-	0.00	123.31	17.79	-	0.00	0.00	0.00
50 th percentile	0.00	0.00	0.00	-	0.00	148.40	26.76	-	0.00	0.00	0.00
75 th percentile	0.00	0.00	0.00	-	0.00	179.59	41.11	-	0.00	0.00	0.00
95 th percentile	0.00	0.00	0.00	-	19.49	248.83	90.22	-	0.00	0.00	0.00
CH ₄ (mg/m ³ , dry)	Measurement port F - Transversal distance (m)										
	-0.45	-0.30	-0.15	-0.10	-0.05	0	0.05	0.10	0.15	0.30	0.45
Mean	0.00	0.00	0.00	-	-	0.00	-	-	0.00	0.00	0.00
Std. deviation	0.00	0.00	0.00	-	-	0.00	-	-	0.00	0.00	0.00
Uncertainty	123.96	123.96	123.96	-	-	123.96	-	-	123.96	123.96	123.96
5 th percentile	0.00	0.00	0.00	-	-	0.00	-	-	0.00	0.00	0.00
25 th percentile	0.00	0.00	0.00	-	-	0.00	-	-	0.00	0.00	0.00
50 th percentile	0.00	0.00	0.00	-	-	0.00	-	-	0.00	0.00	0.00
75 th percentile	0.00	0.00	0.00	-	-	0.00	-	-	0.00	0.00	0.00
95 th percentile	0.00	0.00	0.00	-	-	0.00	-	-	0.00	0.00	0.00
CH ₄ (mg/m ³ , dry)	Measurement port G - Transversal distance (m)										
	-0.45	-0.30	-0.15	-0.10	-0.05	0	0.05	0.10	0.15	0.30	0.45
Mean	0.00	0.00	0.00	-	-	0.00	-	-	0.00	0.00	0.00
Std. deviation	0.00	0.00	0.00	-	-	0.00	-	-	0.00	0.00	0.00
Uncertainty	123.96	123.96	123.96	-	-	123.96	-	-	123.96	123.96	123.96
5 th percentile	0.00	0.00	0.00	-	-	0.00	-	-	0.00	0.00	0.00
25 th percentile	0.00	0.00	0.00	-	-	0.00	-	-	0.00	0.00	0.00
50 th percentile	0.00	0.00	0.00	-	-	0.00	-	-	0.00	0.00	0.00
75 th percentile	0.00	0.00	0.00	-	-	0.00	-	-	0.00	0.00	0.00
95 th percentile	0.00	0.00	0.00	-	-	0.00	-	-	0.00	0.00	0.00

B.2.7 Local Nitric Oxide Concentration

NO (mg/m ³ , dry)	Measurement port A - Transversal distance (m)										
	-0.45	-0.25	-0.15	-0.10	-0.05	0	0.05	0.10	0.15	0.25	0.45
Mean	646.31	714.85	646.64	398.69	361.05	199.52	347.59	386.00	478.19	735.53	393.29
Std. deviation	13.71	17.88	24.25	16.42	13.49	9.55	6.21	16.13	14.14	8.76	43.29
Uncertainty	30.65	30.72	30.86	30.69	30.64	30.59	30.57	30.69	30.65	30.59	31.55
5 th percentile	622.43	685.56	595.49	381.27	338.76	187.04	337.13	363.34	451.85	720.80	325.88
25 th percentile	638.96	702.55	637.76	384.11	348.04	192.99	343.23	372.38	465.54	729.40	357.89
50 th percentile	650.24	714.33	658.15	392.35	364.96	195.65	347.58	381.55	482.40	734.54	394.86
75 th percentile	656.59	722.41	662.08	418.26	373.29	203.81	352.03	400.65	490.65	741.12	425.22
95 th percentile	663.51	749.88	678.75	424.33	377.01	220.26	356.95	411.39	495.21	752.64	466.67
NO (mg/m ³ , dry)	Measurement port B - Transversal distance (m)										
	-0.45	-0.25	-0.15	-0.10	-0.05	0	0.05	0.10	0.15	0.25	0.45
Mean	609.45	458.46	367.64	697.18	1009.53	845.69	1004.50	750.50	559.74	560.71	666.11
Std. deviation	8.82	9.51	18.17	9.84	40.49	28.40	11.21	48.85	17.53	8.71	9.62
Uncertainty	30.59	30.59	30.72	30.62	31.43	30.84	30.61	31.82	30.71	30.59	30.58
5 th percentile	595.85	443.66	333.70	684.32	938.30	797.28	986.35	674.16	533.16	546.96	648.83
25 th percentile	603.14	452.06	360.59	689.05	975.44	827.13	997.54	718.35	545.47	553.41	658.90
50 th percentile	608.11	457.55	366.03	695.63	1015.78	846.26	1003.40	743.94	557.51	561.73	667.23
75 th percentile	616.91	465.45	380.32	703.51	1040.40	869.18	1013.49	789.66	573.87	566.07	671.57
95 th percentile	623.60	476.68	397.42	714.24	1075.15	895.09	1022.33	829.50	589.57	575.68	685.64
NO (mg/m ³ , dry)	Measurement port C - Transversal distance (m)										
	-0.45	-0.25	-0.15	-0.10	-0.05	0	0.05	0.10	0.15	0.25	0.45
Mean	585.84	651.91	712.20	866.84	671.54	623.01	756.62	902.89	779.58	701.22	643.77
Std. deviation	37.04	18.58	25.86	22.76	35.69	34.54	17.83	26.19	25.86	12.41	17.93
Uncertainty	30.92	30.67	30.91	30.80	31.00	30.80	30.72	30.73	30.91	30.63	30.70
5 th percentile	533.15	616.37	670.97	825.50	617.88	560.51	723.64	865.36	733.94	684.46	613.60
25 th percentile	554.15	635.90	688.17	848.26	649.06	595.63	745.89	878.86	762.56	689.47	625.53
50 th percentile	575.50	656.61	718.16	872.15	672.52	627.32	759.32	904.23	780.42	701.74	648.63
75 th percentile	620.70	666.44	733.34	885.82	689.94	648.92	769.73	919.40	799.29	713.51	657.57
95 th percentile	641.84	676.27	751.06	895.40	745.41	674.86	787.18	948.72	819.33	721.30	669.22
NO (mg/m ³ , dry)	Measurement port D - Transversal distance (m)										
	-0.45	-0.25	-0.15	-0.10	-0.05	0	0.05	0.10	0.15	0.25	0.45
Mean	578.02	596.94	562.40	-	491.33	535.88	674.35	-	648.35	625.60	602.85
Std. deviation	12.41	9.60	15.98	-	50.04	21.03	11.19	-	20.08	11.82	12.86
Uncertainty	30.63	30.58	30.68	-	31.22	31.02	30.59	-	30.69	30.62	30.61
5 th percentile	556.87	582.76	541.33	-	426.54	503.58	655.50	-	606.12	606.92	582.71
25 th percentile	570.99	587.62	547.58	-	445.19	520.21	664.99	-	636.90	619.88	593.77
50 th percentile	578.07	600.14	560.51	-	484.26	539.73	675.53	-	653.21	624.35	602.39
75 th percentile	584.53	605.07	578.70	-	537.23	548.44	684.00	-	666.39	629.32	612.19
95 th percentile	604.00	610.10	586.48	-	581.48	568.36	691.26	-	671.46	649.28	624.83

NO (mg/m ³ , dry)	Measurement port E - Transversal distance (m)										
	-0.45	-0.25	-0.15	-0.10	-0.05	0	0.05	0.10	0.15	0.25	0.45
Mean	667.33	675.36	586.34	-	493.24	564.69	559.26	-	565.88	612.50	640.57
Std. deviation	10.10	17.92	17.11	-	9.49	14.23	4.55	-	7.99	13.99	11.21
Uncertainty	30.66	30.66	30.65	-	30.59	30.60	30.56	-	30.57	30.59	30.61
5 th percentile	645.91	642.74	555.54	-	475.47	543.42	553.35	-	552.35	592.59	623.53
25 th percentile	664.80	662.19	575.94	-	485.37	548.69	556.27	-	560.83	601.78	632.49
50 th percentile	667.80	676.17	589.09	-	496.42	568.20	558.08	-	566.81	611.69	639.76
75 th percentile	675.12	687.97	600.83	-	500.79	577.34	562.37	-	569.60	620.81	652.24
95 th percentile	680.05	705.92	607.88	-	503.33	582.91	567.52	-	579.75	641.47	657.22
NO (mg/m ³ , dry)	Measurement port F - Transversal distance (m)										
	-0.45	-0.30	-0.15	-0.10	-0.05	0	0.05	0.10	0.15	0.30	0.45
Mean	588.80	683.62	598.78	-	-	577.41	-	-	568.90	578.96	590.54
Std. deviation	14.95	19.63	12.93	-	-	18.27	-	-	24.32	27.66	11.55
Uncertainty	30.63	30.68	30.61	-	-	30.64	-	-	30.71	30.96	30.59
5 th percentile	563.59	649.05	587.69	-	-	552.61	-	-	534.19	547.59	578.16
25 th percentile	577.32	667.00	589.62	-	-	563.30	-	-	549.93	563.00	581.04
50 th percentile	588.44	684.68	592.09	-	-	576.18	-	-	564.95	572.99	587.12
75 th percentile	602.50	703.15	605.86	-	-	585.40	-	-	587.05	579.29	598.06
95 th percentile	611.73	709.97	626.68	-	-	615.92	-	-	610.98	645.40	614.11
NO (mg/m ³ , dry)	Measurement port G - Transversal distance (m)										
	-0.45	-0.30	-0.15	-0.10	-0.05	0	0.05	0.10	0.15	0.30	0.45
Mean	563.48	623.60	636.68	-	-	588.77	-	-	594.40	611.82	607.88
Std. deviation	23.88	26.05	22.89	-	-	24.48	-	-	14.93	6.97	18.48
Uncertainty	30.67	30.73	30.69	-	-	30.76	-	-	30.64	30.56	30.66
5 th percentile	508.41	589.69	594.13	-	-	547.91	-	-	568.29	601.28	577.75
25 th percentile	557.53	597.85	620.74	-	-	572.51	-	-	582.29	606.79	590.79
50 th percentile	568.31	622.02	642.02	-	-	593.84	-	-	596.85	610.08	606.79
75 th percentile	576.16	643.52	651.33	-	-	605.79	-	-	608.29	615.73	624.67
95 th percentile	595.71	669.50	669.69	-	-	629.12	-	-	615.09	625.89	635.70

B.2.8 Total Radiative Heat Flux

Heat flux (kW/m ²)	Measurement						
	A	B	C	D	E	F	G
Mean	143.11	154.55	165.14	164.98	150.01	151.66	127.33
Std. deviation	1.10	1.82	1.84	2.17	2.75	2.27	2.56
Uncertainty	9.52	10.07	10.57	10.57	9.86	9.94	8.77
5 th percentile	141.02	150.46	162.54	161.81	146.09	147.84	121.46
25 th percentile	142.53	153.83	163.77	163.09	147.97	150.11	126.61
50 th percentile	143.23	154.73	165.02	164.78	149.37	151.69	127.99
75 th percentile	143.89	155.78	166.47	166.77	152.76	153.17	128.97
95 th percentile	144.64	157.24	168.46	168.39	154.32	155.28	129.97

B.3 Oxy-Flame 2

B.3.1 Furnace Operating Conditions

Operating parameter	
Coal feed rate (kg/h)	56.34 ±0.27
Volume flow rate of primary stream (m ³ /h, STP)	34.81 ±1.58
O ₂ fraction of primary stream (vol%, wet)	19.00 ±1.10
CO ₂ fraction of primary stream (vol%, wet) ¹	81.00
Temperature of primary stream (°C)	17.03 ±1.23
Velocity of primary stream at burner exit (m/s) ¹	23.01
Axial momentum of primary stream at burner exit (N) ¹	0.47
Volume flow rate of secondary stream (m ³ /h, STP)	144 ±2.80
Volume flow rate of tertiary stream (m ³ /h, STP)	72 ±7.05
O ₂ fraction of secondary and tertiary stream (vol%, wet)	33 ±1.91
H ₂ O fraction of secondary and tertiary stream (vol%, wet) ¹	19.27
CO ₂ fraction of secondary and tertiary stream (vol%, wet) ¹	44.27
N ₂ fraction of secondary and tertiary stream (vol%, wet) ¹	3.33
Temperature of secondary and tertiary streams (°C)	153.10 ±1.68
Secondary/tertiary mass flow ratio ¹	2.00
Swirl number of secondary stream ¹	1.65
Stoichiometric ratio ¹	1.17
Overall heat input (kW) ¹	345
Sensible heat input (kW) ¹	13.30
Flue gas	
O ₂ (vol%, dry)	6.29 ±0.83
CO ₂ (vol%, dry)	81.53 ±1.05
N ₂ (vol%, dry) ¹	6.55
H ₂ O (vol% wet)	27.51 ±0.18
Volume flow rate at furnace exit (m ³ /h, STP)	303.70 ±5.35
Volume flow rate of recycled flue gas (m ³ /h, STP)	141.40 ±3.59
Temperature at furnace exit (°C)	502.10 ±3.44
Recycle ratio ¹	0.47
Outer wall surface temperature at the vertical section (°C)	199.56 ±1.86
Inner surface temperature of the cylindrical section (°C)	873.98 ±4.26

¹calculated value

B.3.2 Local Gas Temperature

Temperature (°C)	Measurement port A - Transversal distance (m)										
	-0.45	-0.25	-0.15	-0.10	-0.05	0	0.05	0.10	0.15	0.25	0.45
Mean	899	1077	1079	842	633	1210	1015	942	877	1025	980
Std. deviation	2.29	5.11	2.61	7.15	31.98	11.13	5.16	6.88	3.16	7.74	3.58
Uncertainty	22.55	26.93	26.96	21.24	18.21	30.38	25.41	23.65	22.02	25.70	24.53
5 th percentile	895	1069	1075	832	586	1192	1007	929	871	1015	975
25 th percentile	897	1072	1077	837	607	1201	1011	935	875	1020	977
50 th percentile	899	1077	1079	841	630	1209	1015	945	877	1022	979
75 th percentile	901	1081	1081	848	660	1220	1018	946	880	1033	982
95 th percentile	902	1085	1084	854	684	1224	1022	950	882	1038	986
Temperature (°C)	Measurement port B - Transversal distance (m)										
	-0.45	-0.25	-0.15	-0.10	-0.05	0	0.05	0.10	0.15	0.25	0.45
Mean	972	1075	1009	977	1099	1139	1299	1134	999	1073	1086
Std. deviation	8.15	12.16	9.43	4.22	13.01	3.26	6.83	13.17	7.00	4.12	1.99
Uncertainty	24.42	26.96	25.34	24.47	27.67	28.48	32.55	28.53	25.07	26.83	27.14
5 th percentile	958	1055	996	972	1077	1133	1287	1109	986	1064	1081
25 th percentile	965	1066	1000	975	1092	1137	1295	1122	997	1070	1085
50 th percentile	976	1075	1009	977	1098	1140	1300	1136	1001	1075	1086
75 th percentile	979	1085	1016	980	1112	1141	1305	1146	1005	1076	1088
95 th percentile	981	1093	1023	985	1116	1143	1307	1150	1007	1077	1089
Temperature (°C)	Measurement port C - Transversal distance (m)										
	-0.45	-0.25	-0.15	-0.10	-0.05	0	0.05	0.10	0.15	0.25	0.45
Mean	1045	1139	1185	1229	1304	1256	1247	1137	1079	1086	1038
Std. deviation	2.99	6.30	6.84	4.63	6.86	16.62	4.83	12.16	3.15	5.32	3.03
Uncertainty	26.12	28.49	29.66	30.74	32.67	31.65	31.21	28.55	26.96	27.16	25.95
5 th percentile	1038	1128	1176	1222	1295	1222	1239	1123	1075	1073	1034
25 th percentile	1043	1135	1180	1225	1298	1247	1243	1128	1076	1082	1036
50 th percentile	1045	1139	1183	1229	1305	1261	1249	1135	1078	1087	1038
75 th percentile	1046	1144	1189	1233	1310	1269	1251	1145	1081	1090	1040
95 th percentile	1049	1147	1198	1235	1315	1275	1254	1161	1085	1092	1042
Temperature (°C)	Measurement port D - Transversal distance (m)										
	-0.45	-0.25	-0.15	-0.10	-0.05	0	0.05	0.10	0.15	0.25	0.45
Mean	1097	1226	1240	-	1217	1212	1214	-	1244	1160	1057
Std. deviation	3.44	5.14	1.32	-	2.99	2.73	3.31	-	2.04	6.86	2.38
Uncertainty	26.94	30.06	30.38	-	29.83	29.70	29.76	-	30.48	28.50	25.98
5 th percentile	1091	1218	1238	-	1212	1206	1209	-	1240	1148	1054
25 th percentile	1096	1221	1239	-	1216	1211	1212	-	1243	1156	1056
50 th percentile	1097	1227	1240	-	1217	1212	1214	-	1244	1161	1057
75 th percentile	1099	1230	1241	-	1219	1214	1216	-	1245	1166	1059
95 th percentile	1103	1233	1242	-	1222	1215	1220	-	1247	1168	1061

Temperature (°C)	Measurement port E - Transversal distance (m)										
	-0.45	-0.25	-0.15	-0.10	-0.05	0	0.05	0.10	0.15	0.25	0.45
Mean	1027	1186	1201	-	1115	1109	1147	-	1192	1197	1070
Std. deviation	4.78	3.87	4.25	-	9.45	5.83	10.28	-	4.65	2.85	6.85
Uncertainty	25.25	29.09	29.46	-	27.45	27.25	28.23	-	29.23	29.35	26.33
5 th percentile	1022	1180	1196	-	1101	1100	1131	-	1186	1191	1061
25 th percentile	1024	1184	1197	-	1108	1104	1139	-	1188	1196	1062
50 th percentile	1027	1186	1202	-	1115	1108	1148	-	1190	1198	1069
75 th percentile	1029	1188	1204	-	1120	1114	1155	-	1195	1199	1077
95 th percentile	1036	1193	1209	-	1134	1117	1162	-	1200	1201	1079
Temperature (°C)	Measurement port F - Transversal distance (m)										
	-0.45	-0.30	-0.15	-0.10	-0.05	0	0.05	0.10	0.15	0.30	0.45
Mean	998	1154	1173	-	-	1136	-	-	1133	1092	1075
Std. deviation	5.05	8.70	9.09	-	-	9.94	-	-	9.23	10.57	3.19
Uncertainty	24.56	28.39	28.82	-	-	27.99	-	-	27.85	26.91	26.39
5 th percentile	989	1138	1158	-	-	1118	-	-	1120	1076	1071
25 th percentile	994	1148	1165	-	-	1133	-	-	1126	1082	1073
50 th percentile	997	1154	1174	-	-	1139	-	-	1132	1094	1074
75 th percentile	1003	1161	1179	-	-	1143	-	-	1142	1102	1076
95 th percentile	1005	1165	1188	-	-	1148	-	-	1147	1105	1082
Temperature (°C)	Measurement port G - Transversal distance (m)										
	-0.45	-0.30	-0.15	-0.10	-0.05	0	0.05	0.10	0.15	0.30	0.45
Mean	962	1098	1103	-	-	1112	-	-	1074	1064	1021
Std. deviation	8.84	9.73	11.59	-	-	7.66	-	-	11.04	4.08	3.21
Uncertainty	23.77	27.06	27.17	-	-	27.29	-	-	26.51	26.15	25.11
5 th percentile	947	1083	1082	-	-	1096	-	-	1055	1059	1017
25 th percentile	956	1089	1092	-	-	1107	-	-	1067	1061	1019
50 th percentile	966	1100	1103	-	-	1113	-	-	1073	1064	1021
75 th percentile	969	1104	1111	-	-	1117	-	-	1083	1067	1025
95 th percentile	973	1113	1122	-	-	1122	-	-	1092	1071	1026

B.3.3 Local Oxygen Concentration

O ₂ (vol%, dry)	Measurement port A - Transversal distance (m)										
	-0.45	-0.25	-0.15	-0.10	-0.05	0	0.05	0.10	0.15	0.25	0.45
Mean	13.93	12.61	12.67	26.82	40.97	12.93	36.03	25.14	14.25	9.45	4.96
Std. deviation	0.63	0.61	0.43	0.31	0.20	0.22	0.44	0.49	0.54	1.04	0.91
Uncertainty	0.60	0.60	0.60	0.59	0.59	0.59	0.60	0.60	0.61	0.65	0.62
5 th percentile	13.08	11.78	11.83	26.23	40.63	12.56	35.41	24.30	13.18	7.99	3.63
25 th percentile	13.41	12.02	12.48	26.65	40.81	12.75	35.81	24.90	13.99	8.71	4.14
50 th percentile	13.91	12.62	12.72	26.86	41.00	13.00	35.85	25.05	14.26	9.41	4.92
75 th percentile	14.38	13.07	13.02	27.06	41.10	13.05	36.42	25.52	14.62	9.87	5.81
95 th percentile	15.13	13.69	13.19	27.23	41.27	13.19	36.79	25.95	15.11	11.28	6.41
O ₂ (vol%, dry)	Measurement port B - Transversal distance (m)										
	-0.45	-0.25	-0.15	-0.10	-0.05	0	0.05	0.10	0.15	0.25	0.45
Mean	15.42	19.56	20.46	12.80	5.15	12.54	1.44	10.89	20.34	10.95	12.84
Std. deviation	0.50	0.62	0.88	1.03	1.18	0.21	0.14	0.23	0.32	0.42	0.45
Uncertainty	0.60	0.60	0.61	0.62	0.63	0.59	0.59	0.59	0.59	0.60	0.60
5 th percentile	14.67	18.58	19.02	11.29	3.57	12.23	1.30	10.58	19.86	10.22	12.19
25 th percentile	15.15	19.01	19.56	12.02	4.47	12.35	1.35	10.74	20.14	10.66	12.42
50 th percentile	15.37	19.46	20.75	12.76	4.76	12.55	1.39	10.84	20.30	10.97	12.78
75 th percentile	15.76	20.19	21.19	13.59	5.99	12.75	1.53	10.99	20.44	11.19	13.24
95 th percentile	16.23	20.45	21.62	14.51	7.41	12.86	1.71	11.34	20.97	11.73	13.54
O ₂ (vol%, dry)	Measurement port C - Transversal distance (m)										
	-0.45	-0.25	-0.15	-0.10	-0.05	0	0.05	0.10	0.15	0.25	0.45
Mean	16.41	11.36	8.92	4.86	0.79	1.43	0.58	4.60	8.62	10.57	14.29
Std. deviation	0.57	0.72	1.00	0.53	0.07	0.05	0.12	0.41	0.69	0.68	0.60
Uncertainty	0.60	0.61	0.64	0.62	0.59	0.59	0.59	0.60	0.60	0.61	0.60
5 th percentile	15.60	10.41	7.36	4.03	0.70	1.35	0.45	3.96	7.46	9.44	13.61
25 th percentile	15.97	10.87	8.27	4.50	0.73	1.39	0.49	4.26	8.02	9.95	13.90
50 th percentile	16.29	11.08	8.62	4.70	0.79	1.44	0.55	4.64	8.73	10.76	14.14
75 th percentile	16.84	12.10	9.67	5.26	0.84	1.48	0.62	4.93	9.23	11.13	14.46
95 th percentile	17.46	12.61	10.58	5.75	0.92	1.50	0.84	5.21	9.59	11.51	15.56
O ₂ (vol%, dry)	Measurement port D - Transversal distance (m)										
	-0.45	-0.25	-0.15	-0.10	-0.05	0	0.05	0.10	0.15	0.25	0.45
Mean	8.78	1.84	2.26	-	6.07	9.03	11.01	-	14.46	17.91	20.15
Std. deviation	0.52	0.57	0.66	-	1.42	0.53	1.32	-	1.06	1.79	1.04
Uncertainty	0.60	0.60	0.60	-	0.63	0.60	0.64	-	0.62	0.65	0.63
5 th percentile	7.88	1.11	1.36	-	4.16	8.14	8.50	-	12.33	14.14	18.70
25 th percentile	8.43	1.47	1.66	-	5.25	8.63	10.14	-	13.76	16.99	19.18
50 th percentile	8.81	1.65	2.20	-	5.73	8.95	11.44	-	14.59	18.08	20.37
75 th percentile	9.20	2.16	2.87	-	6.68	9.45	12.16	-	15.23	19.28	20.74
95 th percentile	9.59	3.09	3.35	-	9.55	9.84	12.43	-	16.27	20.25	21.87

O ₂ (vol%, dry)	Measurement port E - Transversal distance (m)										
	-0.45	-0.25	-0.15	-0.10	-0.05	0	0.05	0.10	0.15	0.25	0.45
Mean	5.10	1.76	5.03	-	6.92	7.95	11.06	-	14.95	17.21	19.15
Std. deviation	0.54	1.10	1.35	-	1.41	0.63	1.30	-	0.52	0.46	0.45
Uncertainty	0.60	0.61	0.64	-	0.62	0.60	0.63	-	0.60	0.59	0.60
5 th percentile	4.12	0.84	3.19	-	4.38	7.05	8.69	-	14.23	16.50	18.43
25 th percentile	4.57	0.99	3.99	-	5.90	7.46	9.87	-	14.54	16.90	18.76
50 th percentile	5.35	1.37	4.78	-	7.24	7.89	11.30	-	14.88	17.21	19.21
75 th percentile	5.53	1.89	5.74	-	8.15	8.52	12.15	-	15.29	17.41	19.43
95 th percentile	5.70	4.24	7.62	-	8.62	8.92	12.62	-	15.83	17.94	19.97
O ₂ (vol%, dry)	Measurement port F - Transversal distance (m)										
	-0.45	-0.30	-0.15	-0.10	-0.05	0	0.05	0.10	0.15	0.30	0.45
Mean	5.04	2.47	4.86	-	-	8.08	-	-	10.33	12.01	13.01
Std. deviation	0.86	0.54	0.82	-	-	1.02	-	-	1.13	0.59	1.03
Uncertainty	0.61	0.60	0.61	-	-	0.62	-	-	0.62	0.60	0.61
5 th percentile	3.75	1.61	3.65	-	-	6.21	-	-	8.56	10.96	11.49
25 th percentile	4.48	2.15	4.28	-	-	7.14	-	-	9.36	11.63	12.13
50 th percentile	4.88	2.36	4.77	-	-	8.20	-	-	10.40	11.99	12.99
75 th percentile	5.71	2.71	5.45	-	-	8.83	-	-	11.44	12.41	13.83
95 th percentile	6.59	3.63	6.53	-	-	9.50	-	-	11.83	12.95	14.68
O ₂ (vol%, dry)	Measurement port G - Transversal distance (m)										
	-0.45	-0.30	-0.15	-0.10	-0.05	0	0.05	0.10	0.15	0.30	0.45
Mean	5.63	5.71	6.24	-	-	7.98	-	-	10.52	10.74	10.78
Std. deviation	1.08	0.85	0.59	-	-	0.70	-	-	0.94	0.72	0.66
Uncertainty	0.62	0.60	0.60	-	-	0.60	-	-	0.61	0.60	0.60
5 th percentile	3.51	4.24	5.49	-	-	7.00	-	-	8.94	9.88	9.80
25 th percentile	5.10	5.27	5.83	-	-	7.40	-	-	9.98	10.19	10.09
50 th percentile	5.77	5.76	6.08	-	-	7.83	-	-	10.40	10.44	10.87
75 th percentile	6.47	5.99	6.60	-	-	8.54	-	-	11.55	11.62	11.34
95 th percentile	7.24	7.56	7.43	-	-	9.15	-	-	11.80	11.86	11.74

B.3.4 Local Carbon Dioxide Concentration

CO ₂ (vol%, dry)	Measurement port A - Transversal distance (m)										
	-0.45	-0.25	-0.15	-0.10	-0.05	0	0.05	0.10	0.15	0.25	0.45
Mean	83.17	82.76	84.41	69.35	54.28	83.56	58.93	70.88	82.82	88.30	95.02
Std. deviation	0.74	2.12	0.58	0.39	0.20	0.32	0.47	0.61	0.75	1.09	1.44
Uncertainty	1.64	1.68	1.65	1.56	1.46	1.64	1.49	1.57	1.64	1.69	1.75
5 th percentile	81.76	78.17	83.71	68.84	53.97	83.12	58.14	69.91	81.68	86.57	92.62
25 th percentile	82.63	81.84	83.87	69.01	54.14	83.43	58.57	70.41	82.26	87.60	93.63
50 th percentile	83.26	83.39	84.34	69.29	54.24	83.51	59.10	70.97	82.84	88.26	95.14
75 th percentile	83.77	84.02	84.75	69.60	54.45	83.80	59.19	71.19	83.19	89.17	96.35
95 th percentile	84.13	85.32	85.50	70.06	54.63	84.06	59.67	71.93	84.20	89.95	96.98
CO ₂ (vol%, dry)	Measurement port B - Transversal distance (m)										
	-0.45	-0.25	-0.15	-0.10	-0.05	0	0.05	0.10	0.15	0.25	0.45
Mean	81.27	77.36	76.45	82.87	89.29	82.79	88.04	82.25	76.46	86.91	84.64
Std. deviation	0.49	0.69	1.05	0.83	0.62	0.17	0.20	0.28	0.36	0.48	0.48
Uncertainty	1.62	1.60	1.60	1.64	1.68	1.63	1.67	1.63	1.59	1.66	1.65
5 th percentile	80.48	76.34	75.08	81.67	88.26	82.51	87.73	81.73	75.72	86.01	83.89
25 th percentile	80.93	76.71	75.63	82.20	88.77	82.63	87.87	82.09	76.32	86.65	84.25
50 th percentile	81.30	77.46	76.16	82.81	89.46	82.81	88.00	82.25	76.49	86.90	84.72
75 th percentile	81.56	77.91	77.56	83.71	89.86	82.96	88.23	82.46	76.69	87.28	85.06
95 th percentile	82.09	78.44	78.12	84.09	90.06	82.97	88.36	82.65	76.95	87.73	85.32
CO ₂ (vol%, dry)	Measurement port C - Transversal distance (m)										
	-0.45	-0.25	-0.15	-0.10	-0.05	0	0.05	0.10	0.15	0.25	0.45
Mean	80.27	85.63	87.09	82.91	78.73	79.85	88.90	89.06	89.23	86.69	82.88
Std. deviation	0.68	0.83	0.84	0.80	0.75	0.20	0.36	0.59	0.81	1.00	0.67
Uncertainty	1.62	1.66	1.67	1.64	1.61	1.61	1.67	1.68	1.68	1.67	1.64
5 th percentile	79.01	84.09	85.77	81.84	77.91	79.61	88.36	88.22	88.09	85.24	81.35
25 th percentile	79.83	84.81	86.30	82.24	78.19	79.75	88.70	88.59	88.47	85.80	82.66
50 th percentile	80.38	85.97	87.26	82.83	78.39	79.82	88.85	88.97	89.08	86.71	83.05
75 th percentile	80.81	86.22	87.78	83.59	79.40	79.89	89.12	89.53	89.94	87.74	83.28
95 th percentile	81.34	86.66	88.25	84.24	80.23	80.43	89.64	90.15	90.66	88.15	83.69
CO ₂ (vol%, dry)	Measurement port D - Transversal distance (m)										
	-0.45	-0.25	-0.15	-0.10	-0.05	0	0.05	0.10	0.15	0.25	0.45
Mean	84.70	87.65	87.68	-	91.01	88.45	85.58	-	82.01	78.54	76.09
Std. deviation	0.87	1.40	1.13	-	1.08	0.58	0.76	-	1.06	1.94	1.20
Uncertainty	1.65	1.68	1.68	-	1.70	1.67	1.66	-	1.64	1.63	1.61
5 th percentile	83.70	85.06	85.17	-	88.23	87.58	84.51	-	80.11	76.06	74.08
25 th percentile	84.02	86.44	87.02	-	90.94	88.00	84.88	-	81.20	77.23	75.40
50 th percentile	84.34	88.23	87.64	-	91.11	88.47	85.62	-	82.12	78.32	75.96
75 th percentile	85.37	88.69	88.74	-	91.60	88.83	86.20	-	82.78	79.47	77.13
95 th percentile	86.40	89.36	89.13	-	92.42	89.46	86.68	-	83.82	82.49	77.86

CO ₂ (vol%, dry)	Measurement port E - Transversal distance (m)										
	-0.45	-0.25	-0.15	-0.10	-0.05	0	0.05	0.10	0.15	0.25	0.45
Mean	83.87	91.14	89.79	-	90.67	89.93	85.73	-	81.23	78.77	76.57
Std. deviation	1.32	0.41	0.99	-	1.46	0.76	1.51	-	0.61	0.53	0.51
Uncertainty	1.66	1.69	1.69	-	1.70	1.68	1.67	-	1.62	1.61	1.59
5 th percentile	81.57	90.61	88.27	-	88.93	88.81	83.89	-	80.21	77.90	75.65
25 th percentile	82.84	90.83	88.93	-	89.37	89.17	84.49	-	80.81	78.54	76.28
50 th percentile	83.88	91.06	89.77	-	90.23	90.01	85.45	-	81.25	78.82	76.47
75 th percentile	85.08	91.32	90.64	-	91.85	90.53	87.00	-	81.71	79.15	76.98
95 th percentile	85.87	91.93	91.29	-	93.20	91.05	88.50	-	82.15	79.58	77.39
CO ₂ (vol%, dry)	Measurement port F - Transversal distance (m)										
	-0.45	-0.30	-0.15	-0.10	-0.05	0	0.05	0.10	0.15	0.30	0.45
Mean	80.74	93.15	91.89	-	-	88.82	-	-	86.48	84.53	83.49
Std. deviation	2.05	0.45	0.77	-	-	1.13	-	-	1.27	0.64	1.17
Uncertainty	1.66	1.71	1.70	-	-	1.69	-	-	1.67	1.65	1.65
5 th percentile	76.36	92.24	90.18	-	-	87.27	-	-	84.87	83.45	81.64
25 th percentile	80.00	92.87	91.38	-	-	87.92	-	-	85.16	84.10	82.64
50 th percentile	81.09	93.24	92.01	-	-	88.72	-	-	86.39	84.56	83.50
75 th percentile	82.13	93.48	92.47	-	-	89.88	-	-	87.51	85.02	84.50
95 th percentile	83.60	93.88	92.94	-	-	90.87	-	-	88.48	85.41	85.21
CO ₂ (vol%, dry)	Measurement port G - Transversal distance (m)										
	-0.45	-0.30	-0.15	-0.10	-0.05	0	0.05	0.10	0.15	0.30	0.45
Mean	87.26	90.95	90.86	-	-	89.06	-	-	86.34	85.99	85.95
Std. deviation	2.11	0.99	0.65	-	-	0.77	-	-	1.02	0.79	0.77
Uncertainty	1.71	1.69	1.69	-	-	1.68	-	-	1.67	1.66	1.66
5 th percentile	84.73	88.79	89.50	-	-	87.80	-	-	84.95	84.73	84.83
25 th percentile	85.45	90.52	90.57	-	-	88.43	-	-	85.28	85.11	85.30
50 th percentile	87.08	91.01	91.03	-	-	89.10	-	-	86.36	86.31	85.81
75 th percentile	88.01	91.69	91.32	-	-	89.72	-	-	86.93	86.63	86.67
95 th percentile	91.65	92.39	91.66	-	-	90.15	-	-	88.07	86.93	87.19

B.3.5 Local Carbon Monoxide Concentration

CO (vol%, dry)	Measurement port A - Transversal distance (m)										
	-0.45	-0.25	-0.15	-0.10	-0.05	0	0.05	0.10	0.15	0.25	0.45
Mean	0.01	0.00	0.00	0.04	0.08	2.23	0.62	0.35	0.08	0.02	0.00
Std. deviation	0.01	0.00	0.00	0.00	0.00	0.03	0.04	0.02	0.01	0.00	0.00
Uncertainty	0.35	0.35	0.35	0.35	0.35	0.35	0.35	0.35	0.35	0.35	0.35
5 th percentile	0.00	0.00	0.00	0.04	0.07	2.19	0.56	0.31	0.07	0.01	0.00
25 th percentile	0.01	0.00	0.00	0.04	0.08	2.22	0.60	0.34	0.08	0.01	0.00
50 th percentile	0.01	0.00	0.00	0.04	0.08	2.23	0.62	0.35	0.08	0.02	0.00
75 th percentile	0.02	0.00	0.00	0.04	0.08	2.25	0.65	0.37	0.09	0.02	0.00
95 th percentile	0.03	0.01	0.00	0.04	0.08	2.27	0.67	0.38	0.09	0.02	0.00
CO (vol%, dry)	Measurement port B - Transversal distance (m)										
	-0.45	-0.25	-0.15	-0.10	-0.05	0	0.05	0.10	0.15	0.25	0.45
Mean	0.02	0.03	0.06	2.11	4.17	3.94	9.01	4.55	0.09	0.03	0.00
Std. deviation	0.01	0.01	0.01	0.39	0.76	0.08	0.26	0.13	0.01	0.00	0.00
Uncertainty	0.35	0.35	0.35	0.37	0.38	0.35	0.36	0.35	0.35	0.35	0.35
5 th percentile	0.00	0.02	0.05	1.39	2.73	3.82	8.50	4.30	0.09	0.02	0.00
25 th percentile	0.01	0.03	0.05	1.96	3.86	3.88	8.79	4.44	0.09	0.03	0.00
50 th percentile	0.01	0.03	0.06	2.14	4.21	3.94	9.14	4.61	0.09	0.03	0.00
75 th percentile	0.03	0.04	0.06	2.41	4.75	4.00	9.19	4.64	0.10	0.04	0.00
95 th percentile	0.03	0.04	0.07	2.63	5.19	4.07	9.31	4.70	0.10	0.04	0.01
CO (vol%, dry)	Measurement port C - Transversal distance (m)										
	-0.45	-0.25	-0.15	-0.10	-0.05	0	0.05	0.10	0.15	0.25	0.45
Mean	0.00	0.04	1.69	8.84	15.99	13.71	8.37	4.22	0.07	0.01	0.00
Std. deviation	0.00	0.02	0.51	0.40	0.29	0.10	0.35	0.19	0.03	0.00	0.00
Uncertainty	0.35	0.35	0.36	0.36	0.35	0.35	0.36	0.35	0.35	0.35	0.35
5 th percentile	0.00	0.02	0.92	8.23	15.53	13.55	7.78	3.91	0.04	0.00	0.00
25 th percentile	0.00	0.03	1.24	8.51	15.77	13.64	8.12	4.08	0.05	0.01	0.00
50 th percentile	0.00	0.03	1.73	8.89	16.05	13.71	8.44	4.25	0.06	0.01	0.00
75 th percentile	0.00	0.06	2.12	9.15	16.19	13.78	8.65	4.36	0.08	0.01	0.00
95 th percentile	0.01	0.07	2.48	9.45	16.41	13.89	8.91	4.52	0.12	0.01	0.01
CO (vol%, dry)	Measurement port D - Transversal distance (m)										
	-0.45	-0.25	-0.15	-0.10	-0.05	0	0.05	0.10	0.15	0.25	0.45
Mean	0.57	5.37	5.62	-	0.84	0.08	0.14	-	0.08	0.04	0.00
Std. deviation	0.25	0.52	1.18	-	0.37	0.05	0.10	-	0.04	0.05	0.00
Uncertainty	0.35	0.36	0.39	-	0.36	0.35	0.35	-	0.35	0.35	0.35
5 th percentile	0.36	4.45	3.58	-	0.35	0.02	0.03	-	0.04	0.00	0.00
25 th percentile	0.45	5.08	4.81	-	0.59	0.04	0.09	-	0.06	0.01	0.00
50 th percentile	0.50	5.36	5.81	-	0.73	0.08	0.12	-	0.07	0.01	0.00
75 th percentile	0.57	5.71	6.38	-	1.08	0.10	0.14	-	0.09	0.05	0.00
95 th percentile	1.19	6.13	7.46	-	1.53	0.19	0.39	-	0.17	0.17	0.01

CO (vol%, dry)	Measurement port E - Transversal distance (m)										
	-0.45	-0.25	-0.15	-0.10	-0.05	0	0.05	0.10	0.15	0.25	0.45
Mean	1.13	4.45	2.41	-	0.30	0.05	0.14	-	0.06	0.01	0.00
Std. deviation	0.28	1.29	0.79	-	0.21	0.02	0.08	-	0.02	0.01	0.00
Uncertainty	0.35	0.40	0.38	-	0.35	0.35	0.35	-	0.35	0.35	0.35
5 th percentile	0.76	2.05	0.98	-	0.07	0.02	0.05	-	0.05	0.00	0.00
25 th percentile	0.90	3.98	1.85	-	0.12	0.03	0.09	-	0.05	0.00	0.00
50 th percentile	1.07	4.87	2.45	-	0.23	0.04	0.12	-	0.06	0.01	0.00
75 th percentile	1.34	5.40	3.06	-	0.41	0.06	0.18	-	0.07	0.02	0.00
95 th percentile	1.68	5.95	3.56	-	0.76	0.08	0.30	-	0.09	0.02	0.00
CO (vol%, dry)	Measurement port F - Transversal distance (m)										
	-0.45	-0.30	-0.15	-0.10	-0.05	0	0.05	0.10	0.15	0.30	0.45
Mean	0.77	1.66	0.62	-	-	0.23	-	-	0.02	0.00	0.00
Std. deviation	0.36	0.41	0.35	-	-	0.06	-	-	0.02	0.00	0.00
Uncertainty	0.36	0.36	0.36	-	-	0.35	-	-	0.35	0.35	0.35
5 th percentile	0.20	1.03	0.21	-	-	0.13	-	-	0.00	0.00	0.00
25 th percentile	0.55	1.36	0.32	-	-	0.19	-	-	0.00	0.00	0.00
50 th percentile	0.82	1.57	0.55	-	-	0.23	-	-	0.01	0.00	0.00
75 th percentile	1.05	2.02	0.78	-	-	0.27	-	-	0.02	0.00	0.00
95 th percentile	1.29	2.35	1.36	-	-	0.32	-	-	0.05	0.00	0.01
CO (vol%, dry)	Measurement port G - Transversal distance (m)										
	-0.45	-0.30	-0.15	-0.10	-0.05	0	0.05	0.10	0.15	0.30	0.45
Mean	0.12	0.10	0.06	-	-	0.02	-	-	0.00	0.00	0.00
Std. deviation	0.08	0.10	0.05	-	-	0.02	-	-	0.00	0.00	0.00
Uncertainty	0.35	0.35	0.35	-	-	0.35	-	-	0.35	0.35	0.35
5 th percentile	0.02	0.00	0.00	-	-	0.00	-	-	0.00	0.00	0.00
25 th percentile	0.06	0.03	0.01	-	-	0.01	-	-	0.00	0.00	0.00
50 th percentile	0.10	0.06	0.05	-	-	0.02	-	-	0.00	0.00	0.00
75 th percentile	0.14	0.14	0.08	-	-	0.03	-	-	0.01	0.00	0.00
95 th percentile	0.28	0.32	0.18	-	-	0.05	-	-	0.01	0.00	0.01

B.3.6 Local Methane Concentration

CH ₄ (mg/m ³ , dry)	Measurement port A - Transversal distance (m)										
	-0.45	-0.25	-0.15	-0.10	-0.05	0	0.05	0.10	0.15	0.25	0.45
Mean	0.01	0.00	0.00	3.27	6.54	210.93	46.84	24.90	2.96	1.19	0.01
Std. deviation	0.06	0.02	0.00	0.34	0.67	5.41	3.40	1.96	0.52	0.61	0.04
Uncertainty	123.96	123.96	123.96	123.96	123.96	123.97	123.96	123.96	123.96	123.96	123.96
5 th percentile	0.00	0.00	0.00	2.77	5.54	198.70	42.69	22.37	2.05	0.07	0.00
25 th percentile	0.00	0.00	0.00	3.01	6.02	209.30	44.69	23.61	2.53	0.80	0.00
50 th percentile	0.00	0.00	0.00	3.28	6.56	212.95	45.57	24.27	2.98	1.09	0.00
75 th percentile	0.00	0.00	0.00	3.46	6.92	214.31	48.06	25.70	3.34	1.50	0.00
95 th percentile	0.00	0.00	0.00	3.84	7.68	216.56	53.66	28.71	3.76	2.32	0.07
CH ₄ (mg/m ³ , dry)	Measurement port B - Transversal distance (m)										
	-0.45	-0.25	-0.15	-0.10	-0.05	0	0.05	0.10	0.15	0.25	0.45
Mean	0.00	0.00	0.00	118.36	236.72	999.07	1362.35	681.20	0.06	0.00	0.00
Std. deviation	0.00	0.00	0.00	27.71	55.42	19.04	89.66	44.95	0.24	0.00	0.00
Uncertainty	123.96	123.96	123.96	124.21	124.46	124.02	126.10	125.03	123.96	123.96	123.96
5 th percentile	0.00	0.00	0.00	66.10	132.19	970.50	1230.80	615.40	0.00	0.00	0.00
25 th percentile	0.00	0.00	0.00	106.33	212.65	981.10	1266.34	633.17	0.00	0.00	0.00
50 th percentile	0.00	0.00	0.00	119.12	238.24	997.26	1364.28	682.14	0.00	0.00	0.00
75 th percentile	0.00	0.00	0.00	137.84	275.69	1012.44	1430.35	715.17	0.00	0.00	0.00
95 th percentile	0.00	0.00	0.00	155.33	310.66	1030.57	1501.65	751.14	0.64	0.00	0.00
CH ₄ (mg/m ³ , dry)	Measurement port C - Transversal distance (m)										
	-0.45	-0.25	-0.15	-0.10	-0.05	0	0.05	0.10	0.15	0.25	0.45
Mean	0.00	0.00	39.19	3071.47	6103.75	7027.44	1443.40	721.70	0.00	0.00	0.00
Std. deviation	0.00	0.00	20.95	126.39	231.83	133.04	88.73	44.37	0.02	0.00	0.00
Uncertainty	123.96	123.96	124.02	127.21	130.41	125.71	125.15	124.55	123.96	123.96	123.96
5 th percentile	0.00	0.00	9.18	2892.01	5774.85	6795.71	1260.87	630.44	0.00	0.00	0.00
25 th percentile	0.00	0.00	22.93	2949.30	5875.67	6923.15	1387.48	693.74	0.00	0.00	0.00
50 th percentile	0.00	0.00	36.89	3074.15	6111.41	7048.43	1464.37	732.18	0.00	0.00	0.00
75 th percentile	0.00	0.00	57.62	3188.10	6318.59	7136.92	1508.52	754.26	0.00	0.00	0.00
95 th percentile	0.00	0.00	71.75	3257.61	6443.47	7242.66	1563.30	781.65	0.00	0.00	0.00
CH ₄ (mg/m ³ , dry)	Measurement port D - Transversal distance (m)										
	-0.45	-0.25	-0.15	-0.10	-0.05	0	0.05	0.10	0.15	0.25	0.45
Mean	1.15	371.37	807.25	-	178.70	9.76	3.02	-	0.00	0.00	0.00
Std. deviation	3.18	65.19	183.36	-	108.99	12.73	9.04	-	0.00	0.02	0.00
Uncertainty	123.96	124.34	127.59	-	125.48	123.98	123.97	-	123.96	123.96	123.96
5 th percentile	0.00	259.20	536.59	-	45.34	0.00	0.00	-	0.00	0.00	0.00
25 th percentile	0.00	330.99	666.62	-	95.97	0.00	0.00	-	0.00	0.00	0.00
50 th percentile	0.00	368.91	796.79	-	156.92	4.82	0.00	-	0.00	0.00	0.00
75 th percentile	0.20	411.24	953.09	-	236.16	14.84	0.00	-	0.00	0.00	0.00
95 th percentile	7.54	471.67	1119.92	-	394.02	39.08	28.30	-	0.00	0.00	0.00

CH ₄ (mg/m ³ , dry)	Measurement port E - Transversal distance (m)										
	-0.45	-0.25	-0.15	-0.10	-0.05	0	0.05	0.10	0.15	0.25	0.45
Mean	10.93	332.23	498.41	-	0.94	0.00	4.22	-	0.00	0.00	0.00
Std. deviation	9.21	87.76	125.44	-	1.25	0.04	4.88	-	0.00	0.00	0.00
Uncertainty	123.97	124.65	126.06	-	123.96	123.96	123.96	-	123.96	123.96	123.96
5 th percentile	0.00	176.66	279.14	-	0.00	0.00	0.00	-	0.00	0.00	0.00
25 th percentile	0.00	246.95	409.99	-	0.00	0.00	0.00	-	0.00	0.00	0.00
50 th percentile	11.03	345.42	511.41	-	0.00	0.00	2.11	-	0.00	0.00	0.00
75 th percentile	20.22	383.37	615.17	-	1.94	0.00	8.19	-	0.00	0.00	0.00
95 th percentile	23.64	477.24	658.14	-	3.55	0.00	12.70	-	0.00	0.00	0.00
CH ₄ (mg/m ³ , dry)	Measurement port F - Transversal distance (m)										
	-0.45	-0.30	-0.15	-0.10	-0.05	0	0.05	0.10	0.15	0.30	0.45
Mean	0.00	0.00	0.00	-	-	0.00	-	-	0.00	0.00	0.00
Std. deviation	0.00	0.00	0.00	-	-	0.00	-	-	0.00	0.00	0.00
Uncertainty	123.96	123.96	123.96	-	-	123.96	-	-	123.96	123.96	123.96
5 th percentile	0.00	0.00	0.00	-	-	0.00	-	-	0.00	0.00	0.00
25 th percentile	0.00	0.00	0.00	-	-	0.00	-	-	0.00	0.00	0.00
50 th percentile	0.00	0.00	0.00	-	-	0.00	-	-	0.00	0.00	0.00
75 th percentile	0.00	0.00	0.00	-	-	0.00	-	-	0.00	0.00	0.00
95 th percentile	0.00	0.00	0.00	-	-	0.00	-	-	0.00	0.00	0.00
CH ₄ (mg/m ³ , dry)	Measurement port G - Transversal distance (m)										
	-0.45	-0.30	-0.15	-0.10	-0.05	0	0.05	0.10	0.15	0.30	0.45
Mean	0.00	0.00	0.00	-	-	0.00	-	-	0.00	0.00	0.00
Std. deviation	0.00	0.00	0.00	-	-	0.00	-	-	0.00	0.00	0.00
Uncertainty	123.96	123.96	123.96	-	-	123.96	-	-	123.96	123.96	123.96
5 th percentile	0.00	0.00	0.00	-	-	0.00	-	-	0.00	0.00	0.00
25 th percentile	0.00	0.00	0.00	-	-	0.00	-	-	0.00	0.00	0.00
50 th percentile	0.00	0.00	0.00	-	-	0.00	-	-	0.00	0.00	0.00
75 th percentile	0.00	0.00	0.00	-	-	0.00	-	-	0.00	0.00	0.00
95 th percentile	0.00	0.00	0.00	-	-	0.00	-	-	0.00	0.00	0.00

B.3.7 Local Nitric Oxide Concentration

NO (mg/m ³ , dry)	Measurement port A - Transversal distance (m)										
	-0.45	-0.25	-0.15	-0.10	-0.05	0	0.05	0.10	0.15	0.25	0.45
Mean	542.90	565.46	587.79	478.91	370.04	608.93	369.25	450.60	531.95	526.20	275.74
Std. deviation	5.48	6.09	3.85	4.31	4.76	6.86	7.23	6.39	5.54	17.27	31.25
Uncertainty	30.56	30.57	30.56	30.56	30.55	30.60	30.58	30.58	30.58	30.87	31.36
5 th percentile	535.60	557.34	580.75	471.72	362.69	601.71	354.95	438.20	521.45	495.34	230.96
25 th percentile	538.55	560.66	585.55	475.81	366.08	603.70	368.03	448.36	528.68	512.16	246.94
50 th percentile	541.63	565.77	587.30	479.29	371.29	605.72	370.64	451.93	533.22	532.94	275.84
75 th percentile	547.01	570.27	590.75	482.36	373.97	615.87	373.79	455.47	537.14	539.63	298.08
95 th percentile	553.34	576.47	593.13	484.69	376.26	620.54	379.12	458.80	538.48	546.15	327.55
NO (mg/m ³ , dry)	Measurement port B - Transversal distance (m)										
	-0.45	-0.25	-0.15	-0.10	-0.05	0	0.05	0.10	0.15	0.25	0.45
Mean	423.11	443.82	471.05	648.23	825.41	475.42	920.31	681.64	442.98	537.95	598.13
Std. deviation	34.89	16.62	7.17	8.83	10.49	15.50	11.36	10.15	8.94	4.21	4.50
Uncertainty	31.20	30.75	30.58	30.60	30.62	30.70	30.69	30.64	30.59	30.56	30.56
5 th percentile	346.00	414.99	460.31	633.48	806.66	458.44	896.40	663.97	431.55	530.67	588.77
25 th percentile	409.21	438.27	464.67	642.03	819.40	461.45	913.00	675.03	437.06	534.53	596.78
50 th percentile	425.93	443.17	471.60	648.70	825.80	471.53	922.69	682.29	441.88	539.20	598.13
75 th percentile	456.08	457.00	477.08	653.98	830.88	485.41	928.45	687.23	446.02	541.13	600.98
95 th percentile	459.78	469.00	483.01	665.39	847.76	506.15	933.96	697.57	461.19	543.63	604.20
NO (mg/m ³ , dry)	Measurement port C - Transversal distance (m)										
	-0.45	-0.25	-0.15	-0.10	-0.05	0	0.05	0.10	0.15	0.25	0.45
Mean	518.98	595.54	656.36	564.66	472.97	756.41	471.63	593.42	715.22	697.81	675.45
Std. deviation	6.66	4.38	8.99	17.00	25.01	13.90	16.15	16.20	16.25	10.35	4.23
Uncertainty	30.59	30.56	30.59	30.72	30.86	30.62	30.71	30.70	30.69	30.62	30.56
5 th percentile	510.21	586.99	641.43	534.97	428.51	736.42	449.61	569.82	690.04	676.26	669.89
25 th percentile	512.95	593.13	649.19	546.00	442.81	747.02	457.30	577.85	698.40	691.67	671.84
50 th percentile	519.78	595.49	658.22	569.95	481.69	756.42	471.64	593.16	714.69	702.85	674.67
75 th percentile	521.57	599.28	662.04	577.77	493.49	761.98	483.62	607.79	731.96	704.44	678.67
95 th percentile	530.61	601.14	669.80	584.76	499.71	783.82	500.00	618.09	736.18	707.77	682.56
NO (mg/m ³ , dry)	Measurement port D - Transversal distance (m)										
	-0.45	-0.25	-0.15	-0.10	-0.05	0	0.05	0.10	0.15	0.25	0.45
Mean	522.63	435.77	416.72	-	458.34	479.87	541.38	-	549.89	532.83	534.17
Std. deviation	26.35	47.90	57.21	-	9.16	4.82	8.16	-	4.79	9.65	12.43
Uncertainty	30.91	31.77	32.28	-	30.58	30.56	30.58	-	30.56	30.58	30.66
5 th percentile	490.96	365.32	312.54	-	441.65	471.39	528.75	-	539.72	520.38	519.52
25 th percentile	496.78	405.01	379.28	-	453.90	477.04	536.32	-	547.98	525.82	521.62
50 th percentile	522.82	421.82	427.08	-	462.38	479.51	539.38	-	549.93	530.29	530.94
75 th percentile	530.04	471.50	454.76	-	465.60	482.48	548.28	-	552.79	538.66	546.62
95 th percentile	577.52	518.00	510.03	-	467.64	489.35	556.01	-	557.58	554.74	552.75

NO (mg/m ³ , dry)	Measurement port E - Transversal distance (m)										
	-0.45	-0.25	-0.15	-0.10	-0.05	0	0.05	0.10	0.15	0.25	0.45
Mean	461.58	407.26	427.53	-	376.44	397.71	545.89	-	485.85	469.88	462.36
Std. deviation	16.17	40.41	25.77	-	14.82	8.54	14.76	-	4.26	4.72	5.45
Uncertainty	30.69	31.13	30.91	-	30.66	30.58	30.63	-	30.55	30.56	30.56
5 th percentile	444.20	352.31	378.53	-	356.59	384.37	523.10	-	480.61	461.07	453.79
25 th percentile	450.24	383.25	410.06	-	365.80	393.53	532.44	-	481.81	466.56	458.78
50 th percentile	455.15	395.39	426.79	-	369.39	396.75	546.74	-	485.73	470.21	462.02
75 th percentile	467.71	420.75	446.23	-	391.98	399.90	561.03	-	487.73	473.66	467.33
95 th percentile	491.40	491.83	467.91	-	400.01	415.28	565.87	-	493.78	477.04	469.74
NO (mg/m ³ , dry)	Measurement port F - Transversal distance (m)										
	-0.45	-0.30	-0.15	-0.10	-0.05	0	0.05	0.10	0.15	0.30	0.45
Mean	391.51	401.53	460.09	-	-	470.21	-	-	489.83	463.43	485.02
Std. deviation	19.78	13.66	26.45	-	-	17.46	-	-	12.16	13.08	8.92
Uncertainty	30.74	30.64	30.92	-	-	30.71	-	-	30.62	30.60	30.57
5 th percentile	361.38	378.09	416.95	-	-	444.68	-	-	467.94	447.64	470.25
25 th percentile	374.83	392.93	440.90	-	-	458.10	-	-	481.19	452.61	477.15
50 th percentile	390.92	399.58	458.87	-	-	468.10	-	-	490.42	462.27	485.19
75 th percentile	404.01	410.38	476.36	-	-	482.83	-	-	500.72	469.32	491.94
95 th percentile	426.00	426.16	503.76	-	-	500.29	-	-	507.11	491.81	496.88
NO (mg/m ³ , dry)	Measurement port G - Transversal distance (m)										
	-0.45	-0.30	-0.15	-0.10	-0.05	0	0.05	0.10	0.15	0.30	0.45
Mean	475.32	512.09	504.41	-	-	501.26	-	-	460.72	490.87	487.47
Std. deviation	16.48	29.62	23.54	-	-	19.42	-	-	19.45	6.96	9.39
Uncertainty	30.69	30.78	30.85	-	-	30.67	-	-	30.75	30.57	30.58
5 th percentile	454.58	456.48	465.60	-	-	471.89	-	-	434.76	478.51	472.24
25 th percentile	461.23	497.19	489.38	-	-	494.74	-	-	446.77	485.77	479.76
50 th percentile	475.04	509.26	502.47	-	-	498.50	-	-	456.66	491.63	488.70
75 th percentile	484.84	531.13	529.40	-	-	509.12	-	-	476.32	495.78	496.37
95 th percentile	505.87	564.96	539.99	-	-	538.91	-	-	495.81	502.81	500.37

B.3.8 Total Radiative Heat Flux

Heat flux (kW/m ²)	Measurement port						
	A	B	C	D	E	F	G
Mean	130.66	140.72	155.83	174.51	149.14	147.50	114.56
Std. deviation	1.84	1.80	1.66	2.49	2.19	3.25	2.48
Uncertainty	8.92	9.40	10.13	11.01	9.81	9.74	8.15
5 th percentile	127.46	137.80	153.42	170.42	145.28	140.83	110.77
25 th percentile	129.33	139.35	154.61	172.64	147.75	145.83	112.60
50 th percentile	130.78	140.82	155.73	174.23	148.99	147.73	114.40
75 th percentile	132.08	142.00	157.04	176.45	150.43	149.87	116.22
95 th percentile	133.34	143.95	158.43	178.62	152.89	152.31	118.73

B.4 Oxy-Flame 3

B.4.1 Furnace Operating Conditions

Operating parameter	
Coal feed rate (kg/h)	56.41 ±0.23
Volume flow rate of primary stream (m ³ /h, STP)	34.07 ±1.58
O ₂ fraction of primary stream (vol%, wet)	19.40 ±1.12
CO ₂ fraction of primary stream (vol%, wet) ¹	80.60
Temperature of primary stream (°C)	24.43 ±1.25
Velocity of primary stream at burner exit (m/s) ¹	23.32
Axial momentum of primary stream at burner exit (N) ¹	0.47
Volume flow rate of secondary stream (m ³ /h, STP)	144 ±2.80
Volume flow rate of tertiary stream (m ³ /h, STP)	72 ±7.05
O ₂ fraction of secondary and tertiary stream (vol%, wet)	33 ±1.91
H ₂ O fraction of secondary and tertiary stream (vol%, wet) ¹	20.25
CO ₂ fraction of secondary and tertiary stream (vol%, wet) ¹	43.40
N ₂ fraction of secondary and tertiary stream (vol%, wet) ¹	3.23
Temperature of secondary and tertiary streams (°C)	165.30 ±1.74
Secondary/tertiary mass flow ratio ¹	2.00
Swirl number of secondary stream ¹	2.05
Stoichiometric ratio ¹	1.17
Overall heat input (kW) ¹	347.10
Sensible heat input (kW) ¹	14.90
Flue gas	
O ₂ (vol%, dry)	6.36 ±0.83
CO ₂ (vol%, dry)	87.16 ±1.05
N ₂ (vol%, dry) ¹	6.48
H ₂ O (vol% wet)	28.91 ±0.19
Volume flow rate at furnace exit (m ³ /h, STP)	308.80 ±5.26
Volume flow rate of recycled flue gas (m ³ /h, STP)	143.46 ±3.56
Temperature at furnace exit (°C)	477.30 ±3.31
Recycle ratio ¹	0.47
Outer wall surface temperature at the vertical section (°C)	198.04 ±1.85
Inner surface temperature of the cylindrical section (°C)	872.92 ±4.25

¹calculated value

B.4.2 Local Gas Temperature

Temperature (°C)	Measurement port A - Transversal distance (m)										
	-0.45	-0.25	-0.15	-0.10	-0.05	0	0.05	0.10	0.15	0.25	0.45
Mean	899	1058	1058	990	612	1035	1251	786	948	1101	1039
Std. deviation	2.59	3.00	2.07	4.24	14.94	8.13	10.47	8.00	5.27	2.66	11.43
Uncertainty	22.54	26.44	26.45	24.78	16.20	25.92	31.33	20.03	23.78	27.51	26.14
5 th percentile	894	1053	1054	985	591	1023	1234	774	940	1096	1023
25 th percentile	897	1056	1058	988	599	1029	1240	782	945	1099	1029
50 th percentile	899	1058	1059	990	610	1033	1254	786	947	1101	1040
75 th percentile	900	1060	1060	992	622	1044	1258	791	951	1103	1049
95 th percentile	902	1062	1061	999	636	1047	1265	799	958	1104	1057
Temperature (°C)	Measurement port B - Transversal distance (m)										
	-0.45	-0.25	-0.15	-0.10	-0.05	0	0.05	0.10	0.15	0.25	0.45
Mean	1023	1014	1074	1091	1262	1067	1233	1249	1215	1179	1157
Std. deviation	2.28	4.73	4.60	4.27	4.33	9.92	7.46	4.04	12.14	3.67	4.83
Uncertainty	25.57	25.36	26.85	27.27	31.57	26.69	30.85	31.23	30.45	29.47	28.92
5 th percentile	1020	1006	1066	1084	1253	1054	1221	1242	1197	1173	1150
25 th percentile	1021	1011	1071	1088	1260	1058	1226	1246	1203	1176	1155
50 th percentile	1023	1013	1075	1091	1263	1064	1234	1248	1217	1179	1157
75 th percentile	1024	1017	1078	1093	1265	1077	1239	1252	1225	1182	1159
95 th percentile	1026	1022	1081	1098	1268	1082	1244	1256	1233	1185	1167
Temperature (°C)	Measurement port C - Transversal distance (m)										
	-0.45	-0.25	-0.15	-0.10	-0.05	0	0.05	0.10	0.15	0.25	0.45
Mean	1012	1208	1248	1276	1207	1099	1195	1229	1222	1159	1100
Std. deviation	4.28	4.17	4.44	4.94	12.91	6.02	4.83	6.45	2.73	3.59	3.15
Uncertainty	25.31	30.19	31.20	31.94	30.22	27.47	29.87	30.73	30.54	28.97	27.48
5 th percentile	1004	1201	1240	1268	1192	1090	1187	1216	1217	1153	1095
25 th percentile	1009	1205	1244	1273	1197	1094	1191	1226	1220	1157	1097
50 th percentile	1013	1208	1247	1277	1202	1098	1195	1229	1222	1160	1100
75 th percentile	1016	1210	1251	1280	1216	1103	1198	1233	1224	1162	1102
95 th percentile	1017	1215	1254	1284	1233	1110	1203	1239	1226	1165	1104
Temperature (°C)	Measurement port D - Transversal distance (m)										
	-0.45	-0.25	-0.15	-0.10	-0.05	0	0.05	0.10	0.15	0.25	0.45
Mean	1127	1205	1187	-	1149	1143	1178	-	1192	1116	1045
Std. deviation	2.19	3.65	2.73	-	7.83	7.15	8.72	-	7.33	12.33	8.35
Uncertainty	27.64	29.53	29.09	-	28.21	28.04	28.91	-	29.25	27.45	25.71
5 th percentile	1123	1199	1181	-	1138	1130	1162	-	1178	1093	1033
25 th percentile	1125	1201	1185	-	1142	1138	1172	-	1188	1109	1037
50 th percentile	1127	1205	1187	-	1150	1142	1179	-	1194	1118	1045
75 th percentile	1128	1208	1189	-	1157	1148	1185	-	1198	1125	1052
95 th percentile	1131	1210	1191	-	1161	1155	1190	-	1202	1133	1058

Temperature (°C)	Measurement port E - Transversal distance (m)										
	-0.45	-0.25	-0.15	-0.10	-0.05	0	0.05	0.10	0.15	0.25	0.45
Mean	1100	1193	1169	-	1066	1095	1153	-	1159	1055	973
Std. deviation	4.03	2.33	2.59	-	5.07	5.91	7.44	-	17.78	15.23	4.55
Uncertainty	27.01	29.25	28.67	-	26.17	26.89	28.29	-	28.60	26.03	23.94
5 th percentile	1094	1190	1165	-	1058	1087	1136	-	1134	1034	967
25 th percentile	1097	1192	1167	-	1062	1091	1150	-	1144	1042	970
50 th percentile	1101	1194	1169	-	1065	1095	1154	-	1161	1053	972
75 th percentile	1103	1195	1171	-	1070	1097	1158	-	1169	1069	976
95 th percentile	1107	1197	1173	-	1074	1108	1162	-	1190	1079	981
Temperature (°C)	Measurement port F - Transversal distance (m)										
	-0.45	-0.30	-0.15	-0.10	-0.05	0	0.05	0.10	0.15	0.30	0.45
Mean	1030	1094	1104	-	-	1084	-	-	1062	1044	1017
Std. deviation	13.13	16.47	6.16	-	-	7.54	-	-	3.43	3.90	3.29
Uncertainty	25.41	26.99	27.12	-	-	26.65	-	-	26.10	25.66	25.01
5 th percentile	1012	1062	1094	-	-	1070	-	-	1057	1036	1011
25 th percentile	1018	1084	1102	-	-	1079	-	-	1061	1042	1016
50 th percentile	1032	1096	1105	-	-	1085	-	-	1063	1044	1017
75 th percentile	1040	1107	1108	-	-	1090	-	-	1065	1046	1019
95 th percentile	1048	1114	1112	-	-	1096	-	-	1068	1049	1024
Temperature (°C)	Measurement port G - Transversal distance (m)										
	-0.45	-0.30	-0.15	-0.10	-0.05	0	0.05	0.10	0.15	0.30	0.45
Mean	954	1037	1047	-	-	1060	-	-	1033	1010	979
Std. deviation	13.15	8.14	5.58	-	-	4.68	-	-	4.19	4.84	4.46
Uncertainty	23.60	25.52	25.71	-	-	26.03	-	-	25.38	24.85	24.08
5 th percentile	933	1024	1036	-	-	1052	-	-	1026	1004	972
25 th percentile	945	1030	1042	-	-	1056	-	-	1030	1006	975
50 th percentile	952	1037	1048	-	-	1060	-	-	1032	1010	978
75 th percentile	963	1042	1051	-	-	1063	-	-	1036	1014	982
95 th percentile	976	1051	1055	-	-	1067	-	-	1039	1019	986

B.4.3 Local Oxygen Concentration

O ₂ (vol%, dry)	Measurement port A - Transversal distance (m)										
	-0.45	-0.25	-0.15	-0.10	-0.05	0	0.05	0.10	0.15	0.25	0.45
Mean	13.68	14.08	14.28	41.11	37.00	8.65	29.65	33.27	16.58	11.25	13.68
Std. deviation	0.30	0.32	0.48	0.09	0.12	0.30	0.44	0.27	1.37	0.40	0.30
Uncertainty	0.59	0.59	0.59	0.59	0.59	0.59	0.59	0.59	0.61	0.59	0.59
5 th percentile	13.04	13.44	13.53	41.01	36.80	7.96	28.95	32.75	13.85	10.68	13.04
25 th percentile	13.54	13.95	13.99	41.03	36.93	8.53	29.33	33.13	15.76	10.97	13.54
50 th percentile	13.73	14.14	14.19	41.11	36.99	8.72	29.66	33.37	16.96	11.17	13.73
75 th percentile	13.89	14.28	14.42	41.17	37.09	8.83	29.91	33.45	17.64	11.54	13.89
95 th percentile	14.07	14.51	15.25	41.29	37.16	9.07	30.42	33.59	18.26	11.97	14.07
O ₂ (vol%, dry)	Measurement port B - Transversal distance (m)										
	-0.45	-0.25	-0.15	-0.10	-0.05	0	0.05	0.10	0.15	0.25	0.45
Mean	14.50	20.61	15.37	12.18	2.14	8.12	2.70	13.83	12.70	15.05	16.22
Std. deviation	0.28	0.77	0.99	0.70	0.22	0.21	0.64	0.43	0.86	0.78	0.50
Uncertainty	0.59	0.61	0.61	0.60	0.59	0.59	0.60	0.59	0.61	0.61	0.60
5 th percentile	14.02	19.30	12.98	11.17	1.76	7.68	1.90	13.19	11.31	14.03	15.38
25 th percentile	14.33	20.05	15.21	11.66	1.93	7.98	2.20	13.38	11.86	14.40	15.94
50 th percentile	14.48	20.43	15.62	11.94	2.18	8.22	2.62	13.79	12.78	15.09	16.23
75 th percentile	14.66	21.34	16.06	12.86	2.27	8.28	2.99	14.23	13.38	15.44	16.69
95 th percentile	15.04	21.79	16.39	13.27	2.42	8.35	3.81	14.40	13.88	16.62	16.94
O ₂ (vol%, dry)	Measurement port C - Transversal distance (m)										
	-0.45	-0.25	-0.15	-0.10	-0.05	0	0.05	0.10	0.15	0.25	0.45
Mean	14.80	4.56	1.95	0.57	0.48	0.71	0.91	2.73	3.78	7.02	12.55
Std. deviation	0.35	0.41	0.41	0.11	0.03	0.03	0.28	0.50	0.70	0.47	0.49
Uncertainty	0.59	0.59	0.59	0.59	0.59	0.59	0.59	0.60	0.60	0.60	0.60
5 th percentile	14.31	3.94	1.22	0.45	0.43	0.66	0.57	1.88	2.62	6.17	11.75
25 th percentile	14.52	4.24	1.74	0.49	0.45	0.69	0.71	2.29	3.39	6.72	12.13
50 th percentile	14.68	4.67	1.94	0.53	0.47	0.71	0.82	2.69	3.61	7.01	12.72
75 th percentile	15.12	4.90	2.24	0.63	0.50	0.73	1.08	3.16	4.41	7.42	12.92
95 th percentile	15.38	5.16	2.68	0.79	0.55	0.77	1.49	3.50	5.12	7.69	13.29
O ₂ (vol%, dry)	Measurement port D - Transversal distance (m)										
	-0.45	-0.25	-0.15	-0.10	-0.05	0	0.05	0.10	0.15	0.25	0.45
Mean	5.31	1.27	3.21	-	5.18	6.59	3.50	-	2.50	5.97	11.82
Std. deviation	0.89	0.24	0.62	-	0.33	0.96	0.59	-	0.57	1.11	1.61
Uncertainty	0.60	0.59	0.59	-	0.59	0.60	0.60	-	0.59	0.61	0.64
5 th percentile	3.95	0.92	2.42	-	4.70	5.13	2.63	-	1.52	4.32	8.54
25 th percentile	4.47	1.09	2.76	-	4.94	5.91	2.95	-	2.00	5.27	10.74
50 th percentile	5.27	1.23	3.02	-	5.13	6.53	3.47	-	2.58	6.06	12.23
75 th percentile	6.11	1.44	3.61	-	5.41	7.44	4.06	-	2.90	6.50	13.00
95 th percentile	6.65	1.72	4.43	-	5.84	8.31	4.39	-	3.42	8.35	13.91

O ₂ (vol%, dry)	Measurement port E - Transversal distance (m)										
	-0.45	-0.25	-0.15	-0.10	-0.05	0	0.05	0.10	0.15	0.25	0.45
Mean	5.04	2.60	2.71	-	4.58	4.59	9.00	-	14.28	17.48	19.48
Std. deviation	0.43	0.25	0.53	-	0.68	0.70	0.98	-	1.15	0.85	0.82
Uncertainty	0.59	0.59	0.60	-	0.60	0.60	0.62	-	0.63	0.61	0.61
5 th percentile	4.24	2.06	1.99	-	3.23	3.83	7.24	-	12.68	15.89	17.94
25 th percentile	4.76	2.43	2.26	-	4.32	4.02	8.42	-	13.36	16.90	18.89
50 th percentile	5.09	2.64	2.72	-	4.67	4.32	9.15	-	14.12	17.69	19.57
75 th percentile	5.33	2.79	2.99	-	5.02	5.35	9.67	-	14.95	18.07	20.07
95 th percentile	5.65	2.96	3.87	-	5.58	5.77	10.51	-	16.48	18.69	20.77
O ₂ (vol%, dry)	Measurement port F - Transversal distance (m)										
	-0.45	-0.30	-0.15	-0.10	-0.05	0	0.05	0.10	0.15	0.30	0.45
Mean	7.21	3.24	5.12	-	-	8.02	-	-	10.39	12.60	14.12
Std. deviation	0.54	0.64	0.51	-	-	0.44	-	-	0.69	0.90	0.54
Uncertainty	0.60	0.60	0.59	-	-	0.59	-	-	0.60	0.61	0.60
5 th percentile	6.33	2.42	4.33	-	-	7.15	-	-	9.32	10.99	13.16
25 th percentile	6.78	2.68	4.69	-	-	7.75	-	-	9.94	12.03	13.72
50 th percentile	7.13	3.20	5.16	-	-	8.02	-	-	10.30	12.73	14.13
75 th percentile	7.70	3.80	5.48	-	-	8.18	-	-	10.80	13.30	14.46
95 th percentile	8.06	4.29	5.99	-	-	8.94	-	-	11.61	13.82	15.26
O ₂ (vol%, dry)	Measurement port G - Transversal distance (m)										
	-0.45	-0.30	-0.15	-0.10	-0.05	0	0.05	0.10	0.15	0.30	0.45
Mean	8.26	5.50	6.26	-	-	7.63	-	-	8.63	10.50	11.25
Std. deviation	0.61	0.50	0.43	-	-	0.68	-	-	0.81	0.59	1.04
Uncertainty	0.59	0.59	0.59	-	-	0.60	-	-	0.60	0.60	0.62
5 th percentile	7.51	4.65	5.40	-	-	6.66	-	-	7.28	9.45	9.31
25 th percentile	7.90	5.17	6.04	-	-	7.16	-	-	7.95	10.06	10.46
50 th percentile	8.14	5.54	6.27	-	-	7.67	-	-	8.61	10.44	11.35
75 th percentile	8.40	5.76	6.53	-	-	8.07	-	-	9.15	11.03	12.16
95 th percentile	9.65	6.56	6.97	-	-	8.98	-	-	10.17	11.44	12.83

B.4.4 Local Carbon Dioxide Concentration

CO ₂ (vol%, dry)	Measurement port A - Transversal distance (m)										
	-0.45	-0.25	-0.15	-0.10	-0.05	0	0.05	0.10	0.15	0.25	0.45
Mean	83.38	82.92	82.45	53.84	57.99	87.50	65.86	62.39	80.43	86.40	83.38
Std. deviation	0.33	0.35	0.51	0.09	0.11	0.27	0.53	0.28	1.54	0.47	0.33
Uncertainty	1.64	1.63	1.63	1.46	1.48	1.66	1.53	1.51	1.63	1.66	1.64
5 th percentile	82.96	82.44	81.43	53.67	57.84	87.01	64.90	62.07	78.56	85.57	82.96
25 th percentile	83.14	82.67	82.22	53.78	57.90	87.33	65.53	62.21	79.24	86.09	83.14
50 th percentile	83.35	82.87	82.52	53.84	57.98	87.50	65.86	62.28	80.02	86.48	83.35
75 th percentile	83.54	83.06	82.81	53.92	58.08	87.63	66.23	62.56	81.31	86.75	83.54
95 th percentile	84.11	83.61	83.26	53.96	58.20	88.06	66.74	62.93	83.54	87.07	84.11
CO ₂ (vol%, dry)	Measurement port B - Transversal distance (m)										
	-0.45	-0.25	-0.15	-0.10	-0.05	0	0.05	0.10	0.15	0.25	0.45
Mean	81.06	74.59	79.54	84.73	84.59	83.54	88.94	83.36	84.74	82.12	80.84
Std. deviation	0.41	1.20	1.94	0.61	0.45	0.07	0.45	0.49	0.96	0.89	0.57
Uncertainty	1.62	1.59	1.65	1.65	1.65	1.64	1.68	1.64	1.65	1.63	1.62
5 th percentile	80.39	72.48	74.91	83.76	83.91	83.44	87.98	82.66	83.41	80.38	80.02
25 th percentile	80.75	73.71	79.13	84.16	84.18	83.46	88.72	82.92	83.92	81.73	80.36
50 th percentile	81.07	74.61	79.82	84.77	84.52	83.53	88.96	83.39	84.64	81.92	80.82
75 th percentile	81.37	75.52	80.96	85.22	85.04	83.60	89.32	83.87	85.71	82.84	81.21
95 th percentile	81.75	76.17	81.87	85.64	85.23	83.66	89.55	84.09	86.24	83.28	81.82
CO ₂ (vol%, dry)	Measurement port C - Transversal distance (m)										
	-0.45	-0.25	-0.15	-0.10	-0.05	0	0.05	0.10	0.15	0.25	0.45
Mean	81.87	93.03	93.91	90.16	83.94	81.96	90.17	94.43	93.94	91.20	85.15
Std. deviation	0.39	0.43	0.19	0.56	1.00	1.19	0.91	0.33	0.46	0.54	0.56
Uncertainty	1.63	1.70	1.71	1.68	1.65	1.64	1.69	1.71	1.71	1.69	1.65
5 th percentile	81.24	92.38	93.67	89.16	82.38	80.35	88.36	93.84	93.13	90.41	84.32
25 th percentile	81.48	92.74	93.75	89.77	83.14	80.92	89.58	94.13	93.63	90.69	84.77
50 th percentile	81.97	92.97	93.89	90.16	83.87	81.83	90.40	94.53	93.90	91.23	84.97
75 th percentile	82.19	93.30	94.03	90.58	84.63	82.67	90.72	94.68	94.32	91.59	85.65
95 th percentile	82.40	93.87	94.26	91.13	85.67	84.23	91.49	94.83	94.66	92.15	85.98
CO ₂ (vol%, dry)	Measurement port D - Transversal distance (m)										
	-0.45	-0.25	-0.15	-0.10	-0.05	0	0.05	0.10	0.15	0.25	0.45
Mean	88.57	90.94	92.48	-	92.76	90.07	89.57	-	91.04	90.75	85.30
Std. deviation	0.73	0.72	0.59	-	0.37	1.09	0.49	-	0.40	1.01	1.71
Uncertainty	1.67	1.69	1.70	-	1.70	1.69	1.68	-	1.69	1.69	1.67
5 th percentile	87.47	89.69	91.50	-	92.08	88.16	88.77	-	90.47	88.55	83.10
25 th percentile	88.02	90.46	92.01	-	92.51	89.25	89.20	-	90.74	90.23	84.07
50 th percentile	88.42	91.02	92.61	-	92.83	90.02	89.49	-	90.97	90.83	84.91
75 th percentile	89.24	91.36	92.90	-	93.07	90.98	90.02	-	91.33	91.36	86.34
95 th percentile	89.75	92.30	93.27	-	93.32	92.05	90.31	-	91.74	92.16	88.83

CO ₂ (vol%, dry)	Measurement port E - Transversal distance (m)										
	-0.45	-0.25	-0.15	-0.10	-0.05	0	0.05	0.10	0.15	0.25	0.45
Mean	79.92	92.36	91.91	-	93.48	93.13	88.02	-	82.18	78.94	76.75
Std. deviation	1.61	0.33	0.38	-	0.60	0.52	1.05	-	1.22	0.94	0.91
Uncertainty	1.63	1.70	1.70	-	1.71	1.71	1.68	-	1.64	1.61	1.60
5 th percentile	76.51	91.91	91.27	-	92.58	92.19	86.44	-	79.95	77.54	75.40
25 th percentile	79.22	92.10	91.60	-	93.14	92.74	87.31	-	81.28	78.32	76.00
50 th percentile	80.15	92.34	91.97	-	93.47	93.22	87.96	-	82.41	78.71	76.66
75 th percentile	80.73	92.60	92.21	-	93.68	93.54	88.69	-	83.13	79.49	77.42
95 th percentile	82.32	92.90	92.45	-	94.61	93.87	89.82	-	83.71	80.81	78.45
CO ₂ (vol%, dry)	Measurement port F - Transversal distance (m)										
	-0.45	-0.30	-0.15	-0.10	-0.05	0	0.05	0.10	0.15	0.30	0.45
Mean	68.13	93.04	91.69	-	-	89.16	-	-	86.84	84.35	82.66
Std. deviation	2.75	0.40	0.48	-	-	0.45	-	-	0.79	1.01	0.62
Uncertainty	1.62	1.70	1.70	-	-	1.68	-	-	1.66	1.65	1.63
5 th percentile	64.17	92.49	90.81	-	-	88.25	-	-	85.49	82.98	81.37
25 th percentile	65.94	92.74	91.41	-	-	88.88	-	-	86.40	83.49	82.32
50 th percentile	68.09	92.96	91.67	-	-	89.17	-	-	86.88	84.27	82.67
75 th percentile	70.28	93.37	91.90	-	-	89.47	-	-	87.30	84.86	83.07
95 th percentile	72.59	93.75	92.66	-	-	89.85	-	-	88.21	86.21	83.64
CO ₂ (vol%, dry)	Measurement port G - Transversal distance (m)										
	-0.45	-0.30	-0.15	-0.10	-0.05	0	0.05	0.10	0.15	0.30	0.45
Mean	74.88	91.57	91.25	-	-	89.88	-	-	88.85	86.75	85.93
Std. deviation	3.47	0.64	0.47	-	-	0.74	-	-	0.88	0.66	1.12
Uncertainty	1.64	1.69	1.69	-	-	1.68	-	-	1.68	1.66	1.66
5 th percentile	68.51	90.21	90.46	-	-	88.44	-	-	87.16	85.74	84.24
25 th percentile	72.49	91.25	90.98	-	-	89.33	-	-	88.30	86.15	85.04
50 th percentile	74.55	91.57	91.18	-	-	89.87	-	-	88.88	86.80	85.81
75 th percentile	78.09	91.98	91.55	-	-	90.43	-	-	89.52	87.28	86.77
95 th percentile	79.99	92.65	92.09	-	-	90.90	-	-	90.20	87.87	88.10

B.4.5 Local Carbon Monoxide Concentration

CO (vol%, dry)	Measurement port A - Transversal distance (m)										
	-0.45	-0.25	-0.15	-0.10	-0.05	0	0.05	0.10	0.15	0.25	0.45
Mean	0.01	0.01	0.01	0.01	0.14	3.48	0.76	0.12	0.04	0.01	0.01
Std. deviation	0.00	0.00	0.00	0.00	0.01	0.10	0.04	0.01	0.00	0.00	0.00
Uncertainty	0.35	0.35	0.35	0.35	0.35	0.35	0.35	0.35	0.35	0.35	0.35
5 th percentile	0.00	0.00	0.00	0.01	0.13	3.32	0.70	0.12	0.04	0.01	0.00
25 th percentile	0.00	0.00	0.00	0.01	0.13	3.39	0.73	0.12	0.04	0.01	0.00
50 th percentile	0.01	0.01	0.01	0.02	0.14	3.50	0.75	0.12	0.05	0.01	0.01
75 th percentile	0.01	0.01	0.01	0.02	0.14	3.57	0.78	0.12	0.05	0.01	0.01
95 th percentile	0.01	0.01	0.01	0.02	0.15	3.63	0.84	0.14	0.05	0.01	0.01
CO (vol%, dry)	Measurement port B - Transversal distance (m)										
	-0.45	-0.25	-0.15	-0.10	-0.05	0	0.05	0.10	0.15	0.25	0.45
Mean	0.01	0.05	0.21	0.62	7.14	6.56	5.75	0.19	0.04	0.01	0.01
Std. deviation	0.00	0.02	0.09	0.17	0.42	0.17	0.70	0.04	0.01	0.00	0.00
Uncertainty	0.35	0.35	0.35	0.35	0.36	0.35	0.37	0.35	0.35	0.35	0.35
5 th percentile	0.01	0.02	0.11	0.32	6.51	6.12	4.84	0.13	0.03	0.00	0.00
25 th percentile	0.01	0.03	0.16	0.53	6.83	6.52	5.24	0.15	0.03	0.01	0.00
50 th percentile	0.02	0.05	0.18	0.61	7.04	6.59	5.60	0.18	0.03	0.01	0.01
75 th percentile	0.02	0.07	0.23	0.74	7.57	6.67	6.29	0.21	0.04	0.01	0.01
95 th percentile	0.02	0.09	0.41	0.87	7.87	6.76	6.92	0.28	0.07	0.01	0.01
CO (vol%, dry)	Measurement port C - Transversal distance (m)										
	-0.45	-0.25	-0.15	-0.10	-0.05	0	0.05	0.10	0.15	0.25	0.45
Mean	0.04	1.05	2.98	7.55	16.10	13.97	6.93	1.59	1.01	0.13	0.05
Std. deviation	0.02	0.14	0.53	0.53	0.20	0.24	0.60	0.29	0.48	0.08	0.03
Uncertainty	0.35	0.35	0.36	0.36	0.35	0.35	0.37	0.35	0.36	0.35	0.35
5 th percentile	0.02	0.83	2.00	6.67	15.72	13.64	6.15	1.24	0.23	0.03	0.01
25 th percentile	0.02	0.94	2.61	7.14	15.97	13.75	6.39	1.34	0.53	0.07	0.03
50 th percentile	0.03	1.03	3.10	7.58	16.13	13.95	6.85	1.53	1.09	0.12	0.04
75 th percentile	0.05	1.14	3.25	7.92	16.26	14.18	7.45	1.79	1.44	0.21	0.06
95 th percentile	0.07	1.33	3.85	8.41	16.37	14.39	8.03	2.18	1.77	0.28	0.10
CO (vol%, dry)	Measurement port D - Transversal distance (m)										
	-0.45	-0.25	-0.15	-0.10	-0.05	0	0.05	0.10	0.15	0.25	0.45
Mean	1.71	5.16	2.19	-	0.39	1.17	4.48	-	4.22	1.04	0.10
Std. deviation	0.35	0.86	0.52	-	0.13	0.40	0.57	-	0.61	0.26	0.08
Uncertainty	0.35	0.38	0.36	-	0.35	0.36	0.36	-	0.36	0.35	0.35
5 th percentile	1.11	3.49	1.29	-	0.18	0.43	3.31	-	3.23	0.65	0.02
25 th percentile	1.52	4.63	1.88	-	0.31	0.98	4.19	-	3.80	0.88	0.04
50 th percentile	1.69	5.10	2.15	-	0.40	1.12	4.50	-	4.19	0.97	0.08
75 th percentile	1.94	5.77	2.54	-	0.47	1.42	4.77	-	4.71	1.22	0.16
95 th percentile	2.37	6.49	3.00	-	0.60	1.79	5.45	-	5.16	1.53	0.24

CO (vol%, dry)	Measurement port E - Transversal distance (m)										
	-0.45	-0.25	-0.15	-0.10	-0.05	0	0.05	0.10	0.15	0.25	0.45
Mean	1.42	2.34	2.94	-	0.51	0.80	0.39	-	0.17	0.00	0.00
Std. deviation	0.30	0.40	0.43	-	0.26	0.35	0.16	-	0.12	0.01	0.00
Uncertainty	0.35	0.36	0.36	-	0.35	0.36	0.35	-	0.35	0.35	0.35
5 th percentile	1.05	1.87	2.33	-	0.18	0.23	0.11	-	0.00	0.00	0.00
25 th percentile	1.22	2.02	2.67	-	0.29	0.48	0.27	-	0.08	0.00	0.00
50 th percentile	1.39	2.29	2.90	-	0.47	0.92	0.43	-	0.16	0.00	0.00
75 th percentile	1.54	2.48	3.25	-	0.72	1.10	0.52	-	0.24	0.00	0.00
95 th percentile	1.82	3.13	3.70	-	0.95	1.19	0.62	-	0.37	0.04	0.00
CO (vol%, dry)	Measurement port F - Transversal distance (m)										
	-0.45	-0.30	-0.15	-0.10	-0.05	0	0.05	0.10	0.15	0.30	0.45
Mean	0.58	1.17	0.82	-	-	0.30	-	-	0.06	0.01	0.00
Std. deviation	0.15	0.48	0.25	-	-	0.16	-	-	0.06	0.02	0.00
Uncertainty	0.35	0.36	0.35	-	-	0.35	-	-	0.35	0.35	0.35
5 th percentile	0.42	0.35	0.46	-	-	0.07	-	-	0.00	0.00	0.00
25 th percentile	0.45	0.84	0.60	-	-	0.16	-	-	0.01	0.00	0.00
50 th percentile	0.54	1.26	0.77	-	-	0.27	-	-	0.05	0.00	0.00
75 th percentile	0.68	1.54	0.99	-	-	0.39	-	-	0.11	0.00	0.00
95 th percentile	0.85	1.91	1.30	-	-	0.60	-	-	0.17	0.07	0.00
CO (vol%, dry)	Measurement port G - Transversal distance (m)										
	-0.45	-0.30	-0.15	-0.10	-0.05	0	0.05	0.10	0.15	0.30	0.45
Mean	0.08	0.11	0.14	-	-	0.07	-	-	0.02	0.00	0.03
Std. deviation	0.06	0.07	0.09	-	-	0.05	-	-	0.02	0.00	0.04
Uncertainty	0.35	0.35	0.35	-	-	0.35	-	-	0.35	0.35	0.35
5 th percentile	0.01	0.03	0.01	-	-	0.01	-	-	0.00	0.00	0.00
25 th percentile	0.03	0.06	0.07	-	-	0.03	-	-	0.00	0.00	0.00
50 th percentile	0.05	0.10	0.12	-	-	0.05	-	-	0.02	0.00	0.00
75 th percentile	0.12	0.14	0.18	-	-	0.09	-	-	0.04	0.00	0.04
95 th percentile	0.17	0.25	0.35	-	-	0.18	-	-	0.07	0.00	0.13

B.4.6 Local Methane Concentration

CH ₄ (mg/m ³ , dry)	Measurement port A - Transversal distance (m)										
	-0.45	-0.25	-0.15	-0.10	-0.05	0	0.05	0.10	0.15	0.25	0.45
Mean	0.00	0.00	0.00	0.00	0.16	529.91	23.24	0.91	0.00	0.00	0.00
Std. deviation	0.00	0.00	0.00	0.00	0.28	25.45	3.44	0.51	0.00	0.00	0.00
Uncertainty	123.96	123.96	123.96	123.96	123.96	124.02	123.96	123.96	123.96	123.96	123.96
5 th percentile	0.00	0.00	0.00	0.00	0.00	483.03	17.44	0.06	0.00	0.00	0.00
25 th percentile	0.00	0.00	0.00	0.00	0.00	514.14	21.37	0.56	0.00	0.00	0.00
50 th percentile	0.00	0.00	0.00	0.00	0.00	527.47	23.06	0.89	0.00	0.00	0.00
75 th percentile	0.00	0.00	0.00	0.00	0.29	550.39	24.96	1.17	0.00	0.00	0.00
95 th percentile	0.00	0.00	0.00	0.00	0.71	568.69	29.18	1.76	0.00	0.00	0.00
CH ₄ (mg/m ³ , dry)	Measurement port B - Transversal distance (m)										
	-0.45	-0.25	-0.15	-0.10	-0.05	0	0.05	0.10	0.15	0.25	0.45
Mean	0.00	0.00	0.33	21.42	1091.91	2136.29	737.93	1.67	0.00	0.00	0.00
Std. deviation	0.00	0.00	1.59	13.31	122.99	71.94	135.51	2.04	0.00	0.00	0.00
Uncertainty	123.96	123.96	123.96	123.98	125.98	124.65	125.59	123.96	123.96	123.96	123.96
5 th percentile	0.00	0.00	0.00	0.00	884.48	1948.32	566.05	0.00	0.00	0.00	0.00
25 th percentile	0.00	0.00	0.00	11.79	1024.89	2131.85	636.62	0.00	0.00	0.00	0.00
50 th percentile	0.00	0.00	0.00	21.61	1085.93	2149.85	706.19	0.28	0.00	0.00	0.00
75 th percentile	0.00	0.00	0.00	30.32	1172.33	2180.58	824.34	3.85	0.00	0.00	0.00
95 th percentile	0.00	0.00	0.79	43.98	1326.66	2212.95	1008.50	5.26	0.00	0.00	0.00
CH ₄ (mg/m ³ , dry)	Measurement port C - Transversal distance (m)										
	-0.45	-0.25	-0.15	-0.10	-0.05	0	0.05	0.10	0.15	0.25	0.45
Mean	0.00	30.71	173.62	846.98	6751.48	6504.40	1056.95	78.26	46.28	0.64	0.00
Std. deviation	0.00	10.20	48.37	117.28	181.56	219.06	112.98	33.28	41.09	1.58	0.00
Uncertainty	123.96	123.97	124.22	125.18	128.31	129.82	125.66	124.11	124.11	123.96	123.96
5 th percentile	0.00	16.29	80.83	639.38	6300.95	6181.34	888.76	44.64	0.00	0.00	0.00
25 th percentile	0.00	23.02	149.15	738.33	6693.96	6358.25	943.81	52.97	4.32	0.00	0.00
50 th percentile	0.00	27.29	185.37	862.47	6799.54	6490.17	1109.75	63.00	41.26	0.00	0.00
75 th percentile	0.00	38.84	200.89	924.93	6878.44	6614.33	1138.27	104.16	75.12	0.00	0.00
95 th percentile	0.00	49.66	248.86	1021.12	6933.22	6984.84	1242.43	149.36	115.74	5.12	0.00
CH ₄ (mg/m ³ , dry)	Measurement port D - Transversal distance (m)										
	-0.45	-0.25	-0.15	-0.10	-0.05	0	0.05	0.10	0.15	0.25	0.45
Mean	51.52	379.19	285.89	-	25.69	275.62	813.95	-	470.70	33.27	0.00
Std. deviation	22.71	298.68	106.23	-	13.85	122.10	156.83	-	95.89	17.69	0.00
Uncertainty	124.00	131.71	124.72	-	123.98	125.10	126.07	-	124.55	123.99	123.96
5 th percentile	10.72	0.00	129.30	-	7.66	57.63	546.20	-	312.78	13.63	0.00
25 th percentile	38.91	0.00	216.38	-	12.79	211.83	701.93	-	391.94	20.94	0.00
50 th percentile	49.93	465.59	274.04	-	23.91	259.64	774.23	-	464.67	28.66	0.00
75 th percentile	57.83	606.74	340.25	-	38.89	362.66	935.20	-	550.53	40.32	0.00
95 th percentile	101.28	803.83	512.82	-	48.40	498.31	1084.20	-	626.37	73.44	0.00

CH ₄ (mg/m ³ , dry)	Measurement port E - Transversal distance (m)										
	-0.45	-0.25	-0.15	-0.10	-0.05	0	0.05	0.10	0.15	0.25	0.45
Mean	42.83	133.25	246.90	-	18.25	42.11	18.22	-	2.60	0.00	0.00
Std. deviation	17.09	43.13	52.46	-	15.36	25.73	12.10	-	5.22	0.00	0.00
Uncertainty	123.98	124.21	124.33	-	123.98	124.03	123.98	-	123.96	123.96	123.96
5 th percentile	14.18	79.79	169.11	-	0.00	0.00	0.00	-	0.00	0.00	0.00
25 th percentile	30.24	106.53	198.95	-	4.70	18.76	6.95	-	0.00	0.00	0.00
50 th percentile	43.95	121.04	245.12	-	15.68	46.42	17.43	-	0.00	0.00	0.00
75 th percentile	55.38	154.95	295.19	-	29.78	61.88	29.61	-	1.42	0.00	0.00
95 th percentile	67.11	216.05	329.29	-	46.91	77.73	34.08	-	17.68	0.00	0.00
CH ₄ (mg/m ³ , dry)	Measurement port F - Transversal distance (m)										
	-0.45	-0.30	-0.15	-0.10	-0.05	0	0.05	0.10	0.15	0.30	0.45
Mean	3.12	23.07	23.17	-	-	4.57	-	-	0.21	0.00	0.00
Std. deviation	4.76	19.03	15.35	-	-	6.18	-	-	0.80	0.00	0.00
Uncertainty	123.96	124.01	123.98	-	-	123.96	-	-	123.96	123.96	123.96
5 th percentile	0.00	0.00	6.27	-	-	0.00	-	-	0.00	0.00	0.00
25 th percentile	0.00	4.76	11.63	-	-	0.00	-	-	0.00	0.00	0.00
50 th percentile	0.80	20.32	19.90	-	-	0.00	-	-	0.00	0.00	0.00
75 th percentile	3.95	38.06	27.04	-	-	8.77	-	-	0.00	0.00	0.00
95 th percentile	13.80	56.33	60.05	-	-	17.76	-	-	2.27	0.00	0.00
CH ₄ (mg/m ³ , dry)	Measurement port G - Transversal distance (m)										
	-0.45	-0.30	-0.15	-0.10	-0.05	0	0.05	0.10	0.15	0.30	0.45
Mean	0.00	0.00	0.00	-	-	0.00	-	-	0.00	0.00	0.00
Std. deviation	0.00	0.00	0.00	-	-	0.00	-	-	0.00	0.00	0.00
Uncertainty	123.96	123.96	123.96	-	-	123.96	-	-	123.96	123.96	123.96
5 th percentile	0.00	0.00	0.00	-	-	0.00	-	-	0.00	0.00	0.00
25 th percentile	0.00	0.00	0.00	-	-	0.00	-	-	0.00	0.00	0.00
50 th percentile	0.00	0.00	0.00	-	-	0.00	-	-	0.00	0.00	0.00
75 th percentile	0.00	0.00	0.00	-	-	0.00	-	-	0.00	0.00	0.00
95 th percentile	0.00	0.00	0.00	-	-	0.00	-	-	0.00	0.00	0.00

B.4.7 Local Nitric Oxide Concentration

NO (mg/m ³ , dry)	Measurement port A - Transversal distance (m)										
	-0.45	-0.25	-0.15	-0.10	-0.05	0	0.05	0.10	0.15	0.25	0.45
Mean	295.21	352.88	391.72	263.58	345.83	552.07	437.73	344.53	456.32	544.42	421.24
Std. deviation	6.67	6.62	7.38	4.12	4.85	10.81	17.70	6.84	5.31	6.99	5.97
Uncertainty	30.56	30.57	30.57	30.55	30.56	30.59	30.63	30.57	30.55	30.57	30.56
5 th percentile	287.28	344.72	381.95	256.38	339.67	537.83	401.22	327.44	448.58	528.75	409.01
25 th percentile	290.21	347.77	385.41	259.63	342.23	542.97	427.10	343.91	452.72	541.13	419.39
50 th percentile	292.93	352.12	391.49	264.86	344.93	549.89	440.31	347.65	455.87	545.56	420.36
75 th percentile	301.73	355.30	396.00	267.04	350.44	561.80	449.79	348.95	459.39	548.78	423.82
95 th percentile	308.17	366.35	405.47	268.41	354.52	571.10	467.81	350.03	467.96	552.93	434.70
NO (mg/m ³ , dry)	Measurement port B - Transversal distance (m)										
	-0.45	-0.25	-0.15	-0.10	-0.05	0	0.05	0.10	0.15	0.25	0.45
Mean	350.44	399.74	477.20	492.97	777.11	919.31	703.43	640.74	587.00	566.60	578.21
Std. deviation	10.24	7.13	6.59	5.83	41.27	64.74	19.19	7.14	6.88	4.86	3.28
Uncertainty	30.60	30.57	30.57	30.56	31.73	33.37	30.68	30.57	30.57	30.56	30.55
5 th percentile	337.20	392.93	470.69	484.73	732.32	805.03	669.34	628.18	573.38	558.62	573.32
25 th percentile	340.66	394.57	472.52	488.66	748.81	860.92	688.19	637.46	581.20	563.69	575.59
50 th percentile	347.97	398.25	475.07	492.78	760.39	937.31	708.57	641.16	588.73	567.09	577.82
75 th percentile	360.02	401.94	479.45	495.67	798.05	978.59	716.65	643.57	592.47	569.42	581.04
95 th percentile	367.32	418.69	494.26	503.96	861.91	994.01	733.18	655.43	596.15	576.25	583.84
NO (mg/m ³ , dry)	Measurement port C - Transversal distance (m)										
	-0.45	-0.25	-0.15	-0.10	-0.05	0	0.05	0.10	0.15	0.25	0.45
Mean	320.01	371.41	414.67	313.18	222.83	401.49	427.00	568.87	525.55	510.40	487.32
Std. deviation	6.33	8.74	15.70	45.74	29.95	42.90	29.97	8.17	31.27	14.28	14.66
Uncertainty	30.56	30.59	30.66	31.29	30.87	31.53	31.03	30.58	30.90	30.66	30.66
5 th percentile	312.74	353.91	384.94	267.04	197.73	336.73	376.09	552.39	484.55	481.64	461.23
25 th percentile	315.03	369.64	404.48	279.13	209.73	374.90	405.87	566.38	491.88	502.11	473.39
50 th percentile	319.61	372.15	417.24	294.15	214.68	392.32	421.71	569.31	520.35	511.34	492.63
75 th percentile	322.36	377.37	425.65	332.06	220.24	440.24	451.42	573.17	558.24	520.13	496.07
95 th percentile	333.11	382.70	434.84	423.61	305.74	472.29	474.83	582.47	566.27	531.06	509.66
NO (mg/m ³ , dry)	Measurement port D - Transversal distance (m)										
	-0.45	-0.25	-0.15	-0.10	-0.05	0	0.05	0.10	0.15	0.25	0.45
Mean	366.16	305.98	400.27	-	334.01	458.10	570.83	-	513.10	543.79	531.05
Std. deviation	8.00	20.71	22.83	-	7.58	18.47	18.22	-	20.78	12.83	18.61
Uncertainty	30.57	30.78	30.80	-	30.57	30.65	30.66	-	30.66	30.60	30.67
5 th percentile	353.00	283.55	361.02	-	319.47	432.22	542.08	-	484.12	527.65	490.27
25 th percentile	360.70	292.00	382.02	-	328.01	438.47	557.24	-	494.71	533.53	521.78
50 th percentile	366.78	301.73	400.15	-	334.74	457.51	569.70	-	513.09	539.34	539.52
75 th percentile	370.47	310.97	421.29	-	341.34	476.50	582.60	-	526.75	556.11	545.24
95 th percentile	379.62	361.35	431.48	-	344.69	483.62	601.48	-	551.30	565.60	550.93

NO (mg/m ³ , dry)	Measurement port E - Transversal distance (m)										
	-0.45	-0.25	-0.15	-0.10	-0.05	0	0.05	0.10	0.15	0.25	0.45
Mean	311.91	349.34	338.08	-	290.47	308.58	403.83	-	440.13	448.01	428.42
Std. deviation	10.75	5.46	13.70	-	3.89	4.97	8.47	-	3.32	3.96	11.47
Uncertainty	30.58	30.56	30.59	-	30.55	30.56	30.58	-	30.55	30.55	30.61
5 th percentile	293.93	341.14	317.82	-	283.34	301.29	388.06	-	434.69	440.20	405.08
25 th percentile	304.63	344.34	328.37	-	287.78	303.66	398.20	-	437.59	445.91	423.25
50 th percentile	313.53	348.58	335.17	-	291.36	308.56	404.94	-	439.95	449.11	431.37
75 th percentile	319.41	354.96	348.36	-	293.82	312.67	411.52	-	442.22	451.00	437.79
95 th percentile	329.78	357.02	362.31	-	295.59	315.84	413.81	-	446.71	452.80	441.83
NO (mg/m ³ , dry)	Measurement port F - Transversal distance (m)										
	-0.45	-0.30	-0.15	-0.10	-0.05	0	0.05	0.10	0.15	0.30	0.45
Mean	249.71	361.30	359.48	-	-	393.22	-	-	410.27	426.03	441.13
Std. deviation	13.36	10.24	14.39	-	-	12.48	-	-	11.99	7.52	3.71
Uncertainty	30.64	30.60	30.63	-	-	30.63	-	-	30.62	30.57	30.55
5 th percentile	225.54	347.36	337.85	-	-	376.19	-	-	396.07	413.95	434.19
25 th percentile	241.29	353.10	346.43	-	-	380.34	-	-	399.22	421.32	438.15
50 th percentile	248.51	358.52	358.66	-	-	395.00	-	-	409.34	424.75	441.63
75 th percentile	260.03	368.46	371.32	-	-	400.08	-	-	418.48	431.01	443.30
95 th percentile	269.21	380.48	382.91	-	-	417.82	-	-	432.98	441.65	447.50
NO (mg/m ³ , dry)	Measurement port G - Transversal distance (m)										
	-0.45	-0.30	-0.15	-0.10	-0.05	0	0.05	0.10	0.15	0.30	0.45
Mean	327.57	399.57	426.51	-	-	408.49	-	-	405.97	407.41	428.50
Std. deviation	19.65	12.34	12.44	-	-	14.46	-	-	16.94	9.45	13.72
Uncertainty	30.65	30.59	30.61	-	-	30.62	-	-	30.65	30.59	30.64
5 th percentile	292.54	382.55	410.48	-	-	384.70	-	-	385.56	394.36	411.83
25 th percentile	309.85	388.19	418.78	-	-	395.62	-	-	391.64	400.94	415.46
50 th percentile	334.88	397.50	423.11	-	-	411.31	-	-	399.83	404.80	424.50
75 th percentile	345.25	412.74	433.55	-	-	420.39	-	-	423.11	415.53	444.10
95 th percentile	350.16	419.11	453.05	-	-	429.91	-	-	433.60	424.75	449.65

B.4.8 Total Radiative Heat Flux

Heat flux (kW/m ²)	Measurement port						
	A	B	C	D	E	F	G
Mean	137.53	149.97	166.73	175.60	162.49	130.82	107.76
Std. deviation	2.17	2.21	1.65	1.80	1.72	1.64	2.24
Uncertainty	9.26	9.85	10.65	11.07	10.45	8.93	7.82
5 th percentile	133.53	145.87	163.47	172.40	159.56	128.19	103.95
25 th percentile	136.32	148.82	165.77	174.55	161.42	129.94	105.93
50 th percentile	137.95	150.38	166.89	176.04	162.34	131.02	107.67
75 th percentile	139.19	151.59	167.83	176.83	163.86	131.79	109.25
95 th percentile	140.30	152.68	169.57	177.93	165.18	133.23	111.45

B.5 Oxy-Flame 4

B.5.1 Furnace Operating Conditions

Operating parameter	
Coal feed rate (kg/h)	56.20 ±0.24
Volume flow rate of primary stream (m ³ /h, STP)	34.47 ±1.58
O ₂ fraction of primary stream (vol%, wet)	19.30 ±1.12
CO ₂ fraction of primary stream (vol%, wet) ¹	80.70
Temperature of primary stream (°C)	22.76 ±1.24
Velocity of primary stream at burner exit (m/s) ¹	23.23
Axial momentum of primary stream at burner exit (N) ¹	0.47
Volume flow rate of secondary stream (m ³ /h, STP)	120 ±3.01
Volume flow rate of tertiary stream (m ³ /h, STP)	96 ±6.17
O ₂ fraction of secondary and tertiary stream (vol%, wet)	33 ±1.91
H ₂ O fraction of secondary and tertiary stream (vol%, wet) ¹	20.57
CO ₂ fraction of secondary and tertiary stream (vol%, wet) ¹	42.49
N ₂ fraction of secondary and tertiary stream (vol%, wet) ¹	3.80
Temperature of secondary and tertiary streams (°C)	169.90 ±1.75
Secondary/tertiary mass flow ratio ¹	1.25
Swirl number of secondary stream ¹	2.05
Stoichiometric ratio ¹	1.17
Overall heat input (kW) ¹	354.70
Sensible heat input (kW) ¹	15.20
Flue gas	
O ₂ (vol%, dry)	6.39 ±0.83
CO ₂ (vol%, dry)	85.92 ±1.05
N ₂ (vol%, dry) ¹	7.69
H ₂ O (vol% wet)	29.37 ±0.19
Volume flow rate at furnace exit (m ³ /h, STP)	306.60 ±5.30
Volume flow rate of recycled flue gas (m ³ /h, STP)	142.84 ±3.57
Temperature at furnace exit (°C)	481.50 ±3.33
Recycle ratio ¹	0.47
Outer wall surface temperature at the vertical section (°C)	199.03 ±1.86
Inner surface temperature of the cylindrical section (°C)	919.92 ±4.33

¹calculated value

B.5.2 Local Gas Temperature

Temperature (°C)	Measurement port A - Transversal distance (m)										
	-0.45	-0.25	-0.15	-0.10	-0.05	0	0.05	0.10	0.15	0.25	0.45
Mean	945	1043	1039	869	582	1081	914	975	943	1066	1054
Std. deviation	9.39	2.46	2.27	5.87	8.46	28.51	2.87	3.73	2.06	6.92	2.74
Uncertainty	23.76	26.07	25.97	21.85	15.17	27.39	22.93	24.42	23.62	26.68	26.35
5 th percentile	926	1039	1035	860	572	1034	911	969	939	1055	1050
25 th percentile	941	1041	1038	865	576	1059	912	972	942	1061	1052
50 th percentile	946	1043	1039	868	579	1087	914	976	944	1067	1054
75 th percentile	953	1045	1040	871	589	1106	916	978	944	1072	1057
95 th percentile	959	1046	1042	879	597	1118	920	981	946	1076	1058
Temperature (°C)	Measurement port B - Transversal distance (m)										
	-0.45	-0.25	-0.15	-0.10	-0.05	0	0.05	0.10	0.15	0.25	0.45
Mean	946	968	882	957	1257	893	1288	1190	1162	1166	1123
Std. deviation	3.07	13.25	2.27	6.55	4.60	13.45	3.23	6.30	6.62	5.35	6.08
Uncertainty	23.71	24.40	22.15	24.02	31.45	22.53	32.22	29.77	29.09	29.16	28.08
5 th percentile	941	956	878	946	1251	872	1281	1179	1147	1157	1115
25 th percentile	944	959	881	952	1254	883	1286	1186	1159	1162	1120
50 th percentile	947	962	883	957	1256	892	1288	1190	1163	1167	1121
75 th percentile	949	977	884	962	1260	903	1290	1193	1167	1171	1125
95 th percentile	950	996	885	966	1266	915	1292	1200	1171	1173	1137
Temperature (°C)	Measurement port C - Transversal distance (m)										
	-0.45	-0.25	-0.15	-0.10	-0.05	0	0.05	0.10	0.15	0.25	0.45
Mean	1030	1097	1129	1184	1242	1171	1256	1243	1187	1112	1057
Std. deviation	3.31	4.43	3.34	1.94	4.35	7.89	6.42	6.29	3.84	7.04	2.65
Uncertainty	25.76	27.43	28.21	29.58	31.07	29.31	31.44	31.09	29.66	27.81	26.43
5 th percentile	1026	1091	1123	1181	1233	1159	1246	1232	1182	1103	1053
25 th percentile	1027	1094	1127	1182	1240	1166	1250	1239	1184	1106	1056
50 th percentile	1031	1096	1129	1184	1242	1169	1257	1243	1186	1113	1057
75 th percentile	1033	1100	1131	1185	1246	1176	1262	1248	1190	1118	1059
95 th percentile	1035	1104	1133	1187	1247	1186	1264	1252	1193	1123	1061
Temperature (°C)	Measurement port D - Transversal distance (m)										
	-0.45	-0.25	-0.15	-0.10	-0.05	0	0.05	0.10	0.15	0.25	0.45
Mean	1066	1235	1221	-	1168	1148	1212	-	1250	1223	1091
Std. deviation	3.23	7.07	5.26	-	3.81	9.65	3.78	-	2.47	3.19	3.96
Uncertainty	26.18	30.30	29.92	-	28.64	28.23	29.71	-	30.63	29.97	26.78
5 th percentile	1060	1224	1212	-	1163	1128	1205	-	1246	1217	1084
25 th percentile	1065	1229	1218	-	1166	1141	1210	-	1248	1221	1088
50 th percentile	1066	1238	1221	-	1168	1152	1212	-	1251	1223	1091
75 th percentile	1067	1240	1224	-	1169	1155	1214	-	1252	1226	1093
95 th percentile	1071	1244	1229	-	1174	1160	1217	-	1254	1228	1098

Temperature (°C)	Measurement port E - Transversal distance (m)										
	-0.45	-0.25	-0.15	-0.10	-0.05	0	0.05	0.10	0.15	0.25	0.45
Mean	976	1168	1145	-	991	1105	1172	-	1182	1091	1006
Std. deviation	7.53	4.88	6.03	-	10.43	7.03	4.52	-	6.24	7.50	2.48
Uncertainty	24.08	28.64	28.12	-	24.43	27.15	28.76	-	29.02	26.81	24.73
5 th percentile	965	1161	1136	-	976	1091	1164	-	1171	1080	1002
25 th percentile	969	1164	1140	-	982	1099	1170	-	1178	1086	1004
50 th percentile	978	1167	1146	-	990	1108	1173	-	1184	1092	1006
75 th percentile	981	1171	1149	-	998	1110	1175	-	1187	1097	1008
95 th percentile	986	1178	1156	-	1009	1112	1178	-	1191	1104	1009
Temperature (°C)	Measurement port F - Transversal distance (m)										
	-0.45	-0.30	-0.15	-0.10	-0.05	0	0.05	0.10	0.15	0.30	0.45
Mean	1047	1200	1244	-	-	1181	-	-	1116	1067	1032
Std. deviation	16.80	6.59	8.04	-	-	7.87	-	-	5.26	7.11	1.52
Uncertainty	26.08	29.45	30.51	-	-	29.01	-	-	27.41	26.23	25.35
5 th percentile	1019	1190	1231	-	-	1166	-	-	1105	1060	1030
25 th percentile	1039	1194	1238	-	-	1175	-	-	1113	1062	1031
50 th percentile	1049	1200	1245	-	-	1181	-	-	1117	1065	1032
75 th percentile	1063	1206	1250	-	-	1188	-	-	1119	1069	1033
95 th percentile	1071	1209	1259	-	-	1191	-	-	1125	1085	1034
Temperature (°C)	Measurement port G - Transversal distance (m)										
	-0.45	-0.30	-0.15	-0.10	-0.05	0	0.05	0.10	0.15	0.30	0.45
Mean	1004	1041	1107	-	-	1089	-	-	1055	1018	1004
Std. deviation	0.74	1.20	11.38	-	-	3.91	-	-	2.88	2.12	0.74
Uncertainty	24.67	25.57	27.25	-	-	26.75	-	-	25.92	25.01	24.67
5 th percentile	1003	1039	1086	-	-	1084	-	-	1052	1015	1003
25 th percentile	1003	1040	1098	-	-	1085	-	-	1053	1016	1003
50 th percentile	1004	1041	1109	-	-	1090	-	-	1054	1017	1004
75 th percentile	1005	1042	1116	-	-	1093	-	-	1058	1020	1005
95 th percentile	1005	1043	1122	-	-	1095	-	-	1060	1021	1005

B.5.3 Local Oxygen Concentration

O ₂ (vol%, dry)	Measurement port A - Transversal distance (m)										
	-0.45	-0.25	-0.15	-0.10	-0.05	0	0.05	0.10	0.15	0.25	0.45
Mean	14.78	13.53	13.49	42.21	39.10	28.83	40.22	32.51	16.82	11.82	5.40
Std. deviation	1.20	1.47	0.45	0.37	0.31	0.52	0.24	0.44	0.58	0.77	0.38
Uncertainty	0.64	0.64	0.60	0.59	0.59	0.59	0.59	0.59	0.60	0.61	0.60
5 th percentile	13.47	10.87	12.92	41.51	38.64	27.78	39.81	31.89	15.91	10.64	4.64
25 th percentile	13.70	13.17	13.09	41.99	38.77	28.57	40.01	32.11	16.38	11.28	5.24
50 th percentile	14.53	13.77	13.36	42.15	39.23	28.79	40.30	32.52	16.69	11.93	5.49
75 th percentile	15.39	14.15	13.92	42.53	39.32	29.07	40.42	32.85	17.21	12.43	5.67
95 th percentile	17.23	16.14	14.31	42.79	39.52	29.87	40.54	33.23	17.79	13.16	5.93
O ₂ (vol%, dry)	Measurement port B - Transversal distance (m)										
	-0.45	-0.25	-0.15	-0.10	-0.05	0	0.05	0.10	0.15	0.25	0.45
Mean	17.90	24.51	23.15	18.57	3.97	1.90	16.77	20.45	15.34	12.32	13.36
Std. deviation	1.40	0.52	1.44	0.96	1.11	0.47	0.75	0.84	1.02	0.31	0.51
Uncertainty	0.64	0.60	0.66	0.62	0.62	0.60	0.61	0.61	0.62	0.59	0.60
5 th percentile	15.47	23.47	20.16	17.00	2.72	1.36	15.66	18.55	13.91	11.83	12.53
25 th percentile	16.50	24.20	23.00	17.99	3.15	1.52	16.04	20.15	14.61	12.02	12.90
50 th percentile	18.51	24.38	23.46	18.45	3.68	1.75	16.73	20.52	15.12	12.37	13.28
75 th percentile	19.11	24.98	24.24	19.41	4.60	2.26	17.42	21.10	16.34	12.65	13.85
95 th percentile	19.48	25.32	24.75	20.04	6.22	2.67	17.90	21.50	17.21	12.74	14.04
O ₂ (vol%, dry)	Measurement port C - Transversal distance (m)										
	-0.45	-0.25	-0.15	-0.10	-0.05	0	0.05	0.10	0.15	0.25	0.45
Mean	15.10	13.68	9.33	0.52	0.85	0.39	3.46	5.82	7.01	10.39	15.86
Std. deviation	0.88	1.14	0.79	0.15	0.04	0.03	1.23	0.76	0.88	0.89	0.48
Uncertainty	0.63	0.62	0.61	0.59	0.59	0.59	0.63	0.61	0.61	0.60	0.59
5 th percentile	13.96	11.65	8.09	0.32	0.81	0.33	2.10	4.66	5.86	8.89	15.01
25 th percentile	14.33	13.04	8.83	0.38	0.82	0.36	2.65	5.29	6.30	9.81	15.63
50 th percentile	15.02	13.75	9.19	0.48	0.85	0.39	2.93	5.81	6.67	10.40	15.87
75 th percentile	15.80	14.51	9.87	0.67	0.88	0.41	4.09	6.16	7.73	11.06	16.23
95 th percentile	16.59	15.33	10.93	0.75	0.92	0.44	6.24	7.48	8.61	11.70	16.54
O ₂ (vol%, dry)	Measurement port D - Transversal distance (m)										
	-0.45	-0.25	-0.15	-0.10	-0.05	0	0.05	0.10	0.15	0.25	0.45
Mean	1.60	1.18	3.52	-	7.04	1.26	0.79	-	2.96	7.38	15.42
Std. deviation	0.31	0.36	0.58	-	0.60	0.22	0.30	-	0.62	0.67	1.04
Uncertainty	0.59	0.59	0.60	-	0.60	0.59	0.59	-	0.60	0.60	0.61
5 th percentile	1.17	0.64	2.58	-	6.13	0.89	0.51	-	1.96	6.17	14.00
25 th percentile	1.37	0.84	3.05	-	6.50	1.11	0.57	-	2.51	6.95	14.72
50 th percentile	1.60	1.14	3.58	-	7.04	1.27	0.63	-	2.94	7.40	15.14
75 th percentile	1.70	1.46	4.07	-	7.48	1.43	0.96	-	3.44	7.86	15.86
95 th percentile	2.23	1.77	4.35	-	8.08	1.63	1.40	-	4.12	8.59	17.60

O ₂ (vol%, dry)	Measurement port E - Transversal distance (m)										
	-0.45	-0.25	-0.15	-0.10	-0.05	0	0.05	0.10	0.15	0.25	0.45
Mean	4.99	6.20	6.49	-	7.79	7.56	6.98	-	11.53	13.33	18.74
Std. deviation	0.87	1.15	0.95	-	0.55	0.76	0.72	-	0.90	0.95	0.36
Uncertainty	0.60	0.62	0.61	-	0.60	0.60	0.60	-	0.61	0.61	0.59
5 th percentile	3.57	4.42	5.18	-	7.00	6.26	6.04	-	9.79	12.09	18.28
25 th percentile	4.42	5.41	5.95	-	7.37	7.21	6.33	-	10.90	12.49	18.48
50 th percentile	5.06	5.88	6.33	-	7.62	7.45	6.77	-	11.64	13.09	18.63
75 th percentile	5.49	7.37	6.92	-	8.40	7.87	7.74	-	12.32	14.04	18.92
95 th percentile	6.60	7.91	8.41	-	8.59	9.30	8.11	-	12.80	15.08	19.47
O ₂ (vol%, dry)	Measurement port F - Transversal distance (m)										
	-0.45	-0.30	-0.15	-0.10	-0.05	0	0.05	0.10	0.15	0.30	0.45
Mean	5.28	2.83	5.00	-	-	9.09	-	-	13.28	15.69	16.53
Std. deviation	0.80	0.41	0.81	-	-	0.97	-	-	0.96	0.69	0.89
Uncertainty	0.60	0.59	0.61	-	-	0.61	-	-	0.60	0.60	0.60
5 th percentile	4.24	1.87	3.70	-	-	7.28	-	-	11.13	14.39	14.87
25 th percentile	4.54	2.67	4.37	-	-	8.48	-	-	12.78	15.26	16.14
50 th percentile	5.07	2.89	4.93	-	-	9.22	-	-	13.49	15.75	16.43
75 th percentile	6.05	3.04	5.60	-	-	9.69	-	-	14.01	16.10	17.00
95 th percentile	6.69	3.48	6.36	-	-	10.71	-	-	14.53	16.77	17.99
O ₂ (vol%, dry)	Measurement port G - Transversal distance (m)										
	-0.45	-0.30	-0.15	-0.10	-0.05	0	0.05	0.10	0.15	0.30	0.45
Mean	7.32	6.21	6.10	-	-	8.48	-	-	9.43	10.84	10.86
Std. deviation	0.46	0.71	0.46	-	-	0.56	-	-	0.45	0.61	0.47
Uncertainty	0.60	0.60	0.59	-	-	0.60	-	-	0.59	0.60	0.60
5 th percentile	6.51	4.85	5.41	-	-	7.55	-	-	8.60	9.64	10.11
25 th percentile	6.96	5.87	5.75	-	-	8.02	-	-	9.13	10.50	10.47
50 th percentile	7.48	6.35	6.08	-	-	8.51	-	-	9.45	10.87	10.89
75 th percentile	7.69	6.65	6.52	-	-	8.87	-	-	9.77	11.27	11.22
95 th percentile	7.85	7.50	6.89	-	-	9.36	-	-	10.09	11.65	11.53

B.5.4 Local Carbon Dioxide Concentration

CO ₂ (vol%, dry)	Measurement port A - Transversal distance (m)										
	-0.45	-0.25	-0.15	-0.10	-0.05	0	0.05	0.10	0.15	0.25	0.45
Mean	80.31	83.43	83.34	52.77	56.35	67.28	55.17	63.29	79.93	85.75	94.81
Std. deviation	1.34	1.63	0.40	0.52	0.29	0.57	0.22	0.46	0.81	0.90	0.51
Uncertainty	1.64	1.66	1.64	1.46	1.47	1.54	1.47	1.51	1.62	1.66	1.72
5 th percentile	77.59	80.61	82.61	52.00	55.94	66.19	54.86	62.52	78.42	84.25	94.10
25 th percentile	79.72	82.71	82.93	52.25	56.14	67.00	54.99	62.88	79.32	85.16	94.47
50 th percentile	80.49	83.18	83.49	52.84	56.25	67.29	55.12	63.29	80.10	85.67	94.72
75 th percentile	81.44	83.82	83.65	53.15	56.65	67.57	55.36	63.71	80.55	86.38	95.07
95 th percentile	81.89	86.45	83.92	53.67	56.79	68.42	55.51	63.92	80.95	87.34	95.75
CO ₂ (vol%, dry)	Measurement port B - Transversal distance (m)										
	-0.45	-0.25	-0.15	-0.10	-0.05	0	0.05	0.10	0.15	0.25	0.45
Mean	78.47	71.71	73.29	78.47	90.32	86.52	80.41	76.43	82.02	85.26	83.94
Std. deviation	1.48	0.58	1.62	1.10	0.73	0.41	0.81	0.93	1.13	0.38	0.61
Uncertainty	1.62	1.56	1.61	1.62	1.69	1.66	1.62	1.60	1.64	1.65	1.64
5 th percentile	76.89	70.84	71.51	76.78	88.91	85.82	79.15	75.29	79.97	84.74	83.12
25 th percentile	77.18	71.19	71.99	77.49	89.94	86.17	79.68	75.74	81.00	84.90	83.33
50 th percentile	77.91	71.80	73.07	78.69	90.48	86.51	80.49	76.37	82.23	85.22	84.03
75 th percentile	79.88	72.04	73.49	79.23	90.77	86.80	81.12	76.71	82.90	85.62	84.46
95 th percentile	81.01	72.86	76.64	80.28	91.30	87.31	81.66	78.49	83.61	85.88	84.92
CO ₂ (vol%, dry)	Measurement port C - Transversal distance (m)										
	-0.45	-0.25	-0.15	-0.10	-0.05	0	0.05	0.10	0.15	0.25	0.45
Mean	82.20	83.74	88.18	85.84	76.65	81.06	93.17	89.39	90.55	87.01	82.20
Std. deviation	1.04	1.31	0.71	1.51	0.33	0.79	1.09	2.00	0.97	1.03	1.04
Uncertainty	1.65	1.65	1.67	1.68	1.59	1.63	1.72	1.72	1.69	1.67	1.65
5 th percentile	80.60	82.01	86.64	83.73	76.16	79.85	90.36	84.20	88.65	85.50	80.60
25 th percentile	81.34	82.74	87.77	84.63	76.33	80.51	92.96	89.18	89.84	86.31	81.34
50 th percentile	82.33	83.60	88.34	85.73	76.68	81.10	93.64	89.86	90.93	87.07	82.33
75 th percentile	83.16	84.50	88.67	87.06	76.85	81.51	93.89	90.57	91.33	87.71	83.16
95 th percentile	83.65	86.16	89.30	88.15	77.17	82.54	94.12	91.42	91.65	88.80	83.65
CO ₂ (vol%, dry)	Measurement port D - Transversal distance (m)										
	-0.45	-0.25	-0.15	-0.10	-0.05	0	0.05	0.10	0.15	0.25	0.45
Mean	89.80	93.40	93.57	-	90.75	88.70	88.09	-	92.40	90.10	81.54
Std. deviation	0.72	0.54	0.68	-	0.67	0.89	0.71	-	0.50	0.67	1.15
Uncertainty	1.69	1.71	1.71	-	1.69	1.68	1.67	-	1.70	1.69	1.63
5 th percentile	88.42	92.62	92.60	-	89.63	87.05	86.99	-	91.40	88.86	79.12
25 th percentile	89.36	92.90	92.90	-	90.25	88.15	87.48	-	92.13	89.57	81.12
50 th percentile	89.79	93.38	93.62	-	90.64	88.94	88.15	-	92.56	90.16	81.76
75 th percentile	90.55	93.97	94.24	-	91.38	89.37	88.55	-	92.74	90.53	82.32
95 th percentile	90.77	94.13	94.65	-	91.80	89.91	89.46	-	92.92	91.25	83.09

CO ₂ (vol%, dry)	Measurement port E - Transversal distance (m)										
	-0.45	-0.25	-0.15	-0.10	-0.05	0	0.05	0.10	0.15	0.25	0.45
Mean	90.11	90.33	89.98	-	90.94	90.68	89.89	-	85.38	83.64	77.72
Std. deviation	0.96	1.13	0.74	-	0.63	0.88	0.76	-	0.92	1.09	0.41
Uncertainty	1.69	1.69	1.69	-	1.69	1.69	1.69	-	1.66	1.65	1.60
5 th percentile	88.38	88.68	88.32	-	89.96	88.61	88.74	-	84.03	81.65	76.88
25 th percentile	89.54	89.16	89.61	-	90.26	90.38	89.23	-	84.61	82.87	77.56
50 th percentile	90.12	90.71	90.14	-	91.12	90.93	89.77	-	85.31	83.96	77.81
75 th percentile	90.73	91.26	90.53	-	91.44	91.07	90.65	-	86.08	84.56	78.03
95 th percentile	91.72	91.83	90.92	-	91.84	91.97	91.01	-	87.03	85.03	78.25
CO ₂ (vol%, dry)	Measurement port F - Transversal distance (m)										
	-0.45	-0.30	-0.15	-0.10	-0.05	0	0.05	0.10	0.15	0.30	0.45
Mean	82.93	93.57	91.86	-	-	88.13	-	-	83.68	80.99	79.98
Std. deviation	2.20	0.29	0.66	-	-	1.05	-	-	1.06	0.80	0.98
Uncertainty	1.66	1.71	1.70	-	-	1.68	-	-	1.64	1.62	1.62
5 th percentile	79.12	92.81	90.56	-	-	86.50	-	-	82.32	79.79	78.43
25 th percentile	81.62	93.46	91.47	-	-	87.49	-	-	82.88	80.53	79.48
50 th percentile	83.18	93.60	91.93	-	-	87.98	-	-	83.45	80.92	80.06
75 th percentile	84.76	93.76	92.33	-	-	88.87	-	-	84.25	81.41	80.42
95 th percentile	85.68	93.95	92.91	-	-	90.03	-	-	86.08	82.52	81.77
CO ₂ (vol%, dry)	Measurement port G - Transversal distance (m)										
	-0.45	-0.30	-0.15	-0.10	-0.05	0	0.05	0.10	0.15	0.30	0.45
Mean	81.35	91.19	91.58	-	-	89.09	-	-	87.92	86.38	86.34
Std. deviation	1.00	0.84	0.43	-	-	0.72	-	-	0.55	0.68	0.56
Uncertainty	1.64	1.70	1.69	-	-	1.68	-	-	1.67	1.66	1.66
5 th percentile	79.62	89.43	90.78	-	-	87.78	-	-	87.14	85.47	85.49
25 th percentile	80.64	90.76	91.26	-	-	88.58	-	-	87.52	85.86	85.90
50 th percentile	81.48	91.16	91.57	-	-	89.07	-	-	87.89	86.33	86.32
75 th percentile	81.90	91.69	91.87	-	-	89.67	-	-	88.24	86.78	86.80
95 th percentile	82.95	92.61	92.32	-	-	90.19	-	-	88.90	87.70	87.25

B.5.5 Local Carbon Monoxide Concentration

CO (vol%, dry)	Measurement port A - Transversal distance (m)										
	-0.45	-0.25	-0.15	-0.10	-0.05	0	0.05	0.10	0.15	0.25	0.45
Mean	0.01	0.01	0.01	0.01	0.07	0.15	0.05	0.02	0.07	0.02	0.01
Std. deviation	0.00	0.00	0.00	0.00	0.00	0.01	0.00	0.00	0.02	0.00	0.00
Uncertainty	0.35	0.35	0.35	0.35	0.35	0.35	0.35	0.35	0.35	0.35	0.35
5 th percentile	0.00	0.00	0.00	0.01	0.07	0.15	0.05	0.01	0.04	0.01	0.00
25 th percentile	0.01	0.00	0.01	0.01	0.07	0.15	0.05	0.01	0.06	0.01	0.00
50 th percentile	0.01	0.01	0.01	0.01	0.07	0.15	0.05	0.02	0.08	0.02	0.01
75 th percentile	0.01	0.01	0.01	0.02	0.07	0.16	0.05	0.02	0.08	0.02	0.01
95 th percentile	0.01	0.01	0.01	0.02	0.08	0.16	0.05	0.02	0.09	0.02	0.01
CO (vol%, dry)	Measurement port B - Transversal distance (m)										
	-0.45	-0.25	-0.15	-0.10	-0.05	0	0.05	0.10	0.15	0.25	0.45
Mean	0.01	0.02	0.03	0.13	4.45	9.86	0.24	0.05	0.03	0.01	0.01
Std. deviation	0.00	0.00	0.00	0.05	0.71	0.59	0.07	0.02	0.02	0.00	0.01
Uncertainty	0.35	0.35	0.35	0.35	0.37	0.37	0.35	0.35	0.35	0.35	0.35
5 th percentile	0.01	0.02	0.03	0.06	3.32	8.71	0.16	0.04	0.02	0.01	0.01
25 th percentile	0.01	0.02	0.03	0.09	3.98	9.58	0.19	0.04	0.02	0.01	0.01
50 th percentile	0.01	0.02	0.03	0.12	4.41	9.95	0.24	0.04	0.03	0.01	0.01
75 th percentile	0.01	0.02	0.04	0.15	5.11	10.36	0.28	0.06	0.04	0.01	0.01
95 th percentile	0.01	0.02	0.04	0.24	5.59	10.51	0.38	0.10	0.07	0.01	0.03
CO (vol%, dry)	Measurement port C - Transversal distance (m)										
	-0.45	-0.25	-0.15	-0.10	-0.05	0	0.05	0.10	0.15	0.25	0.45
Mean	0.03	0.06	0.56	11.21	16.39	14.19	1.83	0.39	0.22	0.03	0.01
Std. deviation	0.03	0.06	0.31	1.34	0.27	0.57	0.49	0.11	0.08	0.02	0.00
Uncertainty	0.35	0.35	0.36	0.43	0.36	0.37	0.36	0.35	0.35	0.35	0.35
5 th percentile	0.02	0.01	0.22	9.13	15.91	13.14	1.14	0.17	0.09	0.01	0.01
25 th percentile	0.02	0.02	0.36	10.11	16.25	13.88	1.45	0.30	0.16	0.02	0.01
50 th percentile	0.02	0.02	0.47	11.29	16.39	14.10	1.76	0.39	0.21	0.02	0.01
75 th percentile	0.03	0.09	0.64	12.31	16.64	14.58	2.18	0.47	0.31	0.04	0.01
95 th percentile	0.11	0.17	1.35	13.07	16.75	15.08	2.67	0.55	0.35	0.07	0.01
CO (vol%, dry)	Measurement port D - Transversal distance (m)										
	-0.45	-0.25	-0.15	-0.10	-0.05	0	0.05	0.10	0.15	0.25	0.45
Mean	2.87	3.36	1.03	-	0.23	7.55	8.55	-	2.70	0.29	0.02
Std. deviation	0.46	0.84	0.18	-	0.11	0.88	0.72	-	0.35	0.11	0.01
Uncertainty	0.36	0.38	0.35	-	0.35	0.37	0.37	-	0.35	0.35	0.35
5 th percentile	2.22	2.04	0.67	-	0.10	6.27	7.07	-	2.18	0.16	0.01
25 th percentile	2.48	2.56	0.94	-	0.15	6.93	8.17	-	2.43	0.20	0.01
50 th percentile	2.86	3.41	1.00	-	0.20	7.37	8.65	-	2.72	0.26	0.01
75 th percentile	3.21	4.14	1.17	-	0.28	8.07	9.07	-	2.96	0.36	0.03
95 th percentile	3.76	4.62	1.32	-	0.45	9.23	9.50	-	3.29	0.52	0.05

CO (vol%, dry)	Measurement port E - Transversal distance (m)										
	-0.45	-0.25	-0.15	-0.10	-0.05	0	0.05	0.10	0.15	0.25	0.45
Mean	0.79	0.75	1.07	-	0.04	0.26	1.18	-	0.49	0.18	0.01
Std. deviation	0.38	0.38	0.58	-	0.02	0.21	0.50	-	0.14	0.05	0.00
Uncertainty	0.35	0.36	0.37	-	0.35	0.35	0.36	-	0.35	0.35	0.35
5 th percentile	0.41	0.29	0.31	-	0.02	0.09	0.57	-	0.33	0.11	0.00
25 th percentile	0.53	0.42	0.63	-	0.03	0.12	0.86	-	0.38	0.15	0.01
50 th percentile	0.72	0.69	0.88	-	0.04	0.17	1.08	-	0.45	0.17	0.01
75 th percentile	0.88	1.13	1.59	-	0.05	0.33	1.33	-	0.57	0.22	0.01
95 th percentile	1.73	1.38	2.07	-	0.09	0.78	2.34	-	0.80	0.26	0.01
CO (vol%, dry)	Measurement port F - Transversal distance (m)										
	-0.45	-0.30	-0.15	-0.10	-0.05	0	0.05	0.10	0.15	0.30	0.45
Mean	0.63	1.66	1.21	-	-	0.38	-	-	0.03	0.01	0.01
Std. deviation	0.25	0.57	0.38	-	-	0.11	-	-	0.03	0.00	0.00
Uncertainty	0.35	0.36	0.36	-	-	0.35	-	-	0.35	0.35	0.35
5 th percentile	0.22	1.05	0.68	-	-	0.16	-	-	0.01	0.00	0.00
25 th percentile	0.37	1.29	0.82	-	-	0.34	-	-	0.01	0.00	0.00
50 th percentile	0.67	1.50	1.22	-	-	0.39	-	-	0.01	0.01	0.01
75 th percentile	0.82	1.89	1.56	-	-	0.48	-	-	0.03	0.01	0.01
95 th percentile	1.01	3.17	1.76	-	-	0.53	-	-	0.08	0.01	0.02
CO (vol%, dry)	Measurement port G - Transversal distance (m)										
	-0.45	-0.30	-0.15	-0.10	-0.05	0	0.05	0.10	0.15	0.30	0.45
Mean	0.04	0.10	0.09	-	-	0.02	-	-	0.01	0.01	0.01
Std. deviation	0.02	0.08	0.06	-	-	0.01	-	-	0.00	0.00	0.01
Uncertainty	0.35	0.35	0.35	-	-	0.35	-	-	0.35	0.35	0.35
5 th percentile	0.02	0.02	0.04	-	-	0.01	-	-	0.00	0.00	0.00
25 th percentile	0.02	0.04	0.05	-	-	0.01	-	-	0.01	0.01	0.01
50 th percentile	0.04	0.07	0.07	-	-	0.02	-	-	0.01	0.01	0.01
75 th percentile	0.06	0.14	0.13	-	-	0.03	-	-	0.01	0.01	0.01
95 th percentile	0.07	0.28	0.22	-	-	0.05	-	-	0.01	0.01	0.02

B.5.6 Local Methane Concentration

CH ₄ (mg/m ³ , dry)	Measurement port A - Transversal distance (m)										
	-0.45	-0.25	-0.15	-0.10	-0.05	0	0.05	0.10	0.15	0.25	0.45
Mean	0.00	0.00	0.00	0.08	0.00	0.00	0.00	0.00	0.19	0.00	0.00
Std. deviation	0.00	0.00	0.00	0.27	0.00	0.00	0.00	0.00	0.69	0.00	0.00
Uncertainty	123.96	123.96	123.96	123.96	123.96	123.96	123.96	123.96	123.96	123.96	123.96
5 th percentile	0.00	0.00	0.00	0.00	0.00	0.00	0.00	0.00	0.00	0.00	0.00
25 th percentile	0.00	0.00	0.00	0.00	0.00	0.00	0.00	0.00	0.00	0.00	0.00
50 th percentile	0.00	0.00	0.00	0.00	0.00	0.00	0.00	0.00	0.00	0.00	0.00
75 th percentile	0.00	0.00	0.00	0.00	0.00	0.00	0.00	0.00	0.00	0.00	0.00
95 th percentile	0.00	0.00	0.00	0.54	0.00	0.00	0.00	0.00	2.30	0.00	0.00
CH ₄ (mg/m ³ , dry)	Measurement port B - Transversal distance (m)										
	-0.45	-0.25	-0.15	-0.10	-0.05	0	0.05	0.10	0.15	0.25	0.45
Mean	0.00	0.00	0.00	0.00	288.80	1761.52	0.00	0.00	0.00	0.00	0.00
Std. deviation	0.00	0.00	0.00	0.00	81.48	113.16	0.00	0.00	0.00	0.00	0.00
Uncertainty	123.96	123.96	123.96	123.96	124.69	125.68	123.96	123.96	123.96	123.96	123.96
5 th percentile	0.00	0.00	0.00	0.00	167.72	1534.20	0.00	0.00	0.00	0.00	0.00
25 th percentile	0.00	0.00	0.00	0.00	232.90	1695.46	0.00	0.00	0.00	0.00	0.00
50 th percentile	0.00	0.00	0.00	0.00	260.97	1780.09	0.00	0.00	0.00	0.00	0.00
75 th percentile	0.00	0.00	0.00	0.00	346.98	1834.15	0.00	0.00	0.00	0.00	0.00
95 th percentile	0.00	0.00	0.00	0.00	450.22	1908.66	0.00	0.00	0.00	0.00	0.00
CH ₄ (mg/m ³ , dry)	Measurement port C - Transversal distance (m)										
	-0.45	-0.25	-0.15	-0.10	-0.05	0	0.05	0.10	0.15	0.25	0.45
Mean	0.00	0.00	5.74	1134.73	7392.89	4545.95	72.65	0.47	0.33	0.00	0.00
Std. deviation	0.00	0.00	12.13	181.79	0.04	423.51	36.30	0.84	1.07	0.00	0.00
Uncertainty	123.96	123.96	123.98	128.51	123.96	145.60	124.13	123.96	123.96	123.96	123.96
5 th percentile	0.00	0.00	0.00	820.26	7392.80	3836.54	25.63	0.00	0.00	0.00	0.00
25 th percentile	0.00	0.00	0.00	964.42	7392.86	4212.24	41.19	0.00	0.00	0.00	0.00
50 th percentile	0.00	0.00	0.00	1198.05	7392.89	4610.72	62.23	0.00	0.00	0.00	0.00
75 th percentile	0.00	0.00	4.58	1282.88	7392.91	4880.03	101.56	0.37	0.00	0.00	0.00
95 th percentile	0.00	0.00	41.94	1356.48	7392.95	5175.12	137.43	2.40	3.08	0.00	0.00
CH ₄ (mg/m ³ , dry)	Measurement port D - Transversal distance (m)										
	-0.45	-0.25	-0.15	-0.10	-0.05	0	0.05	0.10	0.15	0.25	0.45
Mean	48.79	203.87	74.27	-	36.68	1648.47	1326.54	-	143.57	0.81	0.00
Std. deviation	23.48	75.18	19.63	-	29.51	296.92	271.66	-	36.37	2.40	0.00
Uncertainty	124.03	124.72	124.01	-	124.04	130.56	130.41	-	124.08	123.96	123.96
5 th percentile	20.29	84.98	47.12	-	8.83	1244.97	846.76	-	87.49	0.00	0.00
25 th percentile	31.07	144.81	59.78	-	19.19	1419.17	1129.10	-	119.03	0.00	0.00
50 th percentile	43.65	200.15	66.68	-	24.74	1595.79	1399.12	-	140.16	0.00	0.00
75 th percentile	59.51	269.90	91.96	-	48.68	1862.64	1530.73	-	166.00	0.00	0.00
95 th percentile	102.37	320.42	107.25	-	107.43	2190.19	1724.01	-	223.43	7.44	0.00

CH ₄ (mg/m ³ , dry)	Measurement port E - Transversal distance (m)										
	-0.45	-0.25	-0.15	-0.10	-0.05	0	0.05	0.10	0.15	0.25	0.45
Mean	1.40	8.81	50.46	-	0.00	15.00	93.81	-	3.58	0.00	0.00
Std. deviation	3.22	14.34	45.81	-	0.00	27.38	69.08	-	5.43	0.00	0.00
Uncertainty	123.96	123.98	124.24	-	123.96	124.05	124.53	-	123.96	123.96	123.96
5 th percentile	0.00	0.00	0.00	-	0.00	0.00	17.81	-	0.00	0.00	0.00
25 th percentile	0.00	0.00	10.32	-	0.00	0.00	44.19	-	0.00	0.00	0.00
50 th percentile	0.00	0.00	38.14	-	0.00	0.30	81.06	-	0.35	0.00	0.00
75 th percentile	0.00	9.02	81.88	-	0.00	19.68	107.50	-	4.94	0.00	0.00
95 th percentile	8.62	42.42	133.97	-	0.00	88.12	255.90	-	16.12	0.00	0.00
CH ₄ (mg/m ³ , dry)	Measurement port F - Transversal distance (m)										
	-0.45	-0.30	-0.15	-0.10	-0.05	0	0.05	0.10	0.15	0.30	0.45
Mean	0.22	14.23	10.03	-	-	0.45	-	-	0.00	0.00	0.00
Std. deviation	1.02	25.37	10.42	-	-	1.16	-	-	0.00	0.00	0.00
Uncertainty	123.96	124.01	123.97	-	-	123.96	-	-	123.96	123.96	123.96
5 th percentile	0.00	0.00	0.00	-	-	0.00	-	-	0.00	0.00	0.00
25 th percentile	0.00	1.64	0.00	-	-	0.00	-	-	0.00	0.00	0.00
50 th percentile	0.00	5.56	5.48	-	-	0.00	-	-	0.00	0.00	0.00
75 th percentile	0.00	16.03	20.86	-	-	0.00	-	-	0.00	0.00	0.00
95 th percentile	1.58	78.74	27.34	-	-	3.41	-	-	0.00	0.00	0.00
CH ₄ (mg/m ³ , dry)	Measurement port G - Transversal distance (m)										
	-0.45	-0.30	-0.15	-0.10	-0.05	0	0.05	0.10	0.15	0.30	0.45
Mean	0.00	0.00	0.00	-	-	0.00	-	-	0.00	0.00	0.00
Std. deviation	0.00	0.00	0.00	-	-	0.00	-	-	0.00	0.00	0.00
Uncertainty	123.96	123.96	123.96	-	-	123.96	-	-	123.96	123.96	123.96
5 th percentile	0.00	0.00	0.00	-	-	0.00	-	-	0.00	0.00	0.00
25 th percentile	0.00	0.00	0.00	-	-	0.00	-	-	0.00	0.00	0.00
50 th percentile	0.00	0.00	0.00	-	-	0.00	-	-	0.00	0.00	0.00
75 th percentile	0.00	0.00	0.00	-	-	0.00	-	-	0.00	0.00	0.00
95 th percentile	0.00	0.00	0.00	-	-	0.00	-	-	0.00	0.00	0.00

B.5.7 Local Nitric Oxide Concentration

NO (mg/m ³ , dry)	Measurement port A - Transversal distance (m)										
	-0.45	-0.25	-0.15	-0.10	-0.05	0	0.05	0.10	0.15	0.25	0.45
Mean	497.88	511.75	487.08	305.94	363.10	534.52	306.16	302.49	493.84	611.09	260.80
Std. deviation	11.50	25.37	14.38	5.65	8.09	4.44	6.30	5.50	11.66	8.14	32.64
Uncertainty	30.64	30.82	30.70	30.56	30.58	30.55	30.57	30.56	30.62	30.58	31.69
5 th percentile	474.89	474.97	460.76	292.96	348.57	528.32	299.36	295.08	470.75	594.54	225.76
25 th percentile	491.77	491.60	476.68	305.29	357.47	530.76	301.14	298.87	487.25	604.50	232.31
50 th percentile	502.18	506.15	489.24	307.95	366.39	533.87	304.88	300.73	495.71	614.73	247.87
75 th percentile	507.62	539.30	498.19	309.97	368.89	537.98	308.90	306.66	502.02	616.32	299.46
95 th percentile	509.87	554.26	508.66	310.88	372.25	541.32	320.97	313.24	511.23	618.73	310.88
NO (mg/m ³ , dry)	Measurement port B - Transversal distance (m)										
	-0.45	-0.25	-0.15	-0.10	-0.05	0	0.05	0.10	0.15	0.25	0.45
Mean	505.97	472.14	523.82	674.85	920.42	614.29	503.52	353.35	355.84	648.91	640.06
Std. deviation	5.79	5.59	4.56	9.91	30.56	22.42	10.08	7.05	6.81	3.63	5.23
Uncertainty	30.56	30.57	30.56	30.62	30.96	30.82	30.61	30.57	30.57	30.56	30.56
5 th percentile	498.93	462.16	518.60	656.60	861.41	587.89	486.03	340.21	346.21	643.27	632.90
25 th percentile	501.43	468.72	519.96	669.16	905.06	597.35	496.35	348.44	349.70	644.93	635.70
50 th percentile	505.58	472.93	523.28	673.52	929.16	604.36	503.08	355.37	354.41	650.10	639.66
75 th percentile	508.89	475.59	527.95	683.93	941.89	634.29	510.77	358.31	362.33	651.57	643.98
95 th percentile	518.28	481.33	531.65	687.93	959.10	657.44	518.96	363.49	365.74	654.14	649.06
NO (mg/m ³ , dry)	Measurement port C - Transversal distance (m)										
	-0.45	-0.25	-0.15	-0.10	-0.05	0	0.05	0.10	0.15	0.25	0.45
Mean	527.13	579.49	676.45	427.53	1046.72	455.60	828.35	722.51	663.15	679.95	493.72
Std. deviation	7.51	7.02	10.73	30.82	30.22	16.60	14.82	9.27	8.88	18.12	13.74
Uncertainty	30.61	30.57	30.61	31.08	31.53	30.69	30.66	30.59	30.59	30.66	30.63
5 th percentile	514.37	565.75	663.92	375.24	977.92	432.15	801.31	707.65	649.35	640.19	479.79
25 th percentile	520.49	575.18	666.66	410.45	1028.81	441.03	819.17	715.12	657.79	672.88	484.62
50 th percentile	530.11	580.25	673.27	425.90	1055.19	447.57	827.45	722.63	661.36	683.07	490.77
75 th percentile	532.03	585.76	686.60	454.80	1068.35	471.85	836.12	729.94	666.93	691.48	495.67
95 th percentile	537.35	588.75	693.34	472.81	1080.30	481.35	854.18	738.26	682.71	703.12	528.95
NO (mg/m ³ , dry)	Measurement port D - Transversal distance (m)										
	-0.45	-0.25	-0.15	-0.10	-0.05	0	0.05	0.10	0.15	0.25	0.45
Mean	510.06	443.43	409.74	-	449.09	508.33	509.95	-	528.22	522.56	648.41
Std. deviation	5.95	36.09	51.55	-	11.00	14.82	27.66	-	17.56	4.46	16.62
Uncertainty	30.56	31.21	31.47	-	30.61	30.65	30.73	-	30.64	30.56	30.65
5 th percentile	501.06	371.40	331.52	-	431.05	480.97	480.55	-	506.63	514.73	610.79
25 th percentile	505.51	430.23	365.74	-	437.13	495.49	489.90	-	515.09	519.58	642.03
50 th percentile	510.30	447.71	410.63	-	452.65	514.74	502.32	-	522.67	523.07	651.60
75 th percentile	514.74	471.82	447.55	-	459.16	519.74	517.79	-	539.11	525.57	662.22
95 th percentile	519.76	489.46	491.26	-	462.16	523.50	563.50	-	564.34	529.14	665.61

NO (mg/m ³ , dry)	Measurement port E - Transversal distance (m)										
	-0.45	-0.25	-0.15	-0.10	-0.05	0	0.05	0.10	0.15	0.25	0.45
Mean	533.45	537.14	502.70	-	361.17	426.76	494.85	-	523.34	462.27	457.69
Std. deviation	20.17	14.12	10.61	-	8.02	5.38	11.22	-	4.00	10.30	3.37
Uncertainty	30.66	30.64	30.61	-	30.58	30.56	30.61	-	30.55	30.60	30.55
5 th percentile	496.98	513.36	481.40	-	349.86	420.39	473.10	-	516.74	448.17	453.58
25 th percentile	519.88	524.53	496.66	-	354.73	421.96	489.36	-	519.67	452.42	454.65
50 th percentile	536.19	543.35	502.40	-	360.13	425.33	497.93	-	523.96	461.13	457.08
75 th percentile	548.37	548.14	508.94	-	368.18	430.62	502.34	-	526.48	469.51	461.30
95 th percentile	562.51	553.03	520.89	-	373.68	436.61	511.74	-	529.02	480.04	462.74
NO (mg/m ³ , dry)	Measurement port F - Transversal distance (m)										
	-0.45	-0.30	-0.15	-0.10	-0.05	0	0.05	0.10	0.15	0.30	0.45
Mean	472.02	498.47	524.14	-	-	495.25	-	-	519.22	510.91	519.78
Std. deviation	20.65	31.01	16.27	-	-	19.64	-	-	10.93	13.86	21.72
Uncertainty	30.67	30.88	30.68	-	-	30.73	-	-	30.58	30.61	30.71
5 th percentile	441.92	447.64	501.93	-	-	468.15	-	-	499.23	495.78	489.31
25 th percentile	457.66	472.11	510.09	-	-	480.28	-	-	512.37	499.18	499.91
50 th percentile	472.36	500.93	518.67	-	-	489.06	-	-	518.96	506.44	515.56
75 th percentile	481.49	524.10	540.45	-	-	513.93	-	-	524.68	522.37	538.09
95 th percentile	513.07	549.61	551.39	-	-	529.08	-	-	539.51	534.94	556.05
NO (mg/m ³ , dry)	Measurement port G - Transversal distance (m)										
	-0.45	-0.30	-0.15	-0.10	-0.05	0	0.05	0.10	0.15	0.30	0.45
Mean	486.92	544.73	520.67	-	-	498.18	-	-	534.73	510.63	505.54
Std. deviation	9.98	18.33	25.40	-	-	7.36	-	-	16.67	8.94	7.75
Uncertainty	30.65	30.73	30.75	-	-	30.57	-	-	30.70	30.57	30.58
5 th percentile	476.30	514.31	481.97	-	-	486.13	-	-	508.79	494.52	493.76
25 th percentile	478.69	524.10	497.60	-	-	490.70	-	-	520.53	504.72	500.02
50 th percentile	485.62	550.10	523.03	-	-	498.57	-	-	530.18	511.37	505.44
75 th percentile	489.54	557.79	539.13	-	-	505.44	-	-	550.71	514.31	510.96
95 th percentile	508.29	569.17	559.34	-	-	507.22	-	-	558.78	526.72	519.88

B.5.8 Total Radiative Heat Flux

Heat flux (kW/m ²)	Measurement port						
	A	B	C	D	E	F	G
Mean	138.90	153.17	172.56	186.87	164.51	154.16	129.90
Std. deviation	1.54	1.50	1.84	3.22	2.48	2.57	2.37
Uncertainty	9.32	10.00	10.92	11.60	10.54	10.05	8.89
5 th percentile	136.04	150.63	169.63	181.19	160.07	150.59	125.82
25 th percentile	137.90	152.18	171.48	184.76	162.73	152.29	128.21
50 th percentile	139.02	153.14	172.49	187.36	164.76	153.84	129.93
75 th percentile	140.10	154.52	173.62	189.41	166.27	156.01	131.49
95 th percentile	141.11	155.51	175.58	191.31	168.16	158.70	133.89

